

AFRL-RX-WP-TM-2010-4117

COLLABORATIVE RESEARCH AND DEVELOPMENT (CR&D)

Delivery Order 0020: Novel Low Friction Hard Coatings for Applications in Multiple Environments

Chris Muratore

Universal Technology Corporation

FEBRUARY 2008
Final Report

Approved for public release; distribution unlimited.

See additional restrictions described on inside pages

STINFO COPY

AIR FORCE RESEARCH LABORATORY
MATERIALS AND MANUFACTURING DIRECTORATE
WRIGHT-PATTERSON AIR FORCE BASE, OH 45433-7750
AIR FORCE MATERIEL COMMAND
UNITED STATES AIR FORCE

NOTICE AND SIGNATURE PAGE

Using Government drawings, specifications, or other data included in this document for any purpose other than Government procurement does not in any way obligate the U.S. Government. The fact that the Government formulated or supplied the drawings, specifications, or other data does not license the holder or any other person or corporation; or convey any rights or permission to manufacture, use, or sell any patented invention that may relate to them.

This report was cleared for public release by the USAF 88th Air Base Wing (88 ABW) Public Affairs Office (PAO) and is available to the general public, including foreign nationals. Copies may be obtained from the Defense Technical Information Center (DTIC) (http://www.dtic.mil).

AFRL-RX-WP-TM-2010-4117 HAS BEEN REVIEWED AND IS APPROVED FOR PUBLICATION IN ACCORDANCE WITH THE ASSIGNED DISTRIBUTION STATEMENT.

*//Signature//	//Signature//
MARK GROFF Program Manager Business Operations Branch Materials & Manufacturing Directorate	KENNETH A. FEESER Branch Chief Business Operations Branch Materials & Manufacturing Directorate

This report is published in the interest of scientific and technical information exchange, and its publication does not constitute the Government's approval or disapproval of its ideas or findings.

*Disseminated copies will show "//Signature//" stamped or typed above the signature blocks.

REPORT DOCUMENTATION PAGE

Form Approved
OMB No. 0704-0188

The public reporting burden for this collection of information is estimated to average 1 hour per response, including the time for reviewing instructions, searching existing data sources, gathering and maintaining the data needed, and completing and reviewing the collection of information. Send comments regarding this burden estimate or any other aspect of this collection of information, including suggestions for reducing this burden, to Department of Defense, Washington Headquarters Services, Directorate for Information Operations and Reports (0704-0188), 1215 Jefferson Davis Highway, Suite 1204, Arlington, VA 22202-4302. Respondents should be aware that notwithstanding any other provision of law, no person shall be subject to any penalty for failing to comply with a collection of information if it does not display a currently valid OMB control number. **PLEASE DO NOT RETURN YOUR FORM TO THE ABOVE ADDRESS**.

1. REPORT DATE *(DD-MM-YY)*	2. REPORT TYPE	3. DATES COVERED *(From - To)*
February 2008	Final	02 August 2004 – 01 February 2008

4. TITLE AND SUBTITLE
COLLABORATIVE RESEARCH AND DEVELOPMENT (CR&D)
Delivery Order 0020: Novel Low Friction Hard Coatings for Applications in Multiple Environments

5a. CONTRACT NUMBER
F33615-03-D-5801-0020

5b. GRANT NUMBER

5c. PROGRAM ELEMENT NUMBER
62102F

6. AUTHOR(S)
Chris Muratore

5d. PROJECT NUMBER
4349

5e. TASK NUMBER
L0

5f. WORK UNIT NUMBER
4349L0VT

7. PERFORMING ORGANIZATION NAME(S) AND ADDRESS(ES)
Universal Technology Corporation
1270 North Fairfield Road
Dayton, OH 45432-2600

8. PERFORMING ORGANIZATION REPORT NUMBER
S-531-020

9. SPONSORING/MONITORING AGENCY NAME(S) AND ADDRESS(ES)
Air Force Research Laboratory
Materials and Manufacturing Directorate
Wright-Patterson Air Force Base, OH 45433-7750
Air Force Materiel Command
United States Air Force

10. SPONSORING/MONITORING AGENCY ACRONYM(S)
AFRL/RXOB

11. SPONSORING/MONITORING AGENCY REPORT NUMBER(S)
AFRL-RX-WP-TM-2010-4117

12. DISTRIBUTION/AVAILABILITY STATEMENT
Approved for public release; distribution unlimited.

13. SUPPLEMENTARY NOTES
PAO Case Number: 88ABW 2010-0717; Clearance Date: 22 Feb 2010.

14. ABSTRACT
This research in support of the Air Force Research Laboratory Materials and Manufacturing Directorate was conducted at Wright-Patterson AFB, Ohio and other locations from 02 August 2004 through 1 February 2008. This work has centered on the development of novel plasma-based processes for materials to reduce friction and/or protect against wear. The work has been diverse and extensive, with applications ranging from high mach engines to high frequency micro-switches. Enclosed is a collection of seventeen peer reviewed journal articles authored or co-authored by Chris Muratore while working under this contract. The papers should effectively account for the technical work completed under this task order at AFRL, and with collaborators in industry and academia. In addition to the technical work featured in the journal articles, Chris also worked on proposals for funding, mentoring and advising of graduate students as well as post-doctoral researchers, laboratory maintenance and management. He presented the data at conferences, with three invited talks, and was a session chair at several conferences he attended.

15. SUBJECT TERMS
plasma-based processes

16. SECURITY CLASSIFICATION OF:			17. LIMITATION OF ABSTRACT:	18. NUMBER OF PAGES	19a. NAME OF RESPONSIBLE PERSON (Monitor)
a. REPORT	b. ABSTRACT	c. THIS PAGE			Mark Groff
Unclassified	Unclassified	Unclassified	SAR	168	19b. TELEPHONE NUMBER *(Include Area Code)* N/A

Standard Form 298 (Rev. 8-98)
Prescribed by ANSI Std. Z39-18

Introduction

This document has been submitted to Universal Technology Corporation (UTC) to serve as the final report for Chris Muratore working for the US Air Force Research Laboratory (AFRL) through Universal Technology Corporation under contract number F33615-03-D-5801, Collaborative Research and Development task order 531-20 from August 2004 to May 2008. This work has centered on the development of novel plasma-based processes for materials to reduce friction and/or protect against wear. The work has been diverse and extensive, with applications ranging from high mach engines to high frequency micro-switches. Enclosed is a collection of seventeen peer reviewed journal articles authored or co-authored by Chris Muratore while working under this contract. The papers should effectively account for the technical work completed under this task order at AFRL, and with collaborators in industry and academia. In addition to the technical work featured in the journal articles, Chris also worked on proposals for funding, mentoring and advising of graduate students as well as post-doctoral researchers, laboratory maintenance and management. He presented the data at conferences, with three invited talks, and was a session chair at several conferences he attended.

Explanatory notes for journal articles

All papers are numbered to assist the reader of this report. The collection of papers are divided into two categories; 1) authored papers and 2) co-authored papers. The papers in each category are currently numbered in chronological order. Below, a brief explanation of the nature and extent of the work performed by Chris Muratore as an employee of UTC at AFRL is presented for all papers.

Authored Papers

1. Growth and characterization of Nanocomposite Yttria-Stabilized Zirconia with Ag and Mo.
2. Tribology of Adaptive Nanocomposite Yttria-Stabilized Zirconia Coatings Containing Silver and Molybdenum from 25 to 700°C.
3. Molybdenum Disulfide as a Lubricant and Catalyst in Adaptive Nanocomposite Coatings.
4. Multilayered YSZ-Ag-Mo/TiN Adaptive Tribological Nanocomposite Coatings.
5. Adaptive Nanocomposite Coatings with a Titanium Nitride Diffusion Barrier Mask for High-Temperature Tribological Applications.
6. Oxygen Plasma Treatment and Deposition of CN_X on a Fluorinated Polymer Matrix Composite for Improved Erosion Resistance.
7. Smart Tribological Coatings with Wear Sensing Capability.
8. Control of Molybdenum Disulfide Basal Plane Orientation during Coating Growth in Pulsed Magnetron Sputtering Discharges.

Papers 1-5 focus on high-temperature adaptive tribological coating materials that demonstrate multiple adaptive mechanisms that change the surface chemistry and/or

morphology in order to provide a low shear surface to a sliding contact. Initial mechanisms were diffusion and tribo-oxidation (1-2). Later, techniques to modulate diffusion (papers 4 and 5) and employ catalysis for the production of novel solid lubricant phases (paper 3) were explored. These materials are unparalled in reducing friction over a broad temperature range of 25-700 °C. These materials an techniques were developed by Chris Muratore at AFRL in cooperation with Andrey Voevodin and others as listed on the papers.

Paper 6 describes a novel plasma treatment technique that enables depostion of coating materials on fluorinated polymer surfaces. The paper specifically describes a carbon nitride material that was effective in reducing erosive wear of polymer composites with a fluorinated polymer matrix that has mechanical properties that are suitable for propulsion applications. These materials an techniques were developed by Chris Muratore at AFRL in cooperation with Andrey Voevodin and others as listed on the papers.

Paper 7 describes a new in situ wear sensing technique useful in the laboratory and potentially useful in AF applications. Thin layers of different materials that fluoresce with characteristic spectra under laser illumination were deposited throughout a tribological coating material. By monitoring the light scattered from a worn surface, the extent of wear could be determined. The concept was co-developed with David Clarke at University of California at Santa Barbara, and apparatus for testing was developed by Chris Muratore at AFRL in cooperation with Andrey Voevodin and John G. Jones.

Paper 8 describes new processing structure relationships in MoS_2 thin films that allows remarkable control of the surface properties of the material. The concepts developed in this paper are currently fueling research efforts in diverse areas. This concept was developed entirely by Chris Muratore.

Co-Authored Papers

9. Recent Advances in Hard, Tough, and Low Friction Nanocomposite Coatings.
10. Tribological Performance of Hybrid Filtered Arc-Magnetron Coatings. Part I: Coating Deposition Process and Basic Coating Properties Characterization.
11. Plasma Diagnostics of Hybrid Magnetron Sputtering and Pulsed Laser Deposition.
12. Tunable Friction Behavior of Oriented Carbon Nanotube Films.
13. Self-Lubrication of Hot YSZ-Ag-Mo Nanocomposite Coatings.
14. Silver Diffusion and High-Temperature Lubrication Mechanisms of YSZ-Ag-Mo Based Nanocomposite Coatings.
15. Adaptive Mo_2N/MoS_2/Ag Tribological Nanocomposite Coatings for Aerospace Applications.
16. Plasma Treatment of Carbon Nanotubes.

17. Electrical Switching Using Compliant Metal Infiltrated Multi-Wall Nanotube Arrays.

Paper 9 is a review of nanocomposite coatings. A section on temperature adaptive coatings was included and written by Chris Muratore.

Paper 10 describes a hard coating deposition process. Chris Muratore provided x-ray diffraction analysis that assisted the primary investigators in understanding the process chemistry.

Paper 11 shows plasma characterization results in a novel synchronized pulsed laser/pulsed sputtering coating deposition process, and correlates the results to structural characteristics of materials processed under different conditions. The idea was developed by Chris Muratore and Andrey Voevodin. John Jones and Adam Waite performed spectroscopy in the plasmas.

Paper 12 described the mechanical behavior of oriented carbon nanotubes. Plasma treatment and subsequent characterization of the nanotubes was performed by Chris Muratore and Andrey Voevodin in this collaborative work with Greg Sawyer at the University of Florida.

Paper 13 is a summary of coating concepts developed by Chris Muratore and Andrey Voevodin, (covered in papers 1-5) found in Defense Tech Briefs. The presence of our work in this venue may suggest that this work strongly appeals to the USAF. The author of this document is unknown, but most figures and text were borrowed from papers 1-5 and Paper 14.

Paper 14 describes results from microscopy studies if materials described in Papers 1,2,4 and 5 with some analysis provided by Chris Muratore.

Paper 15 was a collaborative work with Samir Aouadi at Southeren Illinois University, Carbondale. Professor Aouadi used the catalytic tribochemistry concepts described in Paper 3 to further explore surface chemistry phenomena in temperature adaptive tribological coatings.

Paper 16 describes the processing work used in Paper 12. The processes were conceived by Chris Muratore and he also performed characterization of all materials. Spectroscopy was performed by John Jones and Adam Waite.

Paper 17 was submitted to the Journal of Materials Research and is a collaborative effort with Rensselear Polytechnic institute and the University of Florida. Chris Muratore and Andrey Voevodin developed techniques to metallized carbon nanotubes to produce different electrical and mechanical properties of interest for micro-switching applications.

Presentations

Below is a list of presentations that have been given by Chris Muratore on the work performed under this contract.

1. "Adaptive nanocomposite tribological materials and an in situ FIB technique for TEM imaging of sliding contact interfaces", (invited) C. Muratore, J.J. Hu, R. Wheeler, A.A. Voevodin, Materials Research Society Spring Meeting, March 24-28, 2008, San Francisco, California (USA).
2. "Adaptive tribological nanocomposite coatings" (invited) C. Muratore, J.J. Hu, J.G. Jones, A.A. Voevodin, 54th Annual American Vacuum Society Symposium, October 14-19, 2007, Seattle, Washington (USA).
3. "Recent Developments in Nanocomposite Tribological Coatings" (invited), C. Muratore, J.J. Hu, J.G. Jones, A. A. Voevodin, 18th Annual Advanced Coatings and Surface Engineering Workshop, April 19-21 2007 Golden, CO.
4. "Nanocomposite coatings demonstrating temperature adaptation over multiple thermal cycles from 25-700 °C". C. Muratore, J.J. Hu, J.G. Jones, A.A. Voevodin, International Conference on Metallurgical Coatings and Thin Films, April 23-27, 2007, San Diego, CA, p.11.
5. "Adaptive Tribological Coatings for High Temperature Sliding in Air" C. Muratore, J.J. Hu, J.G. Jones, A.A. Voevodin, Society of Tribologists and Lubrication Engineers (STLE) 2007, 62nd Annual Meeting, May 6-10, 2007, Pennsylvania, PA.
6. "Tribological Behavior of Pulsed Laser Deposited Mo (W)-S-Se-Te Composite Thin Films in Dry and Humid Environments." J.J. Hu, R.A. Wheeler, P. Shade, A. Shively, R.B. Kerns, D.H. Sergison, J.E. Bultman, J.S. Zabinski, J.H. Sanders, C. Muratore, A.A. Voevodin, Society of Tribologists and Lubrication Engineers (STLE) 2007, 62nd Annual Meeting, May 6-10, 2007, Pennsylvania, PA.
7. "Adaptive nanocomposite coatings designed to provide lubrication throughout a broad temperature range and over multiple thermal cycles" (invited) C. Muratore, J.J. Hu, J.G. Jones, A.A. Voevodin, French Vacuum Society (SFV) 16th International Colloquium on Plasma Processes, June 4-8, 2007, Toulouse, France.
8. "Nanocomposite tribological coatings exhibiting reversible temperature adaptation" (invited), C. Muratore, J.J. Hu, A.A. Voevodin, 17th Annual Advanced Coatings and Surface Engineering Laboratory Workshop, April 27-29, 2006, Golden CO.
9. "Correlation of plasma flux composition to the structure and properties of engineered surfaces" (invited), C. Muratore, A.A. Voevodin, 17th Annual Advanced Coatings and Surface Engineering Laboratory Workshop, April 27-29, 2006, Golden CO.

10. “Multilayered adaptive nanocomposite coatings exhibiting low friction throughout a broad temperature range” C. Muratore, J.J. Hu, A.A. Voevodin, International Conference on Metallurgical Coatings and Thin Films, May 1-5, 2006, San Diego, CA.

11. “Multilayered adaptive nanocomposite coatings exhibiting low friction throughout a broad temperature range and multiple thermal cycles,” C. Muratore, A. A. Voevodin, J.J. Hu, 10th International Conference on Plasma Surface Engineering, September 10-15, 2006, Garmsich-Partenkirchen (Germany).

12. “Growth and characterization of nanocomposite yttria-stabilized zirconia with Ag and Mo” C. Muratore, A.A. Voevodin, J.J. Hu, J.G. Jones, J.S. Zabinski, presented at the International Conference on Metallurgical Coatings and Thin Films, May 2005, San Diego, CA.

Paper 1

Available online at www.sciencedirect.com

SCIENCE DIRECT®

ELSEVIER

Surface & Coatings Technology 200 (2005) 1549 – 1554

SURFACE & COATINGS TECHNOLOGY

www.elsevier.com/locate/surfcoat

Growth and characterization of nanocomposite yttria-stabilized zirconia with Ag and Mo

C. Muratore [a,*], A.A. Voevodin [b], J.J. Hu [c], J.G. Jones [b], J.S. Zabinski [b]

[a] *UTC Inc., Air Force Research Laboratory, Materials and Manufacturing Directorate, Wright Patterson Air Force Base, OH 45433, United States*
[b] *Air Force Research Laboratory, Materials and Manufacturing Directorate, Wright Patterson Air Force Base, OH 45433, United States*
[c] *UES Inc., Air Force Research Laboratory, Materials and Manufacturing Directorate, Wright Patterson Air Force Base, OH 45433, United States*

Available online 13 September 2005

Abstract

The effect of metal additions on the structure and properties of nanocrystalline yttria-stabilized zirconia (YSZ) thin films deposited by a hybrid magnetron sputtering/pulsed laser deposition technique was studied. The materials are candidates for use as adaptive, "chameleon" nanocomposites for tribological applications subjected to thermal cycling up to high (700 °C) temperatures. The composition, structure and mechanical properties of the films were characterized with X-ray photoelectron spectroscopy, electron dispersive spectroscopy scanning electron microscopy, high-resolution transmission electron microscopy, X-ray diffraction and nanoindentation. Increasing the metal content of the films by increasing the magnetron power resulted in decreased zirconia grain sizes for films with silver and/or molybdenum additions. The reduced zirconia grain size was attributed to a decrease in the ion-to-atom ratio during deposition. Unlike the YSZ–Ag films that exhibited reduced hardness with increasing metal content, YSZ–Mo film hardness increased from 12 to 17.5 GPa at 15 and 24 at.% molybdenum, respectively. Adding molybdenum to the films resulted in cracks and holes in the film surface indicative of molybdenum oxidation during processing. Adding both silver and molybdenum eliminated the undesirable surface features found in the YSZ–Mo films.
© 2005 Elsevier B.V. All rights reserved.

Keywords: Nanocomposites; Pulsed laser deposition; Magnetron sputtering; Hardness

1. Introduction

Composite coatings consisting of hard nanocrystalline phases surrounded by amorphous matrix materials have demonstrated remarkable properties for tribological applications, such as high hardness [1–3], toughness [4–6], wear resistance and low friction in a broad temperature range [7–9]. Adaptive or "chameleon" nanocomposite coatings are a class of materials that independently adjust surface composition and structure to optimize tribological performance as the ambient environment changes, while also displaying the remarkable hardness and toughness common to nanocrystalline/amorphous composites [10]. For aerospace applications, films that can adapt to a broad range of temperatures in order to provide low friction and wear are of significant interest. Yttria-stabilized zirconia based chameleon coatings containing gold and other solid lubricants exhibit low friction at temperatures of 500 °C and under [11], however, improved performance from room temperature up to 700 °C or higher is desired. In this work the effect of metal additions on microstructure and mechanical properties in YSZ-based nanocomposites was investigated in an effort to develop chameleon nanocomposites with improved tribological performance in a broader temperature range.

The hybrid magnetron sputtering/pulsed laser deposition (MSPLD) process [12] is well-suited for growth of YSZ–metal films as electrically insulating targets are preferred for PLD processes and dc magnetron sources operate most predictably with conductive metal targets. Using separate, single phase target materials rather than composite targets also allows for production of an infinite range of compositions by adjustment of laser repetition rate or magnetron target power density. Additionally, the pulsed laser component of the deposition process provides pulses of high ion flux to periodically increase the ion-to-atom ratio during

* Corresponding author. Tel.: +1 937 643 9463.
E-mail address: chris.muratore@wpafb.af.mil (C. Muratore).

0257-8972/$ - see front matter © 2005 Elsevier B.V. All rights reserved.
doi:10.1016/j.surfcoat.2005.08.032

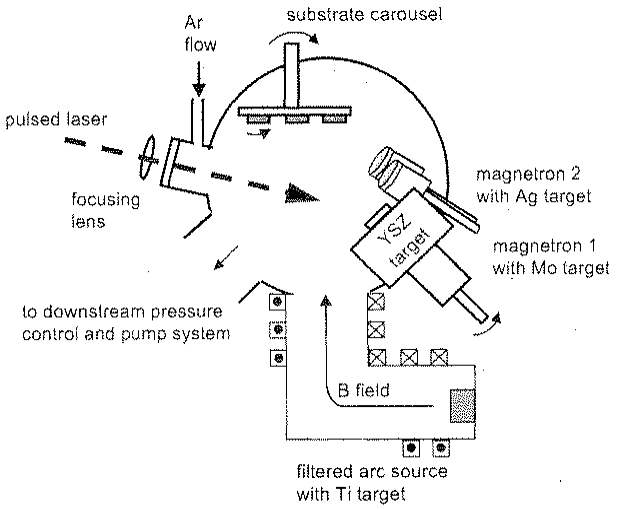


Fig. 1. Schematic of the deposition chamber.

deposition, allowing for control of film microstructure with substrate bias [13]. Metal content was tailored by adjusting the power density to the metal magnetron target or targets, while the laser energy and repetition rate were fixed. YSZ–metal films containing pure silver and pure molybdenum were deposited to examine the effect of inert and reactive metal additions. Films containing both metals were also produced. The details of preparation, structure and mechanical properties of these films are presented in this work.

2. Experimental

All deposition experiments were conducted in a stainless steel chamber evacuated by a 520 l s^{-1} turbomolecular pump to a base pressure of 7×10^{-6} Pa or less. A schematic of the chamber is shown in Fig. 1. Coatings were deposited by magnetron sputtering/pulsed laser deposition (MSPLD) on polished 440C, M50, Inconel 718 substrates, and on (001) Si wafers. Six 1 in. diameter substrates were degreased, then loaded into the chamber and heated to 150 °C and cleaned with energetic argon (≤800 eV) and metal ions (≤650 V) to clean the surface before deposition. The metal ions were produced with a filtered cathodic arc source fitted with a titanium target. The arc source was also used to deposit a thin (<100 nm) titanium adhesion layer, and (<300 nm) graded Ti/ZrO_2 layer to promote film adhesion to the substrates. The chamber was then filled with 1.6 Pa Ar (99.99% pure) at a flow rate of 100 sccm. A KrF excimer laser was used to irradiate a 5 wt.% yttria-stabilized zirconia (YSZ) target with 800 mJ, 25 ns wide UV pulses (248 nm) at a frequency of 30 Hz. Programmable mirrors were used to direct the laser to random positions on the surface of the rotating, 5.0 cm YSZ target. Silver and molybdenum were added to the films by sputtering 3.3 cm targets made of pure silver or pure molybdenum. The dc power density to the magnetrons was adjusted from 1 to 5 W cm^{-2} to control the metal content of each film. During deposition, the substrates were biased to −150 V dc, and maintained at 150 °C. A 2.5 cm^2 planar probe positioned in the substrate carousel and biased to −150 V dc was also used to measure the ion flux from the magnetron for the range of target power densities for the silver target. Deposition times to obtain ≈2 μm thick films varied from 55 to 85 min depending on the magnetron power density.

Film composition was measured with a Surface Science Instruments M-Probe X-ray photoelectron spectrometer (XPS). Samples were sputtered clean with 5000 eV Ar^+ ions immediately prior to all XPS measurements. The structure of the films was characterized using glancing incidence X-ray diffraction, with θ fixed at 8° for all scans. An MTS Nanoindenter XP was used to measure the hardness and elastic modulus of all films. Transmission electron microscopy (TEM), scanning electron microscopy (SEM), and electron diffraction analysis were also used to characterize film microstructure and composition.

3. Results

3.1. YSZ–Ag films

During deposition of the YSZ–silver films, the ion flux from the magnetron was found to increase linearly from 1.6×10^{15} cm^{-2} s^{-1} to 3.3×10^{15} cm^{-2} s^{-1}, as the target power density was increased from 1.5 W cm^{-2} to 3 W cm^{-2}. Increasing the magnetron power had no influence on the ion flux from the pulsed laser plasma, except to slightly increase the baseline flux over the 16 ns laser period and ensuing afterglow (<40 μs). XPS analysis showed that the YSZ–Ag films contained 13–20 at.% silver. The SEM micrograph of the film surface in Fig. 2 shows bright, silver-rich clusters of crystallites approximately 500–1000 nm in

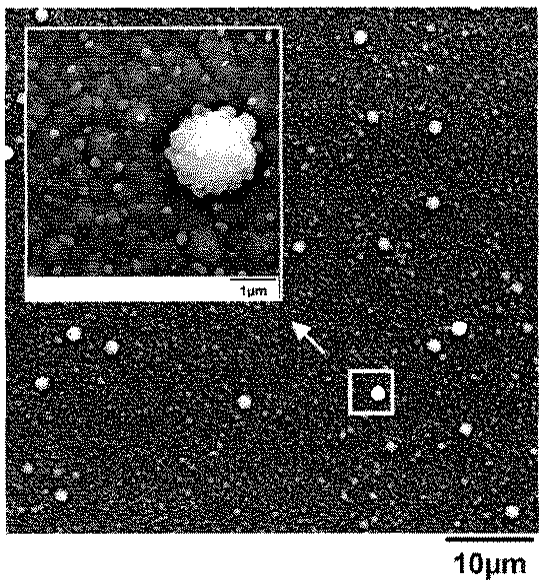


Fig. 2. Secondary electron micrograph of the YSZ–20% Ag film surface.

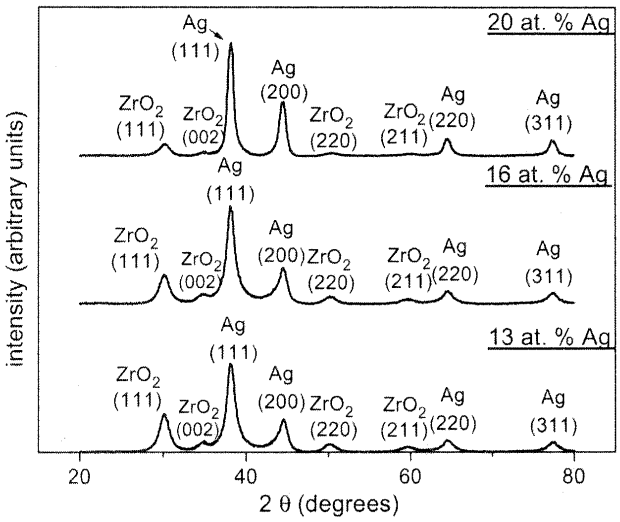


Fig. 3. X-ray diffraction patterns for YSZ–Ag films of different composition.

diameter that protrude above the surface. Smaller clusters of zirconia crystallites with silver at the boundaries make up the bulk of the surface. Fig. 3 shows X-ray diffraction spectra of the YSZ–Ag films, which exhibited broad tetragonal zirconia peaks [14] and sharper silver peaks [15]. The intensity of the t-ZrO_2 (111) peak decreased with increased silver content. The hardness of the YSZ–Ag films decreased monotonically with increasing silver content as shown in Fig. 4, however the modulus stabilized at 230 GPa for the films with more silver.

3.2. YSZ–Mo films

Yttria-stabilized zirconia films containing 9–23 at.% molybdenum were also deposited with the MSPLD technique. Fig. 5a shows the surface morphology of the film containing 9 at.% molybdenum, and Fig. 5b shows the surface for the film with 24 at.% molybdenum. Both surfaces were marked by shallow scratches from the initial condition of the substrate surface (Fig. 5a and b), and fissures as shown by the higher magnification inset in Fig. 5b which is representative of all of the features shown in the lower magnification views. The areal density of the fissures was linearly proportional to the concentration of molybdenum. X-ray diffractograms of the YSZ–Mo films (Fig. 6) showed that the relative intensity of the (111) t-ZrO_2 peak decreased with increasing metal content, following the same trend observed for the YSZ–Ag material. The zirconia peaks were increasingly broader with molybdenum content. The molybdenum diffraction peak [16] sharpness increased with the content of the metal in the film. X-ray peaks from the substrate were also apparent, even though the YSZ–Mo coatings were of the same thickness as the YSZ–Ag coatings. Fig. 7 shows that the hardness and elastic modulus also increased with metal content, contrary to that observed for silver additions to YSZ in this work, and gold additions studied previously [17].

3.3. YSZ–Ag–Mo films

These films all contained approximately 10 at.% molybdenum (±2%), and the silver content was varied from 5 to 24 at.%. Fig. 8 shows that the surface of the YSZ–Ag–Mo film containing 24% silver is similar to the YSZ–Ag film surface with occasional large, silver rich grains and small clusters of silver in the boundaries between clusters of crystallites. None of the fissures present in the YSZ–Mo films were observed in this specimen. Fig. 9 shows the X-ray diffractograms for YSZ–metal composites containing both silver and molybdenum. Again, the t-ZrO_2 (111) peak diminishes with increasing silver content. Molybdenum diffraction peaks were observed in the YSZ–Ag–Mo composite with the lowest Ag content, however were not detected in the films with 16 and 24 at.% silver. In the coating containing 5% silver the sharp Fe (110) peak is present, however, in YSZ–Ag–Mo coatings with higher silver contents, the Ag (200) peak obscured the peak from the substrate. The hardness and modulus decreased significantly between the films containing between 5 and 16 at.% silver, but were maintained for a further increase in silver content as shown in Fig. 10. With hardness values of ≈6 GPa, the YSZ–Ag–Mo films were significantly softer than any of the films containing only one metal. A high resolution TEM micrograph in Fig. 11 reveals nanocrystalline silver grains of <20 nm.

4. Discussion

4.1. YSZ–Ag films

The broad (111) and (002) ZrO_2 X-ray diffraction peaks in Fig. 3 indicate that the t-ZrO_2 was nanocrystalline [18], and the lack of diffraction intensity compared to the other phases present in lesser amount suggests that some amorphous ZrO_2 must also be present. The decrease in intensity of the (111) and (002) ZrO_2 diffraction peaks with increasing metal content shown in Fig. 3 was likely the

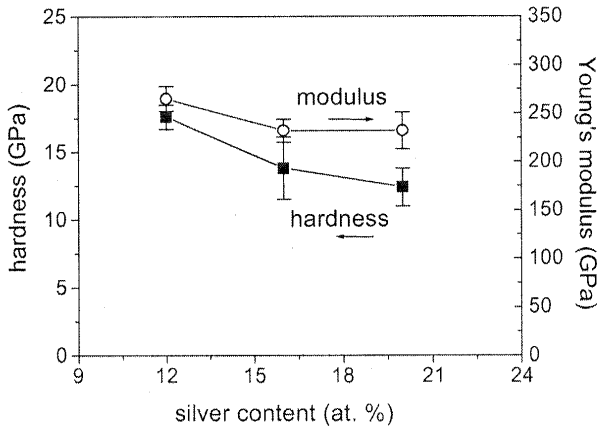


Fig. 4. Hardness and modulus of the YSZ–Ag films of different composition.

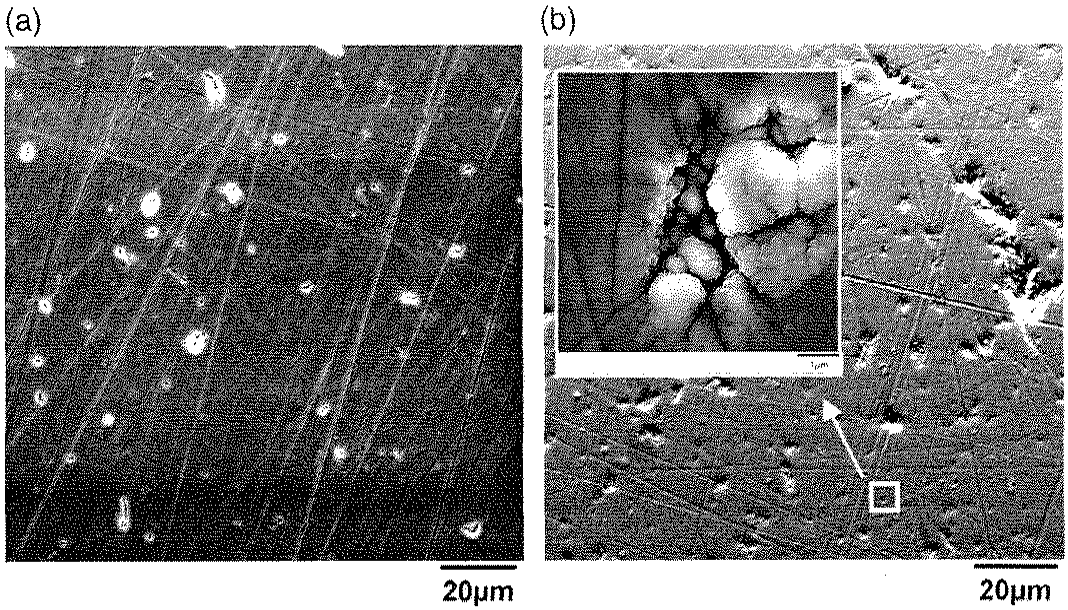


Fig. 5. Secondary electron micrograph of the (a) YSZ–9% Mo and (b) YSZ–24% Mo film surface.

result of increased metal atom flux during deposition when the ion-to-atom ratio is considered. As indicated earlier, the ion flux to the substrate was linearly dependent on the magnetron power for YSZ–Ag deposition. However, based on the accompanying deposition rate increase, the silver atom flux increased by a factor of 10 as the target density was increased from 1.5 W cm^{-2} to 3 W cm^{-2}. For relatively low deposition temperatures comparable to those used in this work, other authors have shown that energetic ions are necessary to induce crystallization of YSZ [13,19], and the energy of the ions can be adjusted for modification of ZrO_2 texture. Thus, increasing magnetron power significantly reduced the energy deposited per atom, and likely inhibited growth of crystalline ZrO_2 at 150 °C, in agreement with results shown by other authors for ion-assisted growth of pure YSZ [13,19].

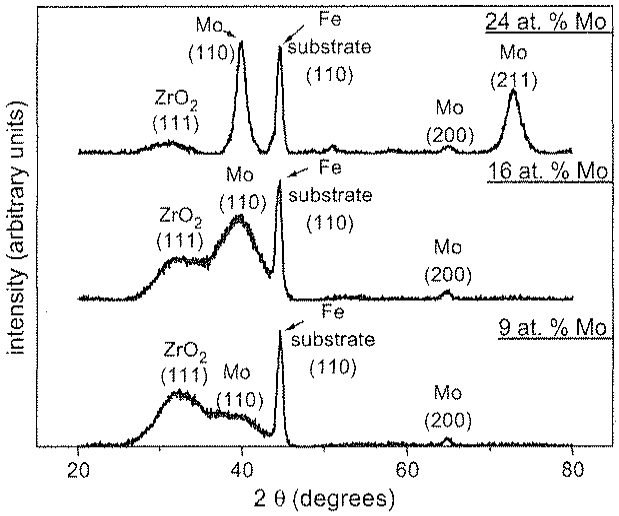


Fig. 6. X-ray diffraction patterns for the YSZ–Mo films of different composition.

Increasing the silver content also reduced the hardness of the films, which is a similar result to that observed for the YSZ–gold system [17], where it was postulated that the addition of soft metal to the matrix increases the ductility of the matrix. Additionally, the absence of chemical bonding between the zirconia nanocrystals and additional silver in the matrix could further reduce the hardness. The modulus for the YSZ–silver films showed stabilization at 230 MPa for the two higher silver compositions also as seen in the YSZ–gold system in the same composition range [17], however there were not enough data points in this work to verify the existence of a clear trend.

4.2. YSZ–Mo films

The fissures shown in Fig. 5 on the surface of the film suggest accommodation of a volume increase, as they were typically accompanied by film material that had been

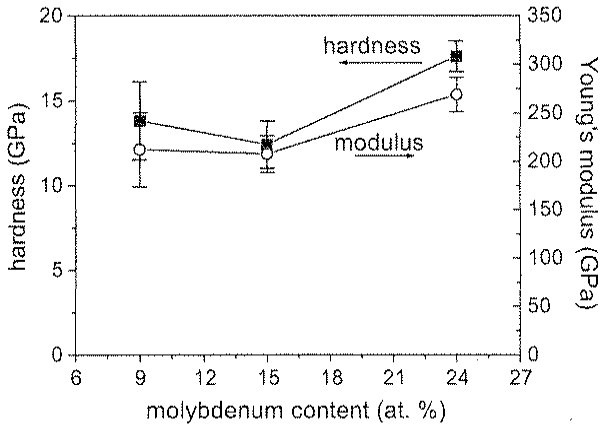


Fig. 7. Hardness and modulus of the YSZ–Mo films of different composition.

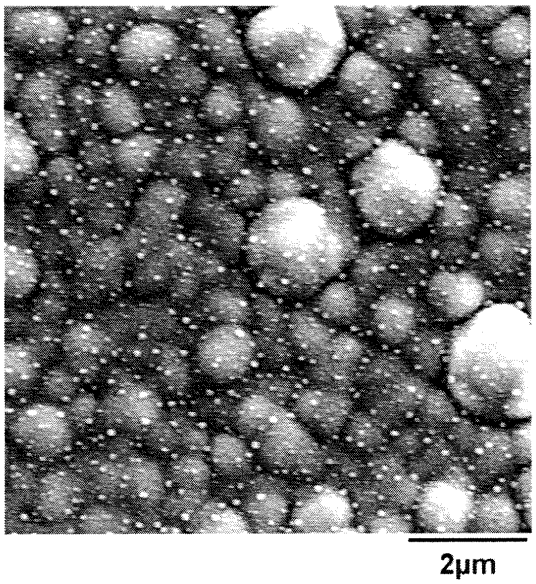


Fig. 8. Secondary electron micrograph of the YSZ–24% Ag–10% Mo film surface.

pushed out relative to the substrate. Such a volume increase could be caused by formation of MoO_3 in the vapor phase [20] or solid phase [21] during processing. Volatilization of MoO_3 is reported to occur only at temperatures above 400 °C in air [20], however no data were found by the authors that applied to a low pressure plasma environment in the presence of atomic oxygen. Whether produced in the gas or solid phase, other authors have shown that production of molybdenum trioxide can result in cracks and enlarged pores similar to those observed here [20,21].

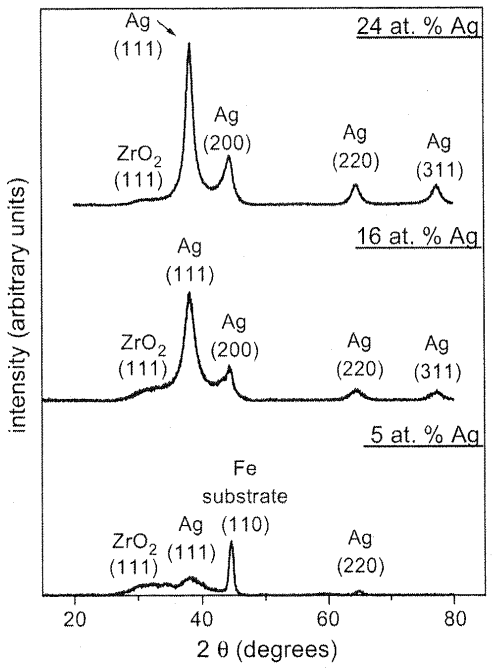


Fig. 9. X-ray diffraction patterns for YSZ–Ag–Mo films of different composition.

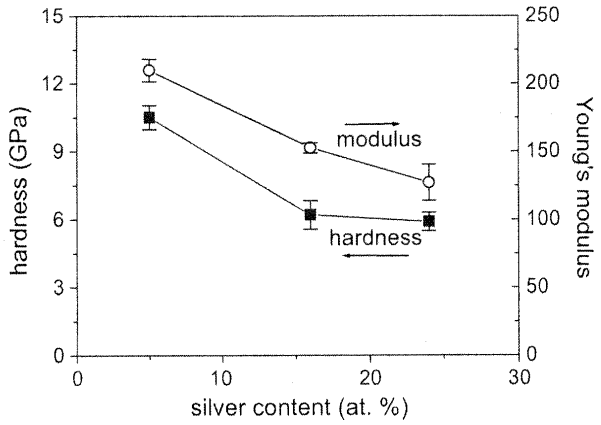


Fig. 10. Hardness and modulus of the YSZ–Ag–Mo films of different composition.

The trend of decreased (111) ZrO_2 diffraction peak intensity and increased width was consistent with that observed in the YSZ–silver films. It is assumed again that the increased neutral metal atom flux from the increased target power density resulted in the composition-dependent structure of zirconia, however, molybdenum has been shown by other authors to inhibit grain growth in zirconia [22]. Further experiments will be conducted to see if molybdenum is effective in maintaining zirconia in the nanocrystalline state for extended periods of time at high temperature. The substrate peaks appearing in Fig. 5 likely appeared because of the absence of silver (with an X-ray absorption coefficient that is nearly twice that of Zr or Mo), which allows for further penetration of the film by the X-rays [18].

Contrary to the YSZ–Ag films, the hardness and modulus values of the YSZ–Mo films increased with metal

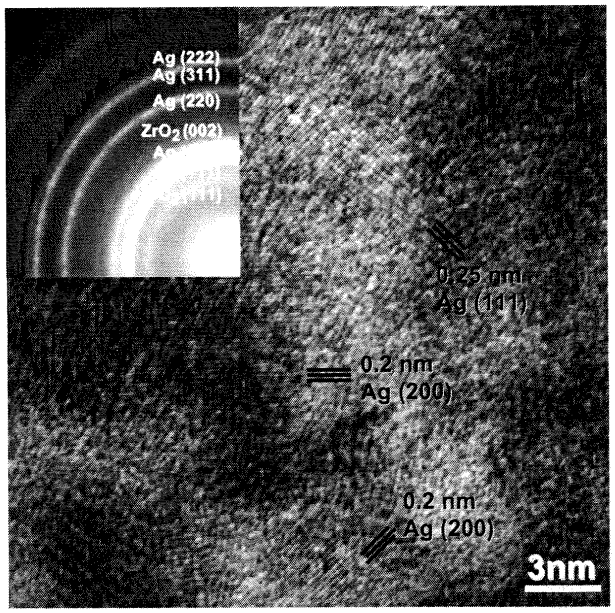


Fig. 11. High-resolution transmission electron micrograph of the YSZ–24% Ag–10% Mo film with selected area diffraction pattern (inset).

content. The hardness increase suggests that the reduction in zirconia grain size and increase in the volume fraction of amorphous zirconia had a stronger effect on mechanical properties than the addition of relatively soft molybdenum metal to the zirconia phase. This hardness increase may have had the same origins as those observed by other authors for nanocrystalline/amorphous matrix composites, where formation and movement of dislocations and cracks are suppressed by interactions between the crystalline and amorphous components [1,23–25]. The effect of increasing Mo content on hardness will be explored, but is expected to result in softening of the films beyond a certain composition due to porosity associated with a reduced ion-to-atom ratio during deposition [26].

4.3. YSZ–Ag–Mo films

Fig. 8 shows that the surface features associated with the addition of molybdenum do not appear when silver is also added. This could have been the result of increased ductility in the matrix associated with the silver addition, or a reduced potential for contact between molybdenum and oxygen due to the increased metal deposition rate [27]. The (111) diffraction peak for zirconia is again diminished between the films containing 16 and 24 at.% silver, but constant molybdenum content, suggesting that ZrO_2 grain growth during deposition was inhibited by the increased neutral flux during the deposition process rather than the presence of molybdenum. Again, all films were 2 μm thick, however the substrate peak was apparent when the silver content was low.

The hardness decreased between the samples containing 5 and 16 at.% silver, presumably because of increased silver content, but then remained constant. This was likely due to competition between the hardening effect from the reduction in zirconia grain size, which significantly decreased between the films with the two higher silver contents and the increase in total metal content. From the X-ray diffraction data in Fig. 9, the grains in the YSZ–Ag–Mo films were significantly smaller for all compositions than for the YSZ–Ag film, which showed a direct correlation between composition and hardness. The YSZ films containing both Ag and Mo were significantly softer than the composite films with only one elemental metal addition, probably because of the combined effects of the reduced ion-to-atom ratio on film porosity [26] and the increased total metal content of the films.

5. Conclusions

A hybrid deposition technique was used to prepare yttria-stabilized zirconia films with a range of silver and molybdenum contents. The films exhibited nanocrystalline and amorphous zirconia phases with a grain size dependence on the atomic percent of metal added to the film. Reduction in zirconia grain size was attributed to the reduction in ion-to-atom ratio during film growth accompanied by increased magnetron power. Zirconia grain size and metal content was also correlated to the mechanical properties of the composite films. The hardness and modulus of the YSZ–Ag materials decreased with increasing metal content, but either increased or stabilized for the YSZ–Mo and YSZ–Ag–Mo films. The addition of pure molybdenum resulted in cracks and holes in the film surface, indicative of molybdenum oxide formation during deposition. Adding silver to the YSZ–Mo films eliminated undesirable surface features.

References

[1] S. Vepřek, J. Vac. Sci. Technol., A, Vac. Surf. Films 17 (1999) 2401.
[2] J. Musil, Surf. Coat. Technol. 125 (2000) 322.
[3] A.A. Voevodin, S.V. Prasad, J.S. Zabinski, J. Appl. Phys. 82 (1997) 855.
[4] J. Musil, J. Vlček, Mater. Chem. Phys. 54 (1998) 116.
[5] C. Mitterer, P.H. Mayrhofer, M. Beschliesser, P. Losbichler, P. Warbichler, F. Hofer, P.N. Gibson, W. Gissler, H. Hruby, J. Musil, J. Vlček, Surf. Coat. Technol. 120 (1999) 405.
[6] A.A. Voevodin, J.S. Zabinski, Thin Solid Films 370 (2000) 223.
[7] A.A. Voevodin, J.P. O'Neill, J.S. Zabinski, Thin Solid Films 342 (1999) 194.
[8] R. Hauert, J. Patscheider, Adv. Eng. Mater. 2 (2000) 247.
[9] A. Savan, E. Pfluger, R. Goller, W. Gissler, Surf. Coat. Technol. 126 (2000) 159.
[10] A.A. Voevodin, T.A. Fritz, J.J. Hu, J.S. Zabinski, J. Vac. Sci. Technol., A, Vac. Surf. Films 20 (2002) 1434.
[11] A.A. Voevodin, J.J. Hu, T.A. Fritz, J.S. Zabinski, Surf. Coat. Technol. 146–147 (2001) 351.
[12] A.A. Voevodin, M.A. Capano, A.J. Safriet, M.S. Donley, J.S. Zabinski, Appl. Phys. Lett. 69 (1996) 188.
[13] A.A. Voevodin, J.G. Jones, J.S. Zabinski, J. Vac. Sci. Technol., A, Vac. Surf. Films 19 (2001) 1320.
[14] JCPDS Powder Diffraction File, International Center for Powder Diffraction Data, Swarthmore, PA, 1998, Card 17-0923.
[15] JCPDS Powder Diffraction File, International Center for Powder Diffraction Data, Swarthmore, PA, 1998, Card 89-3722.
[16] JCPDS Powder Diffraction File, International Center for Powder Diffraction Data, Swarthmore, PA, 1998, Card 47-1320.
[17] A.A. Voevodin, J.J. Hu, J.G. Jones, T.A. Fritz, J.S. Zabinski, Thin Solid Films 401 (2001) 187.
[18] B.D. Cullity, Elements of X-ray Diffraction, 2nd ed., Addison Wesley, Reading, MA, 1978, p. 282.
[19] R.P. Reade, S.R. Church, R.E. Russo, Rev. Sci. Instrum. 66 (1995) 3610.
[20] N. Solak, F. Ustel, M. Urgen, S. Aydin, A.F. Cakir, Surf. Coat. Technol. 174–175 (2003) 713.
[21] K. Kurokawa, H. Houzumi, I. Saeki, H. Takahashi, Mater. Sci. Eng., A Struct. Mater.: Prop. Microstruct. Process. 261 (1999) 292.
[22] K.V.R. Chary, K.R. Reddy, G. Kishan, J.W. Niemantsverdriet, G. Mestk, J. Catal. 226 (2004) 283.
[23] S. Vepřek, S. Reiprich, L. Shizhi, Appl. Phys. Lett. 66 (1995) 2640.
[24] S. Vepřek, S. Reiprich, Thin Solid Films 268 (1995) 64.
[25] S. Christiansen, M. Albrecht, H.P. Strunk, S. Vepřek, J. Vac. Sci. Technol., B 16 (1998).
[26] I. Petrov, P.B. Barna, L. Hultman, J.E. Greene, J. Vac. Sci. Technol., A, Vac. Surf. Films 21 (2003).
[27] D.L. Smith, Thin Film Deposition, McGraw-Hill, Boston, 1995, p. 22.

Paper 2

Available online at www.sciencedirect.com
ScienceDirect
Wear 261 (2006) 797–805
WEAR
www.elsevier.com/locate/wear

Tribology of adaptive nanocomposite yttria-stabilized zirconia coatings containing silver and molybdenum from 25 to 700 °C

C. Muratore [a,*], A.A. Voevodin [b], J.J. Hu [c], J.S. Zabinski [b]

[a] UTC Inc., Air Force Research Laboratory, Materials and Manufacturing Directorate, Wright-Patterson Air Force Base, OH 45433, USA
[b] Air Force Research Laboratory, Materials and Manufacturing Directorate, Wright-Patterson Air Force Base, OH 45433, USA
[c] UES Inc., Air Force Research Laboratory, Materials and Manufacturing Directorate, Wright-Patterson Air Force Base, OH 45433, USA

Received 11 August 2005; received in revised form 23 January 2006; accepted 24 January 2006
Available online 23 March 2006

Abstract

The effect of different types and concentrations of metal additions on the tribological properties of yttria-stabilized zirconia-based coatings was investigated in an effort to develop nanocomposite chameleon coatings exhibiting low friction in air throughout a broad temperature range. A hybrid process of magnetron sputtering and pulsed laser deposition was used to grow nanocrystalline yttria-stabilized zirconia (YSZ) imbedded in an amorphous YSZ/metal matrix. Silver was effective as a lubricant at 500 °C and lower, while molybdenum formed a soft lubricious oxide at higher temperatures. YSZ–Mo composites exhibited cracks and fissures after deposition, which were enlarged after heating. Cracking was eliminated in YSZ-based coatings containing both silver and molybdenum. The YSZ–Ag–Mo coatings also exhibited moderately low friction coefficients across the entire 25–700 °C range. Characterization of the coatings after wear testing revealed that the development of a continuous silver layer protected the underlying YSZ–Mo material from oxidation, provided lubrication up to 500 °C, and allowed for the controlled formation of lubricious molybdenum oxide compounds in the wear track at higher temperatures. High-temperature adaptive lubrication mechanisms resulting from noble metal diffusion and soft oxide formation in areas affected by wear are described.
© 2006 Elsevier B.V. All rights reserved.

Keywords: Adaptive; High-temperature; Nanocomposite

1. Introduction

Adaptive nanocomposites, also known as "chameleon coatings", are a class of materials that automatically adjust surface composition and structure to minimize friction as the ambient environment changes [1–5]. Adaptation results from nanoinclusions in the composite material that assemble into lubricious macrophases when exposed to a particular range of external conditions (i.e., temperature, wear and/or relative humidity). The coatings are designed such that the lubrication mechanisms of each phase are active in the friction contact while exposed to the environment to which they are well-suited, without alteration of the composition or structure of the temporarily dormant solid lubricants.

Nanocomposite chameleon coatings, which evolved from earlier adaptive coating efforts [4–6], employ soft solid lubricant phases in nanocrystalline or amorphous form to avoid the rule-of-mixtures behavior typically observed in larger-grained composites [7], where hardness is proportional to the volume fraction and hardness of each component [8,9]. For example, hard YSZ-based chameleon coatings containing gold (for lubrication up to 500 °C), MoS_2 (for dry air or vacuum), and carbon (for humid conditions) showed relatively low friction when subjected to each of the conditions indicated above, but without a significant reduction in hardness compared to the pure YSZ [3]. In fact, monolithic nanocomposites consisting of hard and soft phases can be harder than the hard phase alone [10,11], and possess superior tribological properties.

In this work, the effect of silver and molybdenum metal additions on the friction coefficient of YSZ-based nanocomposite chameleon coatings between 25–700 °C was investigated in an effort to increase the temperature range in which YSZ–metal nanocomposites, similar to those described above in [3], demonstrate low friction coefficients. YSZ was selected as a matrix material for its excellent thermal and chemical stability at elevated temperatures, high mechanical strength and toughness,

* Corresponding author. Tel.: +937 255 5163; fax: +937 255 2176.
E-mail address: chris.muratore@wpafb.af.mil (C. Muratore).

0043-1648/$ – see front matter © 2006 Elsevier B.V. All rights reserved.
doi:10.1016/j.wear.2006.01.029

and low thermal conductivity. The tribological performance of YSZ, however, is poor [1,12–14], and therefore must be used with a lubricant if it is to come in contact with other surfaces.

Noble metals can be effective solid lubricants for ceramics and other hard materials [15–20]. In previous work with YSZ–Au nanocomposites, Au diffusion and nucleation to the tribo-contact were found to be critical for the adaptive behavior [1,21]. From this perspective, silver is appealing because of its large diffusion coefficient [22,23], which allows the metal to rapidly provide lubrication with increasing tempeature.

Above 500 °C however, silver is less effective in providing lubrication while loaded because of excessive softening [19,24]. One approach for obtaining low friction at the higher end of the desired temperature range (>500 °C) is to incorporate a component that, when heated in air, will readily form soft oxide compounds that deform by plastic flow rather than brittle fracture [25–27]. This mechanism has been observed previously for $ZnO–WS_2$ adaptive coatings, where $ZnWO_4$ was formed during wear at 500 °C [28]. The addition of molybdenum metal was examined in this work to see if lubricious molybdenum trioxide [27,29–31] would form at high temperatures (>500 °C) in air.

Additionally, incorporation of both silver and molybdenum metals in YSZ was studied to see if multiple lubrication mechanisms would operate throughout the 25–700 °C temperature range in a single composite material, with silver lubricating at low and moderate temperatures, and MoO_3 or other molybdenum-based compounds [27,29–33] at higher temperatures.

2. Experimental

Coatings composed of yttria-stabilized zirconia (YSZ) and different concentrations of silver and/or molybdenum metal were deposited with a hybrid filtered vacuum arc/magnetron sputtering/pulsed laser deposition technique [10,34,35]. The metal content was measured with X-ray photoelectron spectroscopy (XPS) after sputter cleaning each sample with 1000 eV Ar^+ ions for 1 min. The microstructure of the coatings was also examined with scanning electron microscopy (SEM) and X-ray diffraction. All coatings used for wear testing were approximately 2 μm thick.

Friction coefficients in air with 30–40% relative humidity were measured with a high temperature ball-on-disc tribometer using a 6.35 mm silicon nitride ball with a 1 N load. The sliding rate was 0.2 m s^{-1}, with the disk rotating clockwise at 200 rpm for all tests. The tribometer thermocouple was calibrated before testing with a separate thermocouple spot-welded to an uncoated substrate. Wear tests were started after coating samples were heated to the desired temperature (25–35 min) and allowed to equilibrate for 5–10 min. A sample of each coating was tested until failure at 25, 300, 500 and 700 °C. Failure was defined by a sharp increase in the friction coefficient equal to or greater than that of the uncoated substrate alone. All films lasted between approximately 5000–15000 cycles throughout the specified temperature range before failure. Selected samples were also worn for only 1000 cycles to allow examination of the wear track before failure. Upon completion of the ball-on-disk tests, samples were immediately removed from the furnace and allowed to cool in air. A new coating sample was used for each wear test to observe the adaptive behavior from the as-deposited condition. Coatings deposited on 440C steel substrates were used for wear measurements at 25 and 300 °C, M50 was selected for testing at 500 °C and Inconel 718 substrates were used for all 700 °C tests. The coefficient of friction for each polished, uncoated substrate was also measured for comparison with the coated samples.

Selected coating samples were re-examined with SEM, energy dispersive spectroscopy (EDS), and X-ray diffraction after wear testing develop an understanding of the operative lubrication mechanisms.

3. Results

3.1. YSZ–Ag coatings

At room temperature the friction coefficient was 0.40 for all YSZ–Ag samples, and was therefore independent of silver content. This value was lower than the value of 0.68 measured for an uncoated 440C substrate at room temperature. Fig. 1 shows that the friction coefficient of the YSZ–Ag coatings was sensitive to silver composition at 300 and 500 °C, where increased silver content generally resulted in a reduction of the friction coefficient and an increase in the number of cycles to failure. At 700 °C, the friction coefficient was 0.80 for coatings of all silver contents, which was greater than that measured for the uncoated Inconel substrate.

Fig. 2a–b shows the surface of (a) the as-deposited YSZ-20%Ag coating and (b) the surface of the same coating after heating to 500 °C. EDS analysis showed that the bright grains in the micrograph were composed of silver, while the background consisted of both YSZ and silver. Qualitatively, the areal density of silver grains on the surface before heating was proportional to the silver content in the as-deposited coating and the temperature of the sample during the wear test.

A micrograph of the wear track on the YSZ-20%Ag coating after 1000 cycles at 500 °C is shown in Fig. 3. EDS analysis of the wear track and adjacent surface revealed a silver-rich composition. The series of parallel lines along the wear track consisted of silver that had coalesced to the surface and was smeared during wear.

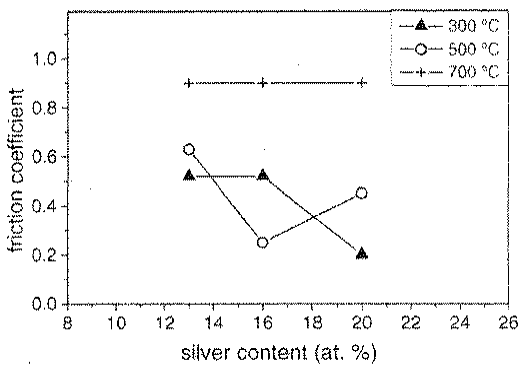


Fig. 1. Friction coefficients of YSZ–Ag composites from 300–700 °C.

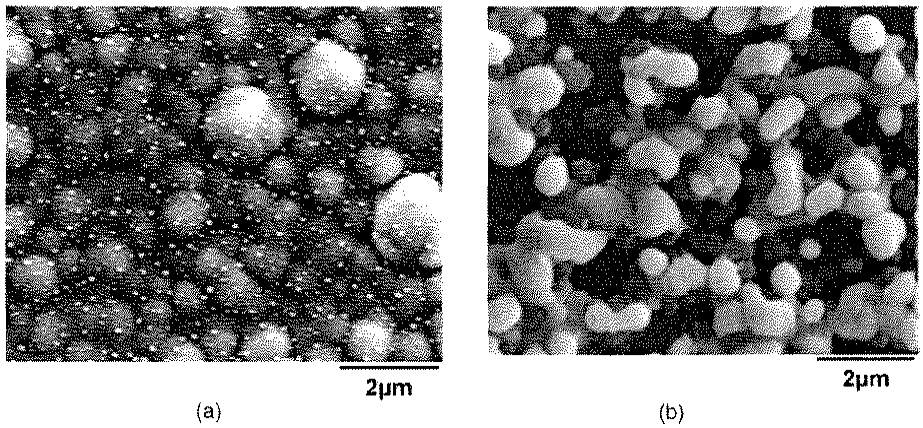


Fig. 2. Scanning electron micrographs of YSZ–20%Ag composite coating surfaces. (a) as-deposited and (b) after heating to 500 °C for approximately 2 h.

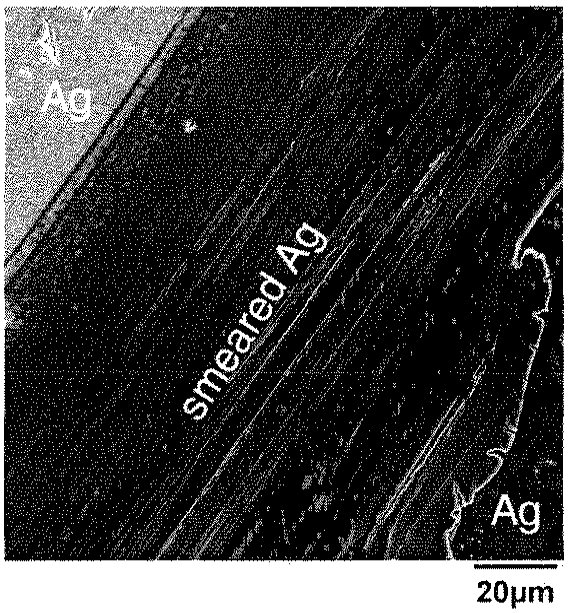


Fig. 3. Wear scar in the YSZ–20%Ag coating after 1000 cycles at 500 °C.

3.2. YSZ–Mo coatings

Fig. 4 shows the friction coefficient at 300–700 °C. Like the friction coefficient, the wear rate also increased with molybdenum concentration at each temperature. These results are contrary to that observed for silver additions in this work and for YSZ–gold coatings studied previously [1]. The friction coefficient at room temperature for all YSZ–Mo coatings was 0.85, which was greater than that measured for the bare 440C substrate.

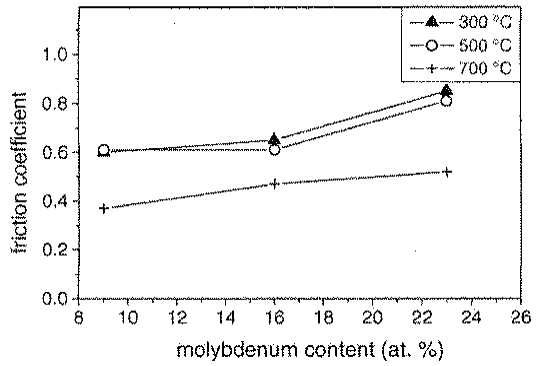


Fig. 4. Friction coefficients of YSZ–Mo composite coatings from 300–700 °C.

The SEM micrographs in Fig. 5(a–d) show the morphological response of two different compositions of YSZ–Mo coatings after heating to 700 °C. The as-deposited coating containing 9 at.% molybdenum was marked with occasional fissures (Fig. 5a), and developed blister-like features that were 5–20 μm in diameter after heating (Fig. 5b). The surface of each blister had the same composition as the neighboring flat areas. The inset in Fig. 5b shows the coating where a blister-cap was removed from the surface. A faceted crystal was found underneath. EDS analysis showed that the crystal was composed entirely of molybdenum and oxygen. YSZ coatings with higher molybdenum concentrations showed more fissures in the same sample area after processing as shown for the coating with 22 at.% Mo in Fig. 5c. After heating, faceted crystals were observed on the surface (Fig. 5d). EDS analysis of these crystals indicated much higher concentrations of Mo and O than in the surrounding area. The wear scar of the YSZ–9%Mo coating, after 1000 cycles at 700 °C, shown in Fig. 6, was also rich in molybdenum and nitrogen. The smeared appearance indicates deformation of a soft phase during wear testing.

Fig. 7a–b show the diffraction patterns from the sample containing 22 at.% molybdenum (a) as-deposited and (b) after heating to 700 °C. The diffraction peaks that appeared after heating corresponded to MoO_3 (PDF 47–1320).

3.3. YSZ–Ag–10%Mo coatings

Fig. 8 shows the friction coefficients for coatings grown with 10 at.% molybdenum and different silver contents, ranging from 5 to 24 at.% at all temperatures. The coating with 5 at.% silver exhibited high friction at all temperatures, similar to the YSZ–Mo coatings described above. YSZ–Ag–Mo films containing 17 at.% silver exhibited high friction at 500 °C and over. The YSZ–24%Ag–10%Mo coatings had a friction coefficient of 0.4 or less for all temperatures from 25 to 700 °C

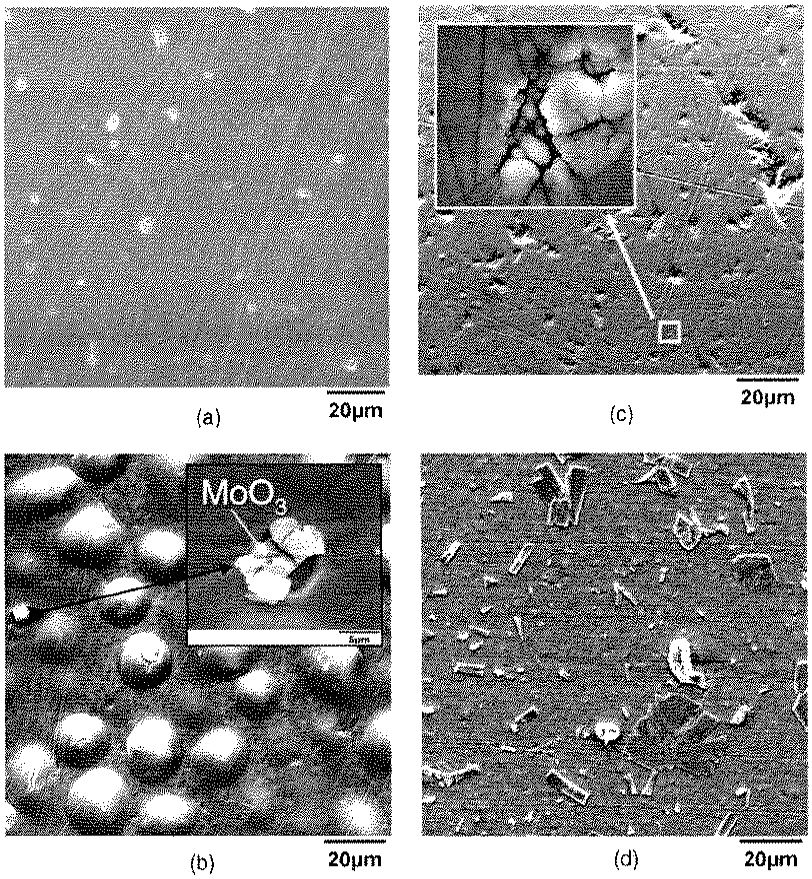


Fig. 5. Scanning electron micrographs of different YSZ–Mo composite coating surfaces. Specifically, (a) as-deposited YSZ-9%Mo. (b) YSZ–9%Mo after heating to 700 °C for approximately 2 h. (c) As-deposited YSZ-22%Mo and (d) YSZ–20%Mo after heating to 700 °C for approximately 2 h.

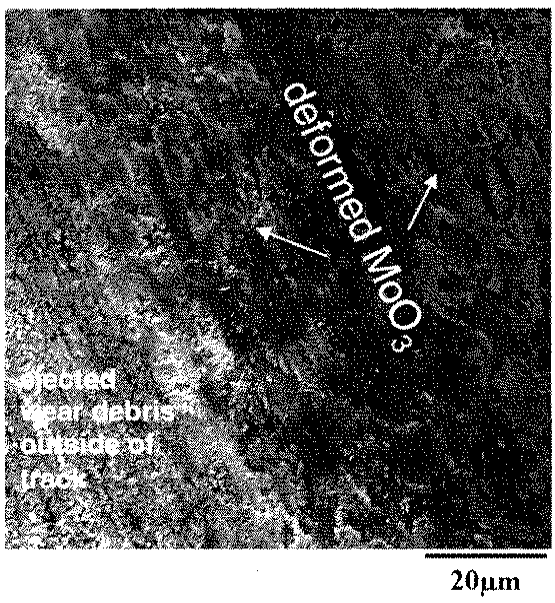


Fig. 6. Wear scar in the YSZ–20%Ag coating after 1000 cycles at 700 °C.

and demonstrated the highest number of cycles to failure at each temperature.

Before heating, all of the coating surfaces looked similar to the YSZ–Ag coatings shown in Fig. 2, with none of the cracking associated with the YSZ–Mo coatings. Fig. 9 shows the YSZ–17%Ag–10%Mo coating after heating to 700 °C. Surface coverage by the silver layer was discontinuous, and the formation of blisters was observed as in the YSZ–Mo coatings. Fig. 10(a–b) show electron micrographs of a YSZ–24%Ag–10%Mo coating (a) in cross-section, and (b) on the surface away from the wear track after heating to 500 °C during wear tests. Fig. 10(a) shows the initially monolithic coating developed two distinct layers after heating. EDS analysis was used to determine that the top layer was pure silver with an average grain size of ≈ 1 μm (Fig. 10b). Only trace amounts of Mo were found at the surface with EDS and XPS analysis techniques. The lower layer shown in Fig. 10a consisted of YSZ and molybdenum, with traces of silver. Fig. 11(a–b) show the wear tracks for the YSZ–24%Ag–10%Mo coatings after 1000 cycles in air at (a) 300 °C and (b) 700 °C. At 300 °C (Fig. 11a), the wear track looks similar to that observed for the YSZ–Ag coating (Fig. 3), with streaks of silver lining contact area. At 700 °C (Fig. 11b), the silver is pushed toward the edges of the track, however formation of crystals similar those formed in the

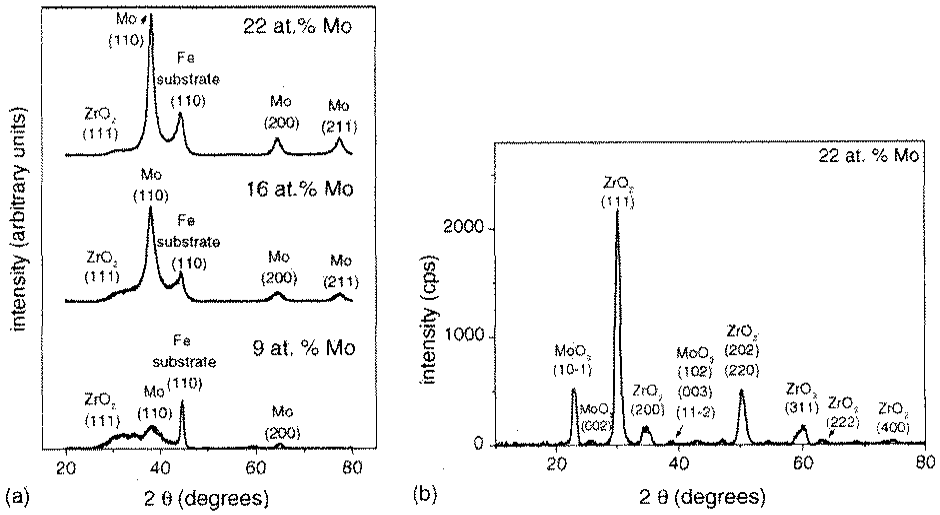


Fig. 7. X-ray diffractograms of the (a) as-deposited YSZ–Mo composites and (b) the YSZ–22%Mo composite after heating to 700 °C for approximately 2 h.

YSZ–Mo coating (Fig. 5b) and deformation of a soft phase in the friction contact were observed.

4. Discussion

4.1. YSZ–Ag coatings

The dependence of friction coefficient on composition and temperature illustrated in Fig. 1 was based on the surface composition during wear testing for each of the coatings. During heating, silver diffused out of YSZ matrix to form lubricious silver grains which coalesced on the coating surface (Fig. 2b), providing easy shear in the friction contact (Fig. 3). Higher initial silver contents and/or temperatures resulted in more lubricant at the surface to facilitate sliding, thereby reducing friction and wear over the hard YSZ material. At 700 °C, it is presumed that the silver was too soft and was pushed out of the sliding contact, reducing its ability to provide suitable lubrication [19,24]. Softening would be especially pronounced for submicron silver grains which are subject to melting at temperatures below the melting point of bulk silver [36,37].

Rapid coalescence of silver or other noble metals at the surface of an initially homogenous composite during processing or heating similar to that reported on in this work has also been reported by other authors [17,21–23]. Falster et al. [23], and later Bates et al. [22] proposed a diffusion mechanism where, upon heating, the noble metal assumes a position on an interstitial site in a solid with a high defect density. With continued heating the silver segregates to the free surface where there is no constraint on lattice sites for the noble metal impurities, and a driving force for coalescence to reduce surface energy is present. Silver has been shown to exhibit high diffusivity in other solids, with a diffusion coefficient of 10^{-7}–10^{-9} $cm^2\,s^{-1}$ depending on the location of the silver atom in the lattice (diffusion coefficients for intersititials are typically 2 orders of magnitude greater than for substitutional atoms). Assuming a low estimate of the diffusion coefficient for silver in YSZ, (10^{-9} $cm^2\,s^{-1}$), a silver atom would travel approximately 1 μm in 15 min at 500 °C. The

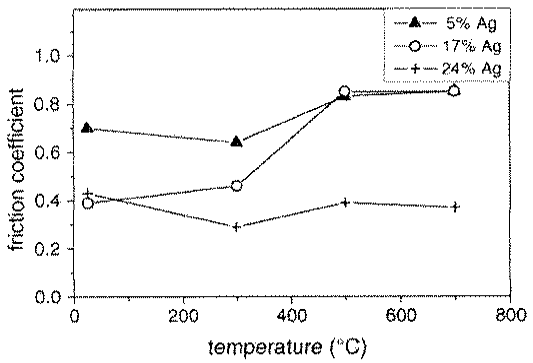


Fig. 8. Friction coefficients of YSZ–Ag–10%Mo composite coatings from 300–700 °C.

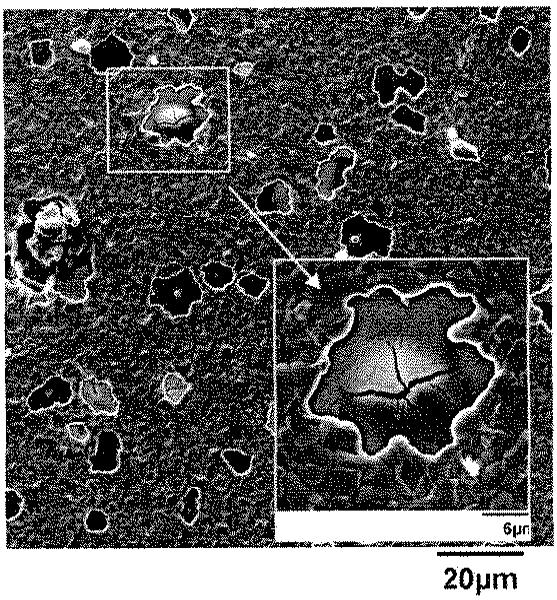


Fig. 9. Scanning electron micrograph of the YSZ–17%Ag–10%Mo coating surface after heating to 700 °C for approximately 2 h.

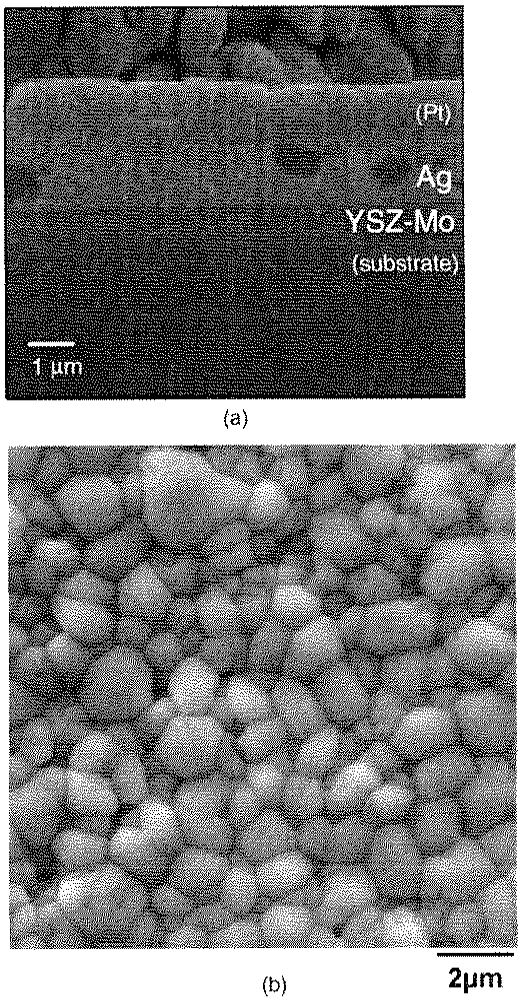


Fig. 10. Scanning electron (a) cross-sectional micrograph and (b) surface micrograph of the YSZ–24%Ag–10%Mo coating after heating to 500 °C.

plasma deposited YSZ used in this work is intrinsically a highly defected material with a large grain boundary surface area due to its nanocrystalline structure [10]. It therefore seems reasonable for enhanced solid state diffusion of silver to take place in the zirconia, allowing for rapid coalescence on the surface in response to heating.

4.2. YSZ–Mo coatings

The friction coefficient was high for all YSZ–Mo coatings at room temperature, which was most likely due to cracks formed in the coating during processing, as shown in Fig. 5a and c. The friction coefficient also increased with temperature which corresponded to the morphological evolution of the film surfaces during heating illustrated by Fig. 4b and d, where disruption of the coating surface increased with temperature. Cracks in the as-deposited films were most likely the result of subsurface pesting, or formation of MoO_3 in either the vapor phase [32,38] or solid phase [39] during coating deposition and heating. For the YSZ–9%Mo coating with the lowest molybdenum content, formation of MoO_3 was limited at high temperature, which minimized crack formation at the surface, but was sufficient to provide enough of the soft phase to allow easy shear in the wear contact and reduce friction (Figs. 4 and 6).

In previous research, it has been reported that crystallization of YSZ was inhibited by the presence of molybdenum metal [40], where the degree of grain growth suppression was proportional to the molybdenum content. However, significant ZrO_2 grain growth was observed in this work for YSZ coatings containing 9–22 atomic percent molybdenum, demonstrated by the sharpened ZrO_2 peaks [41] after heating to 700 °C (Fig. 7b). Maintenance of the nanocrystalline zirconia phase is required for preserving the mechanical and tribological properties of nanostructured coatings over extended periods of time at high temperature, and over many temperature cycles. The possibility of the YSZ crystal growth inhibition with metal doping will therefore be investigated further in future research.

4.3. YSZ–Ag–10%Mo coatings

The YSZ–Ag–10%Mo coatings containing 17% silver or less demonstrated high friction at 500 °C and over, while those with 24% silver, exhibited a stable friction coefficient of 0.4 against

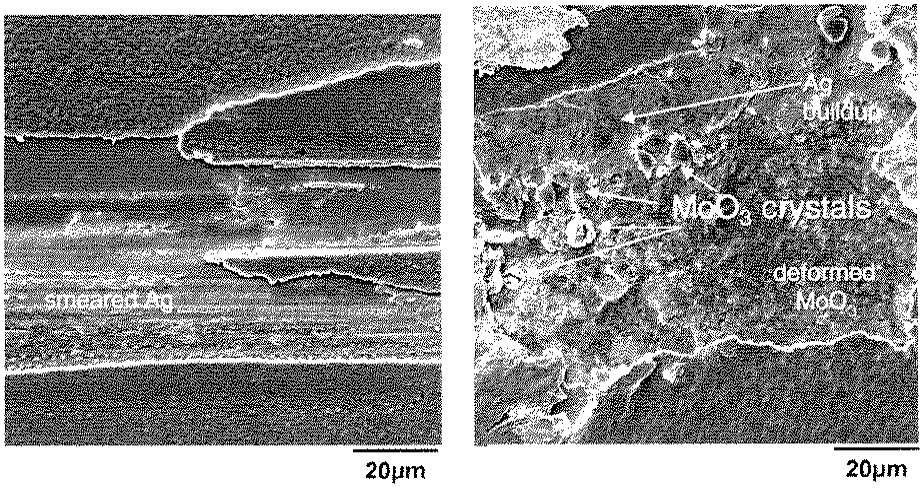


Fig. 11. Scanning electron micrograph of the wear track of the YSZ–24%Ag–10%Mo coating after 1000 cycles at (a) 300 °C and (b) 700 °C.

silicon nitride at all temperatures. For comparison, the friction coefficient for silicon nitride on silicon nitride sliding in air has been reported to be 0.5–0.7 throughout the same temperature range [32,42].

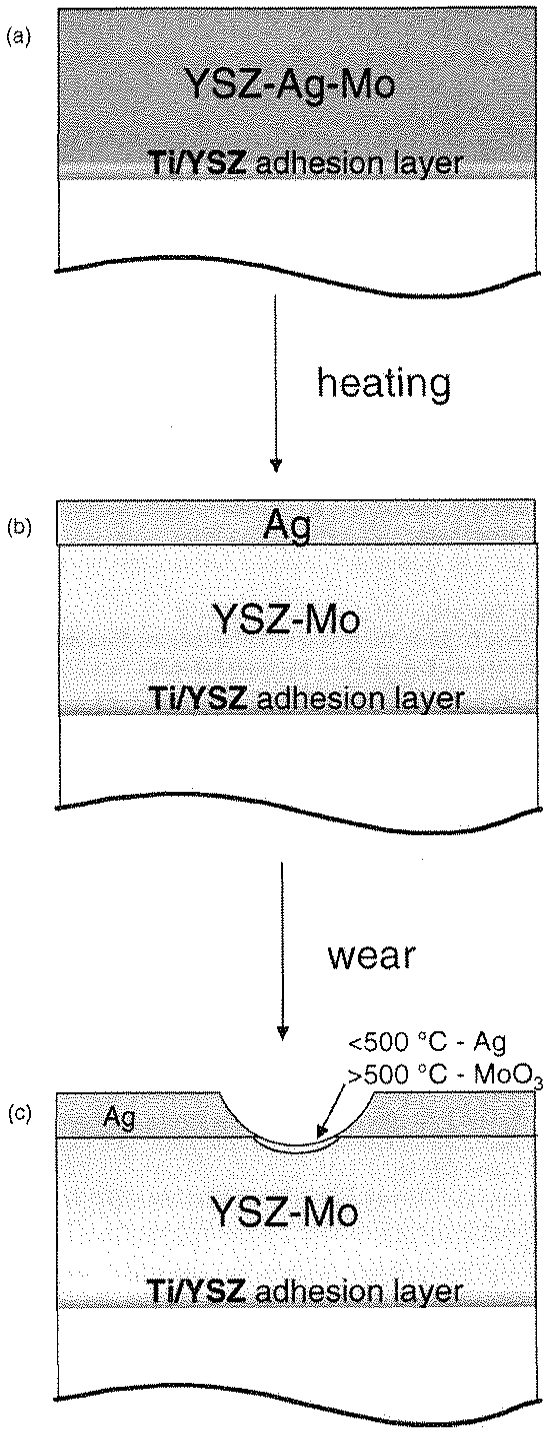


Fig. 12. Schematic of the proposed adaptation mechanisms resulting in lubrication throughout a broad range of temperatures illustrating: (a) the as-deposited coating is subjected to heating, with diffusion of silver to the surface, resulting in (b) a continuous protective layer of silver, providing lubrication up to 500 °C and inhibiting Mo oxidation until (c) wear opens the protective layer to expose Mo, which forms molybdenum-based compounds to provide lubrication above 500 °C.

Figs. 2b, 9 and 10b show that the surface morphology of the YSZ–Ag and YSZ–Ag–10%Mo coatings after heating to 500 °C were strongly dependent on composition. The mechanism described for segregation of silver to the coating surface for the YSZ–Ag coatings, is assumed to valid for YSZ–Ag–Mo composites as well, however surface coverage by silver was only continuous in the YSZ–24%Ag–Mo coating. It is expected that diffusivity of silver was dependent on both silver concentration [17] and the microstructure of the medium through which it diffused. The YSZ–24%Ag–10%Mo coating not only contains more silver, but has been shown to have a higher defect density due the increased total metal content (Ag and Mo), and thus exhibited higher diffusivity and complete silver coverage on the surface.

Both YSZ–Ag–10%Mo coatings also demonstrated an accumulation of silver grains at the surface. . The coating with 17% silver had discontinuous silver coverage, while the coating with 24% silver demonstrated a continuous layer of silver after heating. Coatings with a discontinuous silver layer as shown in Fig. 9 had blisters and cracks associated with MoO_3 formation, similar to those shown for the YSZ-9%Mo coatings heated to 700 °C (Fig. 5b). For coatings with a continuous layer of Ag, no evidence of cracking was observed after heating (Fig. 10a–b). This is likely because the continuous silver layer served not only as a lubricant, but also as a protective layer for the YSZ-Mo coating remaining underneath. Acting as an oxygen diffusion barrier, this layer inhibited excessive molybdenum oxidation, which led to cracking in the other coatings with less silver. Silver alone however, was demonstrated as an ineffective lubricant over 500 °C here (Fig. 1), and in other works [16,18], therefore, an additional lubrication mechanism must have been activated at high temperature.

Molybdenum trioxide, a high temperature lubricant [27,29–31], formed on the wear track surface exposed to air at high temperature (<500 °C) after the silver was worn or pushed away. Silver molybdates could also have formed [29], but the presence of such compounds was beyond the detection limits of the materials characterization tools used here.

A schematic of the proposed adaptive mechanisms is presented in Fig. 12. Upon heating, silver diffused and coalesced on the coating surface. If enough silver was present in the coating, a continuous silver layer formed (Fig. 12b). This layer minimized the exposure of molybdenum in the YSZ-Mo composite to ambient oxygen, thus inhibiting gross oxidation and subsequent MoO_3 grain growth leading to cracking, as depicted in Fig. 4 b and d. The silver layer also provided lubrication up to 500 °C. At higher temperatures, the silver was pushed away from the contact, thereby exposing the molybdenum in the composite to oxygen, and permitting controlled formation of MoO_3, or other lubricious oxide compounds (Fig. 12c) exclusively in the wear track. These mechanisms of metal diffusion, surface encapsulation and oxide formation by interactions with the ambient atmosphere can be employed to design coatings to provide low friction over a broad temperature range.

5. Conclusions

Yttria-stabilized zirconia nanocomposites with silver and molybdenum were investigated for use as wear-resistant materials in sliding applications between 25–700 °C. Silver lubricated the hard YSZ surface at room temperature, and diffused to the surface of the composite material when heated to function as a lubricant up to 500 °C. Molybdenum was a poor lubricant below 500 °C, however, YSZ–Mo composites exhibited moderately low friction at 700 °C. Cracking of the as-deposited YSZ–Mo coatings was observed, which worsened with heating. Incorporating a sufficient quantity of silver in a YSZ–Ag–Mo composite to form a continuous silver layer upon heating resulted in a material that exhibited a friction coefficient of ≤ 0.4 at all temperatures between 25 and 700 °C, with no apparent cracking of the coating. A surface adaptation mechanism for lubrication from 25–700 °C was proposed, with noble metal diffusion forming a lubricating protective barrier at low and moderate temperatures, and surface chemical reactions with the ambient environment in the wear track at higher temperatures.

Acknowledgements

The Air Force Office of Scientific Research (AFOSR) is gratefully acknowledged for financial support. The authors also wish to thank J. Bultman and A. Safriet for technical assistance and A. Korenyi-Both for helpful discussions.

References

[1] A.A. Voevodin, J.J. Hu, T.A. Fitz, J.S. Zabinski, Tribological properties of adaptive nanocomposite coatings made of yttria-stabilized zirconia and gold, Surf. Coat. Technol. 146–147 (2001) 351–356.
[2] A.A. Voevodin, J.G. Jones, J.J. Hu, T.A. Fitz, J.S. Zabinski, Growth and structural characterization of yttria-stabilized zirconia–gold nanocomposite films with improved toughness, Thin Solid Films 401 (2001) 187–195.
[3] A.A. Voevodin, J.J. Hu, T.A. Fitz, J.S. Zabinski, Nanocomposite tribological coatings with "chameleon" friction surface adaptation, J. Vac. Sci. Technol. A 20 (2002) 1434–1444.
[4] S.D. Walck, J.S. Zabinski, N.T. McDevitt, J.E. Bultman, Characterization of air-annealed, pulsed laser deposited ZnO–WS_2 solid film lubricants by transmission electron microscopy, Thin Solid Films 305 (1997) 130–143.
[5] J.S. Zabinski, M.S. Donley, V.J. Dyhouse, C. Melandri, Chemical and tribological characterization of PbO–MoS_2 films grown by pulsed laser deposition, Thin Solid Films 214 (1992) 156–163.
[6] Zabinski, J. S, Prasad, S. V., McDevitt, N.T. Advanced solid lubricant coatings for aerospace systems. Proceedings of the AGARD Conference on Tribology of Space Systems, 3-1-3-12. 1996. 5-6-1996.
[7] A.A. Voevodin, J.S. Zabinski, Supertough wear resistant coatings with 'chameleon' surface adaptation, Thin Solid Films 370 (2000) 223–231.
[8] J. Eckert, Structure formation and mechanical behavior of two-phase nanostructure materials, in: C.C. Koch (Ed.), Nanostructured Materials–Processing, Properties and Potential Applications, William Andrew Publishing/Noyes, 2002, p. 509.
[9] H.S. Kim, C. Suryanarayana, S.J. Kim, B.S. Chun, Numerical investigation of mechanical behavior of nanocrystalline copper, Powder Met. 41 (1998) 217.
[10] C. Muratore, A.A. Voevodin, J.J. Hu, J.G. Jones, J.S. Zabinski, Growth and characterization of nanocomposite yttria-stabilized zirconia with Ag and Mo, Surf. Coat. Technol. 200 (2005) 1549–1554.
[11] S. Veprek, The search for novel, superhard materials, J. Vac. Sci. Technol. A 17 (1999) 2401–2420.
[12] S.W. Lee, S.M. Hsu, M.C. Shen, Ceramic wear maps: zirconia, J. Am. Ceram. Soc. 76 (1993) 1937–1947.
[13] G.W. Stachowiak, G.B. Stachowiak, Unlubricated friction and wear behaviour of toughened zirconia ceramics, Wear 132 (1989) 151–171.
[14] G.W. Stachowiak, G.B. Stachowiak, Unlubricated wear and friction of toughened zirconia ceramics at elevated temperatures, Wear 143 (1991) 277–295.
[15] C. DellaCorte, H.E. Sliney, Tribological properties of PM212: a high temperature, self-lubricating, powder metallurgy composite, Lub. Eng. 47 (1991) 298–303.
[16] C. DellaCorte, The effect of counterface on the tribological performance of a high temperature solid lubricant composite from 25 to 650 °C, Surf. Coat. Technol. 86–87 (1996) 486–492.
[17] J.L. Endrino, J.J. Nainaparampil, J.E. Krzanowski, Microstructure and vacuum tribology of TiC–Ag composite coatings deposited by magnetron sputtering-pulsed laser deposition, Surf. Coat. Technol. 157 (2002) 95–101.
[18] A. Erdemir, R.A. Erck, G.R. Fenske, H. Hong, Solid/liquid lubrication of ceramics at elevated temperatures, Wear 203–204 (1997) 588–595.
[19] H.E. Sliney, Solid lubricant materials for high temperatures–a review, Tribol. Int. 15 (1982) 303–315.
[20] H.E. Sliney, The use of silver in self-lubricating coatings for extreme temperatures, ASLE Trans. 29 (1985) 370–376.
[21] J.J. Hu, A.A. Voevodin, J.S. Zabinski, J. Mater. Res. 20 (2005) 1860–1868.
[22] C.W. Bates, Q.Y. Chen, Segregation effects in Ag–Si composites, Mater. Lett. 23 (1995) 7–12.
[23] R.J. Falster, D.N. Modlin, W.A. Tiller, J.F. Gibbons, Effective gettering of gold in silicon at 900 °C by low-current corona discharge, J. Appl. Phys. 57 (1985) 554–558.
[24] F.P. Bowden, D. Tabor, The lubrication by thin metallic films and the action of bearing metals, J. Appl. Phys. 14 (1943) 141–151.
[25] Gardos, M. N. The problem-solving role of basic science in solid lubrication. Hutchings, I. M. Plenary and Invited Papers from the First World Tribology Congress, 229–250. 1997.
[26] G. Gassner, P.H. Mayrhofer, K. Kutschej, C. Mitterer, M. Katherein, A new low friction concept for high temperatures: lubricious oxide formation on sputtered VN coatings, Tribol. Lett. 17 (2004) 751–756.
[27] M. Woydt, A. Skopp, I. Dorfel, K. Witke, Wear engineering oxides/anti-wear oxides, Wear 218 (1998) 84–95.
[28] S.V. Prasad, N.T. McDevitt, J.S. Zabinski, Tribology of tungsten disulfide-nanocrystalline zinc oxide adaptive lubricant films from ambient to 500 °C, Wear 237 (2000) 186–196.
[29] W. Gulbinski, T. Suszko, W. Sienicki, B. Warcholinski, Tribological properties of silver- and copper-doped transition metal oxide coatings, Wear 254 (2003) 129–135.
[30] M.B. Peterson, S.F. Murray, J.J. Florek, Consideration of lubricants for temperatures above 1000F, ASLE Trans. 2 (1959) 225–234.
[31] K.J. Wahl, L.E. Seitzman, R.N. Bolster, I.L. Singer, Ion beam deposited Cu–Mo coatings as high temperature solid lubricants, Surf. Coat. Technol. 89 (1997) 245–251.
[32] S.F. Murray, S.J. Calabrese, Effect of solid lubricants on low speed sliding behavior of silicon nitride at temperatures to 800 °C, Lubr. Eng. 49 (1992) 955–964.
[33] K.L. Strong, J.S. Zabinski, Tribology of pulsed laser deposited thin films of cesium oxythioimolybdate, Thin Solid Films 406 (2002) 174–184.
[34] A.A. Voevodin, M.A. Capano, A.J. Safriet, M.S. Donley, J.S. Zabinski, Combined magnetron sputtering and pulsed laser deposition of carbides and diamond-like carbon films, Appl. Phys. Lett. 69 (1996) 188–190.
[35] A.A. Voevodin, J.S. Zabinski, Hybrid plasma deposition methods for synthesis of nanostructured materials, in: A.A. Voevodin, D.V. Shtansky, E.A. Levashov, J.J. Moore (Eds.), Nanostructured thin films and nanodispersion strengthened coatings, Kluwer Academic Publishers, Dordrecht, The Netherlands, 2005, pp. 103–111.
[36] Ph. Buffat, J.-P. Borel, Size effect on the melting temperature of gold particles, Phys. Rev. A 13 (1976) 2287–2298.

[37] M. Goto, N. Nakata, F. Honda, Tribological behavior of an Ag sub-nanometer-thick film on an Si (1 1 1) 7 X 7 surface at elevated temperatures, Wear 256 (2004) 726–734.
[38] N. Solak, F. Ustel, M. Urgen, S. Aydin, A.F. Cakir, Oxidation behavior of molybdenum nitride coatings, Surf. Coat. Technol. 174–175 (2003) 713–719.
[39] K. Kurokawa, H. Houzumi, I. Saeki, H. Takahashi, Low temperature oxidation of fully dense and porous $MoSi_2$, Mater. Sci. Eng. A 261 (1999) 292–299.
[40] K.V.R. Chary, K.R. Reddy, G. Kishan, J.W. Niemantsverdriet, G. Mestl, Structure and catalytic properties of molybdenum oxide catalysts supported on zirconia, J. Catal. 226 (2004) 283–291.
[41] B.D. Cullity, Elements of X-Ray Diffraction, Addison Wesley, Reading, Massachusetts, 1978, p. 282.
[42] C. Melandri, M.G. Gee, G. de Portu, S. Guiccardi, High temperature friction and wear testing of silicon nitride ceramics, Tribol. Int. 28 (1995) 403–413.

Paper 5

Available online at www.sciencedirect.com
ScienceDirect
Surface & Coatings Technology 201 (2006) 4125–4130
SURFACE & COATINGS TECHNOLOGY
www.elsevier.com/locate/surfcoat

Molybdenum disulfide as a lubricant and catalyst in adaptive nanocomposite coatings

C. Muratore [a,*], A.A. Voevodin [b]

[a] UTC Inc./Air Force Research Laboratory, Materials and Manufacturing Directorate, AFRL/MLBT, 2941 Hobson Way, Wright-Patterson AFB, OH 45433 USA
[b] Air Force Research Laboratory, Materials and Manufacturing Directorate, AFRL/MLBT, 2941 Hobson Way, Wright-Patterson AFB, OH 45433 USA

Available online 20 September 2006

Abstract

Nanocomposite YSZ–Ag–Mo–MoS_2 coatings with different MoS_2 additions (0–100 at.%) were deposited with a hybrid pulsed laser/magnetron sputtering/filtered cathodic arc process. Wear testing was performed from 25 to 700 °C for each of the coatings. Electron microscopy and other characterization techniques were used to examine the surfaces and wear tracks of the coatings and to determine the mechanisms resulting in the measured tribological properties. Adaptive coatings containing 8 at.% MoS_2 demonstrated a friction coefficient of 0.2 throughout the temperature range examined here, compared to 0.4 for YSZ–Ag–Mo with no MoS_2. Characterization of the YSZ–Ag–Mo–8% MoS_2 coating revealed that MoS_2 and silver provided lubrication at temperatures ≤300 °C, while silver molybdate phases and MoO_3 were effective lubricants at higher temperatures. Silver molybdate was not observed in the coatings containing 0% MoS_2. The role of sulfur in the formation of silver molybdate is briefly discussed.
© 2006 Elsevier B.V. All rights reserved.

Keywords: Adaptive coating; High temperature; Molybdenum disulfide; Tribology

1. Introduction

A broad range of environmental conditions are associated with hypersonic flight and other advanced aerospace applications. Presently, no lubricant is available to provide low friction from takeoff to landing in high-performance flights of this nature, as opposite extremes of humidity, loading and temperature are reached over a single flight cycle. Adaptive nanocomposites, also known as "chameleon coatings", are a class of materials that automatically adjust surface composition and structure to minimize friction as the ambient environment changes, and may provide the properties necessary to reduce downtime for aerospace systems subjected to repeated atmospheric cycling. Adaptation results from the transformation of amorphous and nanocrystalline inclusions into lubricious macro-phases in the friction contact when exposed to changes in the ambient environment. Effective humidity and load adaptation have been reported previously, however, adaptation to temperature is still under development [1–3]. A series of coatings incorporating metals in a nanocrystalline/amorphous yttria-stabilized zirconia (YSZ) matrix was recently designed to provide low friction from 25 to 700 °C [10–12]. These coatings incorporated soft noble metals for lubrication at low to moderate temperatures (<500 °C) [4–12], and transition metals expected to form lubricous oxides at higher temperatures in air [13–15]. For example, a YSZ–Ag–Mo nanocomposite adaptive coating provides lubrication by forming a silver rich surface at 300–500 °C, and MoO_3 at temperatures above 500 °C, resulting in a friction coefficient of ≤0.4 from 25 to 700 °C [9]. Silver molybdate compounds, yielding a friction coefficient of ≈0.2, were expected to form when the YSZ–Ag–Mo coatings were heated to 500 °C or higher [16,17], however, no such compounds were detected. In the current work, YSZ–Ag–Mo nanocomposite coatings with MoS_2 nanoinclusions were grown to reduce friction at low temperature and to promote silver-molybdenum reactions. Coatings with different amounts of MoS_2 were subjected to wear testing at 25–700 °C. The surfaces and wear tracks of the coatings were analyzed and compared to YSZ–Ag–Mo (0% MoS_2) and pure MoS_2 coatings after testing at elevated temperatures to identify the operative lubrication mechanisms.

* Corresponding author. Tel.: +1 937 255 5163; fax: +1 937 255 2176.
E-mail address: chris.muratore@wpafb.af.mil (C. Muratore).

0257-8972/$ - see front matter © 2006 Elsevier B.V. All rights reserved.
doi:10.1016/j.surfcoat.2006.08.014

2. Experimental procedure

Coatings composed of yttria stabilized zirconia (YSZ), silver, molybdenum and different concentrations of molybdenum disulfide were deposited with a hybrid filtered vacuum arc/pulsed laser/magnetron sputtering technique [18–20], with deposition conditions similar to those described previously [18]. Briefly, the filtered vacuum arc source was fitted with a titanium cathode and used to clean the substrates with metal ions and to deposit a 50 nm Ti adhesion layer. YSZ and MoS_2 were deposited by pulsed excimer laser ablation of a segmented 5 cm diameter disk for all composite coatings. The number and size of the segments comprising the disk were varied to alter the fraction of MoS_2 contained in the coatings. Programmable mirrors were used to direct the 25 ns, 800 mJ laser pulses to random positions on the surface of the rotating target. Silver and molybdenum were incorporated into the materials via magnetron sputtering from pure metal targets. The power density of the targets was adjusted between 1 and 5 W cm^{-2} to maintain a constant metal composition of approximately 20 at.% silver and 10 at.% molybdenum. A pure MoS_2 coating was also deposited by magnetron sputtering of a solid MoS_2 target in argon for comparison with the nanocomposites. Substrates were dc biased to −150 V, and heated to 150 °C during coating growth. All coatings were measured with a contact profilometer to be approximately 2 μm thick (±150 nm). The compositions of the as-deposited coatings were measured with X-ray photoelectron spectroscopy (XPS) after sputter cleaning each sample with 5000 eV Ar^+ ions for 15 s.

Friction coefficients in laboratory air (20–30% relative humidity) were measured with a high temperature ball-on-disc tribometer using a 6.35 mm diameter silicon nitride ball with a 1 N load, or approximately 0.7 GPa initial Hertzian stress. The sliding speed was 0.2 m s^{-1}, with the disk rotating clockwise at 200 rpm for all tests. The thermocouple inside the tribometer oven was calibrated before testing for each temperature of interest with a separate thermocouple spot-welded to an uncoated substrate, which was placed into the sample test location and heated without rotation. Wear tests were started after coating samples were heated to the desired temperature (20–25 minutes heating time) and allowed to equilibrate at the temperature setpoint for 5–10 min. A sample of each coating was tested for 10,000 cycles or to failure (whichever came first) at 25, 300, 500 and 700 °C. A new coating sample was used for each wear test to observe the adaptive behavior from the as-deposited condition. Coatings deposited on 440C steel substrates were used for wear tests at 25 and 300 °C, M50 substrates were selected for testing at 500 °C, and Inconel 718 substrates were used for all 700 °C tests. The coefficients of friction for each polished, uncoated substrate were also measured to assist in the identification of coating failure, which was defined by a sharp increase in the friction coefficient, equal to or greater than that of the uncoated substrate alone. Selected samples were also tested for only 1000 cycles to allow examination of the wear track before coating failure. Upon completion of the ball-on-disk tests, samples were immediately removed from the furnace and allowed to cool naturally in air.

Wear tracks and surfaces on the worn samples were examined with scanning electron microscopy (SEM), energy dispersive spectroscopy (EDS), glancing angle X-ray diffraction, XPS and micro-Raman spectroscopy to characterize changes in surface structure and composition after testing at different temperatures. Peaks in the Raman spectra were identified using data found in Ref. [21] in addition to that presented by Gulbinski et al. [17].

3. Results

Table 1 lists the composition, friction coefficient and cycles to failure at temperatures between 25 and 700 °C for YSZ–20% Ag–10% Mo coatings with different MoS_2 additions. The YSZ–Ag–Mo coating (0% MoS_2) maintained a friction coefficient of ≈0.4 for all temperatures. Adding MoS_2 reduced the coefficient of friction of the coating throughout the examined temperature range. The YSZ–Ag–Mo coating with 8 at.% MoS_2 demonstrated a friction coefficient of less than 0.2 for all temperatures. Coatings containing more than 8 at.% MoS_2 did not demonstrate the continuous nanocrystalline/amorphous YSZ matrix associated with the composites containing less MoS_2, and were therefore not considered in the present work. Pure MoS_2 yielded a significantly lower friction coefficient of <0.1 at 25 and 300 °C, but failed within 100 cycles at temperatures above 300 °C.

Fig. 1a–e show the morphological response of coatings with different MoS_2 contents at moderate and high temperatures. The YSZ–Ag–Mo coating formed a continuous silver layer at 300 °C, resulting from diffusion of silver from the coating to the surface as described previously [9] and shown in Fig. 1a. Smearing of the silver layer, with a low shear strength at 300 °C [5–7,11,22], was observed in the wear track (Fig. 1a). Fig. 1b shows that silver was pushed out of the wear track under the ball contact pressure at 700 °C, exposing the molybdenum in the underlying coating to air, and resulting in the formation of lubricious molybdenum trioxide crystals, which were apparent as faceted crystals adjacent to the smeared MoO_3 in the friction contact [9]. For the YSZ–Ag–Mo with 8 at.% MoS_2, equiaxed

Table 1
Average friction coefficients and cycles-to-failure for YSZ–Ag–Mo coatings with different MoS_2 additions

Atomic percent MoS_2	Friction coefficient				Cycles to failure			
	25 °C	300 °C	500 °C	700 °C	25 °C	300 °C	500 °C	700 °C
0	0.4	0.3	0.4	0.4	>10,000	>10,000	4000	>10,000
4	0.5	0.2	0.2	0.3	>10,000	>10,000	1000	1000
8	0.2	0.1	0.2	0.2	>10,000	>10,000	3000	5000
100	0.04	0.06	–	–	>10,000	>10,000	>100	>100

grains appeared to have grown on the coating surface, similar to that observed for the coatings with no MoS_2, however, a stick-like phase was also spread homogenously among these grains away from the wear tracks (Fig. 1c–d). In the wear track of the sample tested at 300 °C, plastic deformation of a soft phase and the presence of a darker, smeared phase at the surface of the wear track were apparent (Fig. 1c). At 700 °C, a stick-like phase with a different morphology than that in Fig. 1c was observed

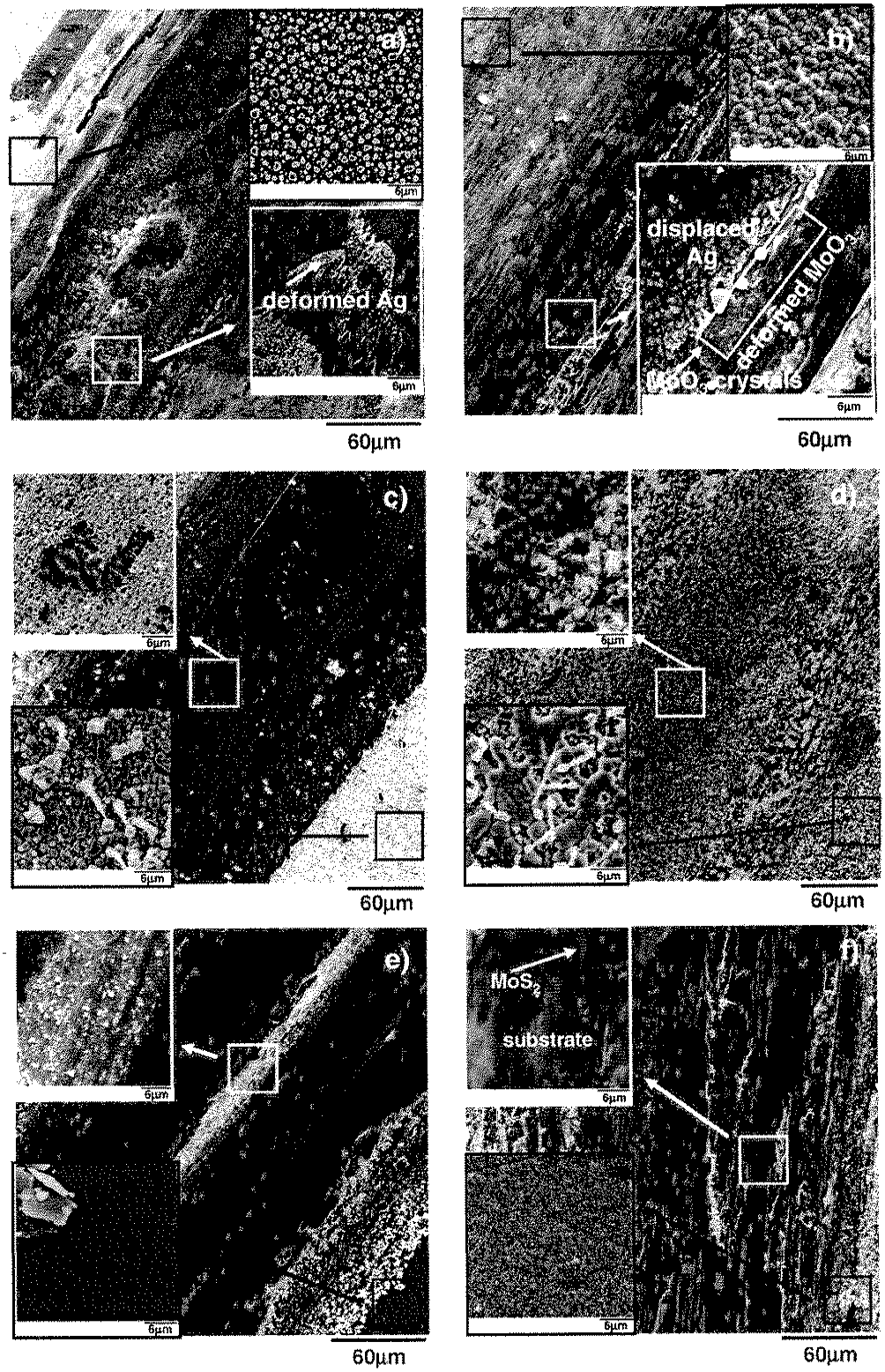


Fig. 1. Scanning electron micrographs of the wear tracks and surfaces of the (a–b) 0% MoS_2 (c–d) 8% MoS_2, and (e–f) 100% MoS_2 coatings after wear testing at 300 and 700 °C, respectively. The insets with black borders show the surfaces away from the wear tracks, and the insets surrounded by white show a higher magnification view of the highlighted wear track feature.

on the coating surface away from the wear track (Fig. 1d). In the wear track of the sample tested at 700 °C, deformed equiaxed grains over faceted crystals were visible. The pure MoS_2 coating surface showed few features at the surface after heating to 300 °C (Fig. 1e), with smearing of the lubricous MoS_2 in the wear track. At 700 °C, more pronounced crystal growth was observed on the coating surface (Fig. 1f). In the wear track, the substrate was visible under the failed coating.

Fig. 2(a–f) show glancing angle X-ray diffractograms for the (a, b) 0, (c, d) 8, and (e, f) 100 at.% MoS_2 coatings after wear testing at 300 and 700 °C for ≈60 min. Silver was the only phase detected for the 0% MoS_2 coatings heated to any temperature ≥300 °C (Fig. 2a–b). For the adaptive coatings containing MoS_2 however, Ag_2MoO_4 (PDF #08-0473) and $Ag_2Mo_2O_7$ (PDF # 21-1339) silver molybdate phases and MoO_3 phases (PDF #47-1320) were present after heating to temperatures >300 °C, as shown in Fig. 2d. X-ray diffraction of the 100% MoS_2 coating heated to 300 °C (Fig. 2e) showed broad MoS_2 peaks (PDF #37-1492). For the sample heated to 700 °C, the same MoS_2 peaks narrowed, and MoO_3 peaks were also detected on the sample surface (Fig. 2f).

To identify the phases present in selected wear tracks, micro-Raman spectroscopy was employed. Fig. 3a shows that the crystals similar to those in the wear track of YSZ–20% Ag–10% Mo coating tested at 700 °C (Fig. 1b) were indeed MoO_3 [21]. The Raman spectrum in Fig. 3b shows that the dark spots observed in the YSZ–20% Ag–10% Mo–8% MoS_2 coating heated to 300 °C (Fig. 1c) were composed of MoS_2 [21]. Fig. 3c

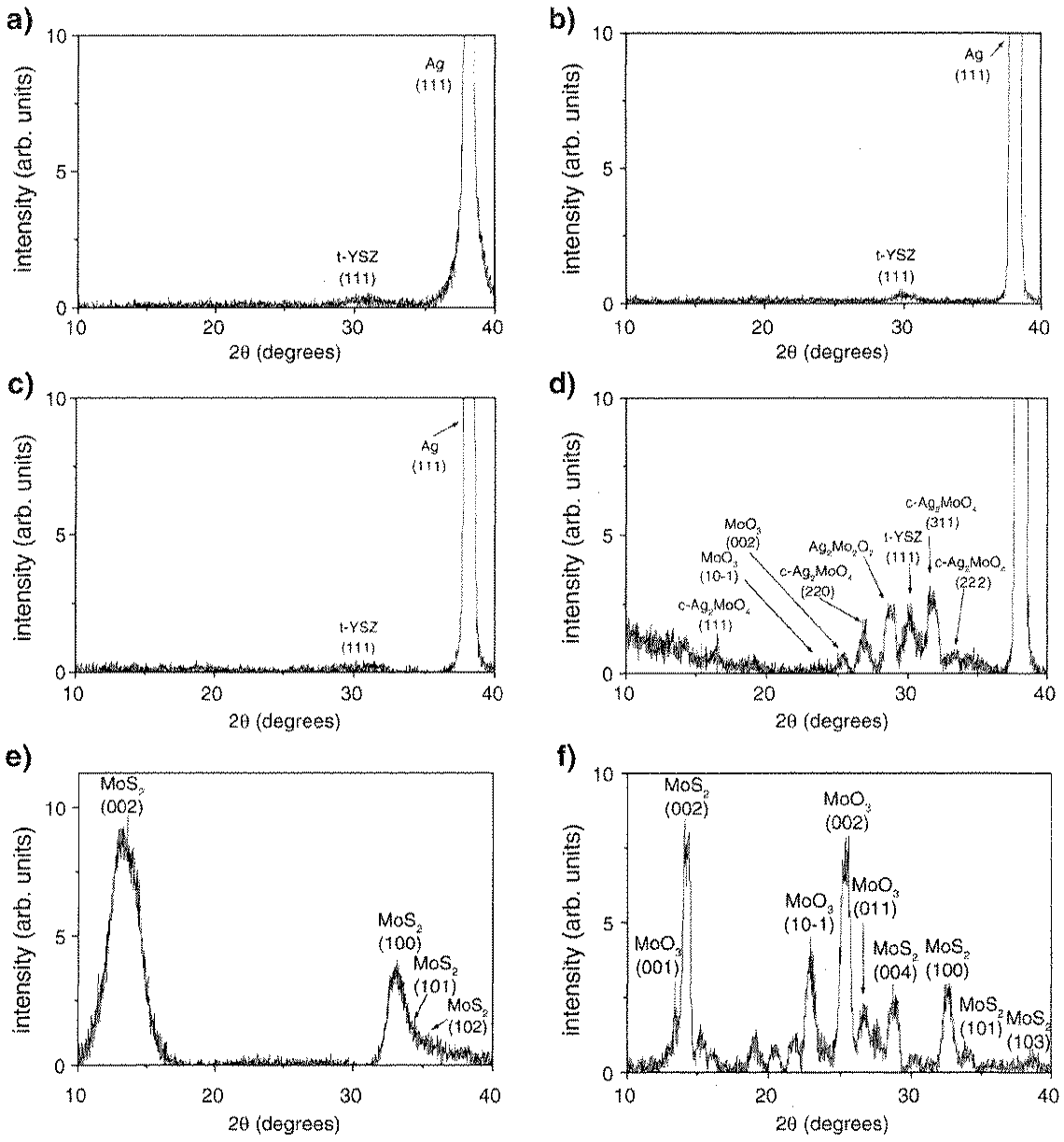


Fig. 2. Glancing incidence X-ray diffractograms of the (a–b) 0% MoS_2, (c–d) 8% MoS_2, and (e–f) 100% MoS_2 coatings after wear testing at 300 and 700 °C, respectively.

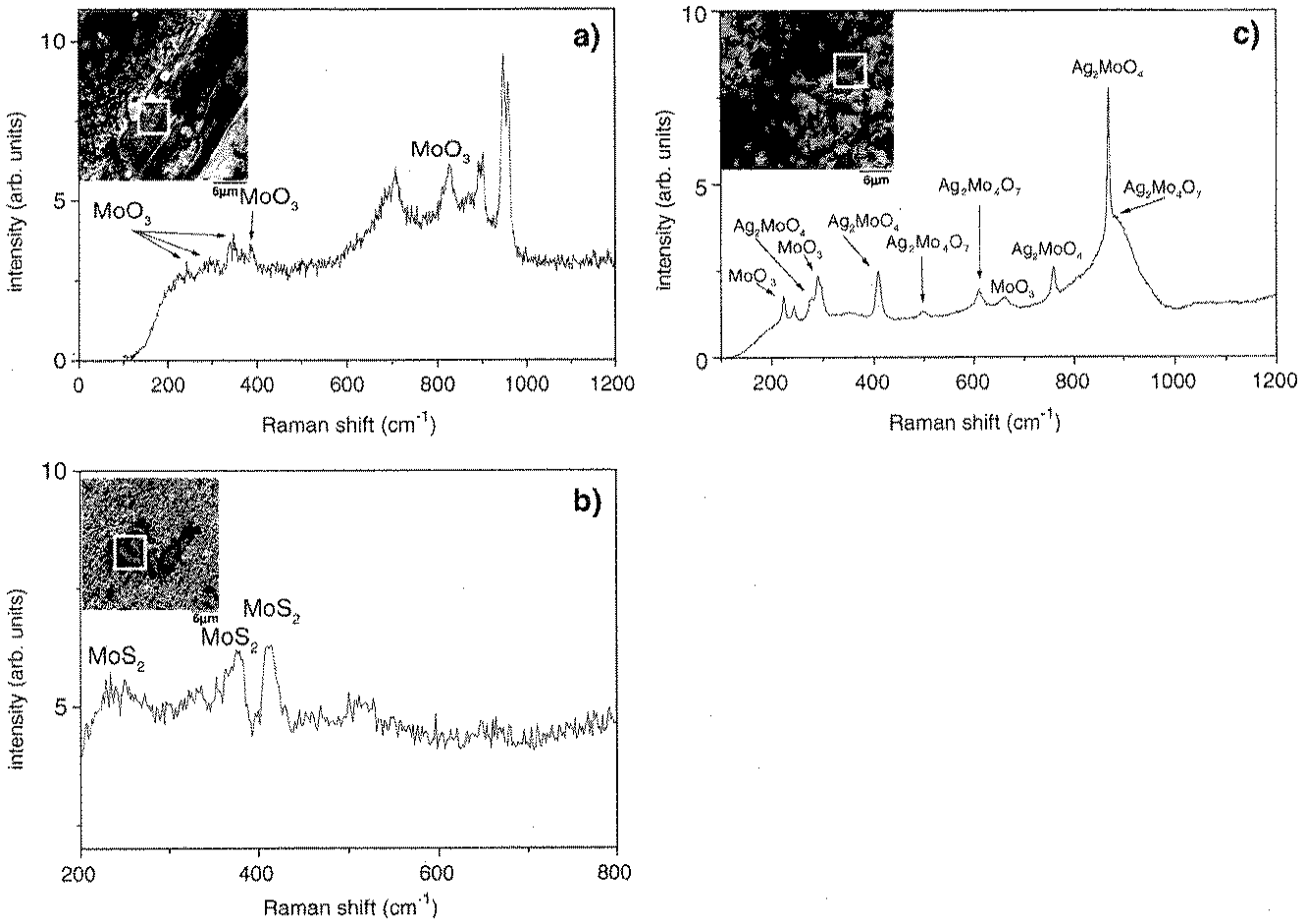


Fig. 3. Raman spectra for the (a) 0% MoS_2 coating tested at 700 °C and (b–c) the 8% MoS_2 coating tested at 300 and 700 °C, respectively. The inset micrograph shows a feature similar to those the laser was focused upon to produce the corresponding spectra.

shows that the phase in the wear track for the 8% MoS_2 coating heated to 700 °C consists of the same silver molybdate and molybdenum trioxide phases detected by X-ray diffraction on the coating surface.

4. Discussion

Comparison of the adaptive nanocomposites with and without MoS_2 shows that the addition of MoS_2 to the YSZ–Ag–Mo adaptive coatings reduced friction. Fig. 1c coupled with the Raman spectrum in Fig. 3b reveals that reduced friction at moderate temperatures (<300 °C) results from MoS_2 lubrication of an already lubricious silver surface. At higher temperatures however, it appears that MoS_2 facilitated the reaction of the Ag and Mo in the coating with ambient oxygen to produce the silver molybdate compounds Ag_2MoO_4 and $Ag_2Mo_2O_7$. These compounds only appeared in coatings containing MoS_2, and were not found in the YSZ–20 Ag–10 Mo (0% MoS_2) composites studied here, nor in any other composition of YSZ–Ag–Mo reported on previously [9,18]. Gulbinski et al. [17] reported on the low friction coefficients of these compounds between 300 and 600 °C, which were comparable to those measured in the present work, but with friction increasing at higher temperatures. The YSZ–Ag–Mo–MoS_2 coatings in the current work probably maintained a low friction (<0.2) coefficient at higher temperatures due to the formation of MoO_3 coupled with the other lubricious silver molybdate phases identified by X-ray diffraction and Raman spectroscopy. The same MoO_3 phase resulting from oxidation of the pure MoS_2 coating did not, however, yield the same low friction coefficient at 700 °C. Failure of MoS_2 at temperatures above 300 °C, is consistent with reports that 300–400 °C is the limit of MoS_2 as an effective lubricant [22]. The wear lifetimes of coatings with MoS_2 additions were also relatively short, however previous work [23,24] has shown that alternating the 0% MoS_2 adaptive coating with TiN diffusion barrier layers in a multilayer stack resulted in an order-of-magnitude lifetime improvement. It is expected that the coatings with MoS_2 additions will demonstrate similar behavior.

While the exact mechanism leading to formation of silver molybdate compounds in the presence of sulfur is not yet entirely clear, Li et al. [25] have shown that heating of a Ag/S/Mo system results in the reaction $MoS_x + Ag \rightarrow AgMoS_x$ upon heating to temperatures above room temperature. In air, at temperatures above 500 °C, it is likely that the sulfur was then replaced with oxygen to form the molybdate [26]. Details of the

mechanisms resulting in the ultimate composition of the coatings are currently being studied, however, it is suspected that the stick-like phase observed on the surface of YSZ–Ag–Mo–MoS_2 coatings after heating was a by-product of silver molybdate formation. Compositional analysis of these small features may be useful for determining the silver molybdate reaction pathway.

5. Conclusions

Friction coefficients of YSZ–Ag–Mo adaptive nanocomposite coatings with different MoS_2 additions were measured from 25 to 700 °C, and correlated to the composition and microstructural evolution of the coatings during testing. Adding 8% MoS_2 to the YSZ–Ag–Mo coatings resulted in a decrease in the friction coefficient from 0.4 to 0.2 from 25 to 700 °C. Lower friction in the 25–300 °C temperature range resulted from MoS_2 lubrication. At higher temperatures the MoS_2 additions did not directly provide lubrication, but rather promoted the formation of lubricious silver molybdate phases at the coating surface.

Acknowledgements

The Air Force Office of Scientific Research is gratefully acknowledged for financial support. The authors also wish to thank J. E. Bultman and A. Safriet for technical assistance.

References

[1] A.A. Voevodin, J.S. Zabinski, Thin Solid Films 370 (2000) 223.
[2] A.A. Voevodin, J.J. Hu, T.A. Fitz, J.S. Zabinski, J. Vac. Sci. Technol., A 20 (2002) 1434.
[3] J.S. Zabinski, M.S. Donley, V.J. Dyhouse, C. Melandri, Thin Solid Films 214 (1992) 156.
[4] C. DellaCorte, H.E. Sliney, Lubr. Eng. 47 (1991) 298.
[5] C. DellaCorte, Surf. Coat. Technol. 86–87 (1996) 486.
[6] J.L. Endrino, J.J. Nainaparampil, J.E. Krzanowski, Surf. Coat. Technol. 157 (2002) 95.
[7] A. Erdemir, R.A. Erck, G.R. Fenske, H. Hong, Wear 203–204 (1997) 588.
[8] J.J. Hu, A.A. Voevodin, J.S. Zabinski, J. Mater. Res. 20 (2005) 1860.
[9] C. Muratore, A.A. Voevodin, J.J. Hu, J.S. Zabinski, Wear, (in press).
[10] H.E. Sliney, Tribol. Int. (October 1982) 305.
[11] H.E. Sliney, ASLE Trans. 29 (1985) 370.
[12] A.A. Voevodin, J.J. Hu, T.A. Fitz, J.S. Zabinski, Surf. Coat. Technol. 146–147 (2001) 351.
[13] M.N. Gardos, in: I.M. Hutchings (Ed.), Plenary and Invited Papers from the First World Tribology Congress, 1997, p. 229.
[14] G. Gassner, P.H. Mayrhofer, K. Kutschej, C. Mitterer, M. Kathrein, Tribol. Lett. 17 (2004) 751.
[15] M. Woydt, A. Skopp, I. Dorfel, K. Witke, Wear 218 (1998) 84.
[16] C. Brechignac, Ph. Cahuzac, N. Kebaili, A. Lando, A. Masson, M. Schmidt, J. Chem. Phys. 121 (2004) 9617.
[17] W. Gulbinski, T. Suszko, W. Sienicki, B. Warcholinski, Wear 254 (2003) 129.
[18] C. Muratore, A.A. Voevodin, J.J. Hu, J.G. Jones, J.S. Zabinski, Surf. Coat. Technol. 200 (2005) 1549.
[19] A.A. Voevodin, M.A. Capano, A.J. Safriet, M.S. Donley, J.S. Zabinski, Appl. Phys. Lett. 69 (1996) 188.
[20] A.A. Voevodin, J.S. Zabinski, in: A.A. Voevodin, D.V. Shtansky, E.A. Levashov, J.J. Moore (Eds.), Nanostructured Thin Films and Nanodispersion Strengthened Coatings, Kluwer Academic Publishers, Dordrecht, The Netherlands, 2005, p. 103.
[21] J.S. Zabinski, N.T. McDevitt, Raman Spectra of inorganic compounds related to solid state tribochemical studies Report No. WL-TR-96-4034, 1996.
[22] H.E. Sliney, Tribol. Int. 15 (1982) 303.
[23] C. Muratore, A.A. Voevodin, J.J. Hu, J.S. Zabinski, Tribol. Lett., (in press).
[24] C. Muratore, J. J. Hu, A. A. Voevodin, Thin Solid Films, (in press).
[25] S.Y. Li, J.A. Rodriguez, J. Hrbek, H.H. Huang, G.-Q. Xu, Surf. Sci. 395 (1998) 216.
[26] M.T. Lavik, T.M. Medved, G.D. Moore, ASLE Trans. 11 (1968) 44.

Paper 4

Tribology Letters, Vol. 24, No. 3, December 2006 (© 2006)
DOI: 10.1007/s11249-006-9143-3

Multilayered YSZ–Ag–Mo/TiN adaptive tribological nanocomposite coatings

C. Muratore[a,*], A.A. Voevodin[b], J.J. Hu[c] and J.S. Zabinski[b]

[a]*UTC Inc., Air Force Research Laboratory, Materials and Manufacturing Directorate, Wright-Patterson Air Force Base, Dayton, OH 45433, USA*
[b]*Air Force Research Laboratory, Materials and Manufacturing Directorate, Wright-Patterson Air Force Base, Dayton, OH 45433, USA*
[c]*UES Inc., Air Force Research Laboratory, Materials and Manufacturing Directorate, Wright-Patterson Air Force Base, Dayton, OH 45433, USA*

Received 29 July 2005; accepted 21 October 2005; published online 15 November 2006

Adaptive nanocomposite coatings provide low friction in broad ranges of environmental conditions through the formation of lubricious surfaces resulting from interactions with the ambient atmosphere. Designing adaptive coatings to withstand wear through repeated thermal cycles is particularly difficult since most demonstrate irreversible changes in surface composition and morphology. This permanent change in the condition of the surface limits the utility of adaptive coatings in applications where thermal cycling is expected. Moreover, some lubrication mechanisms occur over the entire coating surface in addition to the area experiencing wear, which results in a significant waste of lubricant. In an effort to increase the wear lifetime and move toward thermal cycling capabilities of solid adaptive lubricants, a multilayer coating architecture incorporating two layers of adaptive YSZ–Ag–Mo nanocomposite lubricant separated by a TiN diffusion barrier was produced. The multilayer coating lasted over five times longer than a monolithic adaptive coating of identical composition and total thickness for dry sliding tests at 500 °C in air. Analysis of the structure and composition of the films after heating suggests directed, lateral diffusion of lubricant beneath the diffusion barrier toward the wear scar as a mechanism for the increased wear life of the multilayer coating.

KEY WORDS: adaptive, coatings, high-temperature, multilayers

1. Introduction

Adaptive nanocomposites, also known as "chameleon coatings," are a class of materials that automatically adjust surface composition and structure to minimize friction as the ambient environment changes [1–5]. The materials evolved from earlier works in adaptive tribological materials [6,7]. Adaptation results from amorphous and nanocrystalline inclusions that can transform into lubricious macro-phases on the friction surface when exposed to changes in temperature, relative humidity, and/or wear. The "chameleon" coatings are designed in such a way that the lubrication mechanisms of each phase are dominant in the friction contact while exposed to the environment to which they were well-suited. At the same time, the composition and structure of the subsurface matrix and other temporarily dormant solid lubricant nano-inclusions are preserved. Furthermore, nanocomposite tribological coatings have an advantage in that their mechanical properties do not follow the rule-of-mixtures behavior typically observed for composites. Therefore, adding lubricious phases in the nanocrystalline or amorphous form allows for preservation of the high hardness of the composite, even as softer phases are incorporated into a hard matrix [1,8].

Yttria-stabilized zirconia (YSZ) is tough, hard and thermally stable up to high temperatures, while nanocrystalline additives can provide lubrication in different temperature ranges and increase the toughness of the YSZ without severely compromising its hardness [3,8]. Chameleon coatings consisting of various nanoinclusions imbedded in an amorphous YSZ-noble metal matrix have demonstrated low friction coefficients at elevated temperatures resulting from noble metal diffusion to the coating surface [2,4,9]. Recent *in-situ* TEM studies of YSZ–Au nanocomposites during heating showed that the noble metal diffusion process is accompanied by coalescence at the surface [10]. From work on powder-based and other types of composites, it is known that silver is an effective lubricant up to moderately high temperatures [11–16]. YSZ–Mo composites showed moderately low friction above 500 °C [9] due to the formation of lubricious molybdenum-based compounds at high-temperature in air, similar to that shown by other researchers [17–21]. Examination of YSZ–Ag–Mo nanocomposites tested from 25 to 700 °C revealed both the noble metal and the soft oxide lubrication

*To whom correspondence should be addressed.
E-mail: chris.muratore@wpafb.af.mil

1023-8883/06/1200-0201/0 © 2006 Springer Science+Business Media, Inc.

mechanisms operating at the appropriate temperature, resulting in moderately low friction from 25–700 °C [9].

These mechanisms were explored further in this research as YSZ–Ag–Mo was incorporated in a multilayered architecture with two layers of adaptive coating separated by a diffusion barrier. The top layer was expected to behave in the same way as the monolithic nanocomposites described in Refs. [2] and [9], with noble metal diffusion and soft oxide formation at the coating surface upon heating. The TiN diffusion barrier was incorporated to prevent silver diffusion and molybdenum oxidation in the lower composite layer, until a free surface was created by wear, as shown in figure 1. Once the diffusion barrier was breached, it was expected that silver in the buried composite should be drawn to diffuse both vertically and horizontally through the matrix to the worn area. Restricting silver transport to the wear scar with the diffusion barrier, rather than permitting uncontrolled diffusion to the entire coating surface, was expected to increase coating life. It was also anticipated that the multilayer coating architecture should allow the lower layer of lubricant to remain homogeneous during heating, as the top layer adapted by silver diffusion and molybdenum oxidation in air. In this work, a comparison of coating characterization and wear test results for both monolithic and multilayered YSZ–Ag–Mo nanocomposite coatings is presented and discussed to demonstrate the utility of the multilayer adaptive nanocomposite coating concept.

2. Experimental procedure

Monolithic and multilayered nanocomposite coatings of yttria-stabilized zirconia (YSZ) with silver and molybdenum were deposited with a hybrid filtered vacuum arc/magnetron sputtering/pulsed laser deposition technique [22]. The details of the deposition process are given elsewhere [8]. Briefly, a YSZ target was irradiated with 800 mJ of pulsed laser energy at 30 Hz. The metal flux was provided by two magnetrons, each fitted with a silver or molybdenum target. The M50 steel substrates were heated to 150 °C and dc biased to −150 V. A filtered vacuum arc source was used to clean the substrates, deposit a thin (< 100 nm) titanium adhesion layer plus a Ti/YSZ graded layer at the interfaces for all films, and to reactively deposit a ≈100 nm thick TiN diffusion barrier layer between two 1 micron thick layers of YSZ–Ag–Mo for the multilayer coatings. A thin (< 100 nm) silver/molybdenum layer was deposited under the TiN layer to direct the silver composition gradient toward the substrate and to provide lubrication upon initial contact of the ball with the material under the diffusion barrier during wear testing.

The YSZ-based composite layers were examined after deposition using x-ray photoelectron spectroscopy (XPS), and were found to contain 24% silver and 10% Mo in the monolithic and multilayer coatings. A focused ion beam (FIB), transmission electron microscope (TEM), and scanning electron microscope (SEM) were used to characterize the coating cross-sections after heating. Electron dispersive spectroscopy (EDS) was also used to map the different cross-sectional compositions. A platinum film was deposited over the samples prior to cutting with the FIB to preserve the original surfaces during preparation of the cross-sections.

The friction coefficient of the coatings in air (40% relative humidity) at 500 °C was measured with a high temperature ball-on-disc tribometer with a 6.35 mm diameter silicon nitride ball under a 1 N load. The sliding rate was 0.2 m s^{-1}, with the disk rotating at 200 rpm for all tests. The tribometer apparatus was set up at room temperature, with the loaded silicon nitride ball in contact with the sample prior to heating. The coating surface was heated to 500 °C in 15 min, and allowed to equilibrate for 5 min before the sliding test was initiated. All coatings were tested to failure, as detected by an abrupt increase in the friction coefficient.

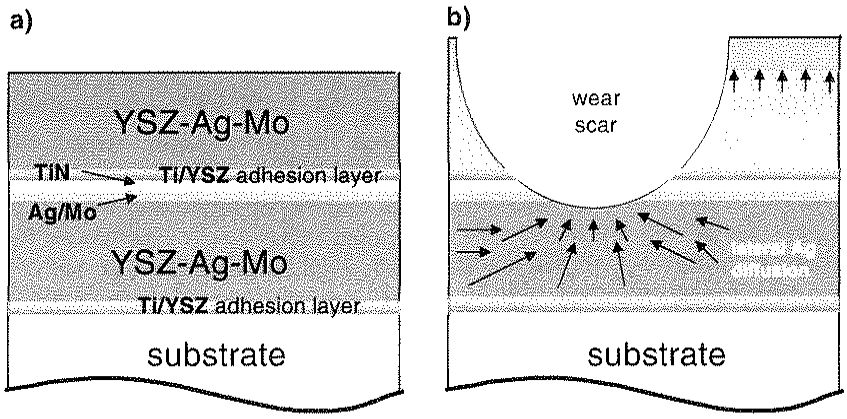


Figure 1. Schematics of the (a) as-deposited multilayer coating and (b) the anticipated response of the coating during high-temperature wear testing.

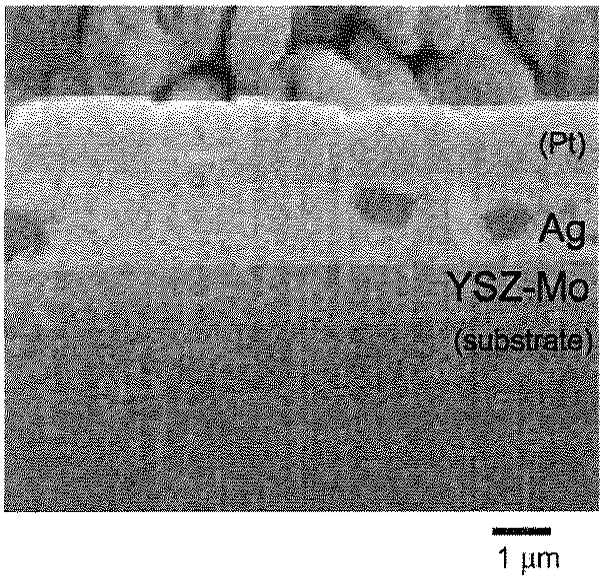


Figure 2. Cross-sectional scanning electron micrograph of the monolithic YSZ–Ag–Mo coating after wear testing at 500 °C.

The wear tracks were examined in an SEM following the wear tests.

3. Results

3.1. Monolithic YSZ–Ag–Mo nanocomposite coatings

The monolithic YSZ–24%Ag–10%Mo coating was initially 1.1 microns thick. After heating to 500 °C for 1.5 h, a diffused Ag layer was observed above the remaining YSZ–Mo layer, as shown in figure 2. Compositional mapping by EDS was used to determine the chemical make-up of the layers. Figure 3 shows a top view of the coating surface illustrating the morphology of the continuous silver layer after heating. XPS, EDS and X-ray diffraction confirmed that the surface consisted of a continuous layer of silver that diffused to the surface out of the remaining YSZ–Mo. The YSZ–Mo layer maintained its original thickness of 1.1 microns, while the silver layer added to the total coating thickness.

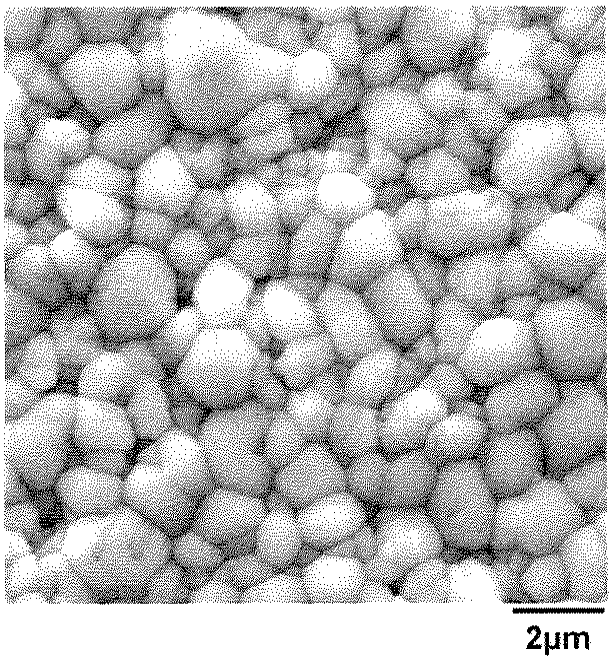


Figure 3. Scanning electron micrograph of the monolithic YSZ–Ag–Mo coating surface after heating to 500 °C.

A 2 micron thick monolithic YSZ–Ag–Mo sample (thicker than that pictured in Figure 2, but of identical composition and architecture) was subjected to wear testing at 500 °C. The film exhibited a friction coefficient of ≈0.4 for approximately 4,000 cycles before failure. Figures 4((a)–(b)) show electron micrographs of a region near the edge of a wear track after testing at 500 °C prior to coating failure. EDS compositional mapping revealed that the smeared regions and most of the surface in contact with the ball were composed of silver, as shown figure 4(b).

3.2. Multilayered (YSZ–Ag–Mo)–TiN–(YSZ–Ag–Mo) nanocomposite coating

Figure 5 shows a cross-sectional micrograph of the multilayered coating after heating to 500 °C for over two hours. The surface of the multilayer coating was very similar to that observed for the monolithic coating shown in figure 3, with the silver migrating to form a continuous layer at the coating surface, leaving behind a YSZ–Mo layer with only a trace amount of silver. The YSZ–Ag–Mo layer under the TiN diffusion barrier, however, remained homogeneous as shown by the EDS composition maps of Zr, Ag, Mo and Ti in figures 6((a)–(d)).

The friction coefficient for both monolithic and multilayered coatings at 500 °C is shown in figure 7. The monolithic coating provided lubrication for about 4,000 cycles. In contrast, the multilayer coating maintained an average friction coefficient of less than 0.4 for over 25,000 cycles. Figure 8 shows a section of a wear track in a multilayered coating sample after failure at 500 °C. This region of the wear track provided a cross-sectional view of different layers after testing, with the inset illustrating the position of the numbered layers relative to the film surface. Distinct differences in the surface morphology and composition of the layers comprising the films were apparent. Layer 1 (at the surface) and layer 3 (beneath the diffusion barrier) were similar in terms of morphology and composition, with silver coalescing to the surface in both layers.

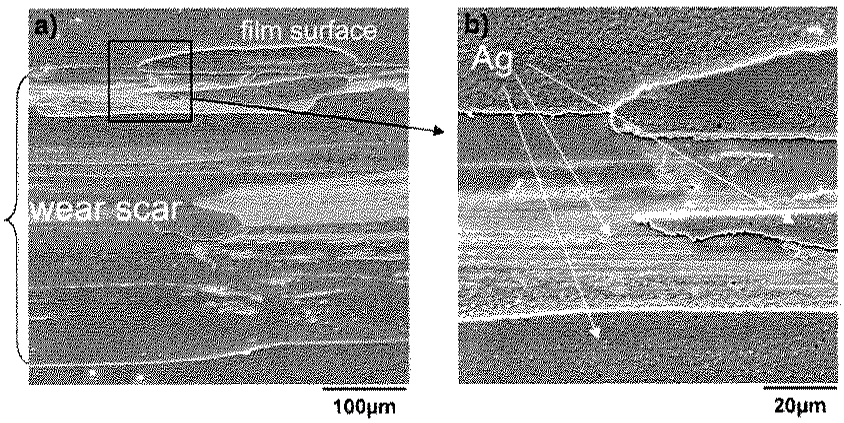


Figure 4. Scanning electron micrographs of (a) the entire wear track from the monolithic coating tested at 500 °C and (b) the edge of the wear track.

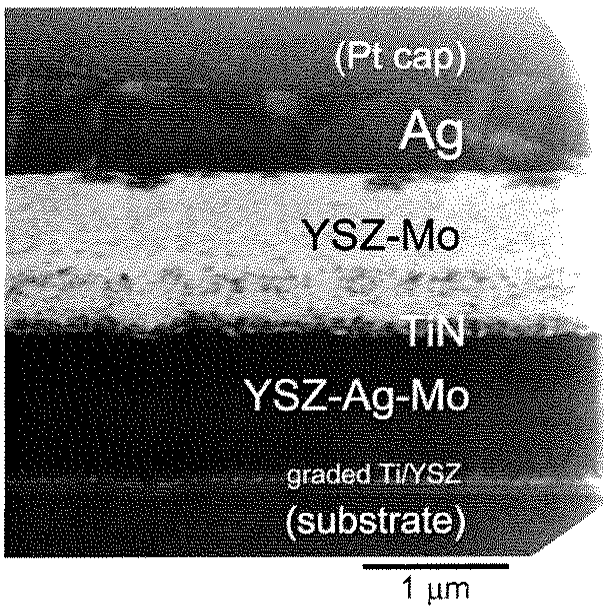


Figure 5. Transmission electron micrograph of the multilayer coating cross section after heating to 500 °C.

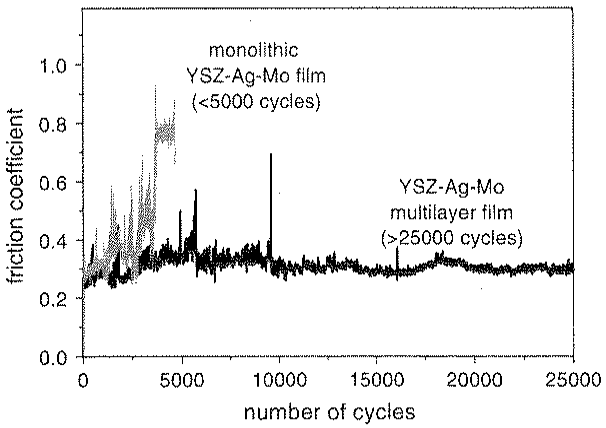


Figure 7. Friction traces for the monolithic and multilayer coatings at 500 °C in air.

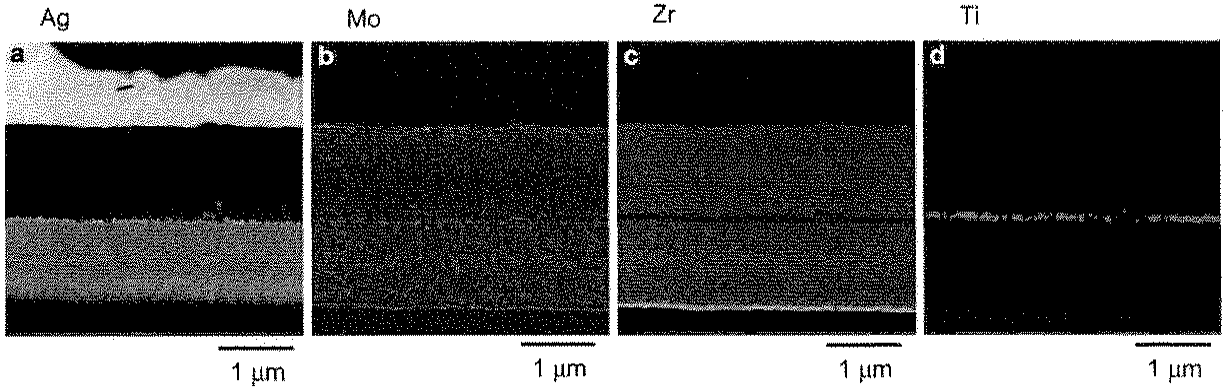


Figure 6. Energy dispersive spectrometry composition maps for (a) silver, (b) molybdenum, (c) zirconium, and (d) titanium.

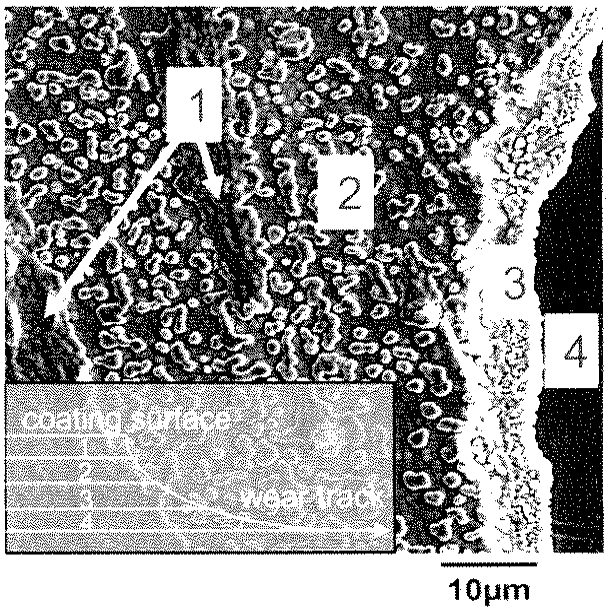


Figure 8. Scanning electron micrograph of a section of a wear track in the multilayer coating after failure.The numbers 1–4 correspond to the numbered layers in the inset to illustrate the topography of the micrograph as follows: 1-surface layer of diffused silver; 2-YSZ–Mo layer above TiN layer with some diffused silver; 3-YSZ–Mo–Ag layer under the diffusion barrier with a surface layer of diffused silver; 4-substrate.

4. Discussion

4.1. Monolithic nanocomposite coating

The monolithic YSZ–Ag–Mo coatings and the mechanisms leading to low friction at elevated temperatures have been discussed in detail previously [9]. To summarize, silver diffuses readily in YSZ to the free surface, and is an effective solid lubricant at lower and moderate temperatures, while MoO_3, and other lubricious compounds form when exposed to air at temperatures over 500 °C. YSZ–Ag–Mo composites demonstrated moderately low friction from 25–700 °C, however, at 500 °C, the monolithic YSZ–Ag–Mo composite exhibited a short lifetime when subjected to sliding wear (figure 7). At this temperature, a significant fraction of the silver in the composite diffused to the surface of the disk before the wear test began [9]. The lifetime of the lubricating silver layer was short due to excessive softening of the surface at a high fraction of its melting point [11,23], and the lack of lubricant supply to the worn area. Additionally, lubrication by MoO_3 formation was likely to be limited, since 500 °C is the lower limit at which Mo oxidation reactions occur in air [20,24]. Also, the residual YSZ–Mo coating became porous with the silver removed (figure 5) after one thermal cycle, resulting in an irreversible change in morphology and degradation of the mechanical properties after of the coating after heating.

4.2. Multilayered nanocomposite coating

A most critical factor contributing to the increased wear life of the multilayered coating was the controlled release of silver from the lower layer of adaptive composite after the first layer was worn through, as suggested in figure 1. Diffusion of the silver from the upper YSZ–Ag–Mo layer at 500 °C was fast enough to cover the surface before the wear test started [9], providing a lubricious and protective silver layer on the surface of a porous YSZ–Mo composite. Once the silver was depleted, the ball had no lubrication on the weakened YSZ–Mo. However, the multilayer architecture provided a fresh layer of nanocomposite after the TiN diffusion barrier was worn through. The release of silver from the buried layer of composite material was initiated only after the ball created a free surface at this layer in the wear scar, which triggered silver diffusion laterally toward the wear track. Lateral diffusion of the silver from within the lower composite layer to the wear track area, which was small compared to the total surface area of the coating, resulted in a longer-lasting supply of silver lubricant, thereby contributing to the longer lifetime of the multilayer composite. The results demonstrate the benefit of the multilayer nanocomposite design for longer lasting lubrication in a broad range of temperatures. Also, the multilayer structure should be useful for applications requiring thermal cycling, which will be explored in future research.

5. Conclusions

A conceptual schematic for a multilayer nanocomposite coating was suggested, where adaptive nanocomposite materials are sealed under a diffusion barrier layer to force lubricant to diffuse laterally to the wear scar and to protect layers under the barrier from the

environment. As an example, two layers of YSZ–Ag–Mo adaptive nanocomposites were separated by a TiN diffusion barrier layer in a multilayer coating architecture. The multilayer coatings demonstrated a marked increase in wear life when compared to a monolithic coating of the same total thickness and adaptive nanocomposite composition. Titanium nitride functioned as an effective diffusion barrier between layers of adaptive coating material, and preserved the homogeneity of the layer unexposed to air at high temperature. The increased wear life was attributed to the channeling of solid lubricants laterally under the diffusion barrier layer to exposed wear areas, rather than to the entire coating surface. Further study is needed to optimize the coating architectures and compositions for maximum wear resistance and minimum friction, however, the principle of preserving adaptive layers under a diffusion barrier and lateral lubricant diffusion to reduce wear rate was demonstrated in this work.

Acknowledgments

The Air Force Office of Scientific Research is gratefully acknowledged for financial support. The authors also wish to thank J. Bultman and A. Safriet for technical assistance.

References

[1] A.A. Voevodin and J.S. Zabinski, Thin Solid Films 370 (2000) 223.
[2] A.A. Voevodin, J.J. Hu, T.A. Fitz and J.S. Zabinski, Surf. Coat. Technol. 146–147 (2001) 351.
[3] A.A. Voevodin, J.G. Jones, J.J. Hu, T.A. Fitz and J.S. Zabinski, Thin Solid Films 401 (2001) 187.
[4] A.A. Voevodin, J.J. Hu, T.A. Fitz and J.S. Zabinski, J. Vac. Sci. Technol. A 20 (2002) 1434.
[5] A.A. Voevodin and J.S. Zabinski, Compos. Sci. Technol. 65 (2005) 741.
[6] S.D. Walck, J.S. Zabinski, N.T. McDevitt and J.E Bultman, Thin Solid Films 305 (1997) 130.
[7] J.S. Zabinski, M.S. Donley, V.J. Dyhouse and C. Melandri, Thin Solid Films 214 (1992) 156.
[8] C. Muratore, A.A. Voevodin, J.J. Hu, J.G. Jones and J.S. Zabinski, Surf. Coat. Technol. 200 (2005) 1549.
[9] C. Muratore, A.A. Voevodin, J.J. Hu and J.S. Zabinski, submitted to Wear, 2005 (doi: 10.1016/j.wear.2006.01.029).
[10] J.J. Hu, A.A. Voevodin and J.S. Zabinski, J. Mat. Sci. 20 (2005) 1860.
[11] H.E. Sliney, Tribol. Int. 15 (1982) 303.
[12] H.E. Sliney, ASLE Trans. 29 (1985) 370.
[13] A. Erdemir, R.A. Erck, G.R. Fenske and H. Hong, Wear 203–204 (1997) 588.
[14] J.L. Endrino, J.J. Nainaparampil and J.E. Krzanowski, Surf. Coat. Technol. 157 (2002) 95.
[15] C. DellaCorte and H.E. Sliney, Lubr. Eng. 47 (1991) 298.
[16] C. DellaCorte, Surf. Coat. Technol. 86–87 (1996) 486.
[17] S.F. Murray and S.J. Calabrese, Lubr. Eng. 49 (1992) 955.
[18] M.B. Peterson, S.F. Murray and J.J. Florek, ASLE Trans. 2 (1959) 225.
[19] K.L. Strong and J.S. Zabinski, Thin Solid Films 406 (2002) 174.
[20] K.J. Wahl, L.E. Seitzman, R.N. Bolster and I.L. Singer, Surf. Coat. Technol. 89 (1997) 245.
[21] M. Woydt, A. Skopp, I. Dorfel and K. Witke, Wear 218 (1998) 84.
[22] A.A.Voevodin and J.S. Zabinski, in: *Nanostructured Thin Films and Nanodispersion Strengthened Coatings*, A.A.Voevodin, D.V. Shtansky, E.A. Levashov and J.J. Moore, eds.(Kluwer Academic Publishers, Dordrecht, The Netherlands, 2005) ch 10.
[23] F.P. Bowden and D. Tabor, J. Appl. Phys. 14 (1943) 141.
[24] N. Solak, F. Ustel, M. Urgen, S. Aydin and A.F. Cakir, Surf. Coat. Technol. 174–175 (2003) 713.

Paper 5

Available online at www.sciencedirect.com
ScienceDirect
Thin Solid Films 515 (2007) 3638–3643
www.elsevier.com/locate/tsf

Adaptive nanocomposite coatings with a titanium nitride diffusion barrier mask for high-temperature tribological applications

C. Muratore [a,*], J.J. Hu [b], A.A. Voevodin [c]

[a] UTC Inc., Air Force Research Laboratory, Materials and Manufacturing Directorate, Wright-Patterson Air Force Base, Ohio, 45433 USA
[b] UES Inc., Air Force Research Laboratory, Materials and Manufacturing Directorate, Wright-Patterson Air Force Base, Ohio, 45433 USA
[c] Air Force Research Laboratory, Materials and Manufacturing Directorate, Wright-Patterson Air Force Base, Ohio, 45433 USA

Received 23 December 2005; received in revised form 27 September 2006; accepted 27 September 2006
Available online 29 November 2006

Abstract

Adaptive nanocomposite coatings that demonstrate low friction throughout broad ranges of temperature, wear, humidity and other environments are currently in development. One effective temperature adaptation mechanism at temperatures ≤ 500 °C is diffusion of noble metal to the coating surface, providing a low shear strength interface at the friction contact supported by a hard surface underneath. To prolong the wear lifetime of chameleon coatings relying upon this mechanism for low friction, a coating architecture incorporating a diffusion barrier mask to inhibit noble metal diffusion was employed. The diffusion barrier-capped coating provided lubrication at 500 °C over ten times longer than the monolithic yttria-stabilized zirconia–silver–molybdenum coating of the same thickness without failure. Characterization of coatings after heating with surface analysis and microscopy techniques revealed the mechanism for increased coating life, and allowed for measurement of silver self-diffusion parameters in the adaptive nanocomposite material.
© 2006 Elsevier B.V. All rights reserved.

Keywords: Adaptive coatings; Nanocomposite; Titanium nitride; Tribology

1. Introduction

Adaptive nanocomposites, also known as "chameleon coatings," are a class of materials that automatically adjust surface composition and structure to minimize friction as the ambient environment changes [1–5]. Adaptation results from amorphous and nanocrystalline inclusions that can transform into lubricious macro-phases on the friction contact surface when exposed to changes in temperature, relative humidity, and/or wear. A series of adaptive coatings incorporating metals in a nanocrystalline/amorphous yttria-stabilized zirconia (YSZ) matrix were designed especially for use as solid lubricants from 25–700 °C. These coatings incorporated soft noble metals for lubrication at low and moderate temperatures, and other transition metals known to form lubricous oxides at higher temperatures. A YSZ–Ag–Mo coating, which provides lubrication by forming a silver rich surface at 300–500 °C, and a MoO_3 surface at temperatures above 500 °C, was selected for the present work.

While the adaptive lubrication mechanisms are effective in reducing the friction of pure YSZ coatings from ≈0.8 to 0.2 [2,6], the coating lifetime is generally limited to 10,000 cycles or less. One reason for the relatively short lifetime is the homogeneous diffusion of silver or gold to the entire coating surface, illustrated in Fig. 1a and b. The coatings are produced in a metastable condition, by forced co-deposition of metal and crystalline YSZ at substrate temperatures of 150 °C. As-deposited, these nanocomposite coatings have noble metal atoms distributed in a YSZ matrix, as either dispersed atoms or nanoinclusions in distorted YSZ nanocrystals or amorphous YSZ regions. Heating activates metal diffusion out of highly strained sites in the YSZ matrix to the open surface, where metal grain nucleation and growth is thermodynamically driven by the reduction of system potential and surface energy. Upon heating, the noble metal rapidly distributes itself over the entire surface, as the coating bulk becomes depleted in lubricious metal phases. While the depletion of the metal from the composite matrix to the

* Corresponding author.
E-mail address: chris.muratore@wpafb.af.mil (C. Muratore).

0040-6090/$ - see front matter © 2006 Elsevier B.V. All rights reserved.
doi:10.1016/j.tsf.2006.09.051

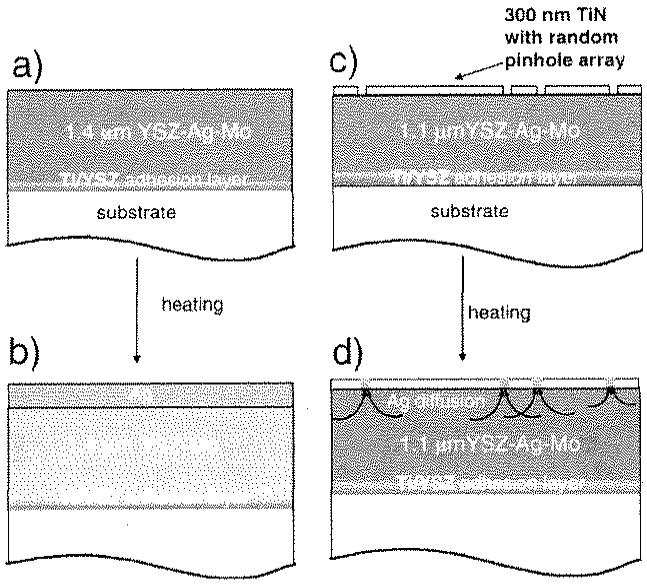


Fig. 1. Schematic of (a) the monolithic adaptive coating, and (b) its response to heating. The pinholes in the as-deposited TiN–YSZ–Ag–Mo coating (c) should allow for control of silver migration to the coating surface upon heating (d).

surface is essential for chameleon adaptive behavior, the controlled restriction of diffusion is needed to extend the coating service life.

Transition metal nitrides are documented as effective diffusion barrier materials for noble metals [7–9]. It was presumed that a TiN barrier layer with a random array of pinholes could be coupled with an adaptive coating layer (Fig. 1c) to limit lubricant transport to the coating surface only through those holes (Fig. 1d), thus reducing the rate of lubricant depletion in the adaptive coating layer and prolonging the life of the coating during sliding wear at elevated temperatures. A YSZ–Ag–Mo coating design incorporating a TiN surface "mask" layer was

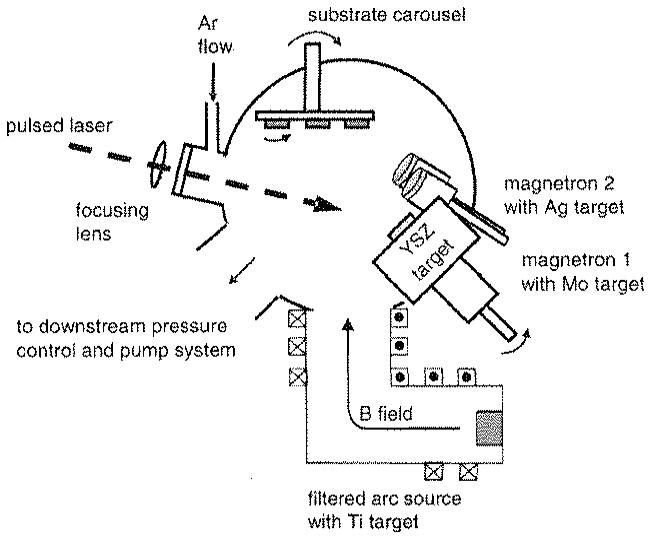


Fig. 2. Schematic of the hybrid filtered vacuum arc/magnetron sputtering/pulsed laser deposition system.

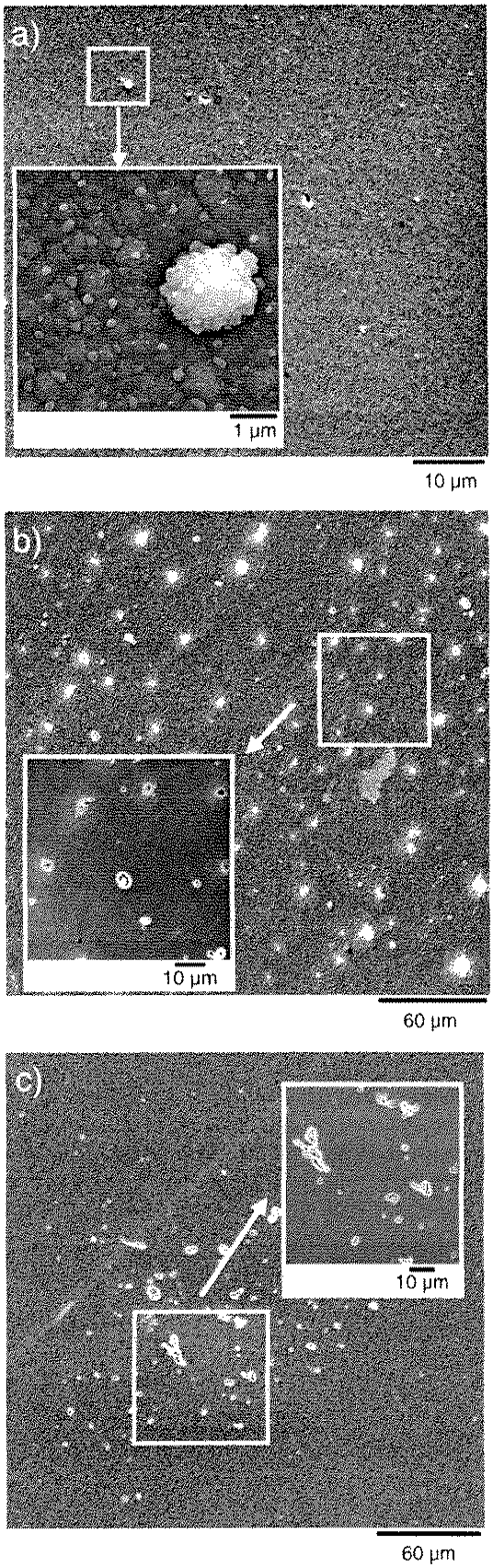


Fig. 3. Scanning electron micrographs of the as-deposited coatings: (a) monolithic YSZ–Ag–Mo, (b) monolithic TiN, and (c) TiN/YSZ–Ag–Mo.

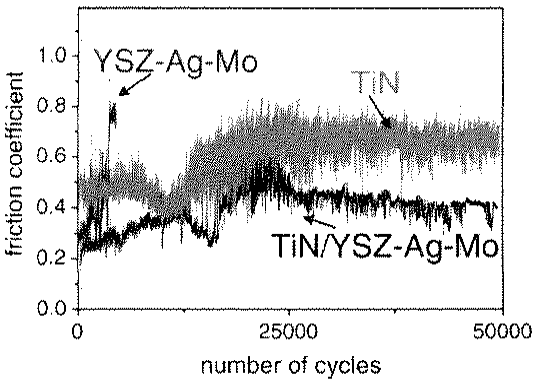


Fig. 4. Friction traces of the three coatings in air at 500 °C.

used to test this concept in the current work. The TiN/YSZ–Ag–Mo coating architecture also allowed for determination of the diffusion rates and coefficients of silver through the adaptive coating matrix to the coating surface.

2. Experimental procedure

Coatings were deposited with a hybrid filtered vacuum arc/magnetron sputtering/pulsed laser deposition technique [10,11] in a stainless steel chamber shown schematically in Fig. 2. For each deposition, six 1 in. diameter M50 steel substrates were degreased ultrasonically and loaded into the chamber. The chamber was pumped with a 520 l s^{-1} turbomolecular pump to a base pressure of 7×10^{-6} Pa or less. The substrates were heated to 150 °C, then bombarded with energetic argon ions (≤800 eV) and metal ions (≤650 eV) to clean the surface before deposition. The metal ions were produced with a filtered arc plasma source fitted with a titanium cathode. After cleaning, the titanium ion-based plasma was used to deposit a thin (<80 nm) adhesion layer. Pulsed laser deposition (PLD) of YSZ was then initiated while operating the arc source to produce a ≈300 nm graded Ti/YSZ transition layer to further promote coating adhesion. The PLD process employed a KrF excimer laser (248 nm) to deliver 800 mJ, 25 ns wide UV pulses (248 nm) at incrementally increasing pulse frequencies from 2–30 Hz to a 5 wt.% yttria-stabilized zirconia (YSZ) target, with the substrates biased to −150 V dc and maintained at 150 °C. Programmable mirrors were used to direct the laser to random positions on the surface of the rotating, 5.0 cm diameter YSZ

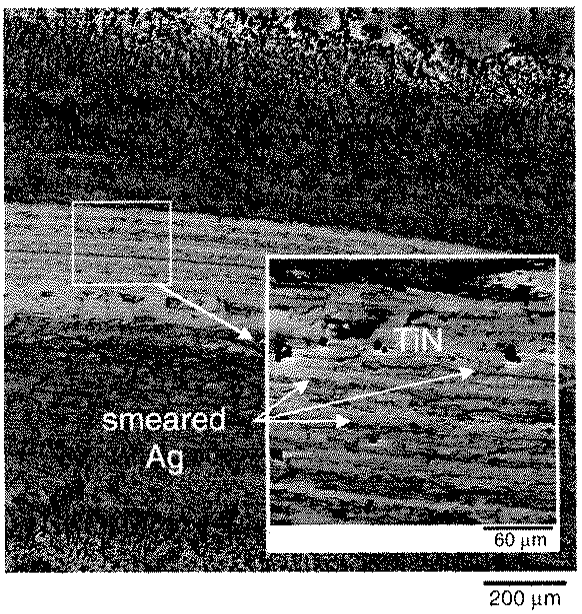
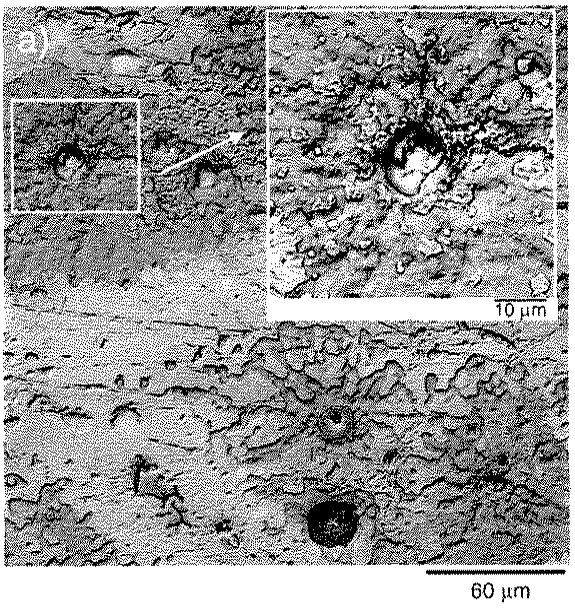


Fig. 5. Scanning electron micrograph of the TiN/YSZ–Ag–Mo wear track after wear testing for 50,000 cycles at 500 °C.



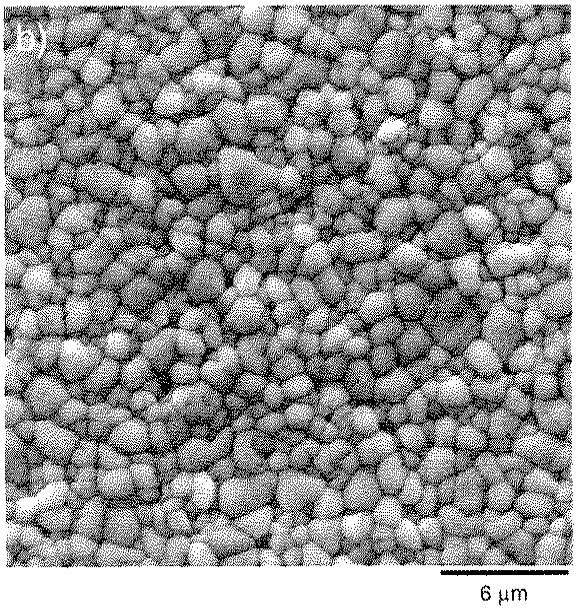


Fig. 6. Scanning electron micrographs of (a) the TiN/YSZ–Ag–Mo coating surface and (b) the surface of the monolithic adaptive coating after wear testing at 500 °C.

target. The chamber was then filled with 1.6 Pa Ar (99.99% pure) at a flow rate of 100 sccm. The arc source was turned off and two magnetrons, each fitted with a 3.3 cm pure metal target and configured as shown in Fig. 2, were used to add silver and molybdenum to the YSZ. After depositing 1.1 μm of adaptive YSZ–Ag–Mo nanocomposite material, a 300 nm TiN layer was deposited by flowing 30 sccm nitrogen into the chamber while operating the filtered titanium arc plasma source. For this final step, the uppermost magnetic field coil on the filtered arc source was deliberately defocused to reduce the ion flux density and energy to produce a TiN layer with the desired array of randomly dispersed holes. Monolithic YSZ–Ag–Mo and TiN coatings were also produced under the same applicable conditions as those described above for comparison in sliding friction. X-ray photoelectron spectroscopy (XPS) was used to determine that the YSZ–Ag–Mo coatings contained 24 at.% Ag and 10 at.% Mo. XPS was also used to determine that the TiN coatings were stoichiometric.

The as-deposited coatings were examined with electron microscopy techniques, and then subjected to ball-on-disc wear testing at 500 °C in air with 40% relative humidity. A 6.35 mm silicon nitride ball with a 1 N load was used for all tests. The sliding rate was ≈ 0.075 m s^{-1}, with the disk rotating at approximately 75 rpm. The tribometer thermocouple was calibrated before testing with a separate thermocouple spot-welded to an uncoated M50 substrate that was heated without rotation. Wear tests were started after the coating samples were heated to the desired temperature (≈20 min) and allowed to equilibrate for 5 min. Upon completion of the ball-on-disk tests, samples were immediately removed from the furnace and allowed to cool in air. The coatings were examined again with electron microscopy and X-ray energy dispersive spectroscopy, after wear testing.

A series of annealing experiments were also performed to better understand the adaptive lubrication mechanisms demonstrated by the TiN/YSZ–Ag–Mo coating. Three different samples were annealed for 45 min at 425, 500 and 575 °C. A focused ion beam (FIB) along with scanning and transmission electron microscopes (SEM and TEM) were used to produce and examine cross sections of the coatings after heating [6,12].

3. Results

Fig. 3a–c are scanning electron micrographs of the as-deposited coatings. In Fig. 3a, the surface of the adaptive YSZ–Ag–Mo coating is shown to have sub-micron clusters of silver and larger YSZ–Mo grains. X-ray diffraction and cross-sectional transmission electron microscopy revealed that the coating consisted of an amorphous/nanocrystalline YSZ matrix with nanocrystalline metal inclusions [10]. Fig. 3b shows the monolithic TiN coating with randomly dispersed holes on the surface. Fig. 3c shows the TiN/YSZ–Ag–Mo coating. The YSZ–Ag–Mo coating can be observed through the TiN holes, which looks similar to that shown in Fig. 3a.

Fig. 4 shows the friction behavior of each film in the ball-on-disc tests at 500 °C. The monolithic adaptive coating demonstrated a steady state friction coefficient of 0.4 before failure at 4500 cycles, as indicated by a sudden increase in the friction coefficient. The friction coefficient of the titanium nitride was maintained at 0.5 for approximately 12,000 cycles before increasing to 0.65, which is consistent with the friction coefficient observed for the uncoated M50 substrate at 500 °C under similar conditions [6]. The TiN/YSZ–Ag–Mo coating did not fail over the 50,000 cycles, and maintained a friction coefficient of ≈ 0.4. Micrographs of the TiN/YSZ–Ag–Mo wear track are shown in Fig. 5. X-ray energy dispersive spectroscopy measurements were used to find that the wear track was composed of a layer of silver smeared over the TiN. A micrograph of the heated TiN/YSZ–Ag–Mo surface away from the wear track is shown in Fig. 6a. From the higher-magnification inset, it appears that silver diffused out of the lower YSZ–Ag–Mo layer through the holes in the TiN masking layer, whereas in the monolithic YSZ–Ag–Mo coating, the equiaxed grains of silver were homogeneously distributed over the entire coating surface

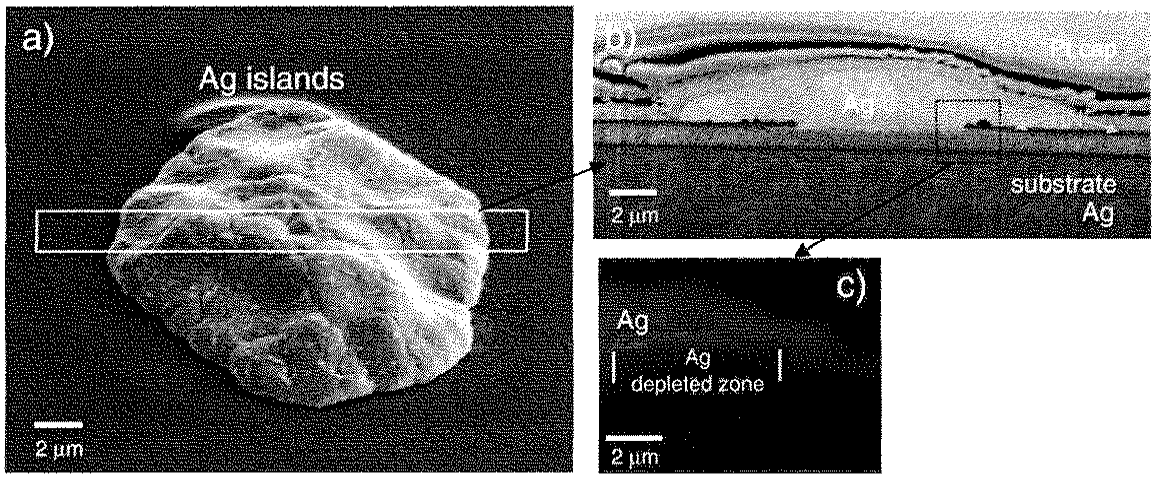


Fig. 7. Scanning electron micrographs showing (a) the surface of the annealed TiN/YSZ–Ag–Mo coating after 45 min. The rectangle indicates the cross-sectioned area in (b). An XEDS map of a similar cross-section (c) shows that the silver diffused laterally to the coating surface, out of the pinhole, leaving a clearly defined region depleted in silver.

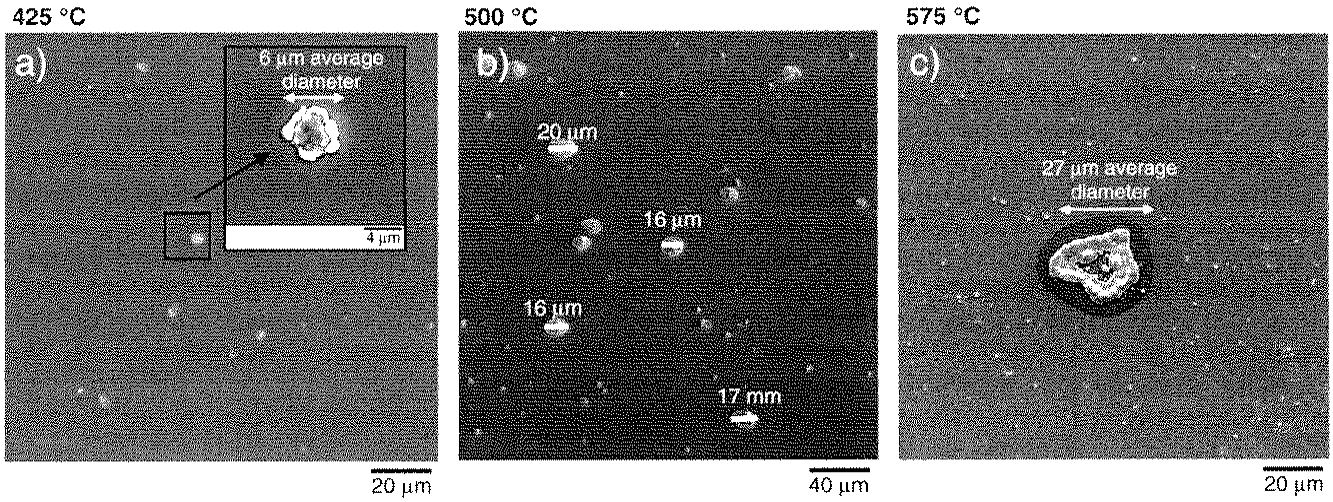


Fig. 8. Scanning electron micrographs of the TiN–YSZ–Ag–Mo coatings after annealing for 45 min at (a) 425 °C, (b) 500 °C, and (c) 575 °C.

(Fig. 6b). Several samples were subjected to a 12 h duration wear tests, with a subsequent analysis by both Auger and XPS techniques. This analysis confirmed that the surface of the adaptive composite coating which was capped with a "holey" TiN masking layer consisted of silver with some oxygen. Measurement of the wear scar to determine the wear rate was inconclusive since the total thickness of the coating increased by an unknown amount because of silver segregation to the surface, as shown in Fig. 6a. The relatively low wear rate can be predicted however, from the fact that XPS in the wear scar of the TiN/YSZ–Ag–Mo coating did not reveal any substrate elements, only silver, titanium, nitrogen and oxygen. Thus, 50,000 sliding cycles (or 3 km) were not enough to wear through the total coating thickness.

Another TiN/YSZ–Ag–Mo sample was heated to 500 °C in the tribometer furnace and maintained at that temperature for 45 min to observe evolution of the surface morphology and composition in the early stages of heating. Fig. 7a shows the surface of the coating after annealing. The FIB was used to cut out sections across the diameters of silver islands, as shown in Fig. 7a and b. EDS composition maps were generated for all of the elements detected in the cross sections. Silver EDS maps revealed that silver migrated upwards, from below the TiN layer to the surface, leaving behind a section of YSZ–Mo coating material (Fig. 7c).

From the micrograph in Fig. 7c, it was determined that a silver atom had to travel an average minimum distance of 6 μm from the border of the silver depleted region inside YSZ–Ag–Mo layer indicated on the figure. Based on this observation of the diffusion controlled depletion length, the diffusivity (D) of silver in YSZ at 500 °C was estimated to be 1×10^{-10} cm^2 s^{-1} assuming parabolic diffusion, where $x\approx(Dt)^{1/2}$. It was also observed that a 17 μm average silver island size corresponded to an average depletion length of 6 μm. As-deposited samples of the TiN/YSZ–Ag–Mo coating were annealed at 425 and 575 °C for 45 min to observe the temperature dependence on diffusion length. This somewhat narrow range of annealing temperatures was selected to minimize the difference in heating and cooling time. The time to heat to 425 °C was approximately 15 min compared to ≈20 min to heat to 575 °C. The diffusion distance for the samples annealed at 425 and 575 °C were obtained by assuming a linear relationship between the silver island diameter and the length of the depleted silver zone beneath the TiN layer for each sample, proportional to that observed for the sample annealed at 500 °C. Electron micrographs of the surfaces of the coatings annealed at the three different temperatures are shown in Fig. 8. The average island diameters were 6 mm for the sample heated to 425 °C (Fig. 8a), and 26.5 mm for the sample heated to 575 °C (Fig. 8c). A log plot of the silver migration rate squared versus inverse temperature yielded a straight line shown in Fig. 9. The migration rate was based on an average diameter of at least 10 Ag islands located at least 2 island diameters away from neighboring islands for each temperature. The data yielded an estimated diffusion prefactor (D_o) of 4.0×10^{-4} cm^2 s^{-1} and activation energy of 1.0 eV/atom for diffusion of silver in the YSZ-based nanocomposite material.

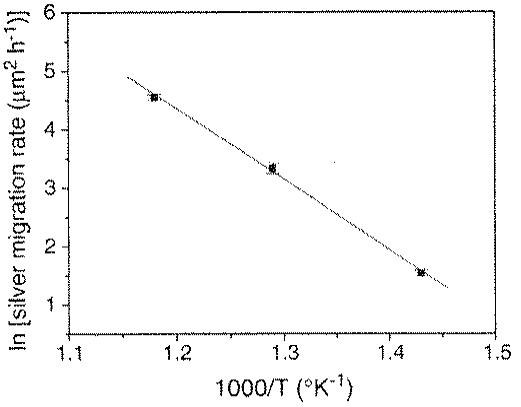


Fig. 9. Arrhenius plot of the temperature dependent migration rate data. The line is a least squared fit to the data.

4. Discussion

Noble metal diffusion from the YSZ-based matrix to the composite surface at temperatures ≥300 °C has been observed in several other works [2,4,6,12], and similar phenomena have also been reported in other composite materials [13,14]. The migration of silver to the surface at elevated temperatures is of interest for tribological applications, as silver demonstrates a relatively low shear strength, and can reduce the friction coefficient on hard surfaces during sliding wear [15,16]. The monolithic YSZ–20Ag–10Mo coating in this work demonstrated a friction coefficient of 0.4 at 500 °C, which has been attributed to lubrication of the hard YSZ by silver [6]. The lifetime of the monolithic coating was short compared to the TiN-capped adaptive coating, because nearly all of the silver diffused to the surface in approximately 45 min. Comparison of the surface shown in Fig. 7a to that in Fig. 6b reveals that the rate of Ag depletion in the TiN/YSZ–Ag–Mo coating was substantially slower, as both samples were maintained at 500 °C for the same amount of time.

While the rate of silver transport was reduced in the TiN capped coating, Fig. 4 shows that the friction coefficient was comparable to that observed in the monolithic coating with rapid silver transport and complete surface coverage. The micrographs of the wear track in Fig. 5 indicate that silver was distributed over the TiN surface, which showed little wear after the 50,000 cycle wear test at 500 °C. Nevertheless, 0.4 appears to be the lower limit of friction coefficient for hard surfaces lubricated by diffused silver. Adaptive composite materials exhibiting lower friction coefficients over a broad temperature range demonstrate similar diffusion mechanisms [17], and will be used in similar, future studies.

The Arrhenius plot shown in Fig. 9 suggests that diffusion through pinholes in the diffusion barrier layer is the means by which silver is supplied to the coating surface during heating. Although the estimated diffusion prefactor and activation energy were low compared to typical published values in the literature for silver volume self-diffusion in metal [18] or ceramic matrices [19], the values were consistent with published values for silver grain boundary self-diffusion [20,21] and for self-diffusion in amorphous materials [22]. Indeed, the relationship of the diffusion prefactor to the activation energy was consistent with that discussed by Naundorf et al. for self-diffusion of metals in an amorphous matrix [22]. Moreover, the relatively large surface and strain energies of the silver inclusions, immiscible in the YSZ matrix, may have further contributed to rapid diffusion and coalescence of silver to the coating surface [13].

5. Conclusions

An adaptive solid lubricant coating layer capped with a "holey" TiN layer demonstrated a lower friction coefficient and wear rate than monolithic TiN or adaptive coatings. The increased wear life was attributed to the reduced depletion rate of silver lubricant resulting from restricted flow through the holes in the TiN. The friction coefficient was typical of soft noble metal lubrication of hard surfaces. The mechanism of silver transport to the coating surface during heating was identified to be diffusion from the adaptive composite matrix to the free surface of the coating. The architecture of the coating allowed for a measurement of the diffusion prefactor (D_o) and activation energy for silver in nanocrystalline/amorphous YSZ, which were 4.0×10^{-4} cm^2 s^{-1} and 1.0 eV/atom, respectively. These values were attributed to the large number of defects in the YSZ matrix in addition to the reduction in surface and strain energy accompanied by migration to the surface.

Acknowledgements

The Air Force Office of Scientific Research is gratefully acknowledged for funding this research. The authors also wish to thank John E. Bultman and Art Safriet for their technical assistance.

References

[1] A.A. Voevodin, J.S. Zabinski, Thin Solid Films 370 (2000) 223.
[2] A.A. Voevodin, J.J. Hu, T.A. Fitz, J.S. Zabinski, Surf. Coat. Technol. 146–147 (2001) 351.
[3] A.A. Voevodin, J.G. Jones, J.J. Hu, T.A. Fitz, J.S. Zabinski, Thin Solid Films 401 (2001) 187.
[4] A.A. Voevodin, J.J. Hu, T.A. Fitz, J.S. Zabinski, J. Vac. Sci. Technol., A, Vac. Surf. Films 20 (2002) 1434.
[5] A.A. Voevodin, J.S. Zabinski, Compos. Sci. Technol. 65 (2005) 741.
[6] C. Muratore, A.A. Voevodin, J.J. Hu, J.S. Zabinski, Wear 261 (2006) 797.
[7] D. Adams, G.F. Malgas, N.D. Theodore, R. Gregory, H.C. Kim, E. Misra, T.L. Alford, J.W. Mayer, J. Vac. Sci. Technol., B 22 (2004) 2345.
[8] L. Chen, Z. Yuxiao, P. Nyugen, T.L. Alford, Mater. Chem. Phys. 76 (2002) 224.
[9] M.-A. Nicolet, Thin Solid Films 52 (1978) 415.
[10] C. Muratore, A.A. Voevodin, J.J. Hu, J.G. Jones, J.S. Zabinski, Surf. Coat. Technol. 200 (2005) 549.
[11] A.A. Voevodin, M.A. Capano, A.J. Safriet, M.S. Donley, J.S. Zabinski, Appl. Phys. Lett. 69 (1996) 188.
[12] C. Muratore, A.A. Voevodin, J.J. Hu, J.S. Zabinski, Tribol. Lett., in press.
[13] C.W. Bates, Q.Y. Chen, Mater. Lett. 23 (1995) 7.
[14] J.L. Endrino, J.J. Nainaparampil, J.E. Krzanowski, Surf. Coat. Technol. 157 (2002) 95.
[15] F.P. Bowden, D. Tabor, J. Appl. Phys. 14 (1943) 141.
[16] A. Erdemir, R.A. Erck, G.R. Fenske, H. Hong, Wear 203–204 (1997) 588.
[17] C. Muratore, A.A. Voevodin, J.J. Hu, J.S. Zabinski, World Tribology Congress, Washington DC, U.S.A., September 12–16 2005, ASME Proceedings of the Third World Tribology Congress, 2005, p. 5.
[18] H. Gleiter, Prog. Mater. Sci. 33 (1990) 223.
[19] O. Gorur, C. Terzioglu, A. Varilci, M. Altunbas, Supercond. Sci. Technol. 18 (2005) 1233.
[20] S. Schumacher, R. Birringer, R. Strauss, H. Gleiter, Acta Metall. 37 (1989) 2485.
[21] J. Sommer, C. Herzig, J. Appl. Phys. 72 (1992) 2758.
[22] V. Naundorf, M.-P. Macht, A. Bakai, N. Lazarev, J. Non-Cryst. Solids 224 (1998) 122.

Paper 6

Oxygen plasma treatment and deposition of CN_x on a fluorinated polymer matrix composite for improved erosion resistance

C. Muratore[a)]
UTC Inc., Materials and Manufacturing Directorate Air Force Research Laboratory, AFRL/MLBT, 2941 Hobson Way, Wright-Patterson AFB, Ohio 45433

A. Korenyi-Both
TXI Inc., Materials and Manufacturing Directorate Air Force Research Laboratory, AFRL/MLBT, 2941 Hobson Way, Wright-Patterson AFB, Ohio 45433

J. E. Bultman
UDRI, Materials and Manufacturing Directorate Air Force Research Laboratory, AFRL/MLBT, 2941 Hobson Way, Wright-Patterson AFB, Ohio 45433

A. R. Waite
SOCHE, Materials and Manufacturing Directorate Air Force Research Laboratory, AFRL/MLBT, 2941 Hobson Way, Wright-Patterson AFB, Ohio 45433

J. G. Jones
Materials and Manufacturing Directorate Air Force Research Laboratory, AFRL/MLBT, 2941 Hobson Way, Wright-Patterson AFB, Ohio 45433

T. M. Storage
Materials and Manufacturing Directorate Air Force Research Laboratory, AFRL/MLBC, 2941 Hobson Way, Wright-Patterson AFB, Ohio 45433

A. A. Voevodin
Materials and Manufacturing Directorate Air Force Research Laboratory, AFRL/MLBT, 2941 Hobson Way, Wright-Patterson AFB, Ohio 45433

(Received 7 December 2006; accepted 8 May 2007; published 29 June 2007)

The use of polymer matrix composites in aerospace propulsion applications is currently limited by insufficient resistance to erosion by abrasive media. Erosion resistant coatings may provide necessary protection; however, adhesion to many high temperature polymer matrix composite (PMC) materials is poor. A low pressure oxygen plasma treatment process was developed to improve adhesion of CN_x coatings to a carbon reinforced, fluorinated polymer matrix composite. Fullerene-like CN_x was selected as an erosion resistant coating for its high hardness-to-elastic modulus ratio and elastic resilience which were expected to reduce erosion from media incident at different angles (normal or glancing) relative to the surface. *In situ* x-ray photoelectron spectroscopy was used to evaluate the effect of the plasma treatment on surface chemistry, and electron microscopy was used to identify changes in the surface morphology of the PMC substrate after plasma exposure. The fluorine concentration at the surface was significantly reduced and the carbon fibers were exposed after plasma treatment. CN_x coatings were then deposited on oxygen treated PMC substrates. Qualitative tests demonstrated that plasma treatment improved coating adhesion resulting in an erosion resistance improvement of a factor of 2 compared to untreated coated composite substrates. The combination of PMC pretreatment and coating with CN_x reduced the erosion rate by an order of magnitude for normally incident particles. © *2007 American Vacuum Society.* [DOI: 10.1116/1.2746049]

I. INTRODUCTION

Advanced polymer matrix composites (PMCs) are lightweight and exhibit mechanical properties that meet or exceed aerospace alloys in some applications;[1] however, their use in propulsion applications such as air intake and compression in jet engines or leading edges of rotor blades is currently limited by susceptibility to erosive wear.[2,3] Coating PMC parts with a thin (5–100 μm) layer of protective material may allow the use of PMCs in components that are vulnerable to high-velocity sand or other particulate media carried in the air. Such protective coatings should be hard in order to resist microcutting from media impinging at grazing angles, yet be elastically or plastically compliant to absorb impact energy to resist cracking and decohesion under direct particle impacts normal to the surface.[4,5]

Fullerene-like carbon nitrde (CN_x) is a material that has demonstrated high hardness (15–30 GPa) and elasticity (>80%), and therefore has potential for PMC erosion protection.[6] Moreover, the coefficient of thermal expansion (CTE) of fullerene-like CN_x, with its high fraction of sp^2

[a)]Electronic mail: chris.muratore@wpafb.af.mil

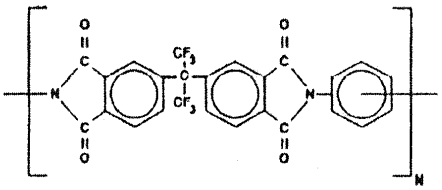


FIG. 1. Molecular structure of fluorinated polymide matrix of the composite material.

TABLE I. Erosion test conditions.

Media	80 μm Al_2O_3 powder
Feed rate	2 g min^{-1}
Gas pressure	80 psi
Sample position	10 mm from nozzle tip
Cycle description	50 s on/50 s off
Number of cycles	10
Total mass of erodent	16.7 g

bonding,[6,7] should demonstrate less CTE mismatch with a PMC substrate than other metallic erosion resistant coatings.[8] Matching the coating CTE to that of the substrate is desirable, as it would expand the range of potential propulsion applications of PMCs to include those that operate at both subzero and elevated temperatures.[2]

Erosion resistance is also dependent on adhesion of the coating to the substrate.[9–11] The majority of protective ceramic coatings currently in use were developed for metal alloys and utilize mechanical interlocking of the coating with the roughened workpiece surface.[12] The relatively low yield strength of the polymer matrix limits the utility of this approach for improving adhesion. Furthermore, many high-temperature PMC materials are comprised of stiff fibers embedded in a fluorinated polymer matrix. The fluorinated polymer chemistry, combined with the resin-rich mold release agent-coated surface, severely inhibits coating adhesion.[13–17]

To explore the effect of adhesion on the erosion resistance of CN_x coatings on the composite of interest (with the polymer matrix molecule shown in Fig. 1), it was necessary to introduce a predeposition treatment method. Exposure to low pressure plasmas, or reactive species produced in a plasma, is a well-documented technique for defluorinating and roughening fluorinated polymer surfaces.[15,17–22] Generally these treatments are performed by exposing the polymer to a remotely generated plasma produced away from the workpiece.[15,18,19,21–23] In the current work, midfrequency pulsed power was applied directly to the PMC workpiece to drive a pure oxygen dc glow discharge. CN_x coatings were grown on oxygen treated and untreated substrates, which were then subjected to qualitative adhesion tests to determine the effect of the plasma treatment. Erosion testing further demonstrated the effectiveness of the substrate treatment technique for improving coating adhesion in addition to the erosive wear resistance associated with application of the CN_x coating material.

II. EXPERIMENTAL PROCEDURE

Figure 2 shows a schematic of the processing and characterization chamber. The processing chamber was pumped to a base pressure $\leq 4 \times 10^{-5}$ Pa, then 40 SCCM of ultrahigh purity oxygen or argon gas was admitted to the chamber. A throttle valve was used to maintain a total pressure of 4 Pa as measured with a low pressure capacitance manometer. The power lead from an Advanced Energy Pinnacle Plus power supply was connected to a 25.4 mm diameter $\times$ 4.0 mm thick PMC disk, which consisted of an electrically insulating fluorinated polyimide resin matrix reinforced with T650/35-3K carbon fibers. The composite substrates were fabricated into laminates with approximately 60% fiber volume using standard autoclave processing techniques and then waterjet machined into the disk geometry. Samples of PMC were biased to −600 V (nominally) at 150 kHz with a 1 μs reverse time for a duration of 30–240 s. The PMC workpiece was surrounded by a 20 mm thick PTFE holder to eliminate plasma generation from any surface other than that intended for treatment. A new polymer sample was used for each treatment time investigated. An optical emission monitor was used to measure the time-averaged spectra resulting from the pulsed oxygen plasma approximately 1 cm above the cathode surface.

After exposure to the plasma, the treated PMC was transferred to the x-ray photoelectron spectroscopy (XPS) analysis chamber under vacuum (Fig. 2). The XPS system employed a magnesium anode and was used to analyze the changes in surface chemistry of the PMC substrates after each plasma treatment. Upon completion of the surface analysis, samples were removed from the characterization chamber and examined in the scanning electron microscope. The contact angle of water was also measured on the surface of treated and untreated PMC materials. Based on the results from examination of treatment time on surface chemistry and morphology, oxygen plasma exposure times (prior to CN_x coating deposition) of 0, 60, and 240 s were selected. Substrates were treated under identical conditions for the different times prior to the coating growth.

For CN_x coating growth on plasma treated PMC samples, oxygen was evacuated from the chamber and the applied potential on the PMC substrate was adjusted to −70 V dc. A

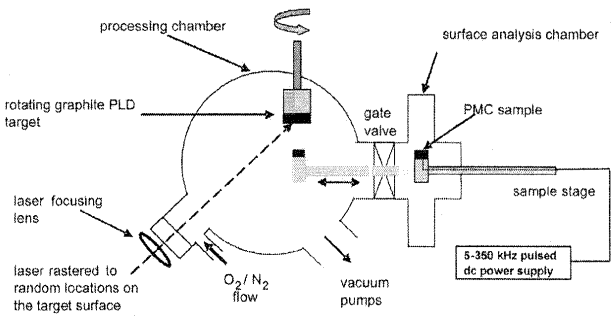


FIG. 2. Schematic of the processing and surface analysis chambers.

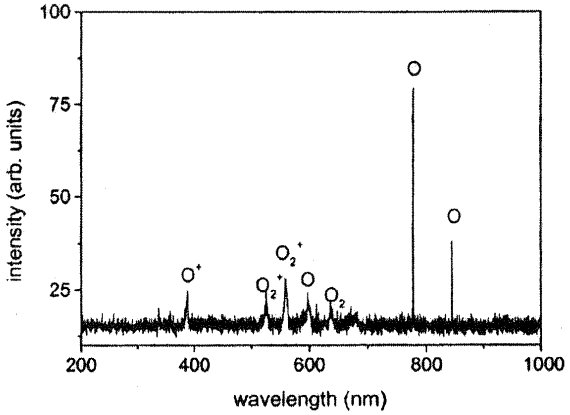


FIG. 3. Optical emission spectrum of the pulsed dc oxygen plasma used for pretreatment.

carbon interlayer was deposited by laser ablation from a rotating graphite target for 1 min using 840 mJ, 248 nm laser pulses (Fig. 2). The 20 ns laser pulses were directed to random positions and focused to an approximately 15

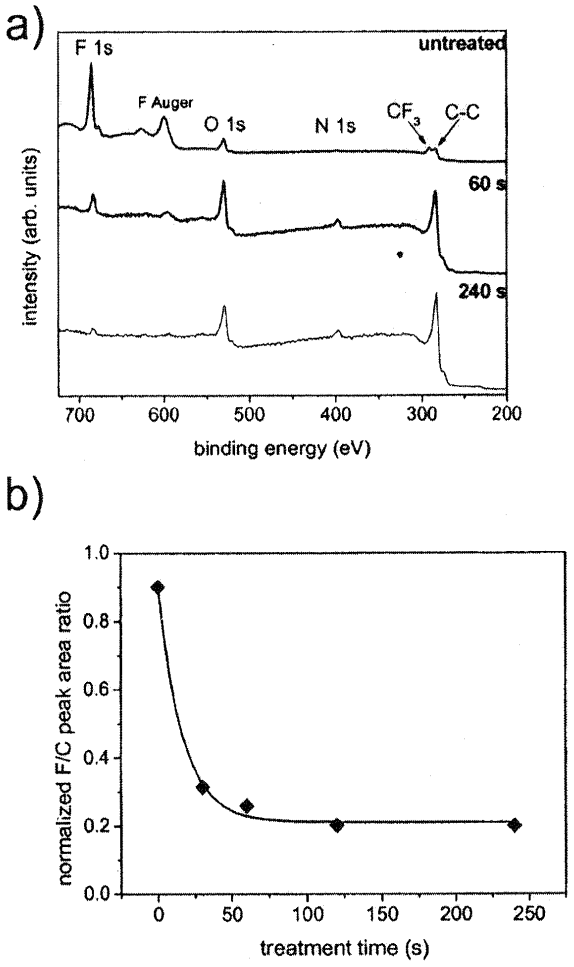


FIG. 4. (a) XPS spectra from the polymer matrix composite after exposure to the oxygen plasma and processed data (b) showing the fluorine-to-carbon peak intensity ratios from PMCs exposed to oxygen plasma.

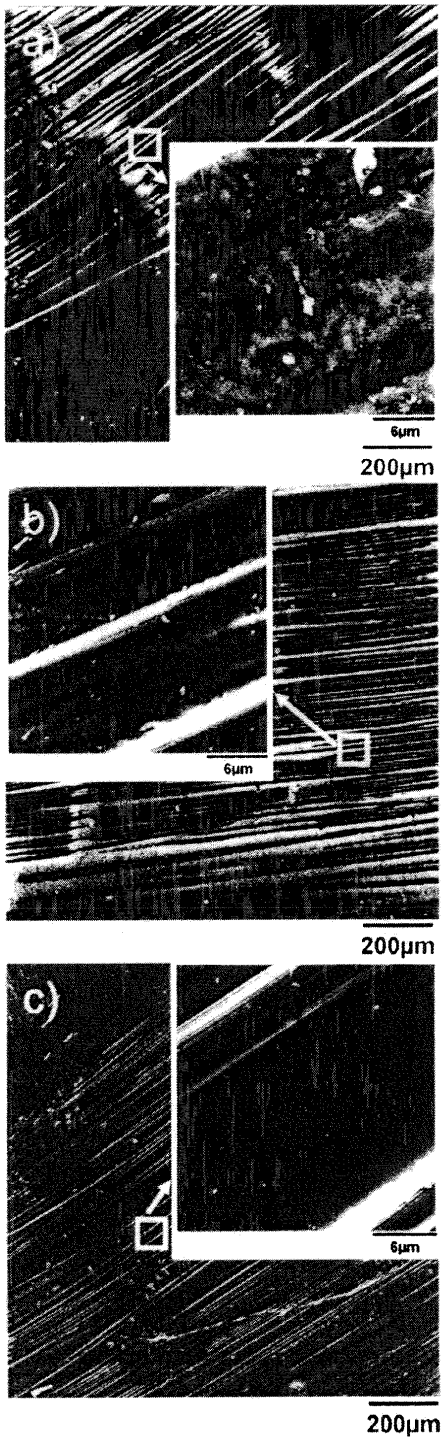


FIG. 5. Scanning electron micrographs of polymer matrix composite surfaces (a) as received, and after (b) 60 s and (c) 240 s of exposure to oxygen plasma.

$\times 5.0$ mm^2 spot on the 50 mm diameter target surface at a repetition rate of 10 Hz. After the initial carbon layer deposition, nitrogen was introduced at a flow rate of 27.5 SCCM (SCCM denotes cubic centimeter per minute at STP), and the system throttle valve adjusted to maintain a total chamber pressure of 1.33 Pa. The laser continued to operate in the

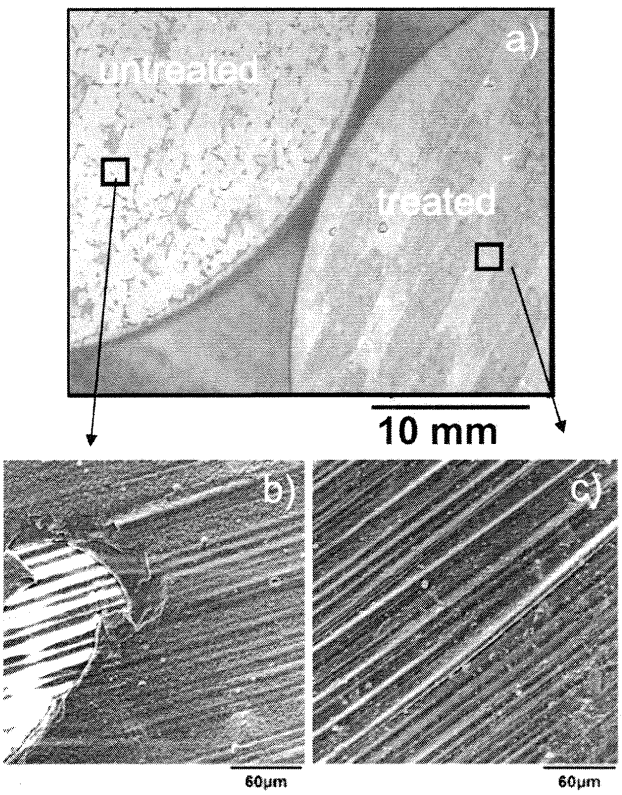


FIG. 6. (a) Micrographs of the treated and untreated polymer samples after coating with CN_x. (b) and (c) show higher magnification views of each sample.

nitrogen atmosphere for 9 h to produce a CN_x layer of approximately 5 μm thickness (±150 nm), as measured with a contact profilometer. These coating growth conditions were consistent with those used in a previous study for the deposition of hard and elastically resilient fullerene-like CN_x.[6]

The coating surfaces were examined after deposition in optical and electron microscopes and in the XPS. The mechanical properties of the CN_x material were examined with nanoindentation. Coatings deposited on treated and untreated PMC substrates were subjected to scratch testing and Daimler-Benz tests[24] to qualitatively determine the effect of treatment time on adhesion. Scratch tests were conducted with a 0.2 mm radius diamond tip dragged with a constant speed of 5 mm min^{-1} on the coating surface. The applied load was increased linearly up to 100 N at a rate of 50 N min^{-1}. Daimler-Benz testing consisted of indentation at 60 and 150 kg with a diamond Rockwell C indenter. Both adhesion tests were followed by examination in optical and electron microscopes. Samples were also tested in a FALEX erosion test unit with the conditions listed in Table I. Erosion testing was performed at incident angles of 40° and 90° relative to the surface of the test specimens at room temperature. The wear scars on each sample were examined with a Wyco white light interferometer to measure the wear volume after erosion testing.

III. RESULTS

Figure 3 shows the optical emission spectrum from the pure oxygen plasma generated with the midfrequency bipolar pulsed PMC cathode. A large peak corresponding to atomic oxygen was measured, as were peaks attributed to positively charged atomic and molecular oxygen ions. Examination of the surface composition by XPS immediately after processing revealed decreased concentrations of fluorine and the loss of the $C-F_3$ peak in the spectrum [Fig. 4(a)] after exposure to the oxygen plasma. Figure 4(b) shows how the fluorine-to-carbon ratios at the surface changed with treatment time. The line shown in the figure is an exponential decay function fit to the data. Substantial defluorination occurred after 60 s, with only a small decrease after longer treatments.

Figure 5(a) is a scanning electron micrograph of as-received PMC composite surface, where the carbon fibers were coated with the fluorinated polymer matrix. The space between fibers in the as-received polymer appeared to be filled with rough, poorly adherent material exhibiting fiber/matrix decohesion at the interface. After exposure to the oxygen plasma for 60 s [Fig. 5(b)], the polymer was partially etched away, leaving some fiber surfaces exposed. The pulsed oxygen plasma treatment reduced the number of topographical features on the polymer matrix between fibers. Increasing the plasma treatment time to 240 s [Fig. 5(c)] resulted in complete exposure of the carbon fibers. The remaining polymer matrix had no evidence of any decohesion along the matrix/fiber interface.

Water contact angles on the PMC surfaces were also examined. A 60 s treatment resulted in a reduction in contact angle from 105° to 43°. This reduced contact angle was consistent with both the changes in surface chemistry and morphology, revealing a PMC surface with a higher surface energy and chemical reactivity after plasma treatment.

Micrographs of the coatings deposited on treated and untreated substrates are shown in Figs. 6(a)–6(c). The coating deposited on the untreated substrate demonstrated periodic delamination of the coating across the surface [Figs. 6(a) and 6(b)], while the substrates treated for 60 s or longer were uniformly coated [Figs. 6(a) and 6(c)]. XPS of all coated samples showed that the coating was composed of approximately 80 at. % carbon and 20 at. % nitrogen, independent of the processing history of the substrate.

Nanoindentation was performed on the coated samples. Results from nanoindentation tests of the coatings on untreated polymer substrates were difficult to interpret due to excessive scatter in results between measurements; however, coatings on treated substrates demonstrated repeatable measurements of hardness at 19 GPa and an elastic modulus of approximately 120 GPa. The elasticity of the coating was measured to be approximately 75% for a 1000 nm displacement (Fig. 7). These measurements were consistent with mechanical properties of fullerene-like CN_x coatings.[6,25]

Figure 8 shows how the predeposition oxygen treatment affected coating adhesion after severe substrate deformation. As seen in Fig. 8(a), the coating showed extensive cracking around the perimeter of the 150 g indent on the untreated

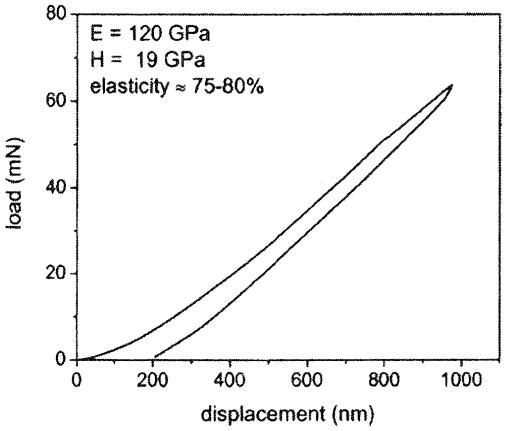


FIG. 7. Load-displacement curve for the treated and coated PMC.

sample, while the edges remained intact for the samples treated for (b) 60 and (c) 240 s. Examination of the scratch tracks in Fig. 9 also showed differences in adhesion resulting from plasma pretreatment of the substrates. The inset in Fig. 9(a) shows a low-magnification view of the scratch track in the region loaded to approximately 10 N, with alternating coated and uncoated regions at the bottom of the scratch. On the treated substrate, the coating adhered throughout the scratch. In Fig. 9(b), the scratch is shown where a 90 N load was applied. Some cracking perpendicular to the scratch directions is shown, but the coating still covers the substrate, and appears to be fully adherent.

Table II lists the worn volume and erosion rates (in terms of mass lost per gram of erodent) for the coated and uncoated samples. The CN_x coating coupled with the oxygen plasma treatment yielded an erosion rate that was roughly an order of magnitude less than that measured for the PMC alone in the normal incidence test, and a factor of 3 less for the glancing angle test. Samples that were coated without oxygen pretreatment had an erosion rate that was approximately twice that of the treated and coated samples for both normal and grazing angle erosion tests.

IV. DISCUSSION

Driving an electrically insulating fluorinated polymer workpiece with a midfrequency pulsed dc power supply as a plasma cathode in pure oxygen was a simple and effective way to alter the structure and surface chemistry of the polymer to improve coating adhesion compared to ion beam, rf biasing, and other methods.[15,18,19,26,27] The reactive oxygen plasma generated with the pulsed dc PMC cathode produced reactive neutral and ionized oxygen species, which altered the surface chemistry and morphology of the PMC prior to coating deposition in a manner consistent with that reported by workers using other techniques. A frequency of 150 kHz was selected as it was the minimum frequency required to maintain a continuous glow discharge with power delivered via the insulating polymer substrate. Driving the discharge with dc power resulted in the loss of electrons at the insulating surface as the incident positive ions were neutralized by

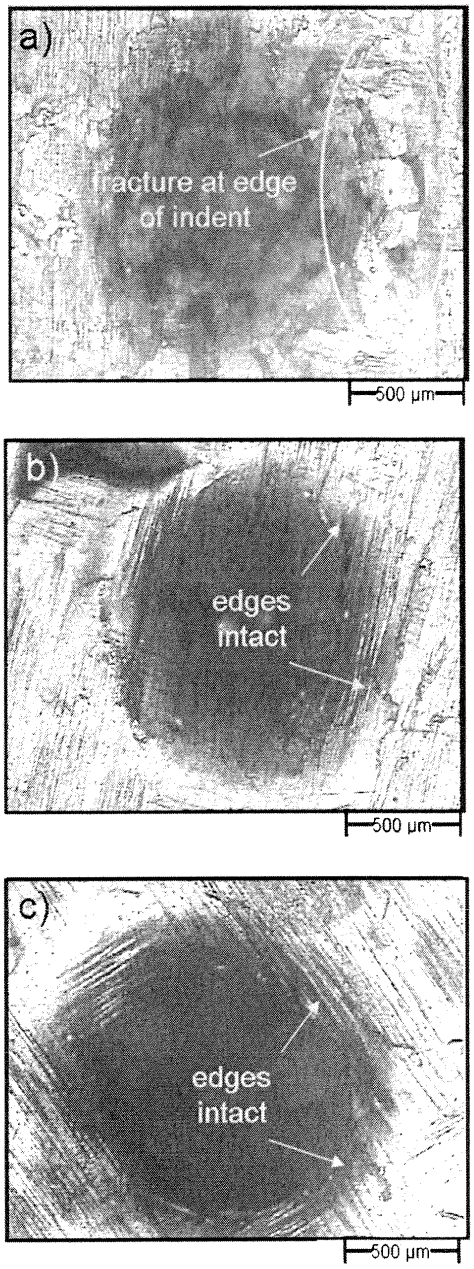


FIG. 8. Optical micrographs of 150 kg indents on coated samples (a) with no pretreatment, (b) 60 s oxygen pretreatment and (c) 240 s oxygen pretreatment.

electrons at the surface, thus reducing the voltage below that required to sustain the discharge. As argued by Chapman,[28] an overestimate of the time required to charge up the surface can be compared to the time to charge up a capacitor, where

$$C = Q/V = it/V,$$

thus $t = CV/i$.

For the expected values of capacitance ($\approx$1 pF/cm^2), discharge voltage ($\approx$500–1000 V), and current ($\approx$1 mA/cm^2), the required frequency should be roughly 1 MHz. Lower frequencies (5–500 kHz) are generally sufficient as the current delivered to the insulator decreases as it charges up, unlike

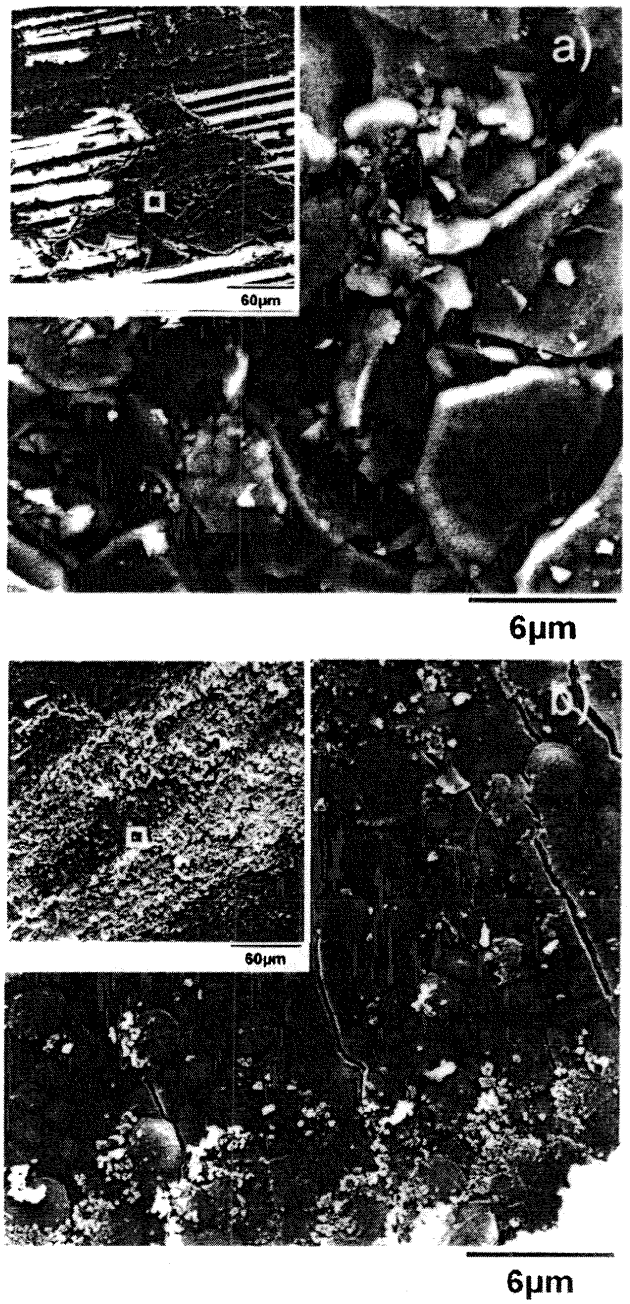


FIG. 9. Electron micrographs of scratch tracks on the coated surfaces of the (a) untreated and (b) 60 s treated PMC substrates.

the constant current model above. The PTFE holder was much thicker and had different dielectric properties than the PMC material and therefore did not produce a discharge at 150 kHz.

Coating adhesion was qualitatively shown to improve after exposure to the oxygen plasma via indentation, scratch testing, and erosion testing. Rabinovich *et al.* describe how cracking due to indentation [as shown in Fig. 8(a)] is related to weak interfacial bonding.[29] The crack patterns in Figs. 9(a) and 9(b) are consistent with those described by Burnett and Rickerby for scratch testing of slightly different coating/substrate systems.[30] They illustrated how spallation resulting from total coating failure results in scratch tracks that look like that shown in Fig. 9(a). Tensile cracking, which is characterized by cracks that are normal and concave with respect to the scratch direction rather than normal and convex as in Fig. 9(b), results from tensile bending moments within the coating as it is pushed down underneath the indenter, and occurs only when the coating is fully adherent. Last, the erosion rate of the coated PMC decreased when the sample was treated, consistent with reports found in the literature relating coating adhesion to erosion resistance.[9–11]

CN_x coatings deposited on oxygen plasma treated polymer matrix composite substrates were hard, with a low modulus, resulting in H/E ratio of 0.16, which is quite high in comparison with typical ceramic wear protective coatings.[7] The erosion rate of the uncoated PMC was slightly higher when the erodent media was incident on the surface at 40° compared to that measured when the media were directed normal to the surface. Such dependence on the angle of incidence is expected for a softer, polymer-based material. For the coated PMC material, the erosion rates were significantly reduced. Erosive wear from media directed at 90° relative to the coated surface was suppressed more than that directed at 40°, suggesting that the elastic properties of the CN_x coating made a stronger contribution to the protective nature of the coating than the hardness. Deposition of adherent CN_x coatings substantially reduced the erosion rate of the polymer, even though the 5 μm coating was very thin compared to those typically found in erosion resistant applications.[2,3] Typical thicknesses of erosion protective hard coatings used on metal alloys in jet engines are on the order of 100–1000 μm. A thicker CN_x coating should provide an increased capability for elastic damping of normal incidence sand impacts and a longer scratch endurance of sand impacts at oblique angles. The production of such thick coatings requires modifications to the deposition process to increase the CN_x coating growth rates, which are currently in development. The erosion performance of thicker CN_x coatings and coatings with different hardness-to-modulus ratios will be evaluated in a future work.

V. CONCLUSIONS

Midfrequency pulsed power was applied directly to a fluorinated polymer matrix composite workpiece in an oxygen atmosphere to generate a reactive plasma and reduce the surface fluorine concentration and remove loosely adhered surface material. A CN_x coating with a very high hardness-to-modulus ratio of 0.16 with >75% elasticity was produced by laser ablation of carbon in a nitrogen atmosphere. Indentation, scratch, and erosion testing all showed that the adhesion of CN_x coatings deposited after oxygen plasma treatment of the PMC substrate was improved when compared to the same coatings deposited on the untreated PMC material. Improvements in coating adhesion reduced the erosion rate by a factor of 2 when compared to untreated, CN_x coated

TABLE II. Erosion data for all samples.

		40° incidence		90° incidence	
Substrate pretreatment	CN_x coating (μm)	Volume loss ($cm^3 \times 10^{-3}$)	Erosion rate ($cm^3\ g^{-1}$)	Volume loss ($cm^3 \times 10^{-3}$)	Erosion rate ($cm^3\ g^{-1}$)
(None)	(None)	1.20	0.07	1.00	0.06
(None)	5	0.34	0.02	0.70	0.04
oxygen plasma	5	0.18	0.01	0.36	0.02

PMC samples. Uncoated substrates wore approximately ten times faster for normally incident abrasive particles compared to the treated and coated samples.

ACKNOWLEDGMENTS

The authors wish to thank John O'Keefe and Chris Bowman at ARCOMAC Surface Engineering LLC for performing the erosion tests. Carl Hager is gratefully acknowledged for his assistance with the erosion crater measurements, as is Art Safriet for his technical assistance. This research was supported by the Air Force Office of Scientific Research.

[1]National Materials Advisory Board, *Going to Extremes: Meeting the Emerging Demand for Durable Polymer Matrix Composites* (The National Academy, 2005), p. 10.
[2]M. Ivosevic, R. Knight, S. R. Kalindindi, G. R. Palmese, and J. K. Sutter, Surf. Coat. Technol. **200**, 5145 (2006).
[3]K. Miyoshi, J. K. Sutter, R. A. Horan, S. K. Naik, and R. J. Cupp, Tribol. Lett. **17**, 377 (2004).
[4]Y. Gachon, P. Ienny, A. Forner, G. Farges, M. C. Sainte Catherine, and A. B. Vannes, Surf. Coat. Technol. **113**, 140 (1999).
[5]D. W. Wheeler and R. J. K. Wood, Wear **258**, 526 (2005).
[6]A. A. Voevodin, J. G. Jones, J. S. Zabinski, Zs. Czigany, and L. Hultman, J. Appl. Phys. **92**, 4980 (2002).
[7]H. Riascos, J. Neidhardt, G. Z. Radnoczi, J. Emmerlich, G. Zambrano, L. Hultman, and P. Prieto, Thin Solid Films **497**, 1 (2006).
[8]A. Champi, R. G. Lacerda, G. A. Viana, and F. C. Marques, J. Non-Cryst. Solids **338–340**, 499 (2004).
[9]D. S. Rickerby and P. J. Burnett, Surf. Coat. Technol. **33**, 191 (1987).
[10]K. L. Rutherford and I. M. Hutchings, Surf. Coat. Technol. **86–87**, 542 (1996).
[11]P. H. Shipway and I. M. Hutchings, Surf. Coat. Technol. **71**, 1 (1995).
[12]A. Liu, M. Guo, M. Zhao, H. Ma, and S. Hu, Surf. Coat. Technol. **200**, 3073 (2006).
[13]C.-A. Chang, J. E. E. Baglin, A. G. Schrott, and K. C. Llin, Appl. Phys. Lett. **51**, 103 (1987).
[14]S. Han, Y. Lee, H. Kim, G. H. Kim, J. Lee, J. H. Yoon, and G. Kim, Surf. Coat. Technol. **93**, 261 (1997).
[15]Y. W. Park and N. Inagaki, Polymer **44**, 1569 (2003).
[16]R. R. Rye, A. J. Howard, and A. J. Ricco, Thin Solid Films **262**, 73 (1995).
[17]T. G. Vargo, J. M. Calvert, K. J. Wynne, J. K. Avlyanov, A. G. MacDiarmid, and M. F. Rubner, Supramol. Sci. **2**, 169 (1995).
[18]K. De Bruyn, M. Van Stappen, H. De Deurwaerder, L. Rouxhet, and J. P. Celis, Surf. Coat. Technol. **163–164**, 710 (2003).
[19]J. M. Grace and L. J. Gerenser, J. Dispersion Sci. Technol. **24**, 305 (2003).
[20]S. Han, Y. Lee, H. Kim, G. H. Kim, J. Lee, J. H. Yoon, and G. Kim, Surf. Coat. Technol. **93**, 261 (1997).
[21]D. Leonhardt, C. Muratore, S. G. Walton, and R. A. Meger, Surf. Coat. Technol. **188–189**, 299 (2004).
[22]N. Vandencasteele, H. Fairbrother, and F. Reniers, Plasma Processes Polym. **2**, 493 (2005).
[23]C. Muratore, S. G. Walton, D. Leonhardt, R. F. Fernsler, and R. A. Meger, 47th Annual Technical Conference Proceedings, Society of Vacuum Coaters, April 2004 (unpublished), p. 412.
[24]H. Jehn, G. Reiners, and N. E. Siegel, in *DIN Fachbericht 39, Charakterisierung Dunner Schichten* (Beuth, Berlin, 1993), p. 213.
[25]J. F. Palacio, S. J. Bull, J. Neidhardt, and L. Hultman, Thin Solid Films **494**, 63 (2006).
[26]S. Han, Y. Lee, H. Kim, G. H. Kim, J. Lee, J. H. Yoon, and G. Kim, Surf. Coat. Technol. **93**, 261 (1997).
[27]G. B. Hoflund and M. L. Everett, J. Phys. Chem. B **108**, 15721 (2004).
[28]B. Chapman, *Glow Discharge Processes* (Wiley, New York, 1980), pp. 139–142.
[29]V. L. Rabinovich and V. K. Sarin, Mater. Sci. Eng., A **209**, 82 (1996).
[30]P. J. Burnett and D. S. Rickerby, Thin Solid Films **154**, 403 (1987).

Page 7

Available online at www.sciencedirect.com
ScienceDirect
ELSEVIER
Wear xxx (2008) xxx–xxx
WEAR
www.elsevier.com/locate/wear

Smart tribological coatings with wear sensing capability

C. Muratore [a,*], D.R. Clarke [b], J.G. Jones [c], A.A. Voevodin [c]

[a] *UTC Inc./Air Force Research Laboratory, Materials and Manufacturing Directorate, Wright-Patterson AFB, OH 4543, United States*
[b] *Materials Department, College of Engineering, University of California, Santa Barbara, CA 93106-5050, United States*
[c] *Air Force Research Laboratory, Materials and Manufacturing Directorate, Wright-Patterson AFB, OH 45433, United States*

Received 30 July 2007; received in revised form 8 January 2008; accepted 4 February 2008

Abstract

Tribological coatings were developed to allow automatic reporting of remaining wear life while in use. Monitoring of coating health was achieved by embedding sensor layers, known to produce distinctive luminescence spectra when exposed to laser illumination, throughout the thickness of a solid lubricant coating. For the current work, erbium- and samarium-doped yttria stabilized zirconia (YSZ) layers were used as sensor materials. One sensor layer was placed approximately midway through a molybdenum disulfide coating and another was located at the coating/substrate interface. Placement of the luminescent coatings in these positions allowed detection of wear depth and provided a warning of impending coating failure during testing. This smart coating concept is generally applicable to tribological coatings and can easily be implemented to safely increase reliance upon protective materials subject to wear and other damage mechanisms. The soft MoS_2 coatings with the imbedded ceramic sensor layers also demonstrated long wear lives (≈200,000 cycles) in humid air compared to monolithic MoS_2 coatings (<10,000 cycles) with the same thickness, microstructure, morphology and composition. The mechanism for the observed wear life increase was examined and discussed together with the general use of embedded wear sensors in smart tribological coatings.
© 2008 Elsevier B.V. All rights reserved.

Keywords: Smart coatings; Sliding wear; Molybdenum disulfide; Sensors

1. Introduction

Coating materials are used to prolong the lifetime, expand the effective operating range and/or enhance the performance of mechanical components and assemblies in diverse applications. Specific examples are tribological coatings designed to reduce friction and wear at interfaces between parts and thermal barrier coatings (TBCs) used to provide thermal insulation to metal turbine blades enabling them to operate in hotter gases thereby increasing the turbine efficiency and power. *In situ* monitoring of coated systems to provide an indication of remaining coating life and sufficient warning before failure would allow designers to rely more heavily upon coating materials, thereby reducing the degree of over-engineering and pre-mature replacement that accompanies uncertainty about the condition of critical coated parts. Employing sensors to indicate the extent of coating wear would also assist researchers in developing new materials by providing additional insight on damage mechanisms before coating failure without stopping tests for *ex situ* characterization.

Luminescence spectroscopy has been proposed as a technique to measure damage in optically translucent TBCs without interrupting their use while in service [1–4]. In these works, luminescence spectra of materials were used for damage sensing by monitoring the intensity of the spectra from subsurface species located in discrete layers buried throughout the thickness of the TBC that luminesce when excited with an incident laser beam. As the upper layers of the coating erode away, the intensity of spectra generated by the subsurface sensor layers is intensified. When layers containing active luminescing species are damaged, the characteristic spectra fade or disappear. By such analysis, the health of the coating can be monitored *in situ*.

Multilayered tribological coatings differ from TBCs in that they are typically opaque and suffer from damage mechanisms such as abrasion, adhesion, and other contact-based phenomena. Nevertheless, the principle of exposing buried layers throughout the depth of a tribological coating to provide a detectable response indicating the extent to which the coating has worn is an appealing technique for *in situ* wear monitoring of surfaces

* Corresponding author.
E-mail address: chris.muratore@wpafb.af.mil (C. Muratore).

0043-1648/$ – see front matter © 2008 Elsevier B.V. All rights reserved.
doi:10.1016/j.wear.2008.02.003

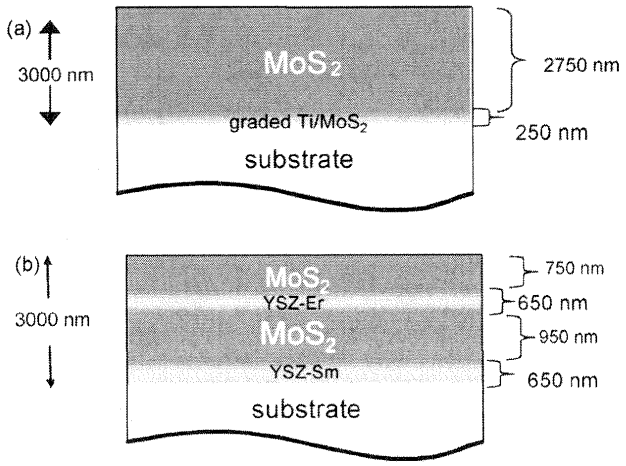


Fig. 1. Schematic diagram of (a) a monolithic coating and (b) a multilayered coating with imbedded, luminescing wear sensor layers.

in contact. The current work describes deposition, characterization and demonstration of a smart solid lubricant coating with one sensor layer located approximately midway through the thickness of the coating to report the wear depth, wear rate and remaining coating life. The other wear sensor layer was located at the coating/substrate interface to provide a warning to signal the end of coating life. The layered structure is shown schematically in Fig. 1 with doped yttria stabilized zirconia (YSZ) layers as sensor materials. The choice of this structure was based on an ultimate intention to build wear sensors into multilayered adaptive nanocomposites designed for broad temperature range operations [5,6], such as those found in jet engine components and other high performance tribological contacts that are difficult to inspect and would, therefore, benefit from coating life reporting capability. As a first step, the current work was directed towards demonstrating the sensor concept in a single-phase solid lubricant material subjected to room temperature sliding.

Molybdenum disulfide was selected as the solid lubricant material as its response to wear under sliding has been well documented over decades of research, and the introduction of hard ceramic sensor layers was expected to impact the tribological performance of the coating. By comparing monolithic MoS_2 to the doped YSZ/MoS_2 coatings, the effect of the ceramic layers on the measured tribological properties could easily be assessed. Moreover, MoS_2 has a relatively high laser absorption coefficient of $>1 \times 10^5\ cm^{-1}$ for excitation wavelengths of 532 nm and less [7], which means that the effective optical penetration depth of the laser is small, thus eliminating ambiguity about the thickness to which the coating has worn upon the appearance of a new spectral feature. The rare-earth dopants used to provide luminescence in the YSZ layers were selected based on the Dieke diagram [8] which gives the luminescence wavelengths for different rare-earth ions based on their allowed electronic transitions. Trivalent erbium and samarium ions, which both can dissolve in YSZ, were identified as dopants yielding distinctive luminescence spectra with no overlap in the wavelength range on interest, thus providing a clear indication of the wear depth location.

2. Experimental procedure

Monolithic and multilayered coatings comprised of MoS_2 and/or rare-earth-doped YSZ compounds were deposited in a hybrid filtered vacuum arc/magnetron sputtering/pulsed laser deposition system. One-inch diameter 440C steel substrates were ultrasonically degreased and loaded into a rotating fixture within the processing chamber. A $520\ l\ s^{-1}$ turbomolecular pump was used to evacuate the chamber to a pressure of $<5 \times 10^{-7}$ Torr (7×10^{-5} Pa). The rotating substrates were then heated in vacuum to 150 °C, degassed for 30 min and maintained at that temperature throughout all subsequent coating processes. Substrates were then cleaned with positively charged argon and metal ions as they were exposed to glow discharge and then filtered titanium arc plasmas, respectively, with bias voltages of up to −800 V dc. The titanium arc plasma was also used to deposit a thin (<100 nm) adhesion layer for all coatings. The argon flow rate was then increased to 100 sccm and an automated throttle valve was used to increase the chamber pressure to 12×10^{-3} Torr (1.6 Pa). A dc glow discharge from an unbalanced magnetron plasma source with a 32 mm, 99.9% pure MoS_2 cathode was initiated. The power density on the MoS_2 cathode was increased incrementally up to $9\ W\ cm^{-2}$ during titanium deposition to produce a graded lubricant/adhesion layer interface of about 250 nm total thickness, after which the titanium arc source was switched off and magnetron power was maintained throughout coating growth. Substrates were biased to −30 V dc during MoS_2 deposition. These conditions were selected as they were shown in a previous study to yield MoS_2 with preferred basal plane orientation parallel to the coating surface [9]. Doped YSZ layers were deposited between layers of MoS_2 by pulsed laser deposition from rotating YSZ targets with the desired doping concentrations of one atomic percent rare-earth metal [3]. The 28 mm diameter targets were prepared by precipitation processing starting with nitrate solutions of the rare-earth ions as well as the yttrium and zirconium nitrates, calcining the precipitated salt and then sintering at 900 °C for 5 h in air. The Er-doped targets had a composition of $Zr_{0.92}Y_{0.07}Er_{0.01}O_{1.96}$ and the Sm-doped targets had a composition of $Zr_{0.92}Y_{0.07}Sm_{0.01}O_{1.96}$. The YSZ targets were ablated in a mixture of 75% oxygen and 25% argon (by flow) at 15 mTorr using 25 ns pulses from a 248 nm KrF excimer laser at a repetition rate of 30 Hz. Substrates were biased to −150 V dc during YSZ deposition. The YSZ deposition rate was approximately $500\ nm\ h^{-1}$, and all the doped YSZ sensor layers were grown to a thickness of 650 nm. The multilayered MoS_2/doped YSZ coatings had a total thickness of about 3000 nm, with individual layer thicknesses estimated by assuming that the monolithic coating deposition rates for individual components were linear over the actual deposition times used. The intended architecture of the multilayered coating is shown in Fig. 1. As-deposited coatings were examined using X-ray diffraction, scanning electron microscopy, and X-ray photoelectron spectroscopy (XPS).

Coatings were tested in a ball-on-disc tribometer designed to allow *in situ* examination of the wear track by optical spectroscopy during sliding without interrupting the rotation of the sample. The experimental arrangement of the tribospectrometer

Please cite this article in press as: C. Muratore, et al., Smart tribological coatings with wear sensing capability, Wear (2008), doi:10.1016/j.wear.2008.02.003

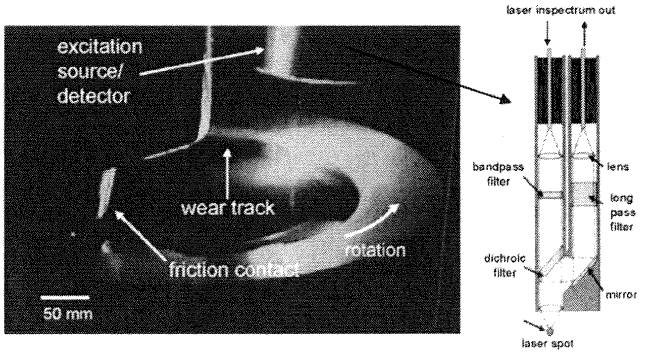


Fig. 2. Photograph of the tribospectrometer system together with a schematic of the laser probe used to excite and collect luminescence.

system is shown in Fig. 2. An InPhotonics RamanProbe (Fig. 2b) was used to simultaneously focus the 300 mW, 532 nm laser into the wear track and direct backscattered light as well as the luminescence from that surface into an EIC Echelle spectrograph. The laser was aimed into the wear track by attenuating it to a small fraction of its full intensity after starting the wear test to allow easy identification of the center of the beam, which was approximately 0.5 mm when attenuated. The laser probe was positioned over the coated sample with an orthogonal pair of micro-translators while watching an image of the beam spot and the developing wear track in a camera zoomed in and focused on the surface. After the excitation laser spot was positioned in the wear track, the attenuating shutter was removed. An automated data acquisition system was used to collect spectroscopic data after every 500 sliding cycles to allow correlation of friction and luminescence events. For sliding contact tests, a 6 mm silicon nitride ball and 1 N applied load were used, resulting in an applied Hertzian contact stress of approximately 650 MPa for the monolithic MoS_2 sample. The sliding speed was 0.2 m s^{-1} and the test environment was 22.5 °C air with controlled 40% relative humidity for all tests. The humid environment was known to be detrimental for MoS_2 lubricants [10], and therefore, was chosen here for the accelerated testing of the coating wear life. After wear testing, samples were examined with contact profilometry for wear depth analyses, scanning electron microscopy for surface morphology, and XPS for contact chemistry. Silicon nitride sliding counterparts were also examined with optical microscopy after wear testing.

3. Results

Fig. 3 shows Bragg-Brentano X-ray diffractograms from 3000 nm thick (a) monolithic MoS_2 and (b) smart multilayered MoS_2/doped YSZ coatings. Both coatings exhibited a preferred (0 0 2) orientation (basal planes parallel to the surface) with approximately the same (0 0 2)/(1 0 0) peak intensity ratios, independent of the presence of the sensor layers. The X-ray diffraction pattern from the multilayered YSZ/MoS_2 coating revealed that the sensor layers consisted of tetragonal ZrO_2 with (1 1 1) texture. Scanning electron micrographs (Fig. 3, insets) of the coating surfaces showed that the YSZ layers had no influence on the surface morphology of the MoS_2, as both had a

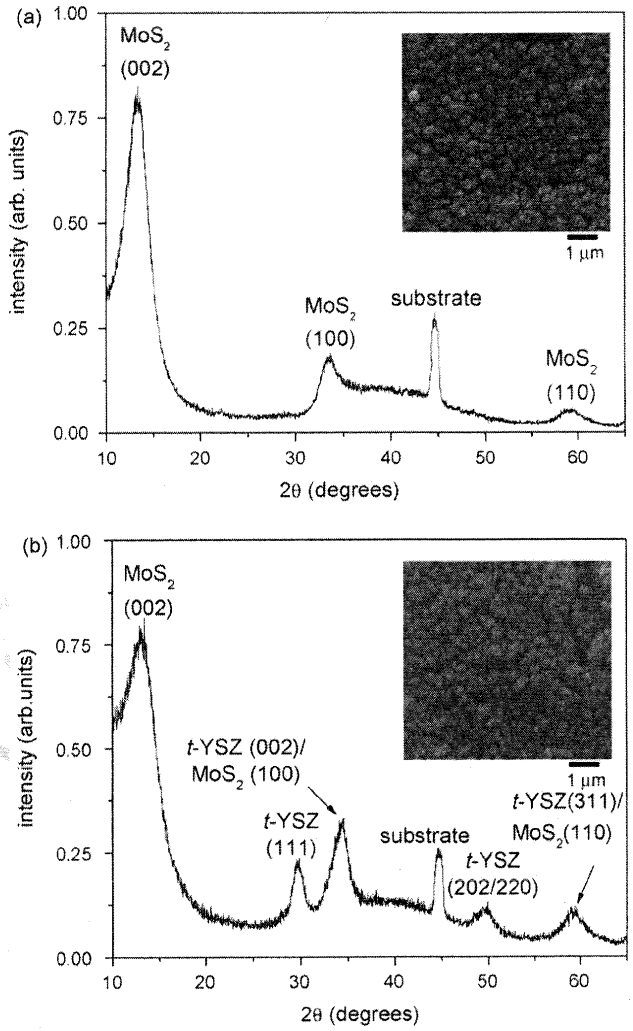


Fig. 3. X-ray diffractograms for (a) monolithic and (b) multilayered MoS_2 with inset electron micrographs of the respective coating surfaces.

nearly identical columnar appearance. XPS analyses indicated that the compositions of both monolithic and multilayer coatings were also indistinguishable and consisted of sub-stoichiometric $MoS_{1.5}$ with approximately 15 atomic percent oxygen.

Friction traces from both coatings are compared in Fig. 4 (note an order of magnitude difference in the maximum number of cycles). The monolithic coating had indications of failure starting at about 6000 cycles, where the average friction coefficient fluctuated from 0.1 to 0.6 (Fig. 4a). The multilayered coating did not show signs of failure until approximately 180,000 cycles as the friction trace was relatively smooth and constant until then (Fig. 4b). Fig. 5 compares profilometry scans of wear tracks for both coatings after 20,000 cycles. The monolithic coating was worn beyond the depth of the original substrate/coating interface (Fig. 5a), while the MoS_2/YSZ coating was only worn down to the top of the first ceramic layer, approximately 750 nm below the coating surface (Fig. 5b). Electron micrographs of the wear tracks after 20,000 cycles are compared in Fig. 6 with wear debris spread over the wear track for the monolithic MoS_2 (Fig. 6a), and a smooth, almost featureless wear track for the multilayered MoS_2/YSZ (Fig. 6b). Microscopy also showed that

Please cite this article in press as: C. Muratore, et al., Smart tribological coatings with wear sensing capability, Wear (2008), doi:10.1016/j.wear.2008.02.003

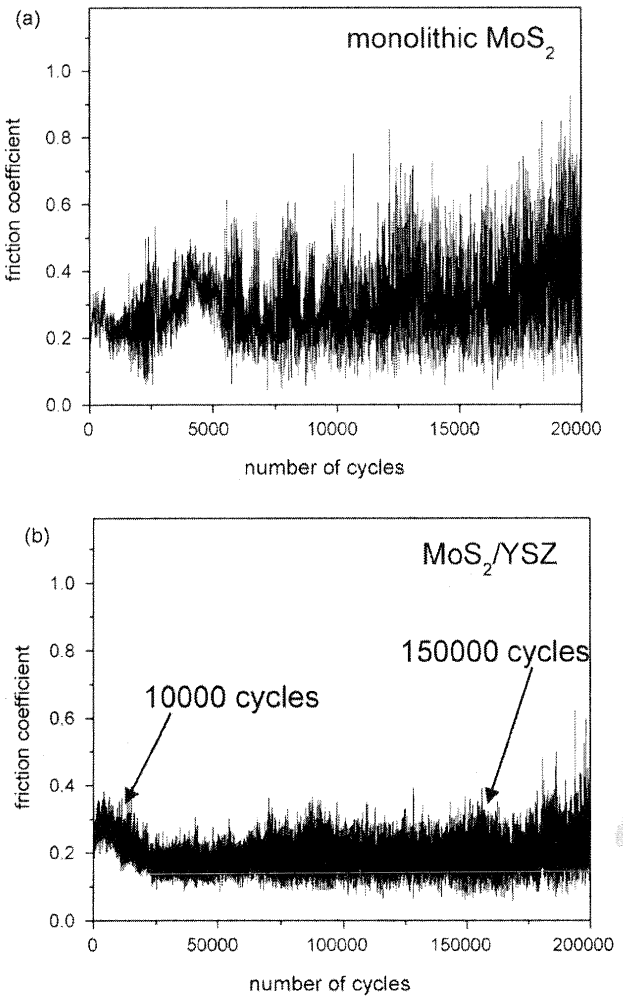


Fig. 4. Friction plots for (a) monolithic MoS_2 and the (b) multilayered sensor coating.

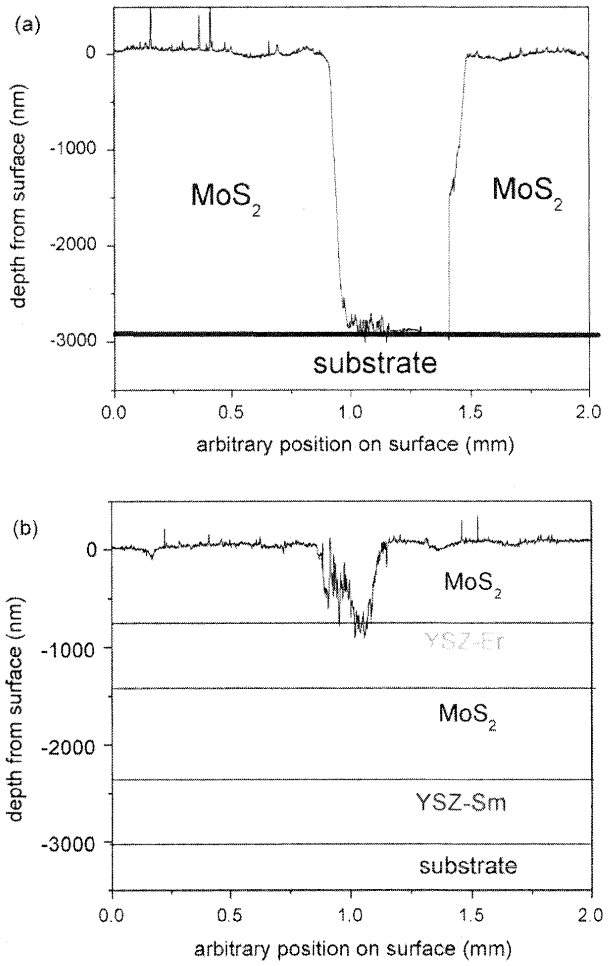


Fig. 5. Profilometry line scans of wear tracks for (a) monolithic and (b) sensor coating after 20,000 cycles in 40% relative humidity.

the buried YSZ–Sm layer adjacent to the substrate was partially exposed by wear after 200,000 cycles (Fig. 6c), as confirmed by XPS analysis of the wear track.

Monolithic Er-doped and Sm-doped YSZ coatings were also produced to determine the response of the sensor layers alone. Luminescence spectra were collected while the coated samples were rotating in the tribotester with identical ambient conditions to those employed for sliding friction experiments of smart multilayered coatings. The spectra are shown in Fig. 7 with the electronic transitions labeled for the individual peaks. Note that the energy of the transitions is reported in terms of Raman shift relative to the 532 excitation laser. There was a slight shift in the peak positions relative to those published elsewhere [3]. The Er-doped YSZ coating exhibited a single broad peak at about 500 cm^{-1} (Fig. 7a), and Sm-doped YSZ layers had a distinct double peak feature in 1100–1400 cm^{-1} region (Fig. 7b).

Spectra for three smart multilayered MoS_2/YSZ coatings were collected *in situ* from their wear tracks during sliding. Examples of such spectra are shown in Fig. 8 (a) before sliding, (b) after 10,000 cycles, and (c) after 150,000 cycles. Before sliding, only Raman peaks were a doublet near 400 nm, characteristic of hexagonal MoS_2 (Fig. 8a). The position of the peaks after 10,000 cycles matched the spectral lines of monolithic YSZ-Er spectra (Fig. 8b). The YSZ-Er spectra were observed up to about 25,000 cycles, but its intensity was rapidly reduced until it was no longer detectable after approximately 30,000 cycles for all samples. No sensor spectra were detected until approximately 150,000 cycles (±4000 cycles), when spectral features matching the YSZ-Sm spectrum (Fig. 8c) were observed on samples examined under the same sliding conditions. Note that Fig. 8a shows spectral artifacts due to saturation of the spectrophotometer detector resulting from Raleigh scattering. The doublet at 300 cm^{-1} was also assumed to be the result of detector saturation as it appeared only when long integration times were used when acquiring spectra. This characteristic pattern at low wave number values was present in all scans, thus the scan acquired before initiation of sliding (Fig. 8a) was subtracted from the raw data and plotted separately in Fig. 8b and c, to make the sensor spectra superimposed upon those artifacts more clearly apparent (insets Fig. 8a–c are plotted on a similar scale as that used for Fig. 7a and b). The MoS_2 Raman peaks appeared in the raw scans collected between 10,000 (Fig. 8b) and ≈130,000 cycles, but were then undetectable throughout the duration of the wear tests (Fig. 8c).

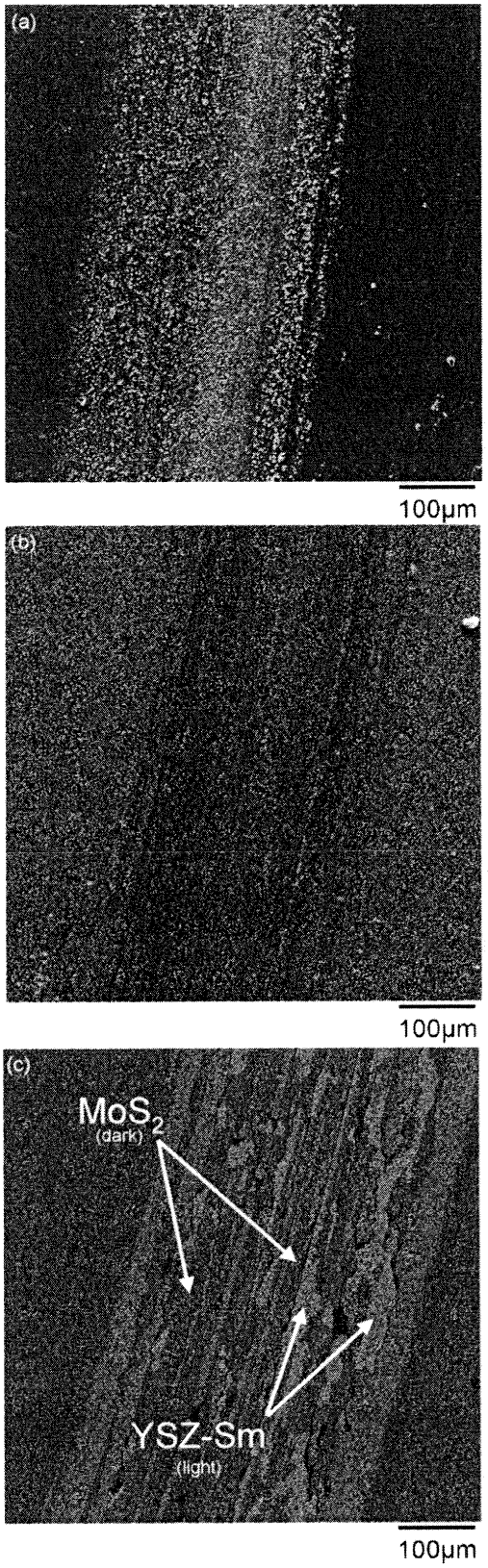


Fig. 6. Electron micrographs of wear tracks from (a) monolithic and (b) multilayered sensor coatings after 20,000 cycle in 40% relative humidity. (c) Shows wear track in the multilayered coating after 200,000 cycles in 40% humidity.

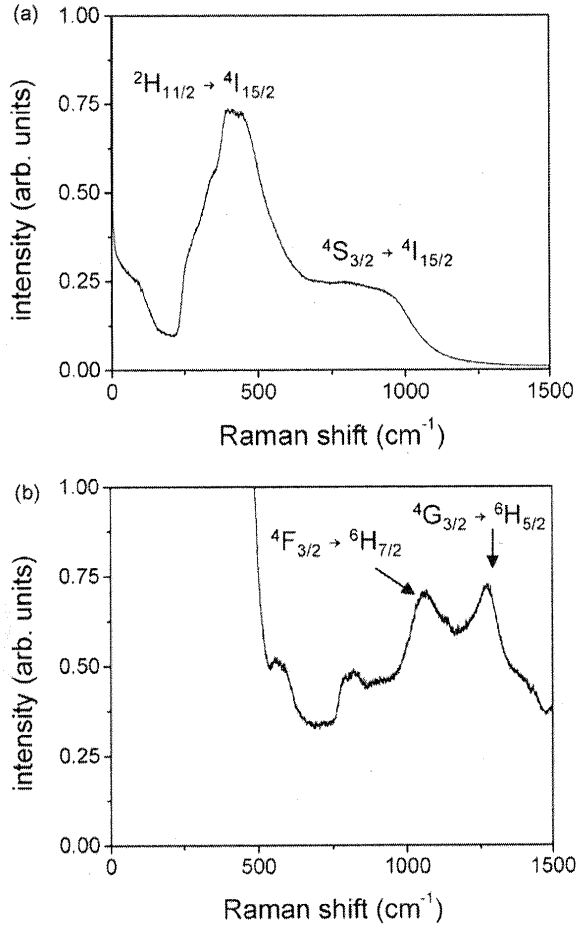


Fig. 7. Luminescence spectra from monolithic (a) YSZ-Er and (b) YSZ-Sm coatings. The electronic transitions corresponding to the observed luminescence peaks are labeled. The shift is relative to the laser at 532 nm used to excite the luminescence.

4. Discussion

From Fig. 3 and XPS chemical analyses, the microstructure and composition of the MoS_2 lubricant layers were the same in the monolithic and multilayered coatings, however, the incorporation of the YSZ sensor layers extended wear life by a factor of 30. There are several possible mechanisms by which the presence of the ceramic layers could contribute to the increased wear life of the coating. For dc magnetron sputtered MoS_2 with an open columnar structure, Spalvins [11] and others [12] have recognized that the wear rate is not linear, with initially rapid wear of the surface until only a thin layer of adherent MoS_2 material remains on the substrate with partial transfer of coating material to the ball counterface. Recent *in situ* investigations of such transfer layer formation with hard nanocomposite coatings containing MoS_2 confirmed the proposed mechanism of sliding velocity accommodation by shearing in this thin <50 nm layer [13]. Similar transfer layer formation was observed in the present work when silicon nitride counterparts were examined with optical microscopy.

The addition of a relatively thick intermediate hard layer of doped YSZ likely served as a hard supporting surface, facil-

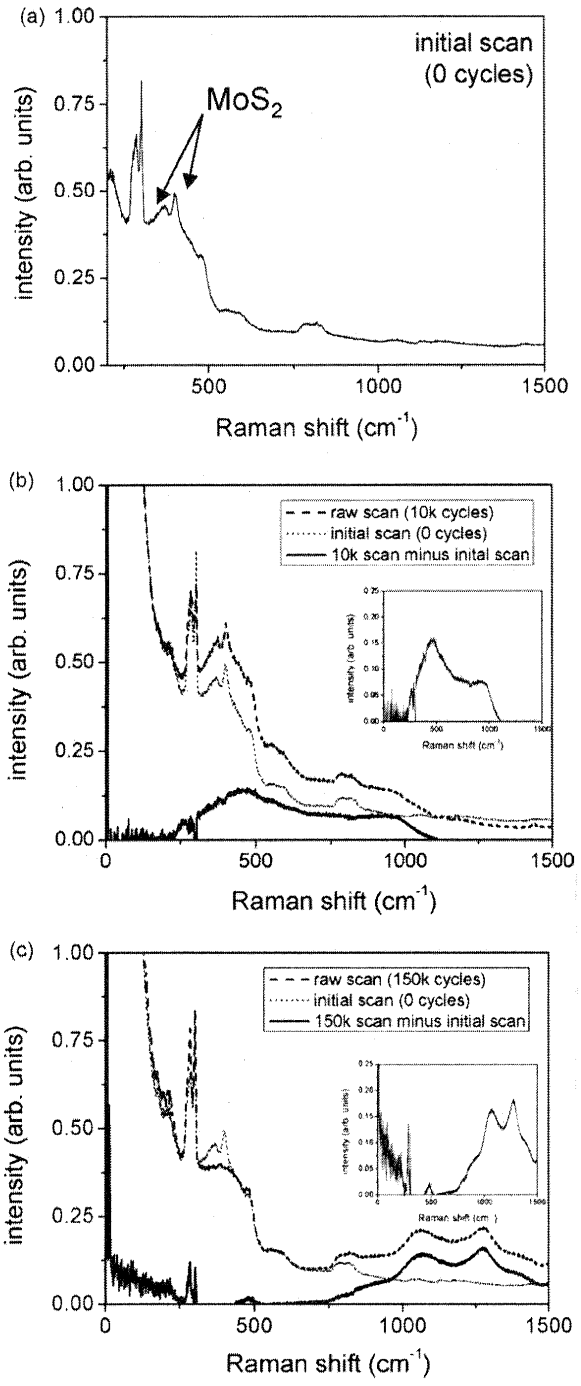


Fig. 8. Optical spectra from the wear track of multilayered sensor coating (a) prior to wear testing, (b) at 10,000 cycles and (c) at 150,000 cycles. Plots in (b) and (c) also show the difference between the initial scan and the scan at the given number of cycles. The insets in (b) and (c) show the difference scans on a scale similar to that used for the monolithic sensor spectra shown in Fig. 7. The characteristic doublet due to Raman scattering from MoS_2 is labeled.

itating the formation of an easy-shearing MoS_2 transfer film between the YSZ-Er sensor layer and ball counterpart. Eventually the MoS_2 transfer film deteriorated in the ambient humid air by tribochemical oxidation and the thin (650 nm) YSZ-Er layer was breached by abrasive wear in the middle of the track where the contact stress was greatest. Based on the disappearance of the YSZ-Er spectrum from the *in situ* measurements, the ceramic layer was worn away after approximately 30,000 sliding cycles. The remaining adjacent YSZ-Er layer, however, continued to provide load support while the fresh lubricant supply from the underlying MoS_2 layer was exposed in the contact area. The profilometry and electron microscopy data presented in Figs. 5 and 6, respectively, confirm that the initial wear of the MoS_2 coating over the first 20,000 cycles was limited to the first available hard YSZ interface. Previous studies of wear tracks with laser drilled grooves in hard ceramic coatings filled with sputtered MoS_2 have shown an increased wear life of multiple orders of magnitude in humid environments [14]. In essence, a similar contact geometry and mechanism was achieved here by wear of the multilayer coating stack.

Additionally, the YSZ layers deposited by PLD had an elastic modulus of ≈300 GPa [15,16] compared to 200 GPa for the steel substrate thereby increasing the Hertzian contact stress by approximately 10%. It is well documented that the friction coefficient of MoS_2 decreases with increasing contact stress [17–19], consistent with the results shown in Fig. 4, where the friction coefficient was lower in the presence of the ceramic layers.

The luminescence spectra from the single-layer-doped YSZ materials were consistent with those reported for similar YSZ-based materials processed at higher temperatures [3], although the peaks in both the monolithic-doped YSZ single layers (Fig. 7) and the multilayered coating (Fig. 8) are shifted slightly and are significantly broader than that of the YSZ-Er and YSZ-Sm powder sintered targets [3]. Dieke [8] describes how a strained crystal lattice can cause a shift in peak position due to lattice imperfections. The broad tetragonal YSZ peaks observed in the X-ray diffractograms (Fig. 3) suggest a highly defective, nanocrystalline structure associated with the low deposition temperature and non-equilibrium processing conditions used here for YSZ deposition. Non-uniformity of the strain in the crystal lattice throughout the coating thickness may also have contributed to the position and shape of the measured luminescence peaks. Other work has shown that PVD coating materials generally exhibit higher strain at the interface, with strain relaxing as the coating grows [20]. These factors may account for the slight shift and broad shape of the observed luminescence spectra in Fig. 8, nevertheless, the different layers were easily identified (Figs. 7 and 8) and corresponded well to distinct events marked by the wear tests (Fig. 4).

Spectra from monolithic-doped YSZ coatings were the same whether the coatings were rotating or stationary at the relatively low 0.2 m s^{-1} sliding speed used for tribological testing. This was as expected, since the luminescence emission begins within picoseconds of laser excitation [21] and the luminescence from the wear surface to the detector travels within few nanoseconds. This provides a practically instantaneous response from the sliding surface, allowing the wear track to be considered a virtually stationary surface within the time frame of signal acquisition. The sensor concept explored here with relatively low sliding speeds will, therefore, be equally applicable for use at relatively high sliding and/or rotating velocities, such as those expected in aircraft turbine engines.

Please cite this article in press as: C. Muratore, et al., Smart tribological coatings with wear sensing capability, Wear (2008), doi:10.1016/j.wear.2008.02.003

Correlation of Fig. 4 with Fig. 8, both of which were generated at the same time, illustrates the utility of the sensor materials as *in situ* wear meters and failure indicators. After 10,000 sliding cycles (indicated in Fig. 4b) the uppermost MoS_2 coating layer thickness was reduced such that the laser could excite the buried YSZ-Er sensor layer, resulting in the appearance of the Er^{3+} luminescence spectrum. The friction was also high in this region, suggesting an ongoing process of MoS_2 layer removal in the wear track. Wear through the topmost MoS_2 layer was rapid, exposing the YSZ-Er layer and giving rise to the characteristic spectra in Fig. 8b. Later in the experiment, the Er^{3+} spectrum was no longer detectable, suggesting that the YSZ-Er interlayer was breached. Towards the end of the wear test, the Sm^{3+} spectrum appeared, indicating that the solid lubricant in the contact was thin enough for the laser beam to excite the buried sensor layer and allow transmission of the emitted light. The appearance of this spectrum occurred with about 30,000 cycles remaining before initial coating failure for all tests.

The number of cycles between activation of the failure warning sensor layer and coating failure will obviously depends on the tribological properties of the solid lubricant coating material and substrate, but will also depends on the degree to which the excitation laser energy is absorbed by the top lubricant layer. A material that strongly absorbs the laser will have a reduced minimum remaining thickness above the sensor layer at which the characteristic luminescence can be activated. To determine this minimum thickness for a material, one can use Beer's law which is based on the empirical observation that there is an exponential decrease in the initial intensity (I_0) of a beam as it passes through any homogeneous solid substance proportional to the linear distance traversed (x), yielding a well known equation for the light absorbance by a solid materials (neglecting surface reflectivity):

$$\frac{I_x}{I_0} = \exp(-\alpha x),$$

where I_x/I_0 is the fraction of the initial intensity that the beam has been reduced to at depth x in the solid, and α is the material-dependent absorption coefficient which is also inversely proportional to the transmitted light wavelength. The minimum value of x at which the intensity falls to 1/e is simply the inverse of the absorption coefficient (α^{-1}). For spectroscopy performed in backscattered mode, the calculated distance x should be halved when considering the sampling depth of the laser, as the scattered light has to traverse a distance equivalent to the incident light which is equivalent to twice the thickness.

The absorption coefficient α of a solid is sensitive to its composition and crystal structure. For 532 nm light incident on a (0 0 2) MoS_2 crystal (with basal planes oriented perpendicular to the direction of the laser), α is about $1.5 \times 10^5\ cm^{-1}$ [7], which provides a total minimum penetration distance of about 60–70 nm. Experimentally, Wahl et al. [22] and Zabinski [23] have found that 30–50 nm of (0 0 2) oriented MoS_2 deposited on a silicon wafer will absorb the incident laser such that the backscattered light from the Si/MoS_2 interface will not be detected. If the coating is thinner, the Raman spectrum from the Si will begin to appear, consistent with the analysis presented above. Furthermore, Scharf and Singer [24] reported that α for 532 nm laser light in diamond-like carbon was $4–5 \times 10^4\ cm^{-1}$, resulting in a minimum thickness of approximately 100–120 nm for complete absorption, which is approximately 2–3 times the minimum thickness of MoS_2 layer. Thus, for the same sensor layer material and excitation laser wavelength, the degree of the remaining coating lifetime will be dependent on the absorption characteristics of the solid lubricant as well as its tribological properties.

While the ability to monitor the remaining wear life of tribological coatings is useful in the laboratory for developing multilayered coating systems, a compact laser and detector system similar to that described here could be also incorporated into a diverse range of mechanical systems with the use of thin fiber optic probes to bring diagnostics close to friction contacts in real machines, thereby allowing service life diagnostics and eliminating unnecessary teardowns and overhauls. The ability of engineers to expand design limits and the safety of end users are both increased when sensors to warn of imminent failure are incorporated into smart coating materials.

5. Conclusions

Multilayered coatings consisting of MoS_2 and rare-earth-doped YSZ sensor layers were deposited and characterized with the intent of developing a technique to report the depth of contact wear, provide a warning for impending failure and to illustrate the concept of smart tribological coatings with built-in wear sensing and reporting capability. Rare-earth-doped sensor layers were activated by green laser light to provide distinctive signals from two different depths within a single coating during sliding wear of a MoS_2 coating in humid air. Considerations for using this technique to monitor coating wear with other tribological materials were also presented, where the impact of the solid lubricant optical properties on sensor performance was discussed as it has a direct influence on the remaining coating thickness and wear life diagnostic capability. The presence of the ceramic sensor layers inserted into MoS_2 coating also altered the tribological properties of this solid lubricant coating, resulting in a significant (>30X) increase in wear life. The *in situ* wear sensing experiments helped to illustrate the proposed wear mechanisms of MoS_2 transfer layer formation on the surface of harder ceramic layers, which resulted in reduced the friction coefficient, arrested sliding wear, and extended wear life for the multilayered MoS_2/YSZ coatings.

Acknowledgements

The authors wish to thank Jeffery S. Zabinski at the Air Force Research Laboratory and Kathy J. Wahl at the Naval Research Laboratory for providing useful insight on laser interactions with tribological materials. Nicholas A. Baine is gratefully acknowledged for writing the data acquisition code for the tribospectrometer. John E. Bultman and Art J. Safriet are thanked for general technical assistance. Funding was provided by the Air Force Office of Scientific Research.

References

[1] D.R. Clarke, R.J. Christensen, V. Tolpygo, The evolution of oxidation stresses in zirconia thermal barrier coated superalloy leading to spalling failure, Surf. Coat. Technol. 94–95 (1997) 89–93.
[2] J.I. Eldridge, T.J. Bencic, Monitoring delamination of plasma-sprayed thermal barrier coatings by reflectance-enhanced luminescence, Surf. Coat. Technol. 201 (2006) 3926–3930.
[3] M.M. Gentleman, D.R. Clarke, Concepts for luminescence sensing of thermal barrier coatings, Surf. Coat. Technol. 188–189 (2004) 93–100.
[4] B. Heeg, D.R. Clarke, Non-destructive thermal barrier coating (TBC) damage assessment using laser-induced luminescence and infrared radiometry, Surf. Coat. Technol. 200 (2005) 1298–1302.
[5] C. Muratore, A.A. Voevodin, J.S. Zabinski, Multilayered YSZ–Ag–Mo/TiN adaptive tribological nanocomposite coatings, Tribol. Lett. 24 (2006) 201–206.
[6] C. Muratore, J.J. Hu, A.A. Voevodin, Adaptive nanocomposite coatings with a titanium nitride diffusion barrier mask for high-temperature tribological applications, Thin Solid Films 515 (2007) 3638–3643.
[7] J.A. Wilson, A.D. Yoffe, in: B.R. Coles (Ed.), The Transition Metal Dichalcogenides: Discussion and Interpretation of the Observed Optical, Electrical, and Structural Properties, Taylor and Francis, London, 1962, p. 193.
[8] G.H. Dieke, H.M. Crosswhite, H. Crosswhite, in: H.M. Crosswhite, H. Crosswhite (Eds.), Spectra and Energy Levels of Rare Earth Ions in Crystals, Interscience Publishers, New York, 1968.
Q1 [9] C. Muratore, A. A. Voevodin, Thin Solid Films, in press.
[10] M.N. Gardos, Anomalous wear behavior of MoS_2 films in moderate vacuum and dry nitrogen, Tribol. Lett. 1 (1995) 67.
[11] T. Spalvins, Morphological and frictional behavior of sputtered MoS_2 films, Thin Solid Films 96 (1982) 17.
[12] I.L. Singer, S. Fayeulle, P.D. Ehni, Wear behavior of triode-sputtered MoS_2 coatings in dry sliding contact with steel and ceramics, Wear 195 (1996) 7–20.
[13] R.R. Chromik, A.A.V.K.J.W.C.C. Baker, In situ tribometry of solid lubricant nanocomposite coatings, Wear 262 (2007) 1239–1252.
[14] A.A. Voevodin, J.E. Bultman, J.S. Zabinski, Investigation into 3-Dimensional Processing of Tribological Coatings, Surf. Coat. Technol. 107 (1998) 12–19.
[15] A.A. Voevodin, J.G. Jones, J.S. Zabinski, Characterization of ZrO_2/Y_2O_3 laser ablation plasma in vacuum, oxygen, and argon environments, J. Appl. Phys. 88 (2000) 1088–1096.
[16] A.A. Voevodin, J.J. Hu, J.G. Jones, T.A. Fitz, J.S. Zabinski, Growth and structural characterization of yttria-stabilized zirconia-gold nanocomposite films with improved toughness, Thin Solid Films 401 (2001) 187–195.
[17] L.E. Seitzman, R.N. Bolster, I.L. Singer, IBAD MoS_2 lubrication of titanium alloys, Surf. Coat. Technol. 78 (1996) 10–13.
[18] I.L. Singer, R.N. Bolster, J. Wegand, S. Fayeulle, B.C. Stupp, Hertzian stress contribution to friction behavior of thin MoS_2 coatings, Appl. Phys. Lett. 57 (1990) 995–997.
[19] W.O. Winer, Molybdenum disulfide as a lubricant: a review of the fundamental knowledge, Wear 10 (1967) 422–452.
[20] M.K. Puchert, P.Y. Timbrell, R.N. Lamb, D.R. McKenzie, Thickness-dependent stress in sputtered carbon films, J. Vac. Sci. Technol. A 12 (1994) 727–732.
[21] J. Lu, F. Shao, K. Fan, S. Du, Dynamical theory of time-resolved fluorescence with pulse excitation, J. Chem. Phys. 114 (2001) 3373–3379.
[22] K.J. Wahl, L.E. Seitzman, R.N. Bolster, I.L. Singer, Low-friction, high-endurance, ion-beam-deposited Pb-Mo-S coatings, Surf. Coat. Technol. 73 (1995) 152–159.
[23] J.S. Zabinski, 2007 personal communication.
[24] T.W. Scharf, I.L. Singer, Thickness of diamond-like carbon coatings quantified with Raman spectroscopy, Thin Solid Films 440 (2003) 138–144.

Please cite this article in press as: C. Muratore, et al., Smart tribological coatings with wear sensing capability, Wear (2008), doi:10.1016/j.wear.2008.02.003

Paper 8

Elsevier Editorial System(tm) for Thin Solid Films
Manuscript Draft

Manuscript Number:

Title: Control of molybdenum disulfide basal plane orientation during coating growth in pulsed magnetron sputtering discharges

Article Type: Full Length Article

Section/Category: A. Synthesis and Characterization

Keywords: molybdenum disulfide; pulsed sputtering; tribology

Corresponding Author: Dr. Chris Muratore, Ph.D

Corresponding Author's Institution:

First Author: Chris Muratore, Ph.D

Order of Authors: Chris Muratore, Ph.D; Chris Muratore, Ph.D

Dear Thin Solid Films Editors,

Attached is an original, unpublished submission for to be considered for publication as an article in *Thin Solid Films*. The article is not being considered for publication elsewhere. The paper is entitled "Control of molybdenum disulfide basal plane orientation during coating growth in pulsed magnetron sputtering discharges," which describes a revealing dependence of MoS_2 coating orientation on ion flux, energy and deposition rate. We suggest the individuals listed below as potential editors.

With thanks and best regards,

Chris Muratore

Suggested Reviewers

Professor Thomas Scharf
University of North Texas
Department of Materials Science and Engineering
North Texas Research Park
3940 North Elm. St. - Suite E-132
Denton, TX 76207

email: scharf@egw.unt.edu
phone: 940-891-6837

Dr. Matt A. Hamilton
University of Florida
Mechanical and Aerospace Engineering Department
UFPO 116300
Room 002 Building 183
Gainesville, FL 32611

e-mail:mah@ufl.edu
phone: (352) 392-8488

Dr. Colin C. Baker
US Naval Research Laboratory
Tribology Division
Code 6176
4555 Overlook Ave. Sw
Washington, DC, 20375

e-mail: colin.baker@nrl.navy.mil
phone: 202-767-5342

C. Muratore et. al.
To be submitted to Thin Solid Films

Control of molybdenum disulfide basal plane orientation during coating growth in pulsed magnetron sputtering discharges

C. Muratore, A.A. Voevodin

[a]*UTC/Air Force Research Laboratory, Materials and Manufacturing Directorate, Wright-Patterson Air Force Base, OH 45433 USA*
[b]*Air Force Research Laboratory, Materials and Manufacturing Directorate, Wright-Patterson Air Force Base, OH 45433 USA*

Abstract

Molybdenum disulfide coatings were grown under selected mid-frequency bi-polar pulsed dc power conditions to control the basal plane orientation relative to the substrate, from parallel (002) to perpendicular (100). Growth mechanisms under different conditions were made apparent by the observed trends. The highest (002)/(100) orientation ratios were obtained with growth rates near 1 atomic layer per second accompanied by high energy ion bombardment (up to 175 eV). These conditions allowed maximum surface diffusion of deposited atoms before burial by incident material or removal by desorption and resputtering. Additionally, high energy ion bombardment during pulsed deposition produced defects on the otherwise inert MoS_2 (002) surface that further enabled adsorption and crystal growth. For growth rates of less than one monolayer per second coupled with low ion energies and fluxes, coatings exhibited strong (100) orientation. Under these low growth rate conditions, the burial rate was still faster than the desorption rate on the (100) surface, and the lack of energetic ion bombardment permitted uninterrupted growth of crystals in this orientation. For sliding wear tests conducted in humid air, the tribological performance of the coatings demonstrated a strong dependence on (002)/(100) ratios.

Introduction

Bipolar pulsing of magnetron targets in the 1-100 kHz frequency range was originally introduced as a technique to reduce arcing at target surfaces during reactive sputtering of dielectric materials [1-3]. Soon afterwards, electrically conductive materials deposited by pulsed dc magnetrons were reported to show structural changes typically observed at higher substrate temperatures and performance improvements over coatings prepared by conventional dc sputtering [4-6]. Research efforts to understand the origins of these microstructural changes revealed that bipolar pulsing of the magnetron target increased the energy and flux of ions impinging upon a substrate immersed in a magnetron plasma and maintained at a fixed potential (via biasing or grounding) by over an order of magnitude [6,7]. Pulse parameters were also shown to affect the deposition rate [8] and, in conjunction with the control of ion kinetic energy and flux, can be adjusted to manipulate the composition, structure and properties of electrically conductive coating materials.

Molybdenum disulfide is an electrically conductive material that has been reported to show strong sensitivity to a long list of processing parameters investigated over the past several decades [9]. Among the intrinsic parameters on that list, the energy [10] and magnitude [11] of the impinging ion flux, in addition to the deposition rate [12], are key factors that can be controlled to tailor MoS_2 coating microstructure independently of other variables . Given that these three intrinsic processing parameters are uniquely coupled in mid-frequency pulsed magnetron sputtering, it was expected that control of the structure and properties of MoS_2 coatings could be obtained with the process.

Experimental procedure

Monolithic MoS_2 coatings were deposited in a hybrid filtered vacuum arc/magnetron sputtering deposition system. Figure 1 shows a schematic of the deposition chamber. Discs of 25 mm diameter x 3 mm thick 440C steel were ultrasonically degreased in acetone and loaded into a rotating fixture within the processing chamber. A 3 x 3 mm^2 adhesive mask was attached to the center of each substrate prior to deposition. A 520 l s^{-1} turbomolecular pump was used to evacuate the chamber to a pressure of <5 x 10^{-7} Torr [10] (7 x 10^{-5} Pa). The rotating substrates were then heated in vacuum to 150 ^{o}C, degassed for 30 minutes and maintained at that

temperature throughout all subsequent coating processes. Substrates were cleaned with positively charged argon and metal ions next, as they were exposed to glow discharge and then filtered titanium arc plasmas, respectively, with bias voltages of up to -800 V dc. The titanium arc plasma operated in 1 x 10^{-4} Torr (0.01 Pa) Ar, which was attained by flowing 8 sccm Ar into the chamber. The arc source was also used to deposit a thin (<100 nm) adhesion layer for all coatings. The argon flow rate was then increased to 100 sccm and an automated throttle valve was continuously adjusted to maintain the chamber pressure at 12 x 10^{-3} Torr (1.6 Pa). A dc glow discharge from an unbalanced magnetron plasma source with a 32 mm, 99.9% pure MoS_2 cathode was then initiated. The nominal power density on the MoS_2 cathode was increased incrementally up to 9 W cm^{-2} during titanium deposition to produce a graded lubricant/adhesion layer interface of about 250 nm total thickness, after which the titanium arc source was switched off and magnetron power was maintained throughout coating growth. A range of different frequencies (dc-200 kHz) and duty factors (58-100%) were used in separate deposition experiments with experimental settings summarized in Table I. The target voltage waveforms were recorded on a digitizing oscilloscope, which averaged 200 scans triggered by the onset of a positive pulse. Substrates were dc biased to -30 V dc during MoS_2 deposition.

A Hiden EQP 1000 plasma analyzer was used to measure the time-averaged kinetic energy distributions of positively charged Ar, Mo and S ions arriving at its grounded front electrode located in the substrate position. A dwell time of 200 ms per .0,5 eV energy increment was used to allow collection over multiple pulse cycles at a particular energy. The analyzer was fitted with a 20 μm orifice, and was differentially pumped to <1 x 10^{-6} Torr for all measurements. An energy range of 0-1000 eV was scanned for all positive ions of interest with the EQP.

As-deposited coatings were examined using electron microscopy, X-ray photoelectron spectroscopy (XPS), and X-ray diffraction in a θ-2θ geometry. The thickness of the coatings was measured by comparing the height of the masked substrate area to the relative height of the coating surface with a contact profilometer. All coatings were grown to a thickness of approximately 2.5 microns (± 200 nm).

For sliding contact tests, a 6 mm silicon nitride ball and 1 N load were used, resulting in an initial Hertzian contact stress of approximately 650 MPa for MoS_2

coatings. The sliding speed was 0.2 m sec^{-1} and the test environment was 23 °C air with controlled 40% relative humidity for all tests. While MoS_2 is known to perform effectively as a lubricant in dry environments, the tests in humid air helped to examine the environmental sensitivity of the coatings, which was known to be closely linked to microstructure and orientation [13,14].

Results

Figure 2 shows selected examples of voltage waveforms applied to the MoS_2 target during selected deposition experiments. The polarity reversal was delayed for frequencies over 150 kHz, and therefore the actual duty factor was lower than that specified using the power supply controls, as shown in Fig. 2d, where a 90% nominal duty factor at 200 kHz was equivalent to an actual duty factor of 58%. It was also noted that the maximum positive potential was approximately 425 V at 85 kHz and 90% duty (Figure 2b), compared to 250-300V for the other frequencies and duty factors explored here.

Ion energy distributions (IEDs) of positively charged argon ions for the indicated target voltage waveforms are shown in Figure 3. All IEDs were collected immediately after each other with the same mass spectrometer tuning parameters to allow direct comparison of energies and intensities. When dc power was applied to the target, the ion energy distribution was within a very narrow energy window, with a maximum ion energy of 12 eV (Fig. 3a), which is typical for a dc magnetron glow discharge [15,16]. When the target was pulsed, the ion energy distributions measured at the grounded plasma analyzer were considerably broader (Fig. 3b and Fig. 3c for example) as reported in previous studies of pulsed sputtering processes [6,7]. The maximum ion kinetic energy was 100-200eV (Fig. 3 b and c)--roughly a factor of 10 times greater then the maximum ion energy measured when dc power was applied to the target. At 85 kHz and with a 90% duty factor (Fig. 3b), ions with energies from 0 to 180 eV were detected, with three defined peaks at 15 eV, 27 eV, and 175 eV. A similar broad energy distribution with the substantial number of high energy ions was observed also for 100 kHz and 90% duty settings (Fig. 3c), except the peak location for the high ion energy ions was only 125 eV. The IEDs of molybdenum and sulfur ions (not shown) were also measured for all

conditions, and demonstrated similar features as those shown in Figure 3, although the heavier molybdenum ions exhibited lower maximum energies than argon and sulfur for measurements in pulsed plasmas. No ions were detected between 200-1000 eV.

Table I compares the effect of the target pulse conditions on the deposition rate, structure and tribological properties of the deposited coatings. As expected, dc sputtering provided the highest deposition rate. When the target was pulsed, the deposition rate decreased monotonically with duty factor, and had an inverse dependence on frequency for equivalent duty factors, consistent with the observations of Kelly [8]. Figure 4 shows X-ray diffractograms of selected coatings and atomic-scale, side view schematics of crystals in the dominant orientation, which illustrate the orientation transition achieved by manipulating the target pulse parameters. For samples grown under high deposition rate conditions, the hexagonal molybdenite phase with an (002) preferred orientation was observed (Fig. 4a). For deposition rates less than 13 nm min^{-1}, the (100) orientation dominated (Fig 4c). Figure 5 shows the relationship between deposition rate and (002)/(100) ratios for the coatings as listed in Table I. Figure 6 shows that MoS_2 coating performance during wear tests in humid air was strongly dependent on the deposition parameters. Coatings with higher (002)/(100) ratios had lower friction and wear coefficients than those with a (100) orientation (Table 1).

Discussion

The trend shown in Figure 5, where the (002)/(100) fraction increased with deposition rate was unexpected as it was contrary to multiple reports in the literature, where an inverse rate-orientation relationship was reported for MoS_2 coatings deposited with both dc and rf sputtering processes [9,12,17,18]. The trend observed here can be understood (and shown to be in agreement with previous work) by considering the effect of deposition rate and incident ion energy on MoS_2 orientation during film growth.

The deposition rate makes a significant contribution to the orientation of the coatings because of the atomic desorption kinetics particular to MoS_2 growth. The relatively inert (002) surface has a surface energy of approximately 250 kJ cm^{-2}, compared to the chemically reactive (100) surface at about 25,000 kJ cm^{-2} [18]. Because of this low surface energy, atoms deposited on the (002) basal plane surface have a higher

probability of being desorbed or resputtered before adsorption or burial by incident target material (i.e. a lower sticking coefficient) than those on a (100) surface [19].

The actual desorption time for atoms on the (002) and (100) surfaces can be estimated by considering absolute reaction-rate theory as discussed by Smith, who derives an equation to determine the time in which a chemisorbed atom is more likely to desorb than to be buried in low flux conditions [20]. The desorption time t is simply given by the inverse of the chemisorption rate constant k_c:

$$t = \frac{1}{k_c} = \frac{1}{v_{oc}} e^{E_S / RT},$$

where E_s is the activation energy for surface diffusion, R is the gas constant, and T is temperature. The term v_{oc} is the characteristic atomic hopping frequency, estimated to be

$$v_{oc} = \frac{kT}{h},$$

for hopping from one identical site to another, where k is Boltzmann's constant and h is Plank's constant. To have an estimate of the expected desorption times for atoms on (100) and (002) MoS_2 surfaces, consider the activation energy for surface diffusion (E_s) of chemisorbed sulfur on MoS_2, which is approximately 120 kJ mol^{-1} for the (100) surface [21] compared to ~95 kJ mol^{-1} on the (002) surface [22]. This results in an estimated desorption time (t) on the (100) surface that is on the order of seconds, compared to that for the (002) orientation, which is less than one second. Therefore, when atoms are deposited on (002) surfaces, the likelihood of desorption is high, especially as the deposition rate decreases below one monolayer per second. For the higher duty factor conditions, in which a strong (002) preferred orientation is observed, the burial rate by the next depositing monolayer is greater than the desorption rate, allowing growth on the basal plane surfaces.

As indicated earlier, other authors reported decreased (002) crystal growth with increasing deposition rate, however, those authors used processes that yielded deposition rates of 15 nm min^{-1} (or ~ 1 ML sec^{-1}) or more [17,18]. This is the critical rate identified on Figure 5, above which the (002)/(100) orientation ratio is maximized. In the current work there was a slight decrease in the (002)/(100) orientation ratio as the deposition rate

increased beyond 15 nm min^{-1}, in agreement with the observations of other authors, as mentioned earlier.

For conventional rf or dc sputtering, the reduced deposition rates allowed maximum surface diffusion of the atoms to the lowest energy adsorption sites, increasing the film density and the fraction of (002) oriented material. This is the case for pulsed dc sputtering as well, however, the conditions yielding higher ion energies (75-85 kHz, 90% duty) resulted in the highest (002) ratios and the best tribological performance. Energetic (>100 eV) ion bombardment has been reported to promote growth of (002) oriented MoS_2 by creating high energy sites for adsorption on the chemically inert surface [19], and by reducing shadowing effects of the rapidly growing (100) oriented material that can further suppress (002) growth [23]. Conventional sputtering processes rely on an auxiliary ion beam or other techniques to obtain high energy ions. In this work, the increased ion energy shown for pulsed target operation in Figure 3 is directly related to the target voltage waveform (Fig. 2), which produces a time-dependent plasma potential.

To understand the mechanism by which high energy ions are generated in a pulsed dc magnetron process, one can first consider the origin of the plasma potential, which is the potential difference between the electrically neutral electron-ion plasma and a grounded electrode immersed in it [24]. Near the grounded electrode the plasma is rapidly depleted in electrons, resulting in a positive space charge developing over a region (on the order of millimeters for the average sheath potentials and plasma densities considered here) surrounding the electrode, referred to as a plasma sheath. The magnitude of this space charge is referred to as the plasma potential. If the plasma is further depleted in electrons from a powered electrode with a positive potential, as it is by the sputtering target during the off-time in bipolar pulsed sputtering, the magnitude of the space charge will increase such that the plasma potential is the highest positive potential in the chamber. The response of the plasma potential to the changing target polarity is rapid, with a characteristic time equivalent to the inverse of the plasma frequency, which is on the order of GHz for typical magnetron discharges. This is much faster than the characteristic times for target pulse events on the kHz-MHz scale used in this work. The highest energy ions accelerating through the plasma sheath to an electrode at a fixed potential could therefore have a maximum energy equivalent to the plasma potential

minus the substrate potential (zero if grounded or equal to the negative bias potential). Heavier ions will move slower than lighter ions when accelerated across the same distance and potential, and therefore may not completely traverse the sheath over one target pulse period as the physical size and potential of the sheath are time-dependent [25]. For kHz frequency regimes, such ions may take several pulses to reach the substrate, thus arriving at the substrate in a subsequent target pulse from a position nearer the substrate than at the edge of the sheath, resulting in a reduced accelerating potential and final kinetic energy. Thus, molybdenum ions, with a mass of 96 amu, were measured to have a lower maximum energy in the pulsed processes than the lighter argon or sulfur ions.

The measured time-averaged ion energy distributions in the pulsed discharges reflect the time-dependent plasma potential, with the highest energy ions in Figs. 3b and c corresponding to the peak positive voltages on the magnetron target (Figs. 2a and c). Note that the mass-energy analyzer provides measurements averaged over multiple magnetron pulses, and may not detect ions born during short transient voltage spikes, such as the initiation of the positive pulse on the sputtering target (Fig. 2). While ion energies arriving at the growing coating surface during deposition may have exceeded 400 eV based on the spike voltage amplitudes, those ions were not detected by the mass-energy analyzer in its current configuration.

The intermediate peak about 30 eV in Fig. 3b corresponds to the stable positive portion of the waveform at a commensurate voltage during the plasma off time. All IEDs have a peak near 10 eV, corresponding to the negative, "dc like" operating regime of the target voltage waveform.

Comparing IEDs measured at 100 kHz and 85 kHz, the corresponding increase of the ion energy from 125 eV to 175 eV (Fig. 3b and c) also increased the sputtered atom-to-incident ion ratio by about an order of magnitude [26], suggesting that higher energy ion bombardment further assisted defect formation on the (002) surface at the 85 kHz condition, and thereby facilitated growth of crystals in that orientation by increasing the surface energy of the MoS_2 basal planes when the highest energy ions were produced.

The friction coefficients and wear rates both scaled inversely with deposition rate and (002)/(100) ratios (Fig. 6), illustrating how the (100) molybdenite crystal face is not

just more reactive during film growth, but also while in use in humid air. This finding is consistent with many reports of improved tribological performance when basal plane texture is parallel to the coating surface, providing easier shear and less chemical interaction of the sliding mechanical contacts [10,12,27,28]. Interestingly, the coatings yielding the best friction behavior (Fig. 5) were those produced nearest the minimum deposition rate required to induce the preferred (002) orientation. Under these conditions, atoms arriving at the surface had the maximum amount of time to diffuse across the (002) crystal surface without desorbing before burial by the next deposited layer. The combination of the increased ion energy at the surface and increased surface diffusion time provided coatings with maximum resistance against oxidation and degradation in humid air, which was most likely due to the denser microstructure and stronger (002) texture. Indeed, Stupp [9] and Fleischauer [12] had noticed in the experiments with dc sputtering that the lower rates generally produced MoS_2 coatings with superior tribological performance, provided the (002) orientation was obtained.

Conclusions

Process-structure relationships were explored for a pulsed magnetron sputtering of MoS_2 coatings. General mechanisms for MoS_2 were suggested, where the deposition rate and ion energy accounted for the crystallographic texture evolution. The findings imply that the maximum (002)/(100) ratio is obtained at an optimum deposition rate, which is low enough to allow deposited atoms to diffuse the maximum distance before burial by the next layer of coating material, yet high enough to prevent desorption. This rate was found here to be approximately 13 nm min^{-1}, or 1 ML sec^{-1}, but was also dependent upon the parallel process of energetic ion bombardment during coating growth. Pulsed dc sputtering was shown to generate broad ion energy distributions with a significant fraction of ions having kinetic energies greater than 100 eV, as compared to dc sputtering where all incident ions had a kinetic energy < 10 eV. Furthermore, the optimization of frequency and duty factor was shown to increase the maximum ion energy from 125 to 175 eV. The mechanism of high energy ion generation in the pulsed discharges was briefly discussed. Deposition processes with ion energies >175 eV were found to promote (002) orientation of MoS_2 coating material due to formation of atom

absorption sites that facilitated growth on the lowest energy MoS_2 surface and suppressed (100) crystal growth. Coatings with increased (002)/(100) ratios yielded lower friction coefficients and wear rates, which was due to easier shear of the oriented basal planes and the increased resistance of the inert (002) orientation to degradation in reactive environments.

Acknowledgments

The Air Force Office of Scientific Research is acknowledged for financial support. The authors also wish to thank John Bultman and Art Safriet for technical assistance.

REFERENCES

[1] D. A. Glocker, J. Vac. Sci. Technol. A 11 (1993) 2989.

[2] P. J. Kelly, O. A. Abu-Zeid, R. D. Arnell, J. Tong, Surf. Coat. Technol. 86-87 (1996) 28.

[3] W. D. Sproul, M. E. Graham, M. S. Wong, S. Lopez, D. Li, R. A. Scholl, J. Vac. Sci. Technol. A 13 (1995) 1188.

[4] K. E. Cooke, A. Goodyear, J. Hampshire, D. G. Teer, Surf. Coat. Technol. 188-189 (2004) 750.

[5] P. S. Henderson, P. J. Kelly, R. D. Arnell, H. Backer, J. W. Bradley, Surf. Coat. Technol. 174-175 (2003) 779.

[6] C. Muratore, J. J. Moore, J. A. Rees, Surf. Coat. Technol. 163-164 (2003) 12.

[7] J. W. Bradley, H. Backer, Y. Aranda-Gonzalez, P. J. Kelly, R. D. Arnell, Plasma Sources Sci. Technol. 11 (2002) 165.

[8] P. J. Kelly, A. A. Onifade, Y. Zhou, C. B. Clarke, M. Audronis, J. W. Bradley, Plasma Process.Polym. 4 (2007) 246.

[9] B. C. Stupp, Thin Solid Films 84 (1981) 257.

[10] T. Spalvins, Thin Solid Films 73 (1980) 291.

[11] D. G. Teer, J. Hampshire, V. Fox, V. Bellido-Gonzalez, Surf. Coat. Technol. 94-95 (1997) 572.

[12] P. D. Fleischauer, ASLE Trans. 27 (1984) 82.

[13] M. N. Gardos, Tribol. Lett. 1 (1995) 67.

[14] J. Moser, F. Levy, Thin Solid Films 228 (1993) 257.

[15] J. Bohlmark, M. Lattemann, J. T. Gudmundsson, A. P. Ehiasarian, Y. randa Gonzalvo, N. Brenning, U. Helmersson, Thin Solid Films 515 (2006) 1522.

[16] S. Kadlec, C. Quaeyhaegens, G. Knuyt, L. M. Stals, Surf. Coat. Technol. 89 (1997) 177.

[17] L. E. Seitzman, R. N. Bolster, I. L. Singer, Thin Solid Films 260 (1995) 143.

[18] K. Weiss, J. M. Phillips, Phys. Rev. B 14 (1976) 5392.

[19] J. Moser, F. Levy, F. Bussy, J. Vac. Sci. Technol. A 12 (1994) 494.

[20] D. L. Smith, Thin Film Deposition, McGraw-Hill, Boston, MA, 1995, pp. 119-136.

[21] Th. Baldinger, E. Bechtold, Surf. Sci. 159 (1985) 406.

[22] D. C. Sorescu, D. S. Sholl, A. V. Cugini, J. Phys. Chem. B 108 (2004) 239.

[23] J. Moser, H. Liao, F. Levy, J. Phys. D:Appl. Phys. 23 (1990) 624.

[24] M. A. Lieberman and A. J. Lichtenberg, Principles of Plasma Discharges and Materials Processing, John Wiley & Sons, New York, 1994, pp. 11-12.

[25] J. W. Coburn, E. Kay, J. Vac. Sci. Technol. 43 (1972) 4965.

[26] Y. Yamamura, H. Tawara, Atomic Data and Nuclear Data Tables 62 (1996) 149.

[27] W. Lauwerens, J. Wang, J. Navratil, E. Wieers, J. D'haen, L. M. Stals, J. P. Celis, Y. Bruynseraede, Surf. Coat. Technol. 131 (2000) 216.

[28] J. Moser, F. Levy, J. Mater. Res. 8 (1993) 206.

List of figure captions

Figure 1: Schematic of the filtered vacuum arc/magnetron sputtering processing chamber.

Figure 2: Selected target voltage waveforms with nominal values of a) 85 kHz with a 1.2 μs reverse time (90% duty), b) 85 kHz with a 5.0 μs reverse time (58% duty), c)100 kHz with a 1.0 μs reverse time (90% duty), and d) 200 kHz with a 0.5 μs reverse time (90% duty). The nominal and actual duty factors are shown on each voltage trace

Figure 3: Ion energy distributions collected during a) dc MoS_2 deposition, b) deposition at 85 kHz and 1.2 μs reverse time (90% duty), and c) deposition at 100 kHz and 1.0 μs reverse time (90% duty). The maximum ion energy is indicated on each IED.

Figure 4: Bragg-Brentano X-ray diffractograms for MoS_2 coatings deposited at a) 85 kHz with a 1.2 μs reverse time (90% duty), b) 100 kHz with a 1.0 μs reverse time and (90% duty) c)85 kHz with a 5.0 μs reverse time (58% duty).

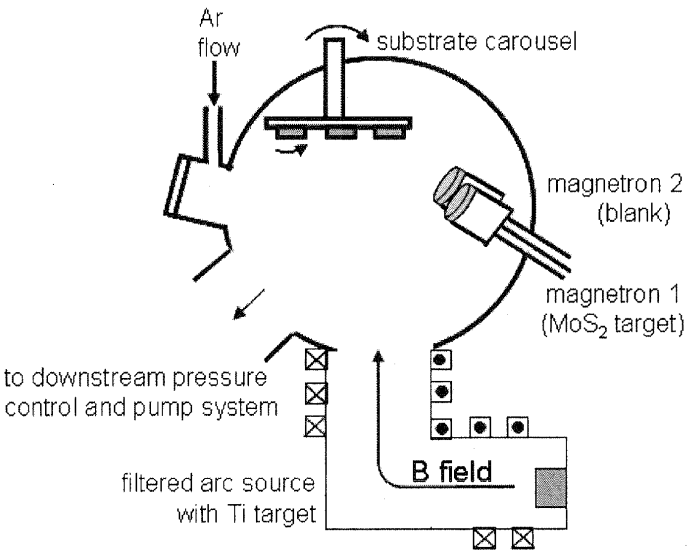
Figure 5: A plot of the (002)/(100) orientation ratio versus deposition rate. The line connecting the points was added to guide the eye.

Figure 6: Friction traces obtained in a air with controlled 40% relative humidity for MoS_2 coatings deposited at a) 85 kHz with a 1.2 μs reverse time (90% duty), b) 100 kHz with a 1.0 μs reverse time (90% duty) and c)85 kHz with a 5.0 μs reverse time (58% duty).

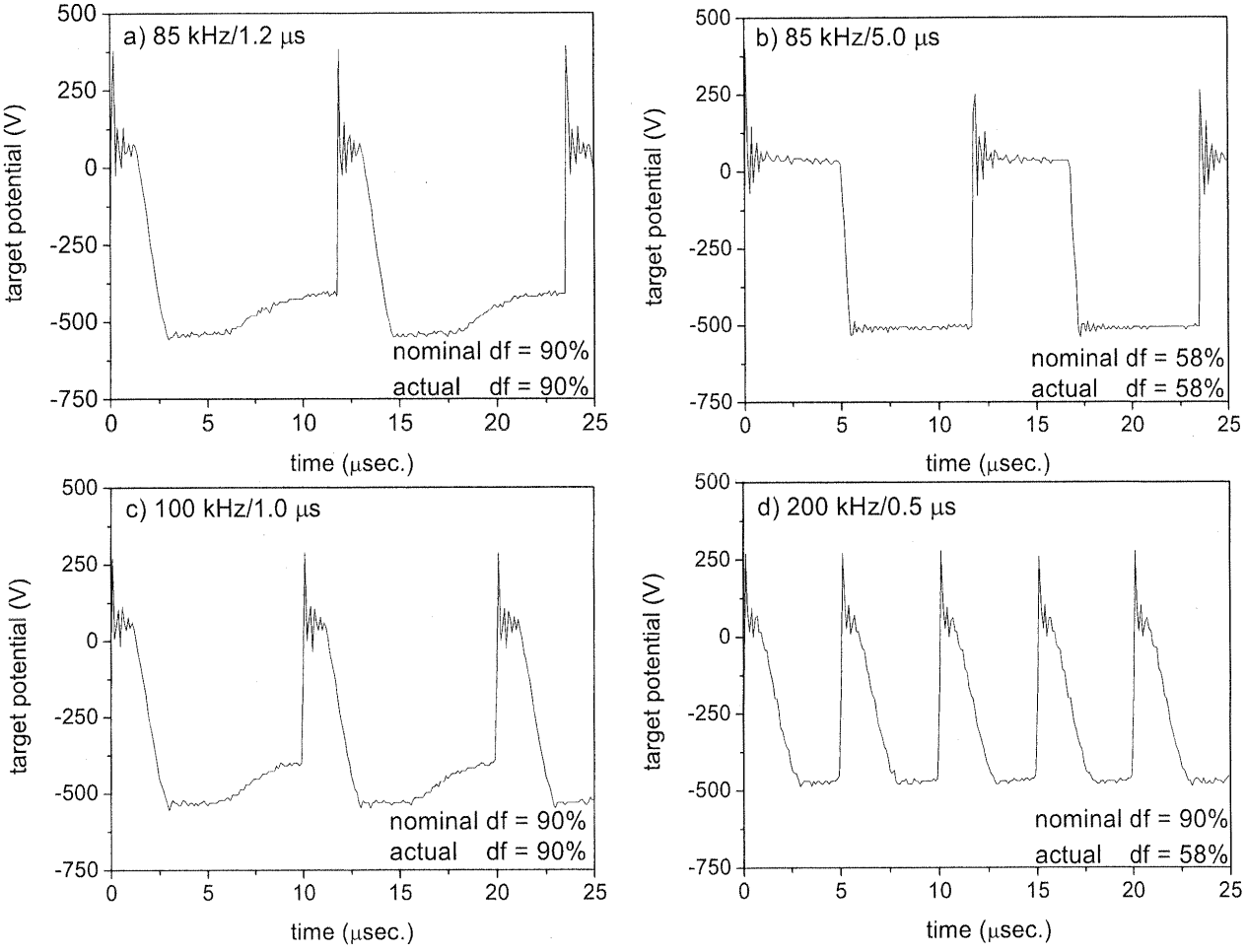
Table I: Summary of processing parameters, deposition rates, orientation ratios and tribological performance for all coatings.

frequency (kHz)	reverse time (μs)	nominal duty factor (%)	actual duty factor (%)	measured growth rate (nm min^{-1}) ± 0.6	(002)/(100) ratio (%) ± 0.2	average friction coefficient	cycles to failure (#)
85	5	58	58	5.0	0.0	0.55	2,500
200	0.5	90	58	5.4	0.0	0.55	1,000
100	1	90	90	12.0	2.1	0.30	<10000
85	1.2	90	90	13.0	4.8	0.23	>20,000
75	1.3	90	90	13.4	4.7	0.24	>20,000
0	0	100	100	19.6	4.4	0.21	<10000

Muratore et. al
Figure 1

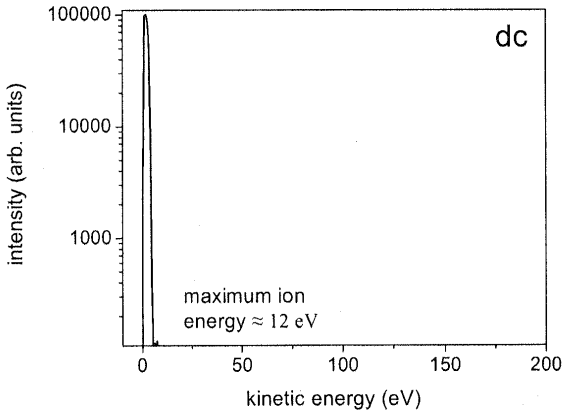


Muratore et. al
Figure 2

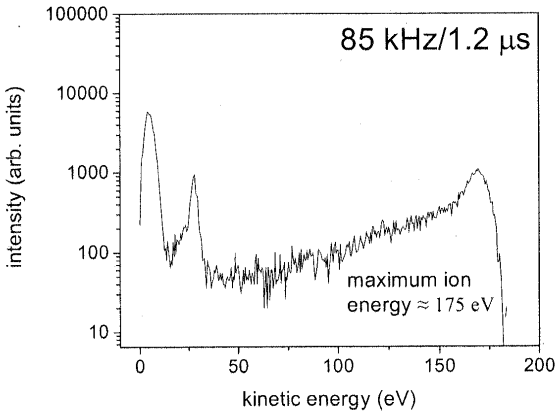


Muratore et. al
Figure 3

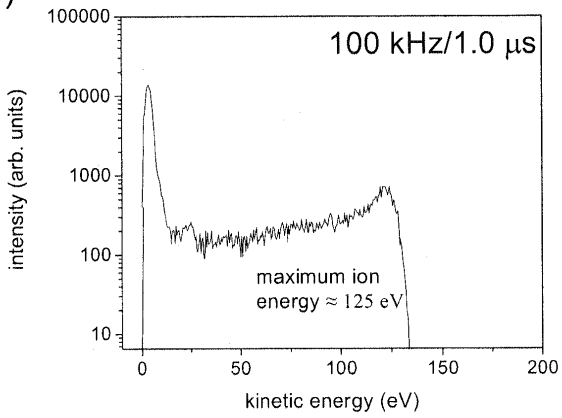
a)



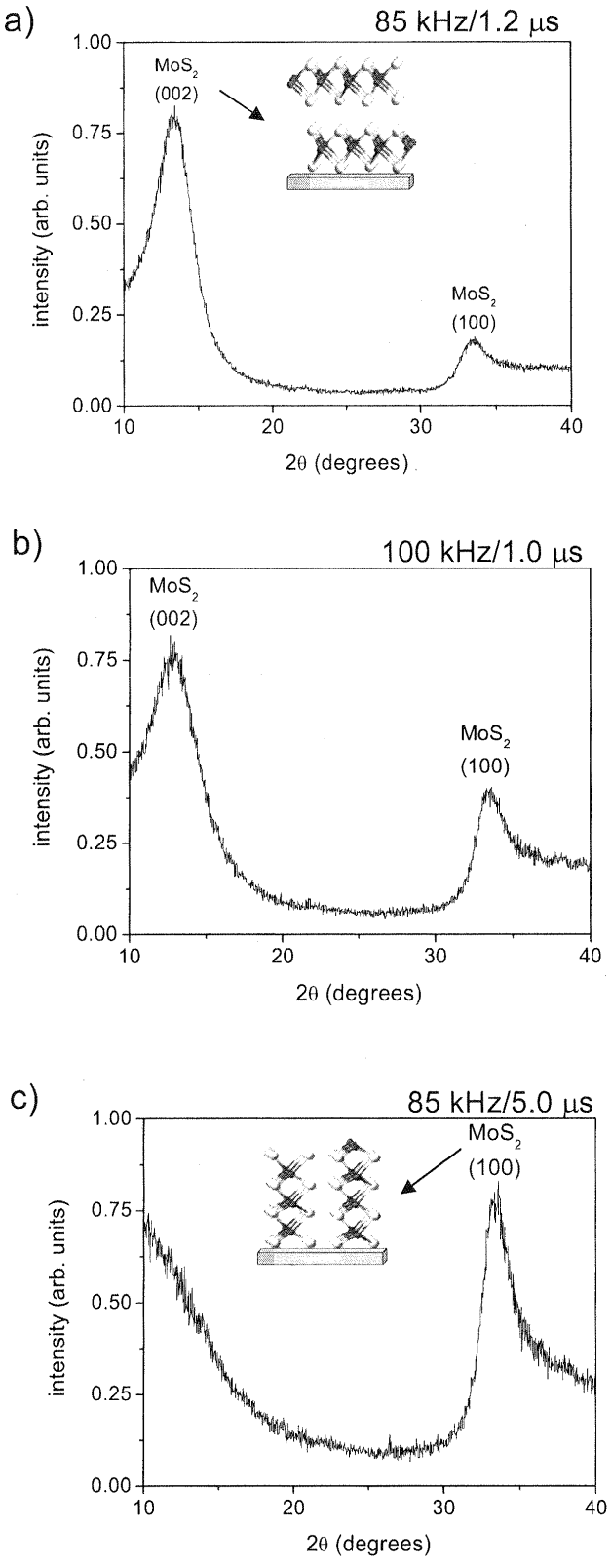
b)



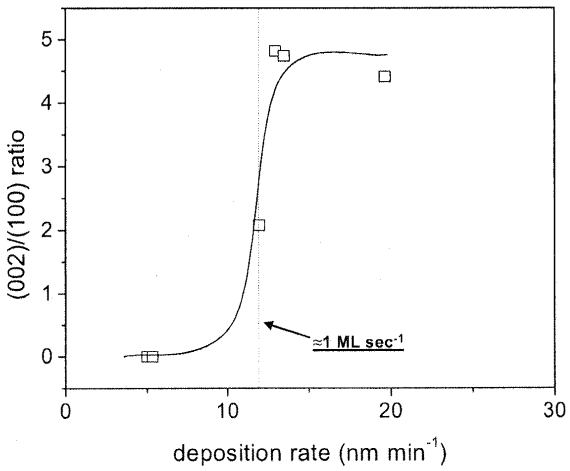
c)



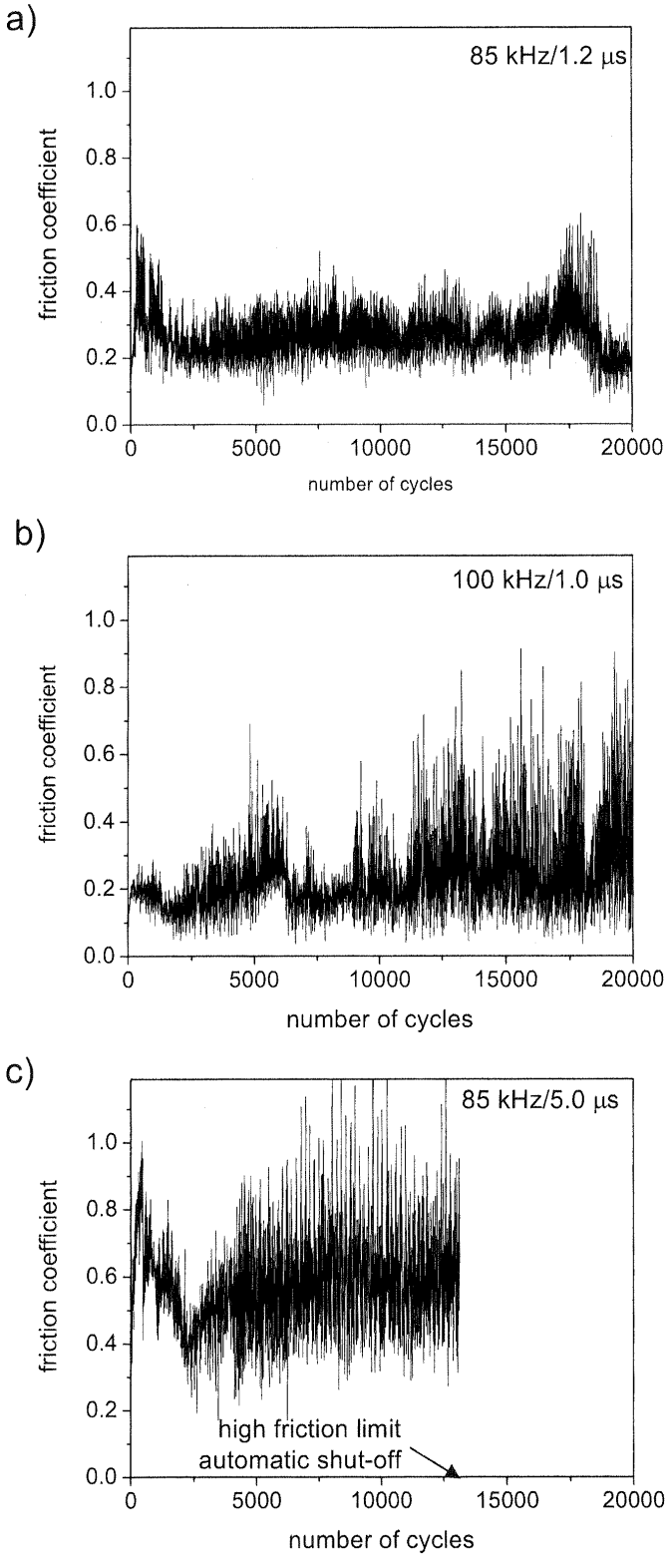
Muratore et. al
Figure 4



Muratore et. al
Figure 5



Muratore et. al
Figure 6



Paper 9

TSINGHUA SCIENCE AND TECHNOLOGY
ISSN 1007-0214 02/11 pp665-679
Volume 10, Number 6, December 2005

Recent Advances in Hard, Tough, and Low Friction Nanocomposite Coatings

A. A. Voevodin**, J. S. Zabinski, C. Muratore

Air Force Research Laboratory, Materials and Manufacturing Directorate, Wright-Patterson AFB, Ohio, USA

Abstract: Nanocomposite coatings demonstrate improved friction and wear responses under severe sliding conditions in extreme environments. This paper provides a review how thin film multilayers and nanocomposites result in hard, tough, low-friction coatings. Approaches to couple multilayered and nanocomposite materials with other surface engineering strategies to achieve higher levels of performance in a variety of tribological applications are also discussed. Encapsulating lubricious phases in hard nanocomposite matrices is one approach that is discussed in detail. Results from state-of-the-art "chameleon" nanocomposites that exhibit reversible adaptability to ambient humidity or temperature are presented.

Key words: nanocomposite coatings; thin film multilayers; tribological coating

Introduction

The clear and intimate relationship between hardness and wear[1-3] has caused the scientific and engineering community to pursue the development of increasingly harder coatings. Wear of materials, however, depends on many other factors, including elastic modulus, fracture toughness, friction, and micro/nano contact geometry (Fig. 1). For the most part, the quest for wear-resistant materials has only recently included considerable effort on these other avenues to reduce wear. Additionally, as the diversity of applications for coatings grows (e.g., automotive and aerospace), so does the range of environments in which they operate. Typically, a material provides its best tribological performance in a limited range of environments. A good example is the behavior of MoS_2, which performs quite well in space, but fails much more quickly in moist terrestrial environments. A significant challenge is to blend together hardness, low friction, and toughness in a coating such that low wear is realized in diverse environments (e.g., hot, cold, wet, dry, and vacuum).

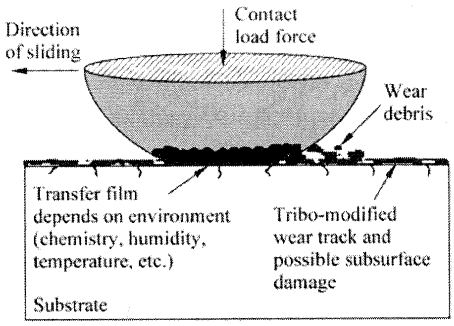


Fig. 1 Schematic representation of a sliding tribological coating.

Thin film coating deposition has undergone tremendous advances and it is now possible to grow multilayered, functionally gradient, and nanocomposite coatings that have impressive properties. Nanostructured designs have the flexibility to impart lubricity over many environments, yet maintain hardness, and dramatically increase toughness.

Received: 2005-05-19

** To whom correspondence should be addressed.
E-mail: Andrey.Voevodin@wpafb.af.mil

The purpose of this paper is to highlight recent developments in tribological coating designs incorporating functional gradients and nanostructures where these features are employed to provide exceptional properties. Special attention is given to the synergism among friction coefficient, hardness, and fracture toughness. These are important for coating performance in terms of wear reduction and reliability, but have not been the focus of most available reviews.

1 New Directions in Hard Coatings

As mentioned in the introduction, there are a number of good reviews on hard coatings that have been published lately. Monolithic coatings of transition metal carbides/nitrides and oxides dominate the literature[1,2]; however, attention has recently been focused on moving away from monolithic coatings to duplex, functionally gradient, multilayer, and nanocomposite coating architectures to improve overall friction and wear response. Work on increasing the hardness of coatings through multilayer and nanocomposite approaches has been recently reviewed in detail, as discussed below. The remainder of this paper is devoted to briefly discussing "hardening" approaches and then focusing on coating architectures that improve toughness and lower friction.

1.1 Methods to increase hardness: Multilayer coatings

Research on using nanoscale multilayers to increase the hardness and toughness of coatings has provided significant advancements.

Early research by Palatnik with multilayers of metals showed that significant improvements in strength were achieved when layer thickness was decreased below 500 nm[4,5]. In early modeling, Koehler[6] predicted that high shear strength coatings could be produced by alternating layers of high and low elastic modulus. Key elements of the concept are that very thin layers inhibit dislocation formation and differences in elastic modulus between layers inhibits dislocation mobility. Lehoczky demonstrated these concepts on Al-Cu and Al-Ag multilayers and showed that a Hall-Petch type equation could be used to relate hardness to $1/\sqrt{\text{periodicity}}$. Springer and Catlett[7], and Movchan et al.[8] reported on mechanical enhancements in metal/ceramic and ceramic/ceramic laminate structures that followed a Hall-Petch relationship. These pioneering works were followed by intensive research in multilayers[9-15], which has produced coatings significantly harder than the individual components making up the layers. To achieve increased hardness, the layers must have sharp interfaces and periodicity in the 5-10 nm range. The multilayer architectures exhibiting high hardness are frequently called superlattices[13]. The different design architectures have been classified and some reports have formalized multilayer design[16-18].

Multilayer architectures clearly increase coating hardness and have commercial application, especially in the tool industry. However, they can be difficult to apply with uniform thickness on three-dimensional components and rough surfaces. If the layers are not of the correct periodicity, the superlattice effect is lost. Another relatively new technology, nanocomposites, offers the same advantages as multilayers (plus has other benefits) and their properties are not critically dependent on thickness or substrate geometry.

1.2 Nanocomposites

Using similar ideas for restricting dislocation formation and mobility as were used in multilayer approaches to "hardening", nanocomposite coatings can also be superhard[19-25]. These composites have 3-10 nm crystalline grains embedded in an amorphous matrix and the grains are separated by 1-3 nm. This design lead to ultra-hard (hardness above 100 GPa) coatings reported by Veprek and co-authors most recently[26,27]. The nanocrystalline phase may be selected from the nitrides, carbides, borides, and oxides, while the amorphous phase may also include metals and diamond-like carbon (DLC) as shown in Fig. 2. These reports suggest that the nanocrystals should have strong interaction with the matrix phase to impart super-hardness.

There are many different nanocrystalline grain/amorphous matrix systems that exhibit superhardness including: TiN/a-Si_3N_4[19,28,29], W_2N/a-Si_3N_4[20,30], VN/a-Si_3N_4[20,30], TiN/c-BN[20,30], TiN/a-(TiB_2+TiB+B_2O_3), TiN/TiB_2[31], TiC/TiB_2[32], TiN/Ni[33], ZrN/Cu[34], ZrN/Y[35], TiAlN/AlN[36], CrN/Ni[23], Mo_2C/a-(carbon+Mo_2N)[37], TiC/DLC[38,39], and WC/DLC[40,41]. Among carbon matrix systems, only hydrogen free DLC coatings were harder than 30-40 GPa[38-41], which

approaches that of ceramic-matrix composites (60-100 GPa)[19,20,22].

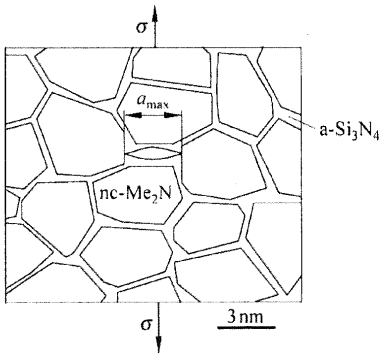


Fig. 2 Schematic design of a super-hard composite coating, combining amorphous and nanocrystalline phases, showing restrictions in the initial crack size and crack propagation. Reproduced from Veprek[30].

The initial model proposed by Veprek to explain hardness in nanocomposites is that dislocation operation is suppressed in small grains (3-5 nm) and that the narrow space between them (1 nm separation) induces incoherence strains[19,20,22]. The incoherence strain is likely increased, when grain orientations are close enough to provide interaction between matched but slightly misoriented atomic planes. In the most recent work by the same author[22], the contribution of coherency strain was dismissed leaving dislocation suppression and crack size reduction as the prime hardness enhancing factors. Without characterization of the stress/structure on a nanoscopic level, it is difficult to verify coherency strain contributions. The coating residual compressive stress (<1 GPa) is relatively small and cannot explain the super hardness effect. In the absence of dislocation activity, Griffith's equation for crack opening was proposed as a simple description of the composite strength, σ[42]:

$$\sigma = \left(\frac{4E\gamma_s}{\pi a} \right)^{1/2} \quad (1)$$

where E is elastic modulus, γ_s is surface energy of the grain/matrix interface, and a is initial crack size, which was accepted to be equal to the average diameter of the grains[30]. This equation suggests that strength can be increased by increasing elastic modulus and surface energy of the combined phases, and by decreasing the crystalline grain sizes. It is noted that elastic modulus is inversely dependent on grain sizes that are in the nm size range due to lattice incoherence strains and the high volume of grain boundaries. In practice, grain boundary defects always exist, and a 3-nm grain size was found to be close to the minimum limit. Below this limit, a reverse Hall-Petch effect has been observed and the strengthening effect disappears because grain boundaries and grains become indistinguishable and the stability of the nanocrystalline phase is greatly reduced [12,13,19,20,43,44].

Nanocomposites with metal matrixes are in a special category for this discussion. They have been demonstrated to increase hardness, but also have good potential for increasing toughness. Mechanisms for toughening within these systems are discussed in the next section, while mechanisms for hardening are discussed here. Irie[33] and Musil[34-36] have recently reported that nanocomposites composed of hard nitride grains and softer metal matrixes exhibit increased hardness, which they relate to coating nanostructure. In a recent review, Veprek has questioned some of these reports and suggested that residual stress and not nanostructure may be responsible for apparent increases in hardness[22].

The composite strength of metal/ceramic nanocomposites may be described by the following form of the Griffith-Orovan model[42] when the dimensions of the metal matrix permit operation of dislocations:

$$\sigma = \left(\frac{4E(\gamma_s + \gamma_p)}{\pi a} \frac{r_{tip}}{3d_a} \right)^{1/2} \quad (2)$$

where γ_p is the work of plastic deformation, r_{tip} is the curvature of the crack tip, and d_a is the interatomic distance. It is noted that crack tip blunting and the work of plastic deformation considerably improve material strength, while the lower elastic moduli of metals causes a reduction in strength as compared to ceramics. However, in nanocomposites, dislocation operation may be prohibited because the separation of grains is very small. For example, the critical dimension, D, for a Frank-Read dislocation source is[42]:

$$D = Gb\tau^{-1} \quad (3)$$

where G is the modulus of rigidity approximated by the expression for Young modulus and Poisson ratio, $G=E(2+2\nu)^{-1}$, b is the Burgers displacement, and τ is shear stress. For a shear stress of 1 GPa, the critical size of Frank-Read source operation is 7.4 nm for a Cu matrix (E=110 GPa, ν=0.34, b=0.181 nm) and 14.1 nm for a Ni matrix (E=210 GPa, ν=0.31, b=0.176 nm).

While 1 GPa is not unrealistic, smaller stresses such as in lubricated contacts would require larger grain sizes for dislocation source operation. Matrix dimensions in hard nanocomposite coatings are typically between 1-3 nm, which is well below the critical size for dislocation source operation, even in very soft metal matrixes. Therefore, the mechanical behavior of such composites can be expected to be similar to that of ceramic matrix composites[34].

Composite designs that increase elastic modulus and hardness, do not necessarily impart high toughness. First, dislocation mechanisms of deformation are prohibited and crack opening is the predominant mechanism for strain relaxation when stresses exceed the strength limit. Second, Griffith's equation does not take into account the energy balance of a moving crack, which consists of the energy required to break bonds and overcome friction losses, potential energy released by crack opening, and kinetic energy gained through crack motion[45]. From crack energy considerations, a high amount of stored stress (in-plane compressive and possible incoherence between adjusted grains) dictates a high rate of potential energy release in the moving crack. In such conditions, a crack can achieve the self-propagating (energetically self-supporting) stage sooner, transferring into a macrocrack and causing brittle fracture. However, nanocomposites contain a high volume of grain boundaries between crystalline and amorphous phases. This type of structure limits initial crack sizes and helps to deflect, split, and terminate growing cracks. Mechanisms to increase the fracture toughness of wear resistant coatings are discussed in the following section.

2 New Directions for Tough Wear Protective Coatings

While superhard coatings are very important, quite notably for protection of cutting tools, most tribological applications for coatings either require, or would receive significant benefit from increased toughness and lower friction. In particular, high fracture toughness is necessary for applications where high contact loads and hence, significant substrate deformations, are encountered. A material is generally considered tough if it possesses both high strength and high ductility. High hardness is directly related to high elastic modulus and high yield strength, but it is very challenging to add a measure of ductility to hard coatings. For example, the superhard coating designs discussed earlier prevent dislocation source activity, essentially eliminating one common mechanism for ductility. Therefore, designs that increase ductility through different mechanisms must be explored to create tough tribological coatings.

In addition to ductility, a tough coating must have high elastic modulus and high hardness, as well as permit strain relaxation and crack termination. Combination of these properties in a coating results in high cohesive toughness. It is also important to prevent failure at the coating/substrate interface by increasing interface toughness and adhesion. For effective wear prevention, there are additional requirements related to the normal (load) and tangential (friction) forces. In general terms, a tough wear resistant coating must support high loads in sliding or rolling contact without failure by wear, cohesive fracture, and loss of adhesion (delamination). As discussed in the introduction, a low friction coefficient reduces friction losses and may increase load support capability. The later is clear from the fact that typical coating failures (deformations, cracks, delaminations, etc.) are caused or accelerated by tangential stress, which is proportional to the contact load through the friction coefficient. Finally, chemical, tribochemical, and thermal stability are required to optimize coating performance and lifetime.

Designs for the tough wear protective coatings described below are roughly divided into three categories: multilayers (including nano-layered materials), functional gradients, and nanocomposites. It is duly noted that the multilayer and nanocomposite approaches permit coating strengthening (hardening), which strongly suggests (and will be shown later) that toughness, hardness, and low friction may be combined in a single coating. Each approach has a set of advantages and combination of approaches may yield the best tribological solution.

2.1 Tough multilayer coatings

Toughening concepts based on multilayer architectures were presented in reports by Holleck and co-authors[10,15,46,47]. Their work highlights the importance of dissipating crack energy and deflecting cracks at interfaces in multilayer structures made of hard

ceramic materials, such as TiC/TiB_2 or TiN/(Ti(C,N). Mechanisms for toughening layered ceramic coatings[15] are schematically represented in Fig. 3. These mechanisms include: i) crack splitting at the boundaries of small sized grains, ii) crack deflection at the interface between layers, iii) reduction of stress concentration by interface opening, and iv) plastic deformation at the interface for energy dissipationk and stress relaxation, "nanoplasticity".

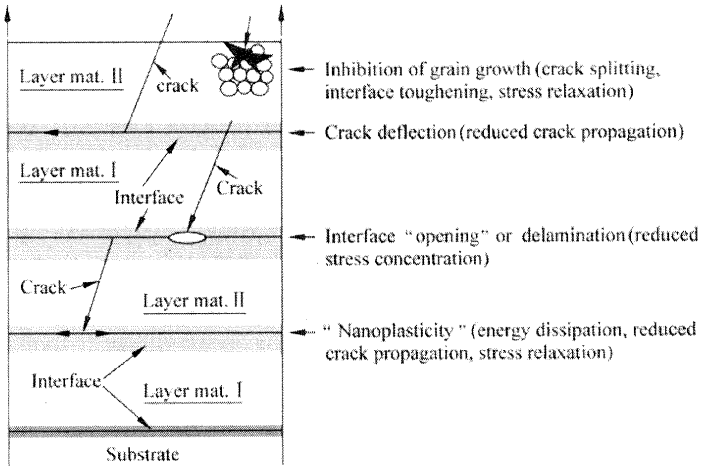


Fig. 3 Mechanisms of toughness enhancement in hard ceramic multilayers. Reproduced from Holleck and Schier[15].

While interfaces in ceramic/ceramic multilayer coatings can deflect cracks and relax stress, they can also initiate brittle fracture. This is especially critical when the adjacent layers have greatly different elastic modulus and chemistry, which causes a sharp change in the stress field across the interface. In the absence of good chemical bonding (adhesion), coating failure is initiated. Depending on the applied stress field and individual layer properties (e.g., elastic modulus, yield strength, residual/induced stress, and thickness), the coating may fail by interfacial crack propagation (shear and tension stress) or buckling (compression stress)[48,49].

2.2 Tough functionally graded coatings

In order to counteract brittle failure and improve fracture toughness, two concepts have been explored. The first involves the use of graded interfaces between the coating and substrate and between layers. For example, a WC-TiC-TiN (outside layer) graded coating for cutting tools was reported by Fella et al. [50], which showed considerably less wear than single layer hard coatings used in the cutting of steels. This type of coating is functionally graded, reflecting the idea of grading chemistry to achieve better adhesion and oxidation resistance, and mechanical properties to improve stress profiles, or other functionality.

One example of how functionally graded architectures improve coating performance is the adhesion of DLC to steels. DLC, and especially hydrogen-free DLC, has a very high hardness and generally has a large residual compressive stress. The coatings are relatively inert, and adhesion failures of coated steel surfaces were a roadblock to success. This problem was solved through designing and implementing graded interfaces between the coating and the substrate. Examples of effective gradient compositions are Ti-TiN-TiCN-TiC-DLC for hydrogenated DLC[51,52] and Ti-TiC-DLC for hydrogen-free DLC[53]. In the development of the later composition, the importance of graded elastic modulus through the substrate coating/interface was highlighted as shown in Fig. 4. The gradual build-up material stiffness from the substrate with E=220 GPa to the DLC layer with E=650 GPa, avoids sharp interfaces that can provide places for crack initiation, provides good chemical continuity, and creates load support for the hard DLC top-coat. The graded coating shown in Fig. 5 did not exhibit any signs of brittle fracture in scratch tests with a 50-N load, which was at least 5 times higher than similar coatings without functionally graded interfaces[53]. The graded approach can be combined with multilayer and

nanocomposite architectures to further enhance tribological properties.

Material	Hardness	Elastic modulus	Thickness
DLC at 10^{-5} Pa	70 GPa	650 GPa	400 nm
DLC at 2×10^{-1} Pa	43 GPa	450 GPa	100 nm
$Ti_{0.10}C_{0.90}$	25 GPa	290 GPa	25 nm
$Ti_{0.25}C_{0.75}$	27 GPa	350 GPa	25 nm
$Ti_{0.30}C_{0.70}$	29 GPa	370 GPa	100 nm
$Ti_{0.50}C_{0.50}$	20 GPa	290 GPa	100 nm
$Ti_{0.70}C_{0.30}$	14 GPa	230 GPa	100 nm
$Ti_{0.90}C_{0.10}$	6 GPa	150 GPa	50 nm
α-Ti	4 GPa	140 GPa	50 nm
440C steel	11 GPa	220 GPa	

Fig. 4 Design of a functionally gradient Ti-TiC_x-DLC coating, where chemistry and elastic modules are transitioned from metallic substrate to hard DLC top layer[53].

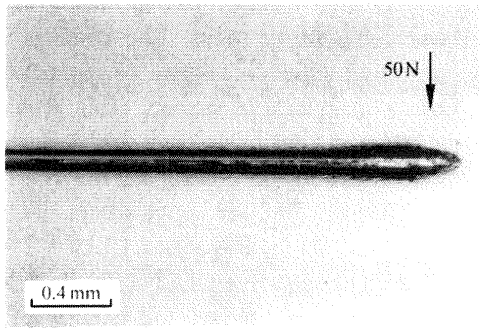


Fig. 5 Scratch produced on the surface of a functionally gradient Ti-TiC_x-DLC coating by a diamond stylus under 50 N load. The absence of cracks demonstrates that the coating has excellent toughness[53].

An effective route for improving toughness in multilayers is the introduction of ductile, low elastic modulus layers into the coating structure to relieve stress and allow crack energy dissipation by plastic deformation in the crack tip. This approach will result in a decreased coating hardness, but the gain in the fracture toughness improvement may be more important in many tribological applications, excluding coatings for the cutting tool industry. For example, $[Ti/TiN]_n$ multilayer coatings on cast iron piston rings relaxed interface stress and improved combustion engine performance[54]. Figure 6a shows a schematic of a multilayer $[Ti/DLC]_n$ coating on a graded load support foundation, where the ductile Ti layers in the multilayer stack were graded at every DLC interface to avoid brittle fracture[18]. A cross-sectional photograph of this coating with 20 [Ti/DLC] pairs is shown in Fig. 6b. The ductile Ti layers reduced the composite coating hardness to 20 GPa as compared to a single layer DLC coating, which has a hardness of about 60 GPa. However, due to dramatic improvements in toughness the multilayer coating design permitted operation during sliding friction at contact pressures as

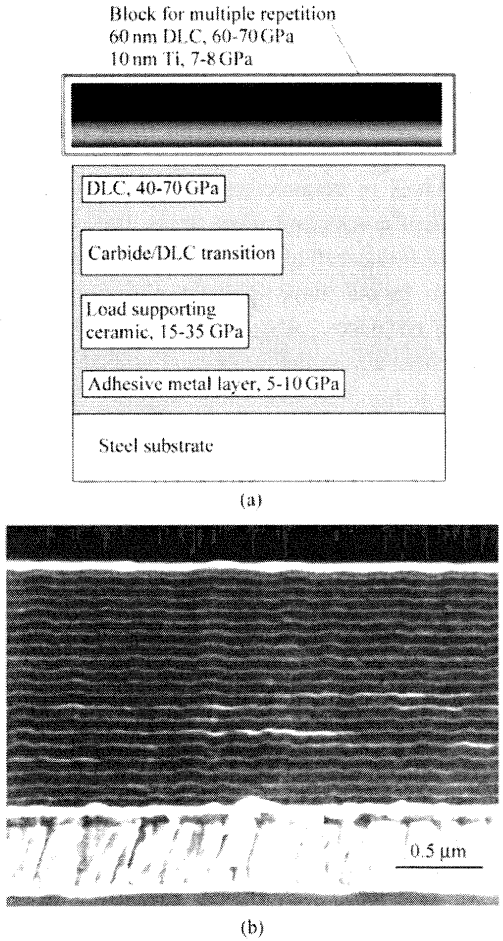


Fig. 6 A multilayer coating with multiple Ti/DLC pairs on top of a functionally gradient layer for an optimum combination of cohesive and adhesive toughness: (a) design schematic; (b) cross sectional photograph of the coating produced with 20 Ti/DLC pairs[18].

high as 2 GPa without fracture failure compared to 0.6-0.8 GPa for single layer DLC.

In general, the combination of multilayer and functionally gradient approaches in the design of wear protective coatings produces exceptionally tough wear protective coatings for engineering applications. One potential drawback slowing the wide spread use of new coatings was the need for reliable process controls to ensure that the correct compositions, structures, and properties are implemented during growth. However, modern process instrumentation and control technologies are able to meet the challenge and permit successful commercialization, e.g., see Ref. [55] for a review of reactive sputtering control methods during multilayer growth. Thus, functional gradient and multilayer designs are commonly utilized in the production of modern tribological coatings.

2.3 Tough nanocomposite coatings

An alternative to employing multilayers to toughen coatings is embedding grains of a hard, high yield strength phase into a softer matrix allowing for high ductility. This approach has been widely explored in macro-composites made of ceramics and metals which are known as cermets[34]. It was recently scaled down to the nanometer level in thin films made of hard nitrides and softer metal matrixes[16-19].

When grain sizes in such composites are reduced to a nanometer level, dislocation activity as a source of ductility is eliminated. However, these types of composites contain a high volume of grain boundaries with a crystalline/amorphous transition across grain-matrix interfaces, limiting initial crack sizes and helping to deflect and terminate growing cracks. These mechanisms may explain the brittle resistance of novel superhard composites[21,22]. In single phase nanocrystalline systems, grain boundary diffusion[56] and grain boundary sliding[56-60] were suggested to improve ductility and provide super-plasticity. The most recent research indicates that high ductility can be more easily achieved in multiphase structures[61] and that grain boundary sliding is a primary mechanism of superplasticity[62-65]. It was also found that equiaxial grain shapes, high angle grain boundaries, low surface energy, and the presence of an amorphous boundary phase facilitate grain boundary sliding[56,57]. These findings were expanded into the field of hard wear resistant coatings to introduce ductility and prevent fracture under a high contact load.

In the course of the development of tough nanocomposite coatings, the following design concepts were formulated:

1) A graded interface layer is applied between the substrate and crystalline/amorphous composite coating to enhance adhesion strength and relieve stresses (combination of functional gradient and nanocomposite design)[18,52,53];

2) Encapsulation of 3-10 nm sized hard crystalline grains in an amorphous matrix restricts dislocation activity, diverts and arrests macro-crack development, and maintains a high level of hardness similar to superhard coating designs[21,24];

3) A large volume fraction of grain boundaries provides ductility through grain boundary sliding and nano-cracking along grain/matrix interfaces[21,32,66-68].

The primary differences between superhard and tough coating designs are selection of a matrix phase with a lower elastic modulus, relaxation of the requirement for strong binding between matrix and grains, and selection from a greater range of acceptable grain sizes of nanocrystalline phase in tough coatings.

Combination of the nanocrystalline/amorphous designs with a functionally graded interface, as shown in Fig. 7, provides high cohesive toughness and high interface (adhesive) toughness in a single coating. Several examples of tough wear resistant composite coatings have been reported. Two of them combined nanocrystalline carbides with an amorphous DLC matrix designated as TiC/DLC and WC/DLC composites. In another example, nanocrystalline yttrium stablized ZrO_2 (YSZ) grains were encapsulated in a

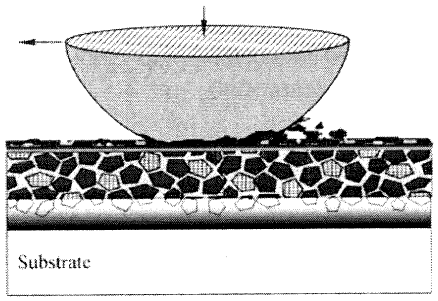


Fig. 7 Schematic of a tough nanocomposite coating, featuring a noncrystalline/amorphous design in the main coating layer for cohesive toughness and a functionally gradient interface layer for adhesive toughness.

mixed YSZ-Au amorphous matrix as shown in Fig. 8. In all cases, the large fraction of grain boundary phase provided ductility by activating grain boundary slip and crack termination by nanocrack splitting. This provided a unique combination of high hardness and toughness in these coatings. Figure 9 compares Vickers indentations made at the highest load of the machine. There are no observable cracks in these coatings, even after significant substrate compliance (indentation marks are 9 μm deep into 1 μm thick coatings). The coating hardness was quite high ranging from 18 to 30 GPa, and for most hard coatings at these loads, cracks in the corners of the indentations are expected.

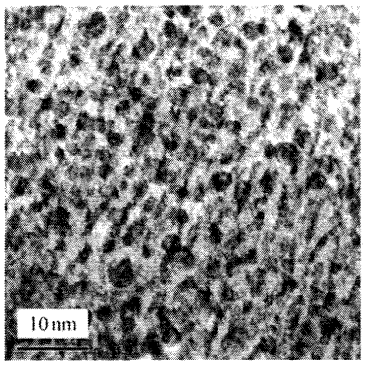


Fig. 8 TEM image of a YSZ/Au nanocomposite coating with improved toughness characteristics[68].

Thus, novel nanocomposite designs for tough tribological coatings are very promising and provide a very attractive alternative to multilayer architectures. Nanocomposite coatings are more easily implemented, since they do not require precise control in the layer thickness and frequent cycling of the deposition parameters, as is required for fabrication of multilayer coatings. They are however relatively recent developments, and suitable scale-up of deposition techniques is currently under intense study.

2.4 Hard, tough, and low friction "chameleon" nanocomposites

Composite coating designs provide a convenient way to implement the combination of high hardness, toughness, and low friction into a single coating. The possibility of mixing hard and lubricious phases in thin nanocomposite coatings has been explored in recent years. Reports on producing TiN/MoS_2 composites by chemical vapor deposition[69,70], and TiB_2/MoS_2, TiB_2/C, and TiN/MoS_2 composites by magnetron sputtering[71-73], demonstrate that low friction can be imparted to hard ceramic coatings. Most recently, WC/DLC/WS_2 and YSZ/Au/DLC/MoS_2 composites produced by a hybrid of laser ablation and magnetron sputtering were shown to have exceptional toughness and provide low friction across dry, vacuum, moist, and high temperature environments[67,74].

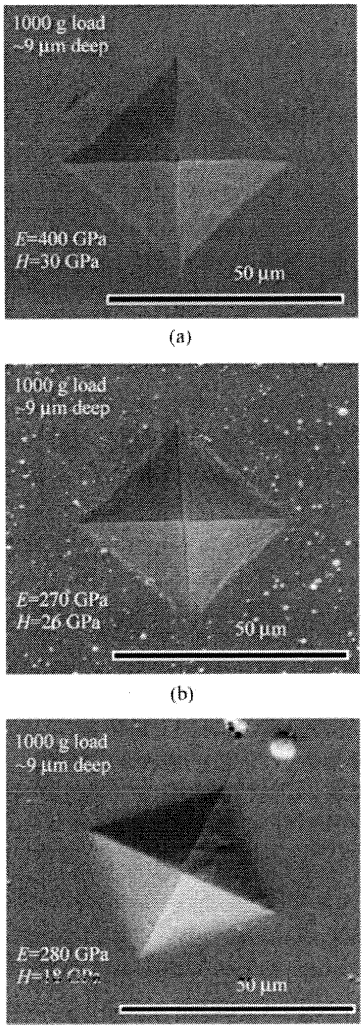


Fig. 9 Vickers indentation marks on the surface of 1 μm thick a) TiC/DLC, b) WC/DLC, and c) YSZ/Au tough nanocomposite coatings. Indents were performed with the maximum available load of 1000 g, providing about 9 μm indentation depth due to the deformation of the steel substrate. Note that there were no cracks at the indention corners, which serve as stress risers.

The tough TiC/DLC and WC/DLC composites

discussed above demonstrated low friction and wear in ambient environment tests[66,75]. In these composites, a hydrogen-free DLC matrix was used to encapsulate carbide nanocrystals. The use of a DLC matrix in long duration aerospace applications may create a problem due to the graphitization of DLC in friction contacts and an associated increase in friction coefficient in high vacuum[76,77]. An alternative approach is to incorporate dichalcogenide space lubricants, such as MoS_2 or WS_2, into the composite coating. One very effective design included formation of MoS_2 reservoirs within a TiC/DLC nanocomposite by laser milling the hard phase and filling with sputtered MoS_2[78], which showed the benefit of the DLC/MoS_2 combination for lubrication in a variable humid/dry environments.

Reduction of the individual phase sizes in the composite coating to few nanometers offered the unique opportunity to design adaptive or smart tribological coatings, which were termed "chameleon" for their ability to resist friction and wear by changing surface chemistry and microstructure in response to environmental and loading variations, much like a chameleon changes its skin color to avoid predators.

The first advancements in adaptive coatings were made using a mix of oxides and dichalcogenides (PbO/MoS_2, Sb_2O_3/MoS_2, and ZnO/WS_2), which could operate in a broad range of temperatures[79-81]. Advanced multilayer structures were then designed to combine these composites with buried diffusion barrier layers and achieve surface self-adaptation during repeated temperature cycling. Recently, novel wear resistant materials were developed, which combine nanocrystalline carbides (TiC, WC), oxide-based ceramics (YSZ and AlON), dichalcogenides (MoS_2 and WS_2), and amorphous DLC into nano-composite structures[67,74,82]. The Rockwell C indentation marks on the surface of TiC/DLC and WC/DLC nanocomposite coatings are shown in Fig. 10. The critical load as a function of carbon content in the TiC/DLC is shown in Fig. 11. The surface chemistry, structure, and mechanical behavior of these nanocomposite materials were shown to reversibly change in the tribological contact, depending on applied loads and operational environment to maintain low friction and prevent wear.

In order to achieve reversible adaptation, the following design concepts should be fulfilled and combined with the concepts of tough nanocomposites described above:

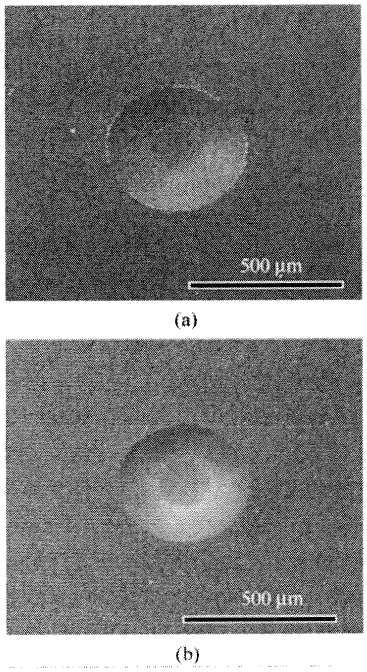


Fig. 10 Rockwell C indentation marks on the surface of 1 μm thick (a) TiC/DLC, and (b) WC/DLC nanocomposite coatings. Indents were performed with the maximum available load of 150 kg, providing about 150 μm indentation depth due to the deformation of the steel substrate. These hard coatings (25-30 GPa) have a very high toughness as demonstrated by the absence of cracks and delaminations.

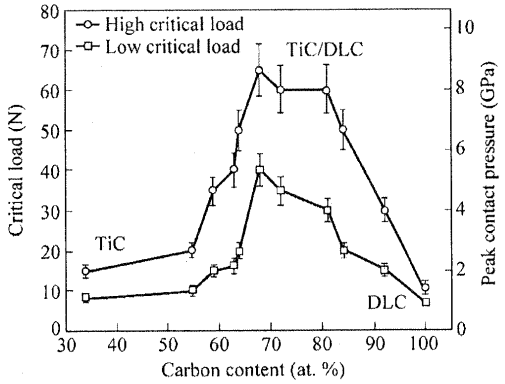


Fig. 11 Effect of the TiC/DLC coating composition on its contact toughness estimated by measuring lower (on-set of cracking) and upper critical loads (adhesive failure) in scratch tests with a 0.2-mm radius diamond stylus under a gradually increasing normal load[66].

1) Solid lubricant reservoirs are introduced as amorphous or poorly crystalline inclusions to minimize reduction in composite hardness and elastic modulus,

since crystalline solid lubricants are typically very soft[67,83];

2) Friction forces and surface reactions with the environment are used to generate a lubricious transfer film or "skin" at the tribological contact, which can self-adjust with each environmental change[67,83]; i.e., coating components serve as reservoirs to supply material for the "tribo-skin", where formation of a lubricating film with the required chemistry and structure reduces friction.

Figure 12 presents a schematic of a nanocomposite coating design that exhibits "chameleon" behavior. This design was implemented in the fabrication of the YSZ/Au/DLC/MoS_2 and WC/DLC/WS_2 "chameleon" coatings where an amorphous matrix and a hard nanocrystalline phase (e.g., YSZ or WC) were used to produce optimum mechanical performance and load support. Nanocrystalline and amorphous Au, MoS_2, and DLC were added to achieve chemical and structural adjustment of transfer films formed in friction contacts during dry/humid environment and low/high temperature cycling. "Chameleon" behavior is observed during the following sequence. As deposited, all lubricant phases (WS_2 or MoS_2, DLC, soft metals, and oxides) are either amorphous or poorly crystalline and are buried in the coating where they are sealed from the environment. When sliding commences, wear processes expose the surface components to the environment, and stress and frictional heat cause changes in chemistry and structure. In low temperature humid environments, a graphitic-like transfer layer is formed by an $sp^3 \rightarrow sp^2$ phase transition of the DLC component, which eventually leads to the formation of some crystalline graphite. This layer provides a low friction coefficient (i.e., 0.10-0.15) and significantly reduces further wear. In humid environments, formation of MoS_2 or WS_2 transfer layers is not favorable, due to their relatively high friction coefficient. Those phases also have a high wear rate and become concentrated in the wear debris as the graphite-like transfer film forms. When the environment changes to dry (N_2 or air) or vacuum and the temperature remains low, a WS_2 or MoS_2 transfer layer is formed by an amorphous $\rightarrow$ crystalline transformation of dichalcogenide inclusions. Rubbing orients the crystalline material such that the low friction basal plane is parallel to the surface. This provides friction coefficients as low as 0.01, reducing further wear of the composite coating. Graphite from a previous cycle in humid air is removed or covered over in the first several hundred cycles in dry conditions due to its high friction/wear in the absence of intercalation by water molecules. As an example of performance in cycling humidity, Fig. 13 shows that the process repeats itself for YSZ/Au/DLC/MoS_2, providing a corresponding switch in tribofilm chemistry and friction response between DLC in humid and MoS_2 in dry conditions.

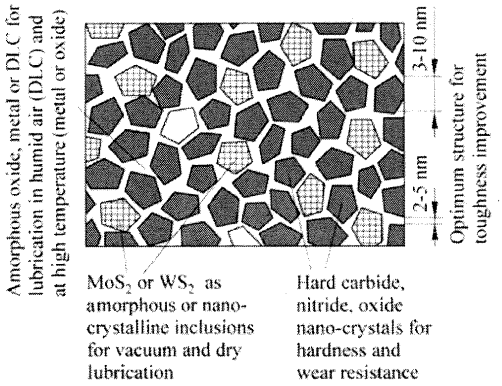


Fig. 12 Schematic of a conceptual design for a nanocomposite tribological coating with chameleon-like surface adaptive behavior.

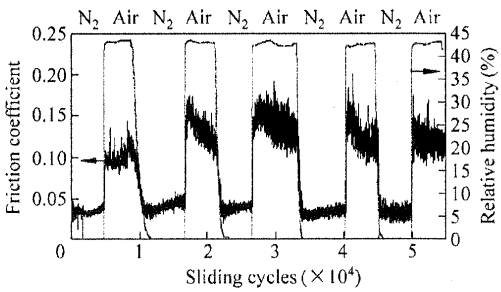


Fig. 13 Friction coefficient variation of a "chameleon" YSZ/Au/MoS_2/DLC coating in a test with cycled relative humidity. Friction response is repeatedly switching from lubrication provided by MoS_2 in dry environments to lubrication provided by DLC in moist conditions[74].

2.5 "Chameleon" nanocomposite coatings for high temperature

Addition of gold in the composition of the discussed above YSZ/Au/DLC/MoS_2 nanocomposite coatings was targeting a high temperature lubrication ability. In high temperature environments (above 500 $^{\circ}$C), diffusion of soft metal from the coating to the surface and

subsequent crystallization occurs. For YSZ/Au/DLC/MoS_2 coatings, this resulted in the formation of an easy-to-shear gold transfer film for high temperature lubrication with a friction coefficient of about 0.2[74]. When temperature is cycled back to 25℃, the friction coefficient stays at about the same level.

YSZ/Ag/Mo and YSZ/Ag/Mo/MoS_2 coatings were also produced to provide low friction through adaptation to temperatures between 25-700℃ in humid air. Figure 14a shows wear test results for a 2-μm thick, monolithic YSZ/Ag/Mo material, and for a multilayer film composed of two 1-μm layers of the same YSZ/Ag/Mo material separated by a TiN diffusion barrier. The monolithic YSZ film containing 24 at.% Ag and 10 at.% Mo exhibited a friction coefficient of about 0.4 for all temperatures (Fig. 14b). By adding 8% MoS_2 to the monolithic YSZ/Ag/Mo film the friction coefficient is reduced to >0.2 for all temperatures between 25℃ and 700℃. The monolithicYSZ/Ag/Mo film lasted for about 10 000 cycles at all temperatures except 500℃, where the film only lasted for 4500 cycles. Figure 15a shows a cross-sectional micrograph

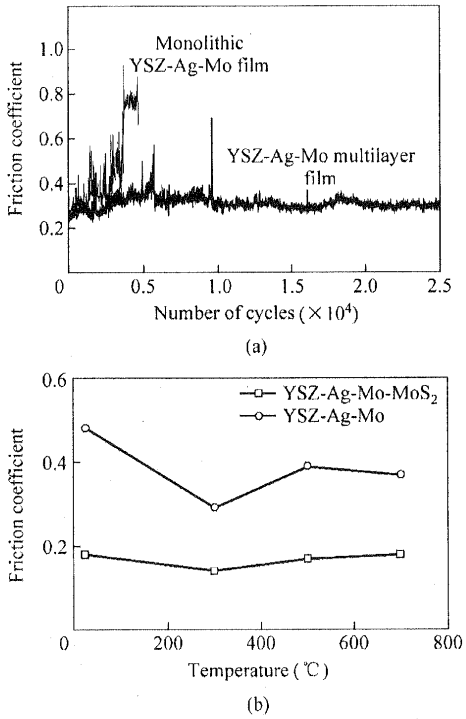


Fig. 14 (a) Friction coefficients for YSZ/24%Ag/10%Mo and YSZ/20%Ag/10%Mo/8% MoS_2 films at 25-700℃ and (b) wear test results for the monolithic and layered YSZ-Ag-Mo films at 500℃.

of the surface of the monolithic film after the 500℃ wear test. The originally monolithic film has segregated into a top layer of pure silver and a bottom layer of YSZ/Mo. The moderate friction coefficient was the result of lubrication of the YSZ/Mo composite with the silver. To improve the wear life of the film, a layered film with two 1-μm layers of monolithic YSZ/Ag/Mo separated by a thin layer of titanium nitride to act as a diffusion barrier layer was produced. The structure was designed to keep the bottom YSZ/Ag/Mo layer in the as-deposited state, while allowing the top layer to adapt to the high temperature wear conditions. The cross-sectional composition map shown in Fig. 15b illustrates that the multilayered architecture effectively prevented silver segregation from occurring in the

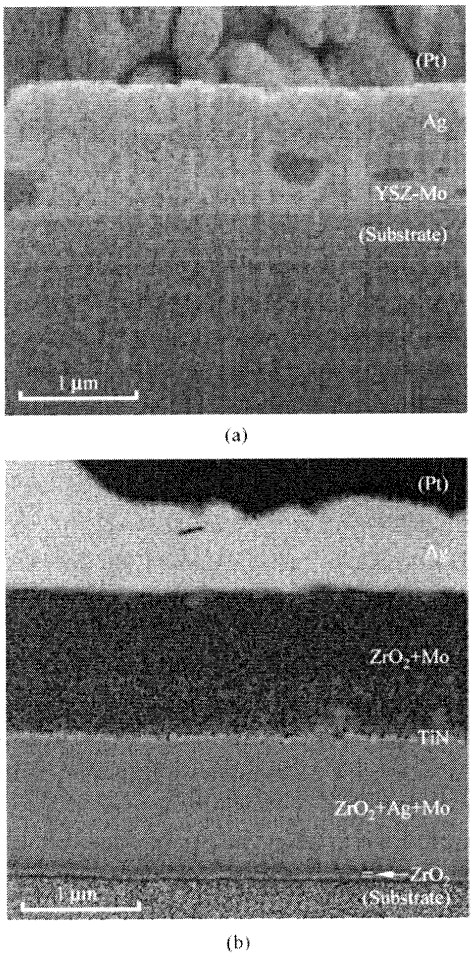


Fig. 15 (a) Cross-sectional micrograph of monolithic YSZ-Ag-Mo film after 1 h at 500℃ and (b) cross-sectional compositional map of the layered YSZ-Ag-Mo film after 2 h at 500℃.

lower film layer, even after over 2 h at 500℃. The film with the layered structure lasted over 5 times longer than the monolithic film of the same composition and total thickness as shown in Fig. 14a.

Using these mechanisms to provide adaptive lubrication, advanced tribological coatings can be produced that survive multiple dry/humid cycling, temperature cycling, and provide long duration operation in many test environments. Various carbides, nitrides, borides, and oxides may be used as the hard nanocrystalline phase in combination with carbon for lubrication in ambient conditions, MoS_2 and WS_2 for lubrication in dry and vacuum environments, and soft metals (Au, Ag, Ni) or low viscosity glasses (network modified SiO_2) for high temperature lubrication. For example, similar success was achieved with $Al_2O_3/MoS_2/CF_x$ composites and $SiC/Cs_2MoOS_2/MoS_2$ /DLC. In the last of these two examples, a Cs-SiO_2 glass provided lubrication above 600℃.

The coating design shown in Fig. 12 and the examples provided previously were primarily tailored to aerospace applications, but similar designs can be developed to produce "chameleon" tribological coatings for other environments. The concepts for producing tough, hard, low friction nanocomposite coatings discussed here are universal such that they can be realized using a variety of material systems and are easily tailored to specific applications.

3 Conclusions

Designs incorporating nanocomposite structures offer significant potential for producing high performance coatings that can operate across multiple extreme environments. Their development will enable increased utilization of coatings in many types of applications including those in the automotive, tool, and aerospace industries where the operational environment is variable and severe. For coatings to become widely accepted, further development and scale-up of deposition processes are required so that engineering components may be coated reliably and inexpensively. To accelerate nanostructured coating availability, process controls, life prediction methodologies, design criteria, and nondestructive evaluation tools must also be further developed. The ultimate goal is to have engineers include surface engineering technologies in their designs from the on-set, instead of as a solution to a problem.

References

[1] Bushan B, Gupta B K. Materials, Coatings, and Surface Treatments. In: Bushan B, Gupta B K, eds. Handbook of Tribology. New York: McGraw-Hill, 1991.

[2] Holmberg K, Matthews A. Coatings Tribology: Properties, Techniques, and Applications in Surface Engineering. Amsterdam: Elsevier, 1994.

[3] Bushan B. Modern Tribology Handbook. Boca Raton: CRC Press, 2001.

[4] Palatnik L S, Il'inskii A I, Sapelkin N P. Strength of multilayered vacuum condensates. *Sov. Pys. Solid State*, 1967, **8**: 2016-2017.

[5] Palatnik L S, Il'inskii A I. Stabilization of high-strength vacuum-deposited films. *Doklady Sov. Phys.: Techn. Phys.*, 1964, **9**: 93-94.

[6] Koehler J S. Attempt to design a strong solid. *Phys. Rev. B*, 1970, **2**: 547-551.

[7] Springer R W, Catlett D S. Structure and mechanical properties of Al_xO_y vacuum-deposited laminates. *Thin Solid Films*, 1978, **54**: 197-205.

[8] Movchan B A, Demchishin A V, Badilenko G F, Bunshah R F, Sans C, Deshpandey C, Doerr H J. Structure-property relationships in microlaminate TiC/TiB_2 condensates. *Thin Solid Films*, 1982, **97**: 215-219.

[9] Kato M, Mori T, Schwartz L H. Hardening by spinodal modulated structure. *Acta Metall.*, 1980, **28**: 285-290.

[10] Holleck H, Schulz H. Advanced layer material constitution. *Thin Solid Films*, 1987, **153**: 11-17.

[11] Jankowski A F. Modelling the supermodulus effect in metallic multilayers. *J. Phys. F*, 1988, **18**: 413-427.

[12] Shinn M, Hultman L, Barnett S A. Growth, structure, and microhardness of epitaxial TiN/NbN superlattices. *J. Mater. Res.*, 1992, **7**: 901-911.

[13] Sproul W D. Multilayer, multicomponent, and multiphase physical vapor deposition coatings for enhanced performance. *J. Vac. Sci. Technol. A*, 1994, **12**: 1595-1601.

[14] Chu X, Barnett S A. A model of superlattice yield stress and hardness enhancements. *Mater. Res. Soc. Symp. Proc.*, 1995, **382**: 291-296.

[15] Holleck H, Schier V. Multilayer PVD coatings for wear protection. *Surf. Coat. Technol.*, 1995, **76-77**: 328-336.

[16] Robinson P, Matthews A, Swift K G, Franklin S. A computer knowledge-based system for surface coating and material selection. *Surf. Coat. Technol.*, 1993, **62**: 662-668.

[17] Voevodin A A, Yerokhin A L, Lyubimov V V. Formal order for search of the principle structure of multilayer coatings at their designing. *Phisik Status Solidi A*, 1994, **145**:

565-574.

[18] Voevodin A A, Walck S D, Zabinski J S. Architecture of multilayer nanocomposite coatings with super-hard diamond-like carbon layers for wear protection at high contact loads. *Wear*, 1997, **203-204**: 516-527.

[19] Veprek S, Reiprich S. A concept for the design of novel superhard coatings. *Thin Solid Films*, 1995, **268**: 64-71.

[20] Veprek S. New development in superhard coatings: The superhard nanocrystalline-amorphous composites. *Thin Solid Films*, 1998, **317**: 449-454.

[21] Veprek S. The search for novel, superhard materials. *J. Vac. Sci. Technol. A*, 1999, **17**: 2401-2420.

[22] Veprek S, Argon A S. Towards the understanding of mechanical properties of super- and ultrahard nanocomposites. *Journal of Vacuum Science & Technology B*, 2002, **20**: 650-664.

[23] Musil J, Vlcek J. Magnetron sputtering of films with controlled texture and grain size. *Mater. Chem. Phys.*, 1998, **54**: 116-122.

[24] Musil J. Hard and superhard nanocomposite coatings. *Surf. Coat. Technol.*, 2000, **125**: 322-330.

[25] Musil J, Vlcek J. Magnetron sputtering of hard nanocomposite coatings and their properties. *Surf. Coat. Technol.*, 2001, **142-144**: 557-566.

[26] Veprek S, Argon A S. Mechanical properties of superhard nanocomposites. *Surf. Coat. Technol.*, 2001, **146-147**: 175-182.

[27] Veprek S, Niederhofer A, Moto K, Bolom T, Männling H -D, Nesládek P, Dollinger G, Bergmaier A. Composition, nanostructure and origin of the ultrahardness in nc-TiN/a-Si_3N_4/a- and nc-$TiSi_2$ nanocomposites with HV=80 to 100 GPa. *Surf. Coat. Technol.*, 2000, **133-134**: 152-159.

[28] Dias A G, Van Breda J H, Moretto P, Ordelman J. Development of TiN-Si_3N_4 nano composite coatings for wear resistance applications. *J. de Physique IV*, 1995, **5**: C5.831-C5.840.

[29] Musil J, Jankovcova H, Cibulka V. Formation of $Ti_{1-x}Si_x$ and $Ti_{1-x}Si_xN$ films by magnetron co-sputtering. *Czech. J. Phys.*, 1999, **49**: 359-372.

[30] Veprek S. Conventional and new approaches towards the design of novel superhard materials. *Surf. Coat. Technol.*, 1997, **97**: 15-22.

[31] Mitterer C, Losbichler P, Hofer F, Beschliesser M, Warbichler P, Gibson P N, Gissler W. Nanocrystalline hard coatings within the quasi-binary system TiN–TiB_2. *Vacuum*, 1998, **50**: 313-318.

[32] Mitterer C, Mayrhofer P H, Beschliesser M, Losbichler P, Warbichler P, Hofer F, Gibson P N, Gissler W, Hruby H, Musil J, Vlcek J. Microstructure and properties of nanocomposite Ti-B-N and Ti-B-C coatings. *Surf. Coat. Technol.*, 1999, **120-121**: 405-411.

[33] Irie M, Nakayama A, Ohara H, Kitagawa N, Nomura T. Deposition of Ni-TiN nano-composite films by cathodic arc ion-plating. *Nucl. Instrum. Methods Phys. Res. B*, 1997, **121**: 133-136.

[34] Musil J, Zeman P, Hruby H, Mayrhofer P H. ZrN/Cu nanocomposite film—A novel superhard material. *Surf. Coat. Technol.*, 1999, **120-121**: 179-183.

[35] Musil J, Polakova H. Hard nanocomposite Zr-Y-N coatings, correlation between hardness and structure. *Surf. Coat. Technol.*, 2000, **127**: 99-106.

[36] Musil J, Hruby H. Superhard nanocomposite $Ti_{1-x}Al_xN$ films prepared by magnetron sputtering. *Thin Solid Films*, 2000, **365**: 104-109.

[37] Benda M, Musil J. Plasma nitriding enhanced by hollow cathode discharge—A new method for formation of superhard nanocomposite coatings on steel surfaces. *Vacuum*, 1999, **55**: 171-175.

[38] Voevodin A A, Prasad S V, Zabinski J S. Nanocrystalline carbide/amorphous carbon composites. *J. Appl. Phys.*, 1997, **82**: 855-858.

[39] Delplancke-Ogletree M P, Monteiro O R. Deposition of titanium carbide films from mixed carbon and titanium plasma streams. *J. Vac. Sci. Technol. A*, 1997, **15**: 1943-1950.

[40] Voevodin A A, O'Neill J P, Prasad S V, Zabinski J S. Nanocrystalline WC and WC/a-C composite coatings produced from intersected plasma fluxes at low deposition temperature. *J. Vac. Sci. Technol. A*, 1999, **17**: 986-992.

[41] Monteiro O R, Delplancke-Ogletree M P, Winand R, Lo R Y, Brown I. Synthesis and characterization of thin films of WC_x produced by mixing W and C plasma streams. *Surf. Coat. Technol.*, 1997, **94-95**: 220-225.

[42] Dieter G E. Mechanical Metallurgy. New York: McGraw Hill, 1976.

[43] Clemens B M, Kung H, Barnett S. Structure and strength of multilayers. *MRS Bulletin*, 1999, **24**: 20-26.

[44] Gleiter H. Nanostructured materials: basic concepts and microstructure. *Acta Mater.*, 2000, **48**: 1-29.

[45] Marder M, Finberg J. How things break. *Phys. Today*, 1996, **49**: 24-29.

[46] Holleck H. Material selection for hard coatings. *J. Vac. Sci. Technol. A*, 1986, **4**: 2661-2669.

[47] Holleck H, Schulz H. Preparation and behaviour or

wear-resistant TiC/TiB_2, TiN/TiB_2 and TiC/TiN coatings with high amounts of phase boundaries. *Surf. Coat. Technol.*, 1988, **36**: 707-714.

[48] Voevodin A A, Lyubimov V V, Yerokhin A L, Spassky S E. Calculation of multilayer ion-plasma coating scheme. *Voprosy Atomnoy Naukii Techniki*, 1991, **19**: 66-69.

[49] Lyubimov V V, Voevodin A A, Spassky S E, Yerokhin A L. Stress analysis and failure possibility assessment of multilayer PVD coating. *Thin Solid Films*, 1992, **207**: 117-125.

[50] Fella R, Holleck H, Schulz H. Preparation and properties of WC-TiC-TiN gradient coatings. *Surf. Coat. Technol.*, 1988, **36**: 257-264.

[51] Monaghan D P, Teer D G, Arnell R D, Efeoglu I, Ahmed W. Ion-assisted CVD of graded diamond like carbon (DLC) based coatings. *J. de Physique IV*, 1993, **3**: 579-587.

[52] Voevodin A A, Schneider J M, Rebholz C, Matthews A. Multilayer composite ceramic-metal-DLC coatings for sliding wear applications. *Tribol. Int.*, 1996, **29**: 559-570.

[53] Voevodin A A, Capano M A, Laube S J P, Donley M S, Zabinski J S. Design of a Ti/TiC/DLC functionally gradient coating based on studies of structural transitions in Ti-C films. *Thin Solid Films*, 1997, **298**: 107-115.

[54] Lyubimov V V, Voevodin A A, Yerokhin A L, Timofeev Y S, Arkhipov I K. Development and testing of multilayer PVD-coatings for piston rings. *Surf. Coat. Technol.*, 1992, **52**: 145-151.

[55] Voevodin A A, Stevenson P, Schneider J M, Matthews A. Active process control of reactive sputter deposition. *Vacuum*, 1995, **46**: 723-729.

[56] Karch J, Birringer R, Gleiter H. Ceramics ductile at low temperature. *Nature*, 1987, **330**: 556-558.

[57] Sherby O D, Wadsworth J. Superplasticity-recent advanced and future directions. *Progr. Mater. Sci.*, 1989, **33**: 169-221.

[58] Wakai F. Superplasticity of ceramics. *Ceram. Int.*, 1991, **17**: 153-163.

[59] Nieh T G, Wadsworth J, Wakai F. Recent advances in superplastic ceramics and ceramic composites. *Int. Mater. Rev.*, 1991, **36**: 146-161.

[60] Langdon T G. The role of grain boundaries in high temperature deformation. *Mater. Sci. Eng. A*, 1993, **166**: 67-79.

[61] Koch C D, Morris D G, Lu K, Inoue A. Ductility of nanostructured materials. *MRS Bul.*, 1999, **24**: 54-57.

[62] Siegel R W, Fougere G E. Grain size dependent mechanical properties in nanophase materials. *Mater. Res. Soc. Symp. Proc.*, 2002, **362**: 219-229.

[63] Langdon T G. The significance of grain boundaries in the flow of polycrystalline materials. *Mater. Sci. Forum*, 1995, **189-190**: 31-42.

[64] Sherby O D, Nieh T G, Wadsworth J. Some thoughts on future directions for research and applications in superplasticity. *Mater. Sci. Forum*, 1997, **243-245**: 11-20.

[65] Schiotz J, Di Tolla F D, Jacobsen K W. Softening of nanocrystalline metals at very small grain sizes. *Nature*, 1998, **391**: 561-563.

[66] Voevodin A A, Zabinski J S. Load-adaptive crystalline / amorphous nanocomposites. *J. Mater. Sci.*, 1998, **33**: 319-327.

[67] Voevodin A A, Zabinski J S. Supertough wear resistant coatings with "chameleon" surface adaptation. *Thin Solid Films*, 2000, **370**: 223-231.

[68] Voevodin A A, Jones J G, Hu J J, Fitz T A, Zabinski J S. Growth and structural characterization of yttria stabilized zirconia-gold nanocomposite films with improved toughness. *Thin Solid Films*, 2001, **401**: 187-195.

[69] Bae Y W, Lee W Y, Besmann T M, Yust C S, Blau P J. Preparation and friction characteristics of self-lubricating TiN-MoS_2 composite coatings. *Mater. Sci. Eng. A*, 1996, **209**: 372-376.

[70] Bae Y W, Lee W Y, Yust C S, Blau P J, Besmann T M. Synthesis and friction behavior of chemically vapor deposited composite coatings containing discrete TiN and MoS_2 phases. *J. Am. Ceram. Soc.*, 1996, **79**: 819-824.

[71] Gilmore R, Baker M A, Gibson P N, Gissler W, Stoiber M, Losbichler P, Mitterer C. Low-friction TiN-MoS_2 coatings produced by dc magnetron co-deposition. *Surf. Coat. Technol.*, 1998, **108-109**: 345-351.

[72] Gilmore R, Baker M A, Gibson P N, Gissler W. Preparation and characterisation of low-friction TiB_2 based coatings by incorporation of C and MoS_2. *Surf. Coat. Technol.*, 1998, **105**: 45-50.

[73] Goller R, Torri P, Baker M A, Gilmore R, Gissler W. The deposition of low-friction TiN-MoS_x hard coatings by a combined arc evaporation and magnetron sputter process. *Surf. Coat. Technol.*, 1999, **120-121**: 453-457.

[74] Voevodin A A, Hu J J. Fitz T A, Zabinski J S. Nanocomposite tribological coatings with "chameleon" friction surface adaptation. *J. Vac. Sci. Technol. A*, 2002, **20**: 1434-1444.

[75] Voevodin A A, O'Neil J P, Zabinski J S. Tribological performance and tribochemistry of nanocrystalline WC/amorphous diamond-like carbon composites. *Thin Solid Films*, 1999, **342**: 194-200.

[76] Zaidi H, Huu T L, Palmer D. Influnece of hydrogen contained in hard carbon coatings on their tribological behaviour. *Diam. Relat. Mater.*, 1994, **3**: 787-790.

[77] Voevodin A A, Phelps A W, Donley M S, Zabinski J S. Friction induced phase transformation of pulsed laser deposited diamond-like carbon. *Diamond Relat. Mater.*, 1996, **5**: 1264-1269.

[78] Voevodin A A, Bultman J E, Zabinski J S. Investigation into a 3-dimensional processing of tribological coatings. *Surf. Coat. Technol.*, 1998, **107**: 12-19.

[79] Zabinski J S, Donley M S, Dyhouse V J, McDevit N T. Chemical and tribological characterization of PbO-MoS_2 films grown by pulsed laser deposition. *Thin Solid Films*, 1992, **214**: 156-163.

[80] Zabinski J S, Donley M S, McDevit N T. Mechanistic study of the synergism between Sb_2O_3 and MoS_2 lubricant systems using Raman spectroscopy. *Wear*, 1993, **165**: 103-108.

[81] Zabinski J S, Prasad S V, McDevit N T. Advanced solid lubricant coatings for aerospace systems. In: Proceedings of NATO Advisory Group of Aerospace Research and Development (AGARD) Conference on Tribology for Aerospace Systems, Sesimbra, Portugal, May 6-7, 1996, AGARD NATO publication CP 589, printed by Canada Communication Group, Hull, Quebec, 1996: 3.1-3.12 .

[82] Voevodin A A, Hu J J, Fitz T A, Zabinski J S. Tribological properties of adaptive nanocomposite coatings made of yttria stabilized zirconia and gold. *Surf. Coat. Technol.*, 2001, **146-147**: 351-356.

[83] Voevodin A A, O'Neill J P, Zabinski J S. WC/DLC/WS_2 nanocomposite coatings for aerospace tribology. *Tribol. Lett.*, 1999, **6**: 75-78.

Tsinghua University Awarded 26 Prizes of National Tertiary Education Achievement

The Prizes awarded to the achievements of tertiary education in China has newly been unveiled on the Fifth Prize Awarding Ceremony of National Tertiary Education held in the People's Great Hall on 8th September, 2005. Up to 26 Prizes were awarded to Tsinghua Faculties.

The excellent prize was awarded to the team led by Tsinghua's former president professor Wang Dazhong for their research work on "The Innovation and Practice of Professional Degree Education Scheme for Master's Degree of Engineering". Other prizes include 7 First-Grade Prizes and 18 Second-Grade Prizes.

The prizes for higher education achievement are awarded every four years and mark the newest approaches and practices of high leveled tertiary education. The number of awards to Tsinghua faculties ranks top among all universities in China.

(From http://news.tsinghua.edu.cn)

Paper 10

Available online at www.sciencedirect.com
ScienceDirect
Surface & Coatings Technology 201 (2006) 3732–3747
SURFACE & COATINGS TECHNOLOGY
www.elsevier.com/locate/surfcoat

Tribological performance of hybrid filtered arc-magnetron coatings Part I: Coating deposition process and basic coating properties characterization

V. Gorokhovsky [a,*], C. Bowman [a], P. Gannon [a], D. VanVorous [a], A.A. Voevodin [b], A. Rutkowski [b], C. Muratore [c], R.J. Smith [d], A. Kayani [d], D. Gelles [e], V. Shutthanandan [e], B.G. Trusov [f]

[a] *Arcomac Surface Engineering, LLC., Bozeman, Montana, USA*
[b] *Air Force Research Laboratory, Wright-Patterson AFB, Ohio, USA*
[c] *UTC Inc./Air Force Research Laboratory, Wright-Patterson AFB, Ohio, USA*
[d] *Montana State University, Bozeman, Montana, USA*
[e] *Pacific Northwest National Laboratory, Richland, Washington, USA*
[f] *Bauman Moscow State Technical University, Moscow, Russia*

Received 15 June 2006; accepted in revised form 11 September 2006
Available online 30 October 2006

Abstract

Aircraft propulsion applications require low-friction and wear resistant surfaces that operate under high contact loads in severe environments. Recent research on supertough and low friction nanocomposite coatings produced with hybrid plasma deposition processes was demonstrated to have a high potential for such demanding applications. However, industrially scalable hybrid plasma technologies are needed for their commercial realization. The Large area Filtered Arc Deposition (LAFAD) process provides atomically smooth coatings at high deposition rates over large surface areas. The LAFAD technology allows functionally graded, multilayer, super-lattice and nanocomposite architectures of multi-elemental coatings via electro-magnetic mixing of two plasma flows composed of different metal ion vapors. Further advancement can be realized through a combinatorial process using a hybrid filtered arc-magnetron deposition system. In the present study, multilayer and nanostructured TiCrCN/TiCr+TiBC composite cermet coatings were deposited by the hybrid filtered arc-magnetron process. Filtered plasma streams from arc evaporated Ti and Cr targets, and two unbalanced magnetron sputtered B_4C targets, were directed to the substrates in the presence of reactive gases. A multiphase nanocomposite coating architecture was designed to provide the optimal combination of corrosion and wear resistance of advanced steels (Pyrowear 675) used in aerospace bearing and gear applications. Coatings were characterized using SEM/EDS, XPS and RBS for morphology and chemistry, XRD and TEM for structural analyses, wafer curvature and nanoindentation for stress and mechanical properties, and Rockwell and scratch indentions for adhesion. Coating properties were evaluated for a variety of coating architectures. Thermodynamic modeling was used for estimation of phase composition of the top TiBC coating segment. Correlations between coating chemistry, structure and mechanical properties are discussed.
© 2006 Elsevier B.V. All rights reserved.

Keywords: Filtered arc; Magnetron; Coatings; Aerospace; Thermodynamics; Nanocomposite

1. Introduction

Aircraft propulsion elements, such as gears and bearings, operate under extreme conditions of high contact loads at high speed, and in aggressive environments. Corrosion attack in moist, saline air is another critical factor that deteriorates surfaces of the tribological pairs if they are exposed to the environment. To provide both mechanical performance and corrosion resistance, advanced carburized stainless steels, e.g. Pyrowear 675 [64] and CSS-42L [65], were introduced for the use in aircraft gears and bearings. While these steels provide a balance between mechanical and corrosion properties, the friction contact areas are still subjected to both wear process and corrosion attack due to the tribochemical accelerated processes. In addition, broad

* Corresponding author. 3626 Fieldstone Dr., Bozeman, Montana, 59715, United States. Tel.: +1 406 522 7620; fax: +1 406 522 7617.
E-mail address: vigase@aol.com (V. Gorokhovsky).

0257-8972/$ - see front matter © 2006 Elsevier B.V. All rights reserved.
doi:10.1016/j.surfcoat.2006.09.007

temperature synthetic lubricants are often used on the tribological surfaces of military aircraft propulsion components. Some of these have a fluorinated chemistry [66], which provides a low viscosity at subzero temperatures, but can release aggressive fluorine agents at elevated temperatures via tribochemical reactions. For reliable operation of aircraft gears and bearings, advanced surface coating technologies are required to mitigate wear and corrosion processes in the contact areas.

Nanocomposite coatings with nanocrystalline/amorphous structures and functionally graded metal-ceramic interfaces with steel substrates have been designed to provide supertough characteristics and capability to withstand high contact loads of bearings and gears in aerospace systems [52–57]. Some of these coatings had contained nanocrystalline carbides embedded in hard amorphous diamond-like carbon (DLC) matrix, which helped to achieve a low friction and wear rates in ambient environments [58,59]. Such properties provide a safety margin of a non-catastrophic low friction and wear performance in an oil lubricant starvation as emergency back-up lubrication. Tribological carbon based coatings can be further improved with addition of carbide-forming non-metallic elements like Si, B, N in a multi-phase nanocomposite cermet structure [13–18,23–28]. Using boron as an alloying element for hydrogenated a-C:H films forms a structure with boron carbide crystals embedded in a-C:H matrix. Sputtered boron carbide coatings are now commercially produced on gears, molds, cutting and forming tools [27]. Complex boron containing carbides and carbonitrides are currently being explored for wear resistant applications [60]. Other carbon rich carbides are also successfully used for gears, bearings, and shafts [14–18,26,35].

Conventional thin film TiN and CrN cermet coatings have been used to prevent corrosion attack but have a limited success on tool steels because they are not thick enough to cover corrosion initiating surface defects sufficiently [1–4,42]. Even in the case of high chromium steel substrates like 440C or carburized Pyrowear 675, thin film coatings only protect against corrosion if a high substrate surface finish eliminates pitting initiation sites [1]. Incorporation of metallic interlayers into multilayer cermet coating, e.g. TiN/Ti or CrN/Cr, improves corrosion by the passivation capability of the incorporated metals [2–4,6]. Substrate pretreatment by plasma nitriding, carbonitriding or carburizing prior to coating deposition (duplex technologies) can also improve corrosion resistance [2–5,42]. Care should be taken to avoid substrate chromium depletion by forming nitrides and/or carbides, which could inhibit the passivation ability of the high chromium steels. Recently developed multiphase nanocomposite Cr-based nitride coatings such as (Ti,Cr)N, (Cr,Al)N have demonstrated improved corrosion resistance in comparison with single phase TiN or CrN cermets [2]. Further improvement in corrosion resistance can be achieved by adding non-metallic elements (C,B,Si) and by reducing the thickness of individual sublayers in the multilayer coatings to nanometer scale [2].

The production of advanced nanocomposite coatings of complex chemistry and nanostructure became possible with development of novel deposition processes, where plasma streams from several sources are combined, mixed, and directed toward the substrate with flexibility in a control of plasma chemistry, density, and energy [34,61]. Such flexibility is a critical requirement for both adhesion enhancing gradient structures and for the formation of advanced nanocomposite and nanolayer coating architectures. Supertough nanocomposite coatings developed in AFRL for high contact load applications were produced by a hybrid of magnetron sputtering-plasma laser deposition (MSPLD), where the high energy of the laser plasma was used to achieve a controlled crystallization [62]. Although promising, MSPLD is difficult to apply to large and complex substrate geometries, such as gears, due to the line of sight of the laser ablated plasma. Filtered vacuum arc is an alternative high energy plasma production source, which does not have this limitation, produces similar high quality carbon based coatings [63], and is very beneficial for the growth of well adhered and particle free metal and ceramic layers [32,33, 43,44].

A unique Large Area Filtered Arc Deposition (LAFAD) technology developed by Arcomac Surface Engineering LLC offers the opportunity for depositing advanced supertough nanocomposite coatings and corrosion resistant multilayer structures on very large and complex shaped surfaces of aircraft bearings and gears [32]. This process combines different types of plasma vapor sources working together in a common filtered arc plasma environment as achieved in the Filtered Arc Plasma Source Ion Deposition (FAPSID) surface engineering system [34]. The combination of large area filtered arc sources and unbalanced magnetron sputtering in the same chamber increases the metal ion flux conveyed by the plasma toward the substrate surface while keeping the flow of neutral atoms generated by magnetron sputtering fixed. This paper assesses the use of novel hybrid, large area filtered arc deposition-unbalanced magnetron sputtering (LAFAD-UBM) surface engineering technology, which was recently developed by Arcomac Surface Engineering LLC [34] for aircraft bearings and gears applications. Advanced coating architectures were designed, following the nanocomposite and functionally gradient concepts developed by AFRL for aerospace friction pairs [52–57]. These concept architectures were enhanced in this study by incorporation of corrosion mitigating multilayer nanocomposite coatings. Analyses and discussions of the coating mechanical properties, corrosion resistance and thermal-chemical synthetic lubricant compatibility on duplex treated coupons made of 440XH stainless steel and of Pyrowear 675 are provided in this paper.

2. Experimental

2.1. Hybrid FAD-UBM surface engineering technology

The FAPSID-700 surface engineering system featuring hybrid FAD-UBM technology is shown in Fig. 1. The FAPSID-700 consists of two dual large area filtered arc deposition (LAFAD) plasma sources, each having two opposite primary direct cathodic arc deposition (DCAD) sources with targets made of the same or different materials. The LAFAD uses a rectangular plasma-guide chamber with two pairs of rectangular deflecting coils installed on the opposite sides of the plasma-guide chamber, as shown in Fig. 1. In this work, two primary cathodic arc sources utilizing Cr and Ti targets were placed opposite to each other on the sidewalls

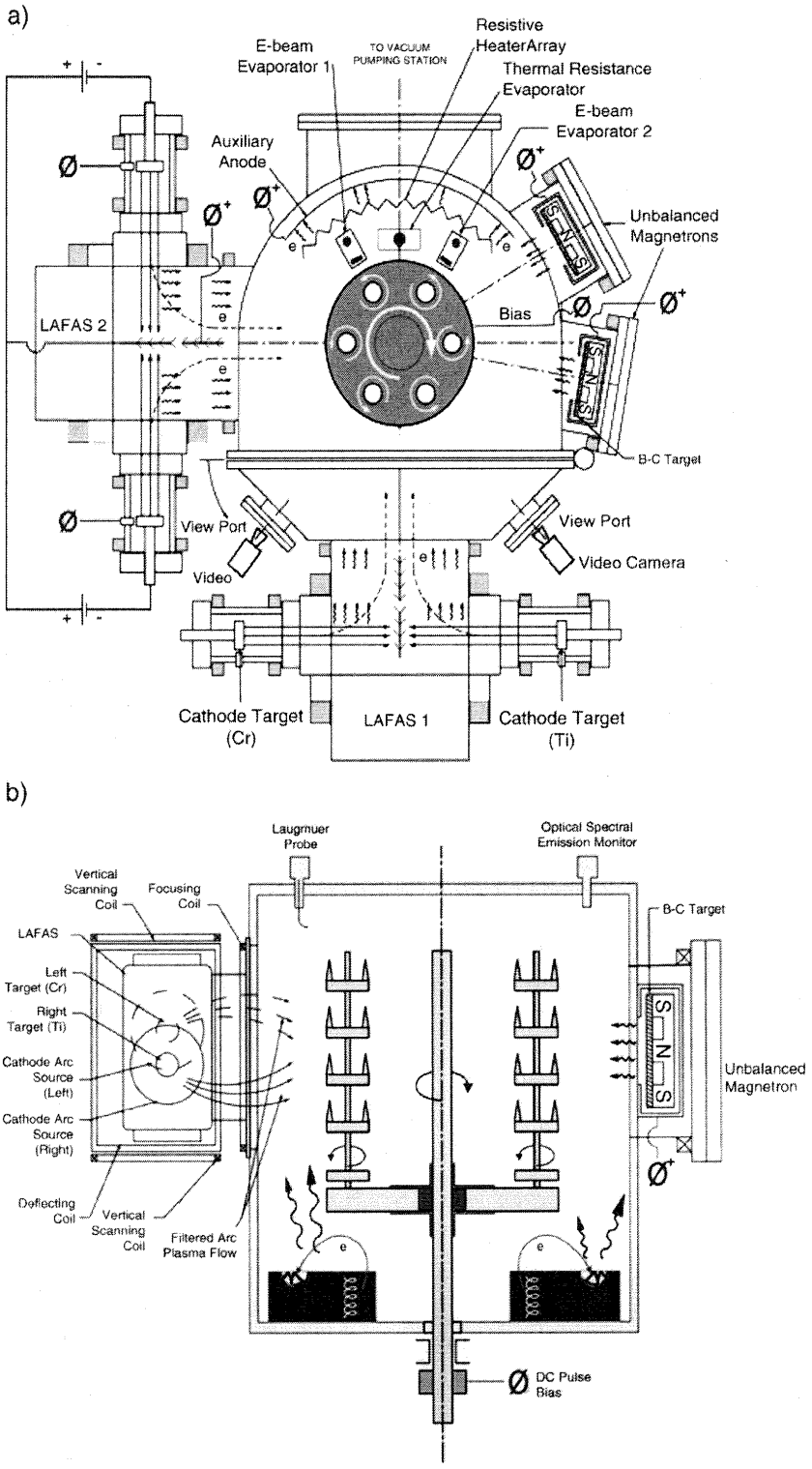


Fig. 1. Schematic illustration of ASE's FAPSID™ surface engineering system. This system utilizes Large Area Filtered Arc Sources (LAFAS) in a Universal Hybrid Layout with conventional PVD sources: (a) – top view, (b) – side view.

of the plasma-guide chamber, surrounded by rectangular deflecting coils, and separated by an anodic baffle plate. The LAFAD vapor plasma source uses a superimposed deflecting magnetic field to turn the metal ion flow 90° toward the deposition chamber and substrates [12,32]. The more massive droplets of material from the source follow straighter trajectories and are captured on baffles, resulting in droplet-free coatings. A set of scanning magnetic coils allows the ion plasma jet to be swept in the vertical direction so as to cover theoretically unlimited large surface areas. At the same time, the arc column is well confined by a magnetic field in the horizontal direction, providing enhanced suppression of the turbulent plasma diffusion, leading to a significant increase

in the metal vapor ion yield. By manipulating the arc plasma jets using strategically placed scanning magnetic coils and auxiliary anodes, this design creates a "plasma-immersion" environment in the coating chamber. This technique allows the plasma flux from different cathodes in a multi-cathode chamber to be uniformly mixed and completely envelop complex parts. The use of auxiliary anodes in conjunction with the filtered arc sources permits extraction of a significant electron current from the arc source, which provides a highly conductive ionized gaseous plasma environment provides added versatility for such processes as ion cleaning, ionitriding, and ion implantation [32]. It was recently found that LAFAD plasma source can be combined with other PVD and low pressure CVD plasma sources in a universal hybrid multi-source chamber layout utilizing plasma flows generated by different PVD and CVD sources in filtered arc plasma immersion environment. This concept has been realized in FAPSID-700 surface engineering system design. In addition to two LAFAD plasma sources the FAPSID-700 system used in this work utilizes two unbalanced magnetrons with $102 \times 546 \times 3.2$ mm B_4C rectangular targets. This system is also equipped with two EB-PVD evaporators and resistive thermal evaporation (RTE) source all incorporated in one universal chamber layout. A universal layout provides the capability to deposit combinatorial coatings using hybrid LAFAD-UBM processes [34]. The substrates to be coated are installed into a carousel type multiple satellite substrate platform, which allows both single and double rotation of the substrates to be coated. A resistive heater array allows for heating of the substrates up to 450 °C independently from plasma heating.

The following process parameters were typically used for the deposition of TiCrN/TiCr-TiCrCN bottom segment and transitional layer by LAFAD plasma source equipped with two (opposite) Ti and Cr targets. The arc currents were set on approximately 100 A for both Ti and Cr targets. The auxiliary arc discharge current was set on 150 A during argon ion cleaning stage and than reduced to 40 A during coating deposition stage. The substrate temperature did not exceed 350 °C. An Advanced Energy Industry MDX-II power supply coupled with a Sparkle-V accessory unit was used as a bias power supply subsytem. The bias voltage was set at −250 V during ion cleaning stage followed by −1000 V during 2 min of metal ion etching stage. The reverse time during ion cleaning/etching stages was set at 2 μs at 48 kHz frequency. The bias voltage during coating deposition stage was set at −60 V DC. The TiCrN/TiCr multi-layer nanolaminated coating was deposited at 4×10^{-2} Pa gas pressure. Each bilayer in the TiCrN/TiCr multilayer architecture was deposited during 30 min with 25 min dedicated to TiCrN and 5 min to TiCr sublayers. The rotation speed of the substrate platform was set at 9 rpm, which corresponds to a 3–4 nm bilayer thickness in the {Ti based/Cr based} nanolaminated architecture, taking into account an approximately 1 μm/hr deposition rate for both TiN and CrN coatings. The pure nitrogen was gradually changed to N_2/40%CH_4 during a 40 min deposition of the intermediate TiCrCN layer. The preliminary set of samples was prepared with a TiCrC upper tribological segment deposited by LAFAD, on top of the transition TiCrCN layer using acetylene as a reactive gas at pressure of 5×10^{-2} Pa. Additional samples were produced with an upper layer consisting of TiBC nanocomposite cermet deposited by a hybrid filtered arc-unbalanced magnetron process. In this case both primary cathodic arc sources of LAFAD plasma source were equipped with Ti targets for generating titanium vapor plasma flow. The magnetron power density was set at approximately 5.5 W/cm^2. A small amount of reactive C_xH_y gas (acetylene or methane) was added to argon at a total gas pressure of 0.2 Pa. For deposition of multilayer TiBC/iBC (ML) coating architecture the deflecting magnetic field of the LAFAD plasma source was cycled off and on every 10 min. In contrast, the LAFAD deflecting magnetic field was activated continuously for deposition of the single layer TiBC (SL) coating architecture.

2.2. Duplex multilayer nanocomposite coating architecture

The coating architecture utilized in this work consists of two segments separated by an intermediate gradient zone as depicted in Fig. 2. The coating segment in contact with the substrate, the bond segment, is composed of a TiCrN based multiphase cermet. Periodic substrate exposure to Ti and Cr vapor plasma flows (Fig. 1) results in nanostructured ceramic and metallic layers in the MeC_xN_{1-x}/Me multilayer nanolaminated architecture as shown in Fig. 3a. This provides substructure through a

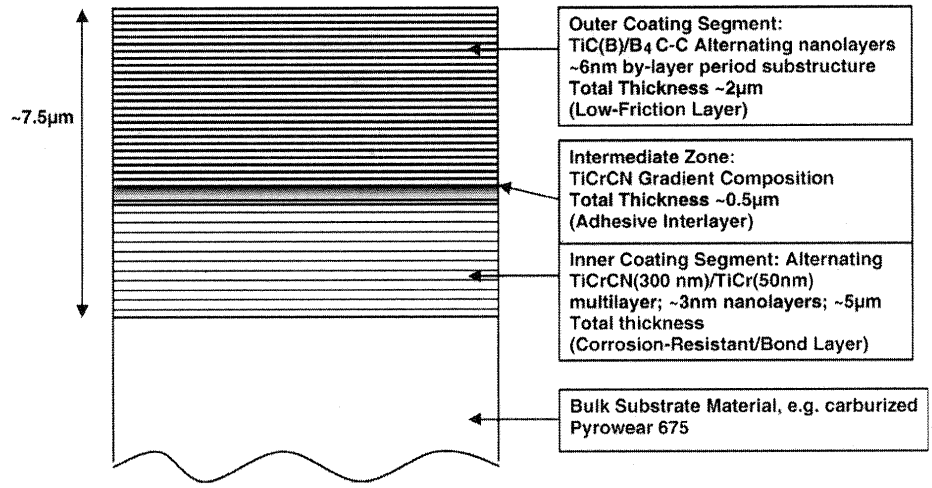


Fig. 2. Schematic illustration of the multilayer nanostructured functionally graded coating design used in this work.

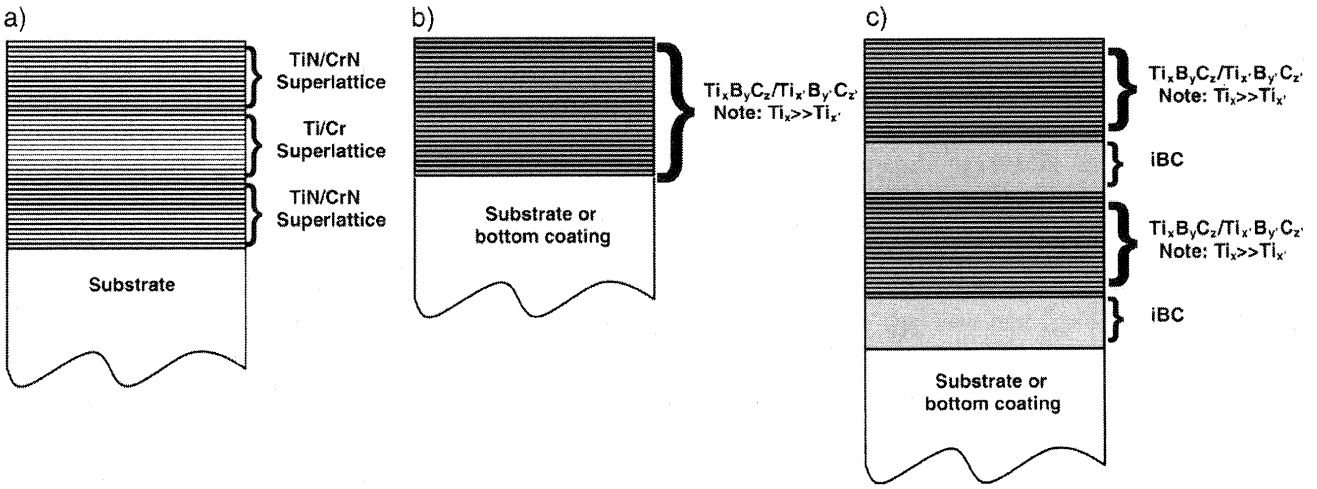


Fig. 3. Coating architecture of the bottom TiCrN/TiCr bond coating segment (a) and top TiBC coating segment (b, c) used in this work: the bottom segment has micrometric size multilayer with substructured nanolaminated periodic architecture; the top segment is deposited as either a nanocomposite single layer TiBC coating (b) or multilayer TiBC/iBC coating (c), where TiBC sublayers have the same nanocomposite structure as single layer TiBC coating shown in figure (b).

superlattice with a bilayer period at the nanometer scale. The bond layer substructure further improves toughness and stress management and is widely employed for corrosion resistant applications [5–7,10,25–30]. Simultaneously, the structure of the bond coating segment provides good adhesion and toughness, and can apply extensive compressive stresses to the substrate surface, made of chromium enriched carburized stainless steel such as Pyrowear 675. Using chromium-based cermet sublayers for enhancing coating adhesion is a well-known approach especially suitable for carbide, DLC, and Me-DLC coatings [25,28,31–34].

The upper segment, composed of TiBC nanocomposite cermet, was produced in two forms: as a single layer (SL) and as a TiBC/iBC multilayer (ML) structure utilizing TiBC layered with boron doped DLC layer as illustrated in Fig. 3b, c. This low friction coating is capable of operating in dry friction conditions as a solid lubricant material [2,27]. Adding boron carbide to the multi-phase tribological coating can improve corrosion resistance and thermal-chemical compatibility with lubricants at elevated temperatures. Sputtered boron carbide coatings are commercially produced and recommended for automotive gears operating under high frictional loads, molds, and cutting and forming tools [38–40]. In addition, boron carbide, as well as many other phases forming in a Ti–B–C system, is known to be chemically inert in extremely aggressive environments [29].

The intermediate zone, separating the inner and outer coating segments, consists of a graded composition providing smooth transition from the nitride-based inner coating segment, to the carbide based outer coating segment. This structure is tailored for optimal compatibility and stress management of the adjacent layers. This zone enhances the bond/adhesion of the outer (low friction) coating segment to the inner (corrosion resistant) coating segment.

Coupons, made of 440XH corrosion resistant martensitic stainless steel hardened to 62–64 HRC, were used during the preliminary experimental study. The 440XH coupons 6.4 mm dia × 3.2 mm thick with duplex treatment utilizing ionitriding followed by a multilayer corrosion resistant tribological coating were prepared in a single plasma immersion vacuum cycle in the FAPSID-700 surface engineering system. When tests confirmed that the desired characteristics were obtained on the 440XH coupons, final trials were prepared on 25.4 mm dia × 6.4 mm thick disk coupons made of carburized Pyrowear 675.

2.3. Basic coating properties characterization techniques

Coating properties were characterized by variety of techniques. The following methods were used to determine the film's properties:

(1) The coating thickness was measured by a spherical wear scar (Calotest™) technique.
(2) The thickness of the ionitrided layer was determined by etching for 4 min in Nital followed by measurement using reflective optical microscopy.
(3) Adhesion characteristics were determined using a Rockwell C 1450 N indentation test method specified by Diamler Benz. Its classification scheme, based on a HF1-HF6 scale, with a HF1 rating being the best is shown in Ref. [36].
(4) A shank of a coated dental instrument was sheared by a standard ductility test device at different locations, and the coating delaminations around the sheared area were examined by optical microscopy. This test was also used for the measurement of ductility of the steel shanks.

Methods (1), (2) and (3) were applied to coated witness-coupons, since they require flat well-polished surfaces, while method (4) was used for evaluation of adhesion on coated round-shape dental instruments of different grades.

(5) Scanning electron microscopy (SEM), high resolution transmission electron microscopy (HRTEM) and reflective

optical microscopy were used to examine morphology of films and instrument surfaces. The backscattering electron imaging (BEI) technique, which displays surface composition, was found to be beneficial for examining wear lands on coated instruments. In order to prepare specimens for HRTEM evaluation, it was decided that specimen preparation would be more efficient if the two samples were mounted with the coatings face-to-face so that both could be prepared simultaneously. Therefore, sections of each sample were cut about 2 mm wide and 10 mm long to contain the wear track in the center of the sample, the samples were glued face-to-face, the thickness of the composite was reduced to fit into a 3 mm (I.D.) tube, and 0.25 thick slices approximately 3 mm in diameter were cut. Slices were mechanically polished on one side using 1 m BN paste, glued to a molybdenum support washer and dimple ground on the other side using 1 μm BN paste leaving a sample thickness less than 15 μm. Gluing operations used a thermal setting epoxy that requires heating to ~150 °C for a few minutes. Final thinning was by argon ion milling using a Precision Ion Polishing System (PIPS) from Gatan, Inc. operating at 5 KeV and a sputtering angle of 6°. Transmission Electron Microscopy (TEM) was performed on a JEOL 2010F with a field emission gun operating at 200 KeV. Scanning Electron Microscopy (SEM) was performed on a JEOL 840 operating at 40 KeV.

(6) Surface profile was evaluated by atomic force microscopy (AFM).
(7) XRD technique was used to identify phase composition in the coatings.

Further evaluation of adhesion and spallation resistance of the coatings was characterized by scratch testing with acoustic emission spectrometry. Adhesion and toughness of the coatings were evaluated with a CSEM scratch tester at AFRL, using a 0.2 mm diamond tip with a constant speed of 5 mm/min on the coating surface. The applied load was linearly increased up to 200 N with a rate of 50 N/min. The burst of acoustic emission was used to determine crack developments and gave a lower critical load for an estimation of the coating cohesion strength. The change of tangential friction force was used to determine penetration to the substrate and give an upper critical load for estimations of the coating adhesion strength [37]. Observations of the scratch paths were used to verify acoustic and friction force data. At least five scratches were performed for each coating and results were averaged to keep an experimental uncertainty within ±5 N. Wear track profiles were investigated with Tencor P-10 contact profilometer, taking scan images of the track segments and calculating depth and width of the produced tracks.

The magnitude of residual coating stress was determined from the change in radius of curvature of Si wafers before and after deposition, using the Stoney equation [38] and assuming wafer elastic modulus of 180.5 GPa. A Tencor FLX-2320 thin film stress measurement system was used. For each coating, at least three measurements were performed and results were averaged.

The mechanical properties of coatings were investigated by nanoindentation measurements using an MTS Nanoindentor XP system with a Berkovich diamond tip. Indentations were performed to a 500 nm displacement depth limit. The hardness and elastic modulus measurements were performed using a continuous stiffness monitoring mode (CSM) and applying a small amplitude tip oscillation. For all coatings, data was averaged over depth ranges when hardness and elastic modulus had minimum variations (exhibited plateaus) as a function of indentation depth to minimize both surface and substrate effects [39]. Ten indents were performed for each of the coatings and the results were averaged. Effective Young's modulus $E^*=E/(1-n^2)$, where n is Poisson's ratio of 0.2, and resistance to plastic deformation (H^3/E^{*2}) was calculated from obtained hardness (H) and Young's modulus (E) data as in Ref. [60]. With each data set indentations into a fused SiO_2 standard were performed to ensure that the nanoindentation system remained calibrated.

Coating composition was analyzed by SEM/EDS and RBS techniques. E-beam energy of 9 kV was used for EDS analysis. In case of thin (<1 μm) coatings the elements from the substrates were subtracted from EDS spectra. Ion beam analysis of the samples was performed using 3 MeV tandem accelerators at the Environmental Molecular Sciences Laboratory (EMSL) at Pacific Northwest National Laboratory (PNNL). Rutherford backscattering spectra (RBS), for the compositional analysis of the coatings, were recorded using a 2.5 MeV beam of He^+ ions with a 7° incident angle and 75° measured from the sample normal. Backscattered ions were collected using a silicon surface barrier detector at a scattering angle of 160°, with an exit angle of 40° from the sample normal. Hydrogen composition in the coatings was recorded using 2.5 MeV beam He^+ ions with an angle of incidence of 75° from the sample normal. Since hydrogen is lighter than He, it can only scatter in the forward direction; therefore, a silicon barrier detector was placed at a scattering angle of 30° with a 10 μm Al foil in front to stop the He particles from entering the detector. Because the Rutherford cross sections are more sensitive to heavier elements, B and C 2.5 MeV protons were used. At this proton energy, the scattering cross sections for B and C are non-Rutherford [40], producing enhanced scattering yields for these two elements. Finally, elemental compositions were determined by comparing SIMNRA computer simulations of the spectra obtained with the original data [41]. The spectrum was modeled in such a way that same composition fits all the spectra taken from the same sample with different beams. In addition, X-ray photoelectron spectroscopy (XPS, PHI Model 5600ci, Casa XPS Analytical Software) was performed to determine the concentrations and binding status of Ti, B and C within the TiBC coatings. XPS spectra were obtained after removing the surface layer of samples by sputtering with Ar^+ ions (3 keV, 15 μA) for 15 s and the spectra were calibrated for the value of the carbon peak C1 s at 284.5 eV.

3. Results

Post deposition AFM analysis demonstrated that surface roughness does not change substantially even after deposition of relatively thick (3–5 μm) TiCrCN/TiCr multilayer coatings. The LAFAD-UBM TiBC coatings with both ML and SL architectures

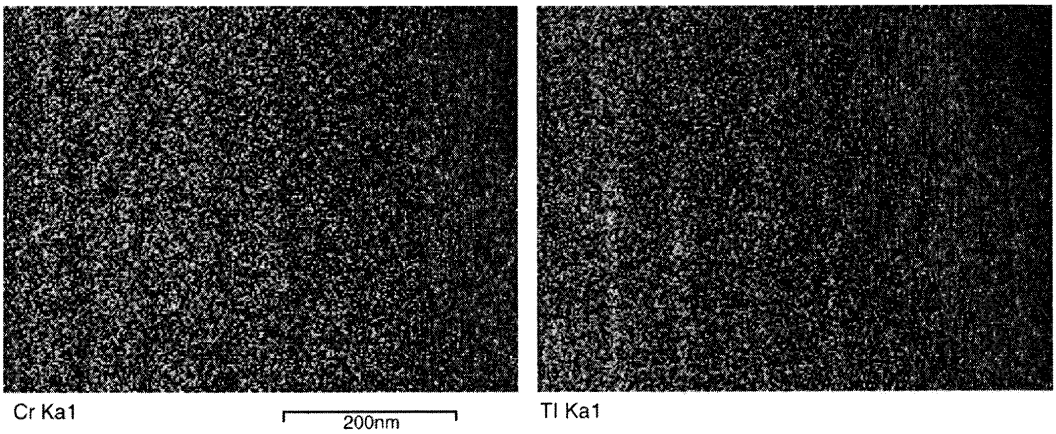


Fig. 4. Cr and Ti X-ray maps of a coating segment bottom bond coating segment showing systematic layers with reduced Cr levels and enhanced Ti levels. Note: the layers with low Cr and enhanced Ti signals are spaced at approximately 100 nm.

also demonstrated extremely smooth surface profiles. The 1 μm thick TiBC SL coating surface on Si wafer did not show any substantial increase in surface roughness relative to the initial roughness. Minor coating defects were observed as distant isolated pits. Auger spectra taken from these pits indicated the presence of a Ca as a likely cause of these surface defects which was associated with environmental dust particles.

The nanolaminated multilayer cermet coatings deposited by LAFAD technology has already been described elsewhere [33,43]. The micro-laminated structure consisting of TiCrN sublayers having thicknesses of approximately 100 nm can be seen in HRTEM mapping shown in Fig. 4. The TiCrN sublayers are separated by metallic interlayers having a thickness of approximately 10 nm. The dual-arc LAFAD process exposes the substrates in turn to Ti and Cr vapor plasma jets resulting in the formation of a nanolaminated substructure in both TiCrN and TiCr sub-layers, illustrated by GD-OES spectra presented in Fig. 5 [33]. A HRTEM image of the nanolaminating substructure of the TiCrN sublayer in TiCr/TiCrN multilayer cermet coating used as the first (bottom) coating segment in this work is shown in Fig. 6. The bilayer period of TiCrN nanolayers results in a thickness of approximately 2.5 nm, which can be explained by rough estimation based on the deposition rate for TiCrN/TiCr coating of about 1 μm/hr for substrates with single rotation arrangement paths in relation to the deposition sources [6,32,67,68]. At 9 rpm, substrates make 540 rotations per hour, which generates 540 biperiods each having thickness approximately 1.85 nm.

The results of the compositional analysis of the hybrid LAFAD-UBM TiBC coatings with different architectures were

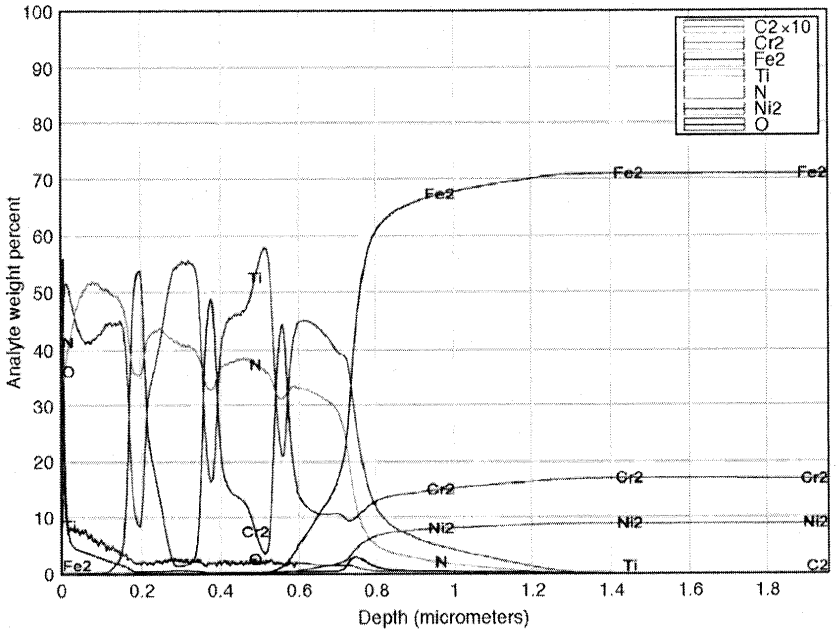


Fig. 5. GDOES spectra of TiCrN/TiCr nanolaminated cermet coating.

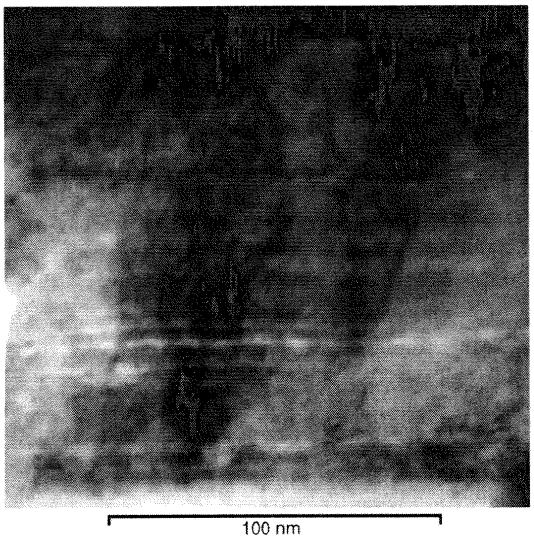


Fig. 6. HRTEM image of the TiCrN sublayer of a TiCr/TiCrN multilayer bond coating segment showing systematic nanolayer architecture with about 2 nm biperiod of TiN/CrN nanometric sublayers deposited by dual filtered arc LAFAD plasma source with primary cathodic arc sources equipped with Ti and Cr targets.

obtained by EDS/RBS techniques. Typical compositions of the TiCrCN transitional layer coating and TiBC upper tribological coating segment with ML and SL architectures are presented in Table 1. RBS and EDS techniques show similar results when coating thickness is greater than 1 μm. It can be seen that RBS provides better resolution of light elements. The carbon and boron concentration in TiBC (SL) and TiBC (ML) coatings are the same since both coatings have identical exposure to B_4C sputtering by UBM sources and carbon deposition from a HC/Ar auxiliary arc plasma environment. At the same time, Ti concentration is reduced in TiBC ML vs. SL coating due to interruptions of the titanium vapor plasma flow during deposition of multilayer TiBC coating architecture. The TiBC coating elemental composition defined by RBS vs. CH_4 flow rate for coatings deposited by different combinations of LAFAD/UBM plasma sources are shown in Fig. 7. Argon flow rate was constant at approximately 70 sccm, while CH_4 flow rate was set to 4 sccm, 8 sccm, and 16 sccm. Further increase in methane flow rate affects coating integrity: when CH_4 flow rate exceeds 18 sccm the carbon rich soot appears on the substrate fixtures and occasionally on substrates, especially when the substrates are processed with double rotation. Carbon

Table 1
Elemental composition of TiCrCN and TiBC coatings

Coating	Elemental Concentration at %					
	B	C	N	Ti	Cr	Ar
TiCrCN by EDS		28	27	31	14	
1 μm TiBC single layer EDS*/RBS	36/52	50/40	0	10/8	0	4/0
1 μm TiBC(5 min)/BC (15 min) multilayer EDS*/RBS	52/52	37/44	0	6/4	0	4/0

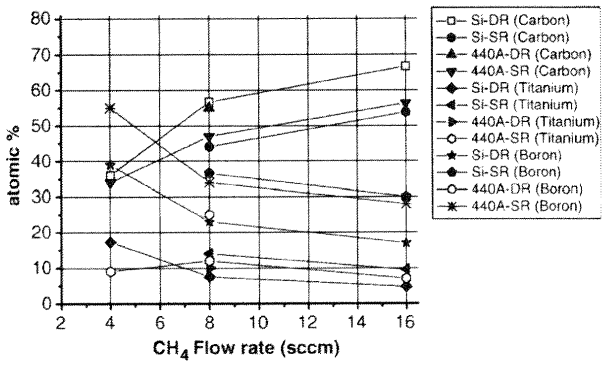


Fig. 7. TiBC coating elemental composition (at.% by RBS) vs. CH_4 flow rate.

concentration is increased for the coatings prepared with double rotation vs. single rotation, which can be attributed to higher level of exposure of double rotating surfaces to hydrocarbon plasma environment. The carbon concentration increases, while concentrations of Ti and B decrease when methane flow rate increases. The XPS spectra taken from two samples with TiBC coatings deposited by FAD/UBM process with 8 sccm methane flow rate show a strong evidence of large free carbon concentration in the coating in addition to boron carbide phase as illustrated in Fig. 8.

Nanohardness (Berkovich) was measured for selected P675 coupons with different TiCrCN+TiBC coatings. An example of the nanoindentation data obtained with a CSM mode is shown in Fig. 9. From this figure, data was leveled at indentation depths between 100 and 300 nm for both hardness (Fig. 9a) and elastic modulus (Fig. 9b). This analysis helped to select indentation depth regions for data averaging when both surface and substrate effects on the indentation response were minimized. The average H and E values were obtained in a similar way for all coatings and results are summarized in Table 2. It can be seen that the hardness of the TiCrCN bottom coating segment is about 20 GPa, which is slightly less than the hardness of TiCN/Ti multilayer coatings deposited by LAFAD technology (~25 GPa [33,43]). These results are in agreement with the data obtained by load-displacement method in [44] for the same

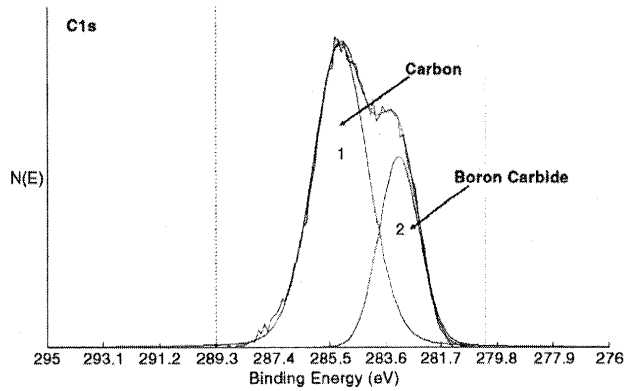


Fig. 8. X-Ray photoelectron spectrum showing carbon peak from typical TiBC coating. Note: ~70% of carbon is bound to itself (amorphous C matrix), whereas ~30% is B_4C (embedded nanocrystallites). Courtesy of Jim Anderson.

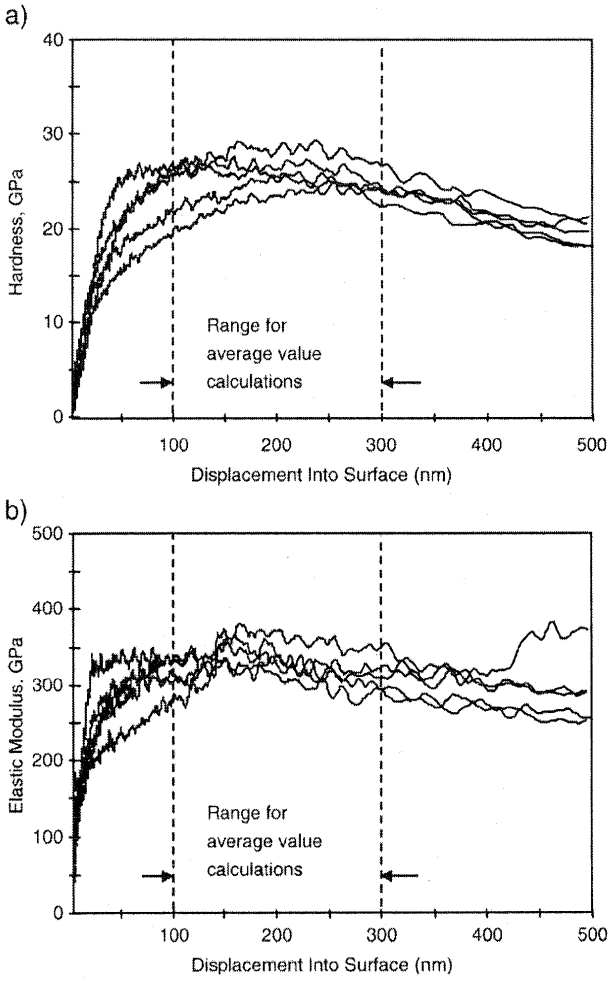


Fig. 9. Examples of nanoindentation data for a) hardness and b) elastic modulus obtained with a continuous stiffness monitoring mode for a TiBC (SL) coating on Pyrowear 675 substrate. Average values of hardness and elastic modulus were calculated over indicated range where their dependence on the indentation depth was minimized. Individual curves represent repeated indentations in different sample locations (only five are shown for clarity).

type of coatings. The nanohardness for two-segmented TiCrCN +TiBC coating is higher, ranging from 23–25 GPa. The nanohardness results for relatively thin (0.3–0.5 μm) coatings on Si wafer substrates are influenced by substrate deformation (indentation depth 500 nm), which explains the observed lower absolute nanohardness values for these coatings in comparison with 25 GPa for relatively thicker (~1.5 μm) TiBC coatings deposited on Pyrowear 675. The substrate effect is further emphasized by the consistent trend towards lower nanohardness in double rotation samples, which have ~60% coating thickness versus single rotation samples. Nevertheless, nanohardness results from each coated sample can be correlated to the vapor process combinations and hydrocarbon flow rates. Results show that control of hydrocarbon flow rates during coating deposition has a marked effect on the resulting coating nanohardness with the highest nanohardness of 25 GPa and 18.4 GPa on Pyrowear 675 and Si respectively for TiBC at 8 sccm CH_4, followed by slightly lower nanohardness of 17.7 GPa on Si results for a B_4C coating deposited without hydrocarbon gas addition. The calculated value of H^3/E^{*2} which has been shown to be related to resistance to plastic deformation and coating toughness [83,84] was found to be in the range of 0.060 GPa–0.167 GPa for the deposited coatings, and also dependent on hydrocarbon flow rate, with the highest value of 0.167 GPa demonstrated for the TiBC architecture at 8 sccm CH_4.

During initial development of TiCrN/TiCrCN/TiCrC coatings, adhesion by Rockwell C (1450 N) indentation testing revealed that the bottom TiCrCN coating deposited by LAFAD process maintained high adhesion in all cases, while top segment thin TiCrC carbide layers showed frequent delamination (HF5HF6). Adhesion testing of the TiCrCN+TiBC coatings by Rockwell C (1450 N) indentation, revealed much higher adhesion of the top TiBC layer (HF1HF3) as compared to TiCrC top layer, and as a result TiBC coatings were selected for further development with (SL) vs. (ML) architectures as the primary variable. It was found that TiBC (SL) in most cases demonstrated better adhesion than TiBC (ML). The TiBC/BC multilayer structure was found to exhibit interlayer delamination failure at multilayer interfaces. The worst adhesion was found on samples having a TiBC/BC multilayer ~1.5 μm segment followed by a TiBC ~1.5 μm segment (HF6 delamination to 2× radius of the indent). The combined adhesion results demonstrate that the maximum thickness of the top TiBC layer is limited to approximately 11.5 μm, due to high stresses in this nanocomposite coating. Conversely, the thickness of the bottom TiCrCN segment does not appear to be a

Table 2
Hardness, elastic modulus and resistance to plastic deformation parameter (H^3/E^{*2}) for coatings deposited by hybrid LAFAD/UBM process vs. process parameters

Coating	TiCrN (LAFAD source only)	TiBC (SL)	TiBC (ML)	TiCrC		TiBC		TiBC		TiBC		BC		TiBC	
(Gas, flowrate)		(CH_4, 8 sccm)	(CH_4, 8 sccm)	(CH4, 8 sccm)		(CH_4, 4 sccm)		(CH_4, 8 sccm)		(CH_4, 12 sccm)		(CH_4, 0 sccm)		(C_2H_2, 4 sccm)	
Rotation	SR	SR	SR	SR	DR	SR	DR	SR	DR	SR	DR	SR	DR	SR	DR
Substrate	Pyrowear 675 carburized	Pyrowear 675 carburized	Pyrowear 675 carburized	Si	Si	Si	Si	Si	Si	Si	Si	Si	Si	Si	Si
Residual stress [GPa]	−0.17	<−1	<−1	<−1	<−1	<−1	<−1	<−1	<−1	<−1	<−1	<−1	<−1	<−1	<−1
H [GPa]	21	25	24	14.5	12.7	16.0	14.6	18.4	16.4	12.7	11.2	17.7	14.1	15.4	11.5
E [GPa]		325	285	179	169	197	174	181	178	176	143	185	183	179	139
H^3/E^{*2} [GPa]		0.14	0.16	0.084	0.063	0.093	0.090	0.167	0.122	0.058	0.060	0.142	0.074	0.100	0.069

Table 3
Summary of scratch test results for selected TiCrCN+TiBC coatings on carburized pyrowear 675

	Sample description		
	TiCrN 1.3 μm*	TiCrN 1.3 μm	TiCrN 1.3 μm
	TiBC (SL) 1 μm**	TiBC (SL) 1 μm	TiBC (SL) 1 μm
Lower critical load (N)	47+/−11	30+/−3	23+/−2
Upper critical load (N)	124+/−3	122+/−8	113+/−4

*Bottom segment, **top segment.

significant variable in terms of the overall two-segment coating adhesion. Acoustic emission scratch test results supported the Rockwell indentation results by exhibiting large variations between upper and lower critical load values, indicating initial top segment failure. Measured lower critical load values correlated to initial fracture and delamination of the top segment architecture from the bottom segment. Complete coating failure and removal from the scratch track was measured as an upper critical load value. Excellent adhesion was indicated by upper critical load values that were consistently measured between 100 N to 120 N. The best lower critical load values were demonstrated by TiBC(SL) top segment architectures. Independence from top segment architecture in upper critical load measurement was observed, which indicated that measured upper critical values represented bottom segment adhesion. A summary of the scratch test results obtained by AFRL is shown in Table 3.

4. Discussion

Carbon rich carbides are well known for their ability to combine high wear resistance with low friction at high contact loads, which make them attractive for machine parts applications like gears, bearings, shafts, etc. [14–18,26,35]. In nanocomposite coatings deposited by FAD/UBM process, the hard amorphous carbon matrix, similar to DLC coatings consisting of a highly cross-linked network of carbon atoms, formed under high fluxes of ionized atoms conveyed by the plasma to substrates [9–25]. Using co-deposition of MeC and carbon from two or more sputtering or evaporating sources in addition to dissociated hydro-carbon reactive gaseous plasma can achieve the highest functional properties, while processing at relatively low temperatures, and without significant hydrogen concentration in the process gas environment [16,17,35]. Boron forms hard and corrosion resistant compounds with titanium, chromium and carbon, which are widely used for surface engineering and in the cermet industry [11–18,27,29]. Incorporating hard phases of transitional metal carbides and borides within the amorphous carbon matrix controls stresses and increases wear resistance and critical load, while retaining low friction [8,10,11,21,23]. It allows the improvement in coating toughness, while retaining a relatively high hardness comparable to conventional hard cermet coatings.

The extreme conditions near the substrate surface created by metal-gaseous ion bombardment (multi-charged metal ion energies ranging from 40 to 200 eV) result in high-energy dissipation at localized collision areas on the substrate surface [45,75,78]. During a very short time period, associated with energy relaxation of ions bombarding the growing film, the equivalent temperature in these areas can substantially exceed the bulk substrate temperature. Effectively, a dramatic increase in ion-substrate interactions and chemical reactivity is realized. In this environment, new compounds form at rates which surpass those predicted by the associated Arrhenius rate laws at the bulk substrate temperature [10–14,45,75,78,79]. In the FAD/UBM TiBC coating deposition process, individual sources of Ti, B, C are separately controlled. In addition, the selected positioning of these sources in the FAPSID chamber layout permits substrate exposure to different deposition vapor flows (e.g. Ti, B, C) during the coating process (Fig. 1). In case of single rotating substrates, Ti plasma vapor is conveyed directly towards the substrates from LAFAD plasma source and indirectly by resputtering of Ti from the UBM target surfaces. B and C species are co-sputtered from the UBM sources. In addition, carbon and carbon containing CH_x radical species are generated as dissociation products from methane-containing gaseous plasma atmosphere. The dual rotating substrates experience increased exposure to gaseous carbon-containing plasma compared with single rotating substrates, which results in lower concentrations of Ti and/or B within these films (Fig. 7). During exposure to methane-precursor gaseous plasma only, the conditions are favorable to the formation of diamond-like carbon [75,79]. With the intense ion-bombardment inherent in the FAPSID system, the sp^3/sp^2 ratio within the resultant a-C coating increases. When Ti and/or B sources are employed in conjunction with the a-C plasma deposition environment, multiple Ti–B–C containing crystalline phases form depending upon the substrate position within the FAPSID system. The XRD patterns presented in Fig. 10 illustrate this occurrence. Peaks identified in these patterns demonstrate the coexistence of strongly crystallized TiB_2 with weakly crystallized $Ti_xB_yC_z$ solid solution phases in the FAD/UBM coatings. The sharp TiB_2 peak indicates strong crystallinity compared with the relatively broad peaks of the $Ti_xB_yC_z$ solid solution phases, indicating the nanocrystalline nature of the solid solution constituents. The exact composition of this ternary solid solution resembles the $(B_{12})_4Ti_{1.86}C_2$ ternary phase having a tetragonal boron structure described in [80]. The near-surface conditions of intense ion bombardment in the FAD/UBM process may also permit formation of other refractory crystalline phases, e.g. TiC, TiB, B_4C and their nonstoichiometric forms; however, due to the extremely small crystallite sizes, these phases will remain undetected via XRD.

Thermodynamic modeling was employed to assess the favored phase compositions of FAD/UBM TiBC coatings. Thermodynamic equilibrium calculations were used to simulate favored mixtures of individual phases and solid solutions at elevated temperatures in the Ti–B–C based coatings. According to the second law of thermodynamics, for the calculation of phase equilibrium in isolated multicomponent system, containing gaseous phase components, immiscible condense phase components and solid solutions, it is necessary to maximize the

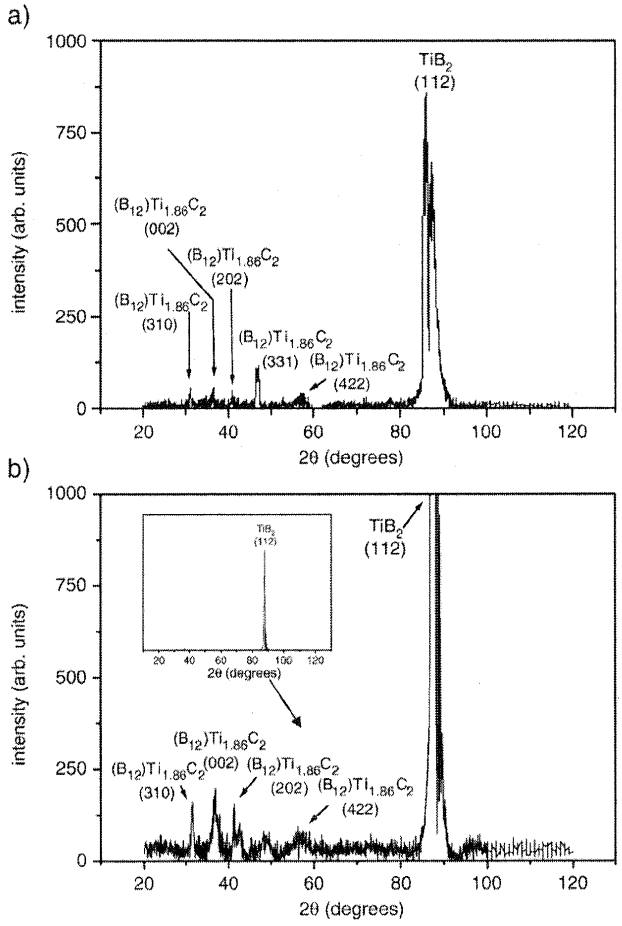


Fig. 10. XRD spectra taken from two samples with TiBC nanocomposite cermet coating deposited by two different FAD/UBM processes with different methane flowrates. (a) – Sample No.41 (8 sccm CH_4): Ti(6 at.%)C(53 at.%)B(26 at.%); (b) – sample No.49 (0 sccm CH_4): Ti(15 at.%)C(15 at.%)B(25 at.%). Note: PDF card numbers used to identify peaks: TiB_2: 35-0741; $(B_{12})_4Ti_{1.86}C_2$: 73-0658.

total entropy of the system. This can be presented in the following form [46]:

$$S = \sum_{i=1}^{k} S_i^{(p_i)} \cdot n_i + \sum_{r=1}^{R} S_r \cdot n_r + \sum_{x=1}^{X} \sum_{q=1}^{Q_x} S_{xq} n_{xq}$$
$$= \sum_{i=1}^{k} \left(S_i^0 - R_0 \ln \frac{R_0 T n_i}{v} \right) \cdot n_i + \sum_{r=1}^{R} S_x^0 \cdot n_x$$
$$+ \sum_{x=1}^{X} \sum_{q=1}^{Q_x} \left(S_{xq}^0 - R \ln(n_{xq}/n_x) \right) \cdot n_{xq}$$

where k is the number of gas phase components; R is the number of a single immiscible condense phase components; X is the number of solid solutions; Q_x is the number of components in a solid solution x; $S_i^{(pi)}$ is the entropy of gas phase component i at the partial pressure $p_i = R_0 T n_i / v$, which it will have in the equilibrium state; v is specific volume of the entire system; S_i^0 is the standard entropy of gas phase component i at the temperature T and pressure of 1 atm; S_r^0 is standard entropy of a single condense phase component r, which is a function of temperature only; S_{xq}^0 is standard entropy of the component q of the solid solution x.

To determine the parameters in the equilibrium state it is necessary to find the values of all variables, including mole fractions of all components when the entire entropy of the system S reaches its maximum with certain additional conditions applied on the system. These additional conditions include: the conservation of the total internal energy of the system, as the system is isolated; the conservation of the total mass of all components of the system; and electroneutrality condition:

$$-U + \sum_{i=1}^{k} U_i \cdot n_i + \sum_{r=1}^{R} U_r \cdot n_r + \sum_{x=1}^{X} \sum_{q=1}^{Q} U_{xq} \cdot n_{xq} = 0;$$
$$b_j = \sum_{i=1}^{k+R+X} a_{ji} n_i, \qquad (j = 1, 2, \ldots m); \qquad \sum_{i=1}^{k} a_{ei} n_i = 0,$$

where U is the total internal energy of the system, U_i, U_r, U_{xr} – are internal energy the gas phase components, single immiscible components of condense phase and components of solid solutions respectively; b_j – mole fraction of the element j in the system; a_{ji}, a_{ei} – stoichiometric coefficients. In case of a regular solution model, the partial enthalpy of mixing has to be added to the total internal energy of solid solutions in addition to the internal energies of components. In the ideal solution model used in this work the enthalpy of mixing is assumed to be zero. In addition, the normalization conditions have to be satisfied for each of the solid solutions:

$$\sum_{q=1}^{Q_x} \frac{n_{qx}}{n_x} - 1 = 0, \qquad n_x \geq 0, \qquad (x = 1, 2, \ldots X)$$

To perform these calculations, the thermodynamic equilibrium code, TERRA was employed. TERRA is a recently developed version of the ASTRA code, which was used extensively for thermodynamic modeling in Eastern Europe during the 1980s–1990s [46]. Its database includes most of the refractory compounds properties compatible with SGTE and JANAF-NIST databases [47,48,69]. Various models of the Ti–B–C

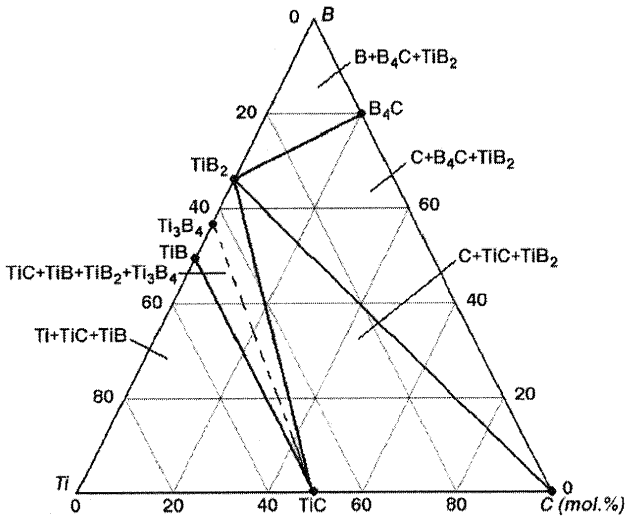


Fig. 11. TiBC ternary phase diagram at $T = 700$ K, $p = 0.1$ Pa.

system were prepared within the temperature range of 300 °C to 1100 °C at a constant pressure of $P=10^{-3}$ Torr. These conditions closely resemble those of the hybrid FAD/UBM TiBC coating deposition process, which provides intense ion bombardment during coating material vapor condensation. A calculated ternary phase diagram of TiBC system at 700 K and 0.1 Pa (typical FAD/UBM TiBC deposition conditions) is shown in Fig. 11. This calculation takes into account the individual stoichiometric

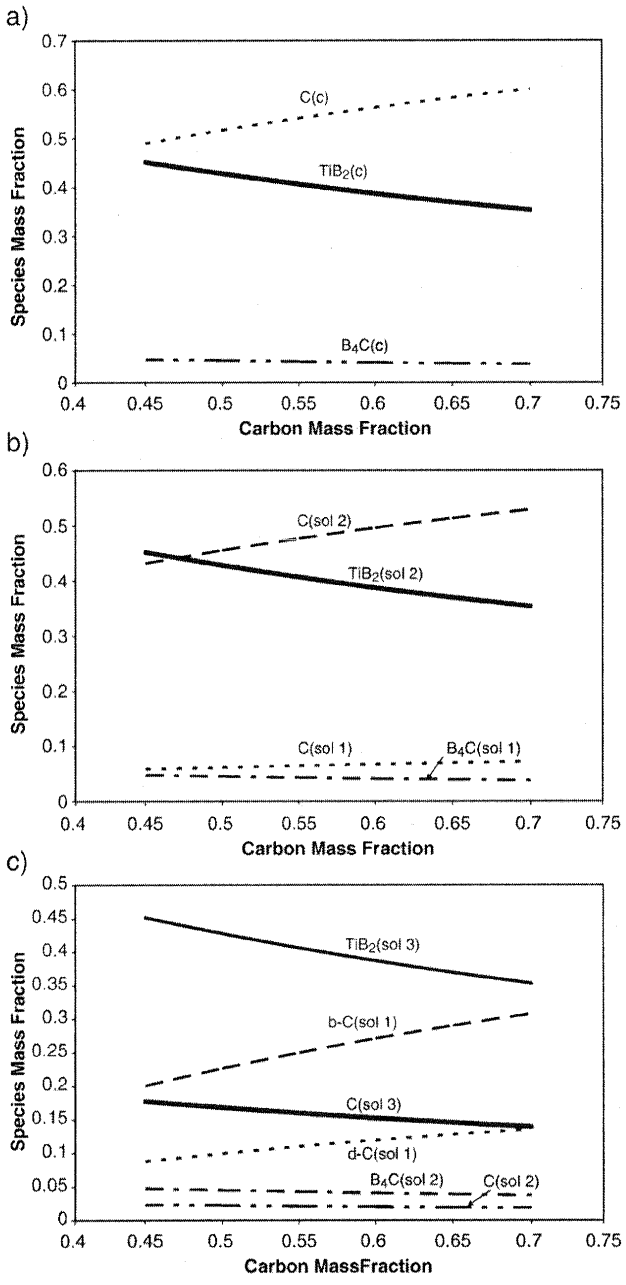


Fig. 12. Thermodynamic modeling results (see detailed modeling parameters in Table 4): a – high boron composition, no solid solutions, with bC (β-Graphite) as the free carbon phase; b – high boron composition, solid solutions without free carbon phase; c – high boron composition, solid solutions with bC + dC solid solution as the free carbon phase; d – high boron composition, solid solutions with bC + aC solid solution as the free carbon phase; e – low boron composition, solid solutions with bC + aC solid solution as the free carbon phase.

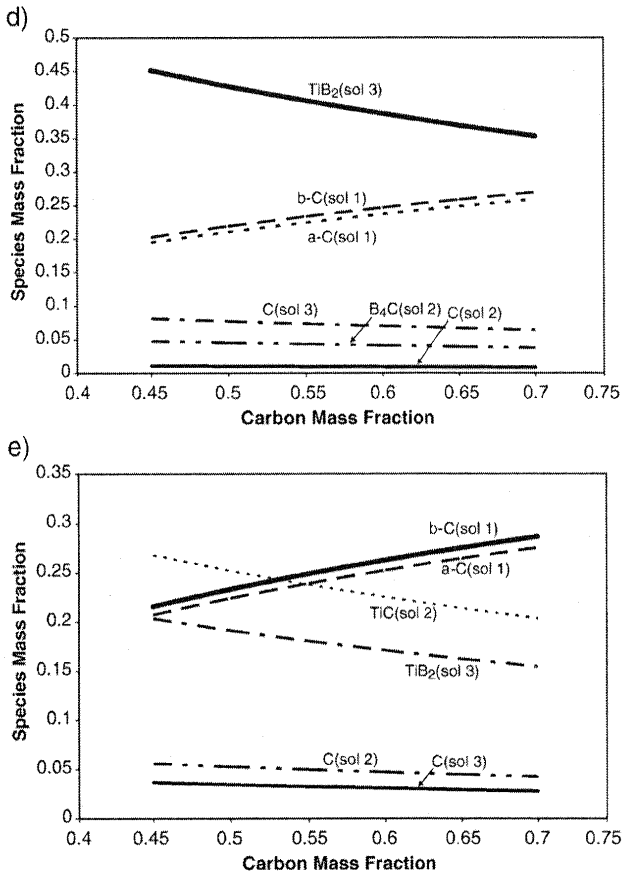


Fig. 12 (*continued*).

compound phases only, which can be considered as a zero-order approximation, providing that it does not take into account solid solutions in the TiBC system. The Ti_3B_4 phase was not included in this calculation. The data associated with this phase is shown in Fig. 11 as it appears in the modeling iagram, calculated by Gusav et al. [49]. The results show that titanium diboride coexists either with TiC or with B_4C. Free carbon (β-Graphite phase) co-exists with both TiB_2+B_4C and TiB_2+B_4C compositions. No ternary TiBC compounds are found in this system. This phase composition exists in wide range of pressures (1 MPa–0.1 Pa) and temperatures (up to 1800 K). These results are in a good agreement with more précised calculations and experimental data with exception of very narrow area boarding between $\{TiB_2+TiC+C\}$ and $\{TiB_2+B_4C+C\}$ areas where TiB_2 coexists with TiC and B_4C, which took into account non-stoichiometric compounds and solid solutions as well as phase diagrams based on experimental data [49–51,69,72–74,86]. Similar results were obtained recently for B–C–N coatings deposited by reactive magnetron sputtering [71]. In this case, the ternary compounds were found to be a small impurity in amorphous films composed of boron, carbon and nitrogen and contained B═C, B═N, C═N, C═C covalent bonding.

Further calculations were performed with different potential solid solution compositions presented in the TiBC elemental system. These calculations were based on ideal solution model as a first-order approximation. This included modeling of

diamond-like carbon phases, whose formation is induced by high compressive stresses and thermal spikes from co-incidental ion bombardment of the growing film. These created conditions for the formation of high pressure sp^3 coordinated (diamond like) phases such as tetrahedral amorphous carbon in addition to sp^2 coordinated (graphite like) carbon [75,78,85]. Two approaches were used for modeling such amorphous carbon mix in the TiBC system. In the first approach, amorphous carbon was modeled as an ideal solid solution including β-graphite (bC) and diamond (dC). In the second approach, free carbon was modeled as an ideal solid solution including β-graphite (bC), having enthalpy of formation $H_f(bC)=0$ as the basic elemental phase, and a hypothetical amorphous carbon (aC) carbon phase, having enthalpy of formation $H_f(aC)$ ranging from 200 to 1000 J/mol K while other thermodynamic parameters (entropy, specific heat capacity) where taken equal to that of graphite. Thermodynamic properties of diamond phase were taken from Refs. [70,81]. Examples of typical results from these calculations presenting phase composition vs. carbon content are shown in Fig. 12a–e. The elemental compositions chosen for this modeling resemble the experimental results from the hybrid FAD/UBM TiBC coating deposition processes, as shown in Fig. 7. Two sets of elemental compositions were considered in these calculations: one with higher boron content; and another one with lower boron content. These sets describe two experimental situations in the FAD/UBM process: when the substrates to be coated are positioned near titanium LAFAD vapor plasma source (lower boron concentration in the coating); and, when the substrates are positioned near UBM sputtering source with B_4C targets (higher boron concentration in the coating). The set of compounds and solid solutions used in these calculations are presented in Table 4. It includes solid solutions of carbon in carbides and TiB_2, binary solutions of carbides and borides, solution of boron in B_4C, and solution of titanium in TiC and in TiB_2. TiB2/B and TiC/B solutions were not included since boron has very low solubility in TiB_2 and TiC at temperatures below 2000 K [68,72–74,86].

The compositions in Fig. 12a assumed that β-Graphite (bC) is the only free carbon phase and there are no solid solutions of carbon in carbide phases. It can be seen that in all cases TiB_2 and B_4C phase concentrations decreased when the free carbon concentration increased. The concentration of TiB_2 was much greater than B_4C. The TiC phase did not co-exist with TiB_2 and B_4C when the elemental composition with increased boron concentration is considered. This result is in good agreement with the ternary phase diagram (Fig. 10). The results of calculations shown in Fig. 12b used the same elemental composition as in Fig. 12a, but 16 binary ideal solid solutions were taken into account (see Table 4) and free carbon was allowed to form solid solutions with other phases. From the calculation results, only two solid solutions could co-exist: TiB_2/C and B_4C/C. No independent stoichiometric phases are thermodynamically favorable along with corresponding solid solutions. In this case all the carbon formed solid solutions with Ti and B and carbon solubility increased with carbon content. In this model, the carbon solubility reaches levels which are much above the known solubility of carbon in B_4C and TiB_2 from prior phase diagram calculations and experimental data [50,71].

Table 4
Phase composition considered in thermodynamic modeling of the TiBC coatings (Fig. 12)

	Fig. 12a	Fig. 12b	Fig. 12c	Fig. 12d	Fig. 12e
Ti/B (mol/kg)	2.8/1.6	2.8/1.6	2.8/1.6	2.8/1.6	2.8/0.5
Stoichiometric phases					
B_4C	X				
TiB_2	X				
TiC	X				
bC (β-Graphite)	X				
Ideal binary solid state solutions					
bC + aC				X	X
bC + dC			X		
bC + B_4C		X	X	X	X
bC + TiC		X	X	X	X
bC + TiB_2		X	X	X	X
TiB + TiB_2		X	X	X	X
TiC + TiB_2		X	X	X	X
B_4C + TiB_2		X	X	X	X
TiC + B_4C		X	X	X	X
Ti + TiB_2		X	X	X	X
Ti + TiC		X	X	X	X
Ti + B_4C		X	X	X	X
B+ B4C		X	X	X	X
B + TiC		X	X	X	X
B + TiB_2		X	X	X	X
TiB + TiC		X	X	X	X
TiB + B_4C		X	X	X	X

Note: bC-β-Graphite ($H_f=0$); aC-hypothetical amorphous carbon phase with increased C=C bonding energy ($H_f=200\div1000$ J/mol K); dC-diamond ($H_f=1895$ J/mol K [81], Cp is taken from Ref. [70]).

As a further model development, a substantial increase of sp^3 bonds in the amorphous carbon matrix was taken into account and the free carbon phase in the coating was modeled as an ideal solution of β-graphite (bC) and diamond which has the highest enthalpy of formation of all carbon phases. The calculation results shown in Fig. 12c used the same elemental composition (higher boron) as in Fig. 12b, including the 16 solid solutions as considered in Table 4 in addition to a graphite–diamond solution. These results are similar to the results presented in Fig. 12a with a clear increasing trend of the free carbon phase concentration, and a decrease of TiB_2/C and B_4C/C solid solution concentrations with increase of carbon content. However, in Fig. 12c, the solubility of carbon does not exceed 20%, which agrees with data on carbon solubility in these compounds. The concentration of sp^3 coordinated carbon in the amorphous carbon matrix is below 30%. For more realistic simulation of the amorphous carbon phase formed by vapor condensation with ion bombardment, the following considerations were taken into account. The amorphous carbon coatings formed by sputtering of carbon containing targets and dissociation of C–H gaseous species under condition of intense ion bombardment consists of small concentration of hydrogen along with a mixture of sp^1, sp^2 and sp^3 bonded carbon atoms [75,78]. The lattice energy of amorphous carbon (aC) is considerably smaller than in diamond, and can be placed between

diamond and graphite with more diamond-like properties associated with aC coatings having higher concentration of sp^3 bonded carbon and more graphite-like properties associated with aC coatings having lower concentration of sp^3 bonded carbon atoms [75,85]. This consideration allows formulation of an amorphous carbon model as a solid solution, including graphite and hypothetical amorphous carbon aC phase having higher lattice energy than that of graphitic carbon. Fig. 12d represents the results of thermodynamic calculations, where amorphous carbon matrix was modeling as a solid solution including β-Graphite (bC) and hypothetical amorphous carbon phase (aC) having enthalpy of formation ranging from 200 to 1000 J/mol K, while other parameters of this phase where taken the same as that of graphite. The results obtained in these calculations show that aC solubility in bC/aC modeling solution decreases from 50% to 40% when the enthalpy of formation of the aC phase increases from 200 to 1000 J/mol K. In addition, the results of calculations show that variation of the enthalpy of formation of aC carbon phase appears to have little influence on the solubility of carbon in B_4C/C, TiB_2/C and TiC/C solid solutions. Taking into account the lack of direct experimental data of amorphous carbon binding energies in TiBC coatings, the enthalpy of formation of aC atoms when modeling the C/aC solid solution was taken as $H_f(aC)=200$ J/mol K for further calculations. In this case, the free carbon constitutes near equal amount of graphite and amorphous carbon phase, which appears to be more realistic than the graphite/diamond solution model. The solubility of carbon in TiB_2 and B_4C at temperatures less than 1000 K does not exceed 15% and 25% respectively. These results are in good agreement with theoretical and experimental data [49–51,68,72–74,86].

The calculation results for the TiBC system with lower boron amount, using the same model, including 16 binary solutions in addition to the bC/aC solid solution (representing the free carbon phase), are presented in Fig. 12e. The difference between results presented in Fig. 12d and e is that TiC replaces B_4C when the boron concentration is low. The concentration of the TiC/C solid solution is nearly equal to the concentration of TiB_2/C solution. The carbon solubility in TiC does not exceed 18%, and slightly increases when carbon content increases. These results are also in good agreement with experimental data and theoretical calculations [68,72–74,86]. These results provide validity for the chosen set of solid solutions including free carbon modeling in the thermodynamic modeling calculations.

These models show that in all cases, a relatively high concentration of TiB_2 is present throughout all ranges of parameters representative of the FAD/UBM coating deposition process. TiB_2 co-exists either with B_4C (higher boron concentration) or with TiC (lower boron concentration), in agreement with ternary phase diagrams. More detailed calculations revealed that B_4C and TiC phases coexist (in low concentrations) in a relatively narrow Ti concentration window – in the transition zone between B_4C, as the sole carbide phase, and TiC as the sole carbide phase. These modeling results agree with those produced previously, including the phase diagram of nonstoichiometric Ti–B–C compounds [49–51,69,71]. It was shown that small B addition (<1 at.%) creates disordering in TiC, resulting in the formation of titanium borides (TiB, TiB_2, and Ti_3B_4). At high boron concentrations, TiB_2 coexists with B_4C and free carbon. At high Ti concentrations, titanium borides coexist with free carbon and TiC, which replaces B_4C in a titanium enriched TiBC composition. This occurs in a wide range of temperatures (500–1800 K), where the phase diagram has two well-defined areas: one with predominately TiB_2+TiC; and another with predominately TiB_2+B_4C, and possible solid solutions [49–51]. The results of thermodynamic modeling assist in the interpretation of XRD patterns from the TiBC coatings in this study (Fig. 10). During the deposition, the substrates are exposed to Ti, C and B containing metal-gaseous vapor plasmas depending upon the position of substrates in the FAPSID system chamber (e.g. either near the LAFAD titanium plasma source, or UBM boron–carbon sputtering source). This provides continuous formation of the most stable (TiB_2) crystalline phase and smaller concentrations of complex Ti–B–C solid solutions, embedded within a quasi-amorphous matrix formed by Ti and B doped diamond-like carbon.

Increase of the elemental carbon concentration in the plasma environment due to increase of the flowrate of C–H gas concentration (methane or acetylene) results in the increase of free carbon and a decrease of carbide and boride based solid solutions of the TiBC coating segment since the carbon concentration in solid solution cannot exceed the solubility limit. These results are in good agreement with experimental data presented in Figs. 7 and 8, which provide evidence for the existence of free carbon in TiBC coatings deposited by hybrid FAD/UBM technique. Similar results were obtained for deposition of boron carbide coatings by magnetron sputtering with addition of methane, where the amount of boron in coatings was decreased and carbon concentration was increased with the increase of CH_4 gas flow [27,77].

Different phase compositions of the deposited TiBC top coating segment have different mechanical properties. Optimizing the concentration of the hard boride and carbide phases in the carbon matrix allows control of the coating hardness, as illustrated in Table 2. The maximum hardness was achieved with the increase of the concentration of C–H gas (8 sccm for methane or 4 sccm for acetylene) which can be explained by contribution of titanium based borides and carbides into the ternary Ti–B–C coating. The Resistance to Plastic Deformation Parameter (RPDP) H^3/E^{*2} also reaches a maximum value when the methane flowrate is at 8 sccm. It should be noted that greater values of the RPDP parameter do not always correlate with actual wear or fracture resistance performance of coatings. There are a number of ways of toughening coatings such as nanostructuring, grain size optimization, composition and structure grading as outlined in Ref. [82]. The free carbon content reduces coating stresses, allows control of coating toughness and reduces the negative effect of high brittleness inherent in coatings composed of the hard carbide and boride phases. This could explain the results of the Rockwell C indentation and scratch adhesion testing. Addition of free carbon can also contribute to lower friction and higher wear resistance of the top coating segment [14,27,77].

From Table 2, coatings deposited with single rotation exhibit higher hardness then those deposited with double rotation and having higher carbon concentration. It has to be noticed that coating structure and morphology are different between TiBC coatings prepared with single and double rotation, which can influence functional properties of the coatings such as adhesion and hardness. Coatings deposited with double rotation have greater roughness than coatings deposited with single rotation. In addition to differences in chemical composition, FAD/UBM TiBC coatings deposited with double rotation are subjected to a lower flux of energetic titanium ions generated by LAFAD plasma source in comparison to the coatings deposited with double rotation. This leads to reduction of adatom mobility at low deposition temperatures, resulting in favorable columnar growth according to Thorton–Messier zone diagram [11]. This observation is also in agreement with results obtained in [76].

5. Conclusions

Multilayer nanocomposite cermet coatings have been developed which consists of two segments: the bottom multilayer nanolaminated TiCr/TiCrN bondcoating corrosion resistant segment, interfacing the steel substrate followed by a top tribological TiBC segment. The metallic interlayers in the TiCr/TiCrN bottom segment contribute to the increase of corrosion resistant properties as well as improvement in coating adhesion and toughness. The TiBC nanocomposite top coating segment consists of titanium carbide and boride crystals embedded in a hard amorphous carbon matrix. Co-deposition of 100% ionized titanium filtered arc vapor plasma with sputtering B–C flow in a highly ionized argon–hydrocarbon gaseous plasma environment allows precise control of the coating elemental composition, which correlates with its mechanical properties. Experimental evaluation and thermodynamic modeling suggest the structure of the top TiBC coating segment includes strongly crystallized non-stoichiometric TiB_2 with weakly crystallized ternary and binary solid solutions and non-stoichiometric carbide phases of the TiBC elemental system incorporates into an amorphous carbon matrix. This coating deposited by hybrid FAD/UBM technology has demonstrated extremely high toughness and adhesion at hardness levels comparable to conventional hard cermet coatings, which make the coating and a deposition method a promising candidate for tribological tasks in high load aircraft applications.

References

[1] Alloy Data, Carpenter Technology Corporation via www.carpenter.com.
[2] J.A. Jehn, Surf. Coat. Technol. 125 (2000) 212.
[3] M.J. Park, A. Leyland, A. Matthews, Surf. Coat. Technol. 43/44 (1990) 481.
[4] M. Hans, E. Bergmann, Surf. Coat. Technol. 62 (1993) 626.
[5] P.K. Vencovsky, R. Sanchez, J.R.T. Branco, M. Galvano, Surf. Coat. Technol. 108–109 (1998) 599.
[6] Vladimir Gorokhovsky, Brad Heckerman, Philip Watson, Nicholas Bekesch, Surf. Coat. Technol. 200 (18–19) (2006) 5614.
[7] H.W. Wang, M.M. Stack, S.B. Lyon, P. Hovsepian, W.-D. Munz, Surf. Coat. Technol. 126 (2000) 279.
[8] O. Knotek, F. Loffler, A. Schrey, B. Bosserhoff, Surf. Coat. Technol. 126 (2000) 138.
[9] Z. Has, S. Mitura, V. Gorokhovsky, Surf. Coat. Technol. 47 (1991) 106.
[10] N. Novikov, V.I. Gorokhovsky, B. Uryukov, Surf. Coat. Technol. 47 (770) (1991).
[11] R.L. Boxman, D.M. Sanders, P.J. Martin, Handbook of Vacuum Arc Science and Technology, Noyes Publications, Park Ridge, N.J., 1995
[12] D. Sanders, A. Anders, Surf. Coat. Technol. 139 (2000).
[13] Hermann A. Jehn, Surf. Coat. Technol. 131 (2000) 433.
[14] K. Bewilogua, C.V. Cooper, C. Specht, J. Schroder, R. Wittorf, M. Grischke, Surf. Coat. Technol. 132 (2000) 275.
[15] Y.L. Su, W.H. Kao, Surf. Coat. Technol. 137 (2001) 293.
[16] M.P. Delpancke-Ogletree, O.R. Monteiro, Surf. Coat. Technol. 108–109 (1998) 484.
[17] E. Bertran, C. Corbella, A. Pinyol, M. Vives, J.L. Andujar, Diamond Relat. Mater. 12 (2003) 1008.
[18] M. Jarratt, J. Stallard, N.M. Renevier, D.G. Teer, Diamond Relat. Mater. 12 (2003) 1003.
[19] A. Erdemir, C. Bindal, G.R. Fenske, C. Zuiker, P. Wilbur, Diamond Relat. Mater. 86–87 (1996) 692.
[20] A. Erdemir, O.L. Eryilmaz, I.B. Nilufer, G.R Fenske, Surf. Coat. Technol. 133–134 (2000) 448.
[21] D. Paulmier, H. Zaidi, H. Nery, T.L. Huu, T. Mathia, Surf. Coat. Technol. 62 (1993) 570.
[22] B. Podgornik, S. Jacobson, S. Hogmark, Proceedings of World Tribology Congress 1, Vienna, 2001, p. 843.
[23] J.S. Zabinsky, J.H. Sanders, J. Najnaparamph, ibid,.
[24] A.A. Voevodin, J.P. O'Neill, J.S. Zabinski, Surf. Coat. Technol. 116–119 (1999) 36.
[25] A.A. Voevodin, J.S. Zabinski, Diamond Relat. Mater. 7 (1998) 463.
[26] Frederik Svahn, Tribology of Carbon Based Coatings for Machine Element Applications Acta Universitatis Upsaliensis. Comprehensive Summaries of Uppsala Dissertations from the Faculty of Science and Technology 1050. 40 pp. Uppsala, 2004.
[27] T. Eckardt, K. Bewilogua, G. van der Kolk, T. Hurkmans, T. Trinh, W. Fleischer, Surf. Coat. Technol. 126 (2000) 69.
[28] A.A. Voevodin, M.A. Capano, A.J. Safriet, M.S. Donley, J.S. Zabinski, Appl. Phys. Lett. 69 (188) (1996).
[29] P.S. Kisliy (Ed.), Cermets, Monograph, Institute of Superhard Materials of the Ukrainian Academy of Sciences, Kiev, 1985.
[30] E.H.A. Dekempeneer, V. Wagner, L.J. van IJzendoorn, J. Meneve, S. Kuypers, J. Smeets, J. Geurts, R. Caudano, Surf. Coat. Technol. 86–87 (1996) 581.
[31] S.J. Harris, G.G. Krauss, S.J. Simko, R.J. Baird, S.A. Gebremariam, G. Doll, Wear 252 (2002) 161.
[32] Vladimir I. Gorokhovsky, Rabi Bhattacharya, Deepak G. Bhat, Surf. Coat. Technol. 140 (2) (2001) 82.
[33] V.I. Gorokhovsky, D.G. Bhat, R. Bhattacharya, A.K. Rai, K. Kulkarni, R. Shivpuri, Surf. Coat. Technol. 140 (3) (2001) 215.
[34] V. Gorokhovsky, US Patent No.6,663,755.
[35] D. Nilsson, F. Svahn, U. Wiklund, S. Hogmark, Wear 254 (2003) 1084.
[36] W.-D. Munz, T. Hurkmans, G. Keiren, T. Trinh, J. Vac. Sci. Technol., A, Vac. Surf. Films 11 (5) (Sep/Oct 1993) 2583.
[37] J. Valli, U. Makela, A. Matthews, Surf. Eng. 2 (1986) 49.
[38] G.G. Stoney, Proc. R. Soc. Lond., A 82 (1909) 172.
[39] W.C. Oliver, G.M. Pharr, J. Mater. Res. 7 (1992) 1564.
[40] M. Chiari, et al., Nucl. Instrum. Methods Phys. Res., B Beam Interact. Mater. Atoms 184 (2001) 309.
[41] M. Mayer, SIMNRA User's Guide, Technical Report IPP 9/113, Max-Planck-Institute fur Plasmaphysik, Garching, Germany, 1997.
[42] M. Bielevski, R. Holt, A Review of Sacrificial Coatings to Replace Cadmium, Report No.LTR-ST-2174, Institute for Aerospace Research, NRC Canada.
[43] S.J. Bull, D.G. Bhat, M.H. Staia, Surf. Coat. Technol. 163–164 (2003) 499.
[44] J.R. Tuck, A.M. Korsunsky, D.G. Bhat, S.J. Bull, Surf. Coat. Technol. 139 (2001) 63.
[45] C.A. Davis, Thin Solid Films 226 (1993) 30.
[46] N.A. Vatolin, G.K. Moiseev, B.G. Trusov, Thermodynamic Modeling in High Temperature Inorganic Systems, Metallurgy, Moscow, 1994 (in Russian).

[47] L.V. Gurvich, I.V. Veitz, et al., Thermodynamic Properties of Individual Substanes. Forth edition in 5 Volumes, vol. 1, Hemisphere Pub., Co., New York, 1989, in 2 parts.
[48] NIST-JANAF, in: M.W. Chase Jr. (Ed.), Thermochemical Tables, Fourth edition, J. of Physical and Chemical Reference Data, Monograph, vol. 9, 1998.
[49] A.I. Gusev, A.A. Rempel, A. Magerl, Disorder and Order in Strongly Non-Stoichiometric Compounds, Springer, 2001, p.607.
[50] H. Duschanek, P. Rogl, H.L. Lukas, J. Phase Equilibria 16 (1995) 46.
[51] P. Rogl, H. Bittermann, International Journal of Refractory Metals and Hard Materials 17 (1999) 32.
[52] A.A. Voevodin, S.D. Walck, J.S. Zabinski, Wear 203–204 (1997) 516.
[53] A.A. Voevodin, J.S. Zabinski, J. Mater. Sci. 33 (1998) 319.
[54] A.A. Voevodin, J.P. O'Neill, J.S. Zabinski, Surf. Coat. Technol. 116–119 (1999) 36.
[55] A.A. Voevodin, J.S. Zabinski, Thin Solid Films 370 (2000) 223.
[56] A.A. Voevodin, M.A. Capano, S.J.P. Laube, M.S. Donley, J.S. Zabinski, Thin Solid Films 298 (1997) 107.
[57] A.A. Voevodin, J.S. Zabinski, Compos. Sci. Technol. 65 (2005) 741.
[58] K. Miyoshi, B. Pohlchuck, K.W. Street, J.S. Zabinski, J.H. Sanders, A.A. Voevodin, R.L.C. Wu, Wear 225–229 (1999) 65.
[59] A.A. Voevodin, J.P. O'Neill, J.S. Zabinski, Thin Solid Films 342 (1999) 194.
[60] In-Wook Park, Kwang Ho Kim, A.O. Kunrath, D. Zhong, J.J. Moore, A.A. Voevodin, E.A. Levashov, J. Vac. Sci. Technol., B 23 (2005) 588.
[61] A.A. Voevodin, J.S. Zabinski, in: A.A. Voevodin, D.V. Shtansky, E.A. Levashov, J.J. Moore (Eds.), Nanostructured thin films and nanodispersion strengthened coatings, Kluwer Academic Publishers, Dordrecht, The Netherlands, 2004, p. 103.
[62] A.A. Voevodin, M.A. Capano, A.J. Safriet, M.S. Donley, J.S. Zabinski, Appl. Phys. Lett. 69 (1996) 188.
[63] A.A. Voevodin, J.G. Jones, T.C. Back, J.S. Zabinski, V.S. Strel'nitzki, I.I. Aksenov, Surf. Coat. Technol. 197 (2005) 116.
[64] D.E. Wert, et al., US Patent 5002729.
[65] James L. Maloney, Adv. Mater. Process. 7 (1) (1998).
[66] Hitesh K. Trivedi, Costandy S. Saba, Lisa C. Carswell, Lois J. Gschwender, Carl E. Snyder, Tribol. Lett. 5 (1998) 211.
[67] R.J. Smith, C. Tripp, A. Knospe, C.V. Ramana, A. Kayani, Vladimir Gorokhovsky, V. Shutthanandan, D.S. Gelles, J. Mater. Eng. Perform. 13 (2003) 295.
[68] P.E. Gannon, C.T. Tripp, A.K. Knospe, C.V.R. Ramana, M. Deibert, R.J. Smith, V.I. Gorokhovsky, V. Shutthanandan, D. Gelles, Surf. Coat. Technol. 188–189 (2004) 55.
[69] P.J. Spencer, H. Holleck, High Temp. Sci. 27 (1990) 295.
[70] A.C. Victor, J. Am. ceram. Soc. 36 (7) (1962) 1903.
[71] V. Linss, S.E. Rodil, P. Reinke, M.G. Garnier, P. Oelhafen, U. Kreissig, F. Richter, Thin Solid Films 467 (2004) 76.
[72] V.I. Malkovich (Ed.), Boron and Refractory Borides, Springer, Verlag, 1977.
[73] G.V. Samsonov, T.I. Serebryakova, V.A. Neronov, Borides, Atmoisdat, Moscow, 1975, p374 (In Russian).
[74] P.S. Kisliy, M.A. Kusenkova, N.I. Bodnaruk, B.L. Grabchuk, Boron Carbide, Naukova Dumka, Kiev, 1988 (in Russian).
[75] J. Robertson, Pure and Appl. Chem., Vol. 66, No. 9, pp. 1789–1796.
[76] N. Panich, Y. Sun, Thin Solid Films 500 (2006) 190.
[77] H.-S. Ahn, P.D. Cuong, K.-H. Shin, Ki-Seung Lee, Wear 259 (2005) 807.
[78] D.R. McKenzie, J. Vac. Sci. Technol., B 11 (1993) 1928.
[79] H. Liepak, K. Bartsch, B. Arnold, H.-D. Bauer, X. Liu, M. Knupfer, A. Leonhardt, Diamond Relat. Mater. 13 (2004) 106.
[80] E. Amberger, H.P. Gerster, Acta Crystallogr., B 36 (1980) 672.
[81] D.D. Wagman, et al., J. Phys. Chem. Ref. Data 11 (supp. 2) (1982).
[82] Sam Zhang, Deen Sun, Yougquing Fu, Hejun Du, Surf. Coat. Technol. 198 (2005) 2.
[83] J. Musil, F. Kurn, H. Zeman, H. Polakova, Surf. Coat. Technol. 154 (304) (2002).
[84] M. Stoiber, S. Perlot, C. Mitterer, M. Beschliesser, C. Lugmair, R. Kullmer, Surf. Coat. Technol. 177 (348) (2004).
[85] A. Lysenko, V. Gorokhovsky, Y. Nikitin, V. Poltoratsky, Molecular Model of Diamond-like Carbon Structure Synthesized under Low Pressure, Reports of the Academy of Sciences of the UkrSSR, 1989 (in Russian).
[86] Handbook of Refractory Carbides and Nitrides, By: Pierson, H.O., William Andrew Publishing/Noyes, 1996.

Paper 11

Available online at www.sciencedirect.com
ScienceDirect
Surface & Coatings Technology 201 (2006) 4040–4045
SURFACE & COATINGS TECHNOLOGY
www.elsevier.com/locate/surfcoat

Plasma diagnostics of hybrid magnetron sputtering and pulsed laser deposition

J.G. Jones *, C. Muratore, A.R. Waite, A.A. Voevodin

Air Force Research Laboratory, Materials and Manufacturing Directorate Wright-Patterson AFB, OH, 45433-7746, United States

Available online 28 September 2006

Abstract

This paper investigates the use of advanced triggering to synchronize a pulsed laser ablated plasma from a ceramic target with a pulsed DC sputtering plasma from a metal target for the purposes of depositing nanocomposite thin-films at low substrate temperatures. A digital oscilloscope and a programmable delay generator were used to prescribe the synchronization time of the two plasmas and frequency of discharge of the laser. Films were grown with different times of synchronization and subsequently characterized using X-ray diffraction and XPS. A multichannel analyzer was used to monitor the plasma emissions to determine spatial evolution of the synchronized pulsed plasma and a spectrometer was used to determine if additional spectra were generated through the interaction of the two plasmas. The studies did not show a clear presence of a new chemical compound formed in the hybrid plasma, but indicated an enhancement of the laser ablated plasma excitation in the presence of pulsed magnetron plasma process. This additional plasma excitation occurred at certain timing of the two pulsed plasma sources and was used to produce a $Zr(Y)O_2$/Mo film containing crystalline ZrO_2. Present results indicate that crystalline ceramic films can be deposited at low substrate temperature in which the film crystallinity is enhanced based on the synchronization timing.
© 2006 Published by Elsevier B.V.

Keywords: Magnetron sputtering; Pulsed laser deposition; Synchronization; Plasma; Film growth

1. Introduction

Magnetron sputtering combined with pulsed laser deposition (MSPLD) forms a unique hybrid process in which a high energy laser capable of depositing oxide materials is combined with the efficient process of magnetron sputtering of metals for depositing low temperature tribological coatings, such as nanocomposites with multiple materials embedded in metal or ceramic matrix [1,2]. These nanocomposite coatings will ideally contain solid lubricants that can operate in different environments, with part of the nanocomposite being a phase of hard nanocrystalline structures that resist coating wear [3,4]. One of the challenges in preparing such composites is obtaining crystalline or nanocrystalline ceramic phases while trying to avoid excessive substrate temperatures that can deteriorate embedded solid dichalcogenide and carbon lubricants, cause grain growth of metallic lubricants, or soften the substrate material. In the interest of maintaining a low substrate temperature, such as below 300 °C, while still obtaining a required degree of ceramic phase crystallinity, the use of synchronization of the laser ablation plume with the pulsed DC magnetron sputtering process is investigated. In a typical MSPLD configuration, the laser ablation process is operated simultaneously without synchronization with the pulsed DC magnetron sputtering process [1,2]. For example, in the low temperature deposition of yttria stabilized zirconia (YSZ) and molybdenum (Mo) tribological coatings [5] the result is an amorphous film in which the metal content and oxide components can be adjusted based on the deposition conditions. Nanocrystallinity of YSZ phase at low substrate temperatures is required for improved abrasion wear resistance. The synchronization of the laser process with the sputtering process in this paper was applied to utilize a high energy of the laser plume for increased mobility of the deposited atoms at low substrate temperatures and promotion of crystalline phase growth. This synchronization was accomplished by configuring a digital oscilloscope to continuously monitor pulsed sputtering voltage and generate a digital reference signal for each transition from negative to positive voltage. Based on this time reference, a delay generator regulated time of the laser pulse in reference to the magnetron pulse throughout the deposition

* Corresponding author.
E-mail address: john.jones@wpafb.af.mil (J.G. Jones).

0257-8972/$ - see front matter © 2006 Published by Elsevier B.V.
doi:10.1016/j.surfcoat.2006.08.096

process. In this study, the laser pulses to a yttria stabilized zirconia (YSZ) target were inserted at the specific time into the pulsed DC magnetron sputtering pattern from molybdenum targets. Synchronized plasma chemistry and energetics were correlated to the produced YSZ–Mo film chemical composition and crystallinity to verify the possibility of the plasma synchronization use for a low substrate temperature growth of crystalline ceramic phases.

2. Experimental setup

The hybrid MSPLD process (Fig. 1) consists of a Lambda Physik LPX 305i excimer laser (248 nm KrF) with 1 J output of 20 ns wide pulses, an ENI model RPG 50 pulsed DC magnetron sputtering controller, a UHV vacuum chamber holding the 3 cm (1¼″) diameter Mo magnetron sputtering target, 5 cm (2″) diameter YSZ (ZrO_2/5 wt.% Y_2O_3) laser target, and substrate sample carousel holding six 1″ diameter ¼″ thick 440 C stainless steel substrates. The distance from the laser target to substrate is 10 cm, from magnetron to substrate is 5 cm, and the distance from laser target to magnetron target is 9 cm. The substrates were heated using a tungsten filament with a thermocouple attached to the substrate carousel. All depositions were performed with the heater set to 200 °C, and the samples were continuously rotated. When the laser began operation, the power demanded by the heater decreased due to the thermal heating imparted on the samples by the laser ablation process. The laser beam is continuously repositioned by a high speed galvanometer system to provide uniformly random coverage of the target by the beam. The 1 cm × 3 cm beam footprint is focused onto the YSZ target to a 1 mm × 3 mm spot area using a lens with a focal length of 0.5 m. A Tektronix high-voltage differential probe model P5200 and Tektronix digital phosphorous oscilloscope (DPO) TDS 540 D was used to sample the sputtering voltage on the magnetron gun. The sputtering current was measured using a Tektronix current probe clamp on the magnetron power feed line. The oscilloscope was configured to continuously monitor the repeating voltage waveform and generate a digital trigger signal at the point where the sputtering voltage rapidly changes from negative to positive. This timing signal was used to trigger a Stanford Research Systems digital delay generator (DG535) consisting of multiple output channels that operate in parallel. The first channel is set to a delay in microseconds and connected to the excimer laser's external trigger input, providing a laser pulse at exactly the same point in the sputtering process, repeatedly throughout the course of a deposition. In order to vary the timing between the magnetron and laser, this channel had set delays ranging from 0 to 10 μs. By setting the second channel of the delay generator to 33.3 ms, the laser pulsed in this synchronized manner at a frequency of 30 Hz. All depositions were performed at pressures of 1.3 Pa of Ar, 800 mJ laser energy, 30 Hz repetition rate, a substrate bias of −150 V, a magnetron frequency of 120 kHz with a power setting of 30 W, and a substrate temperature of 200 °C. All films deposited were approximately 1 μm in thickness.

In order to collect snapshots of the hybrid MSPLD plasma process, the sync output on the laser was used to trigger a Princeton Instruments programmable high voltage pulse generator (PG-200) which gated an image collecting ICCD camera of a multi-channel analyzer. The plasma snapshots were collected over a 20 μs period of time with a gate delay of 100 ns, a gate step of 1.0 μs, and an integration time of 1.0 μs.

Analyses of film properties were performed using a Surface Science Instruments M-Probe X-ray photoelectron spectrometer (XPS) and Rigaku Rotaflex X-ray Diffractometer (XRD). Before XPS analysis, the samples were sputtered clean for 15 s with 5000 eV Ar^+ ions. The XPS analysis was performed with an aluminum X-ray source at 50 W. From the XPS analysis, the relative peak heights were measured to obtain the composition of each elemental specie in the nanocomposite coating. The XRD analysis was performed with a copper X-ray source at 6 kW using glancing incidence X-ray diffraction with a fixed value of 4° for θ.

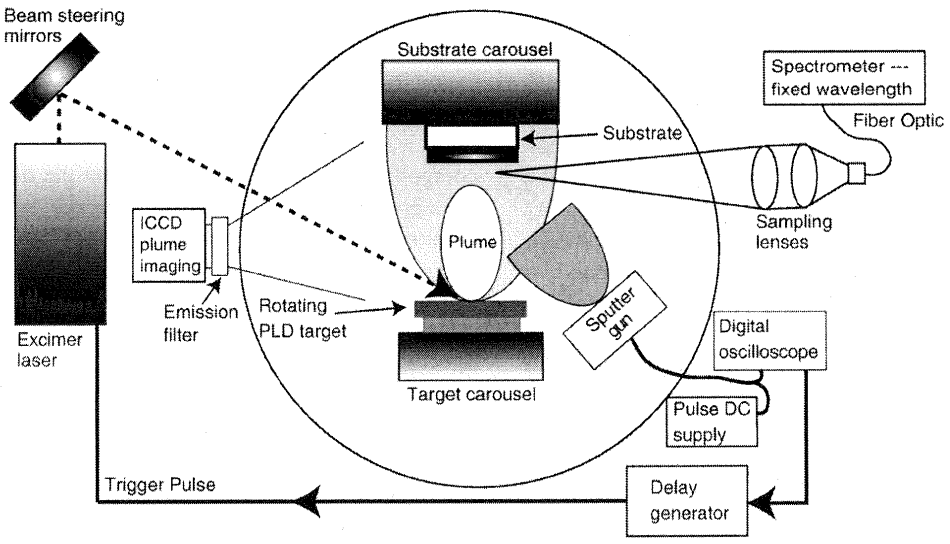


Fig. 1. Magnetron sputtering with pulsed laser deposition process and triggering with magnetron sputtering of molybdenum and pulsed laser deposition of yttria stabilized zirconia.

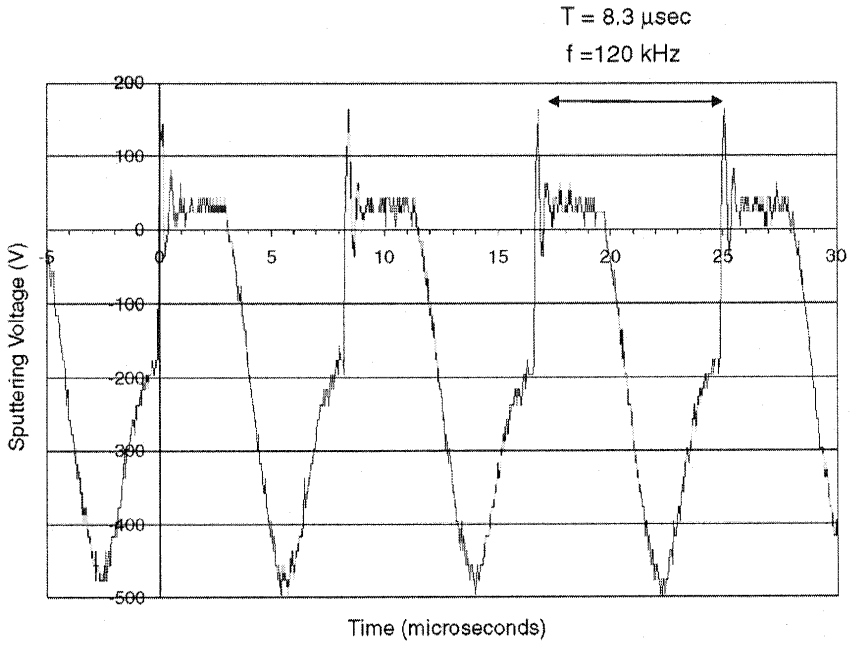


Fig. 2. Magnetron sputtering voltage waveform at 30 W and 1.3 Pa argon.

2.1. Results and discussion

Depositions were performed with and without synchronization of the laser to the pulsed DC magnetron sputtering process and a multichannel analyzer was used to characterize each of the synchronized depositions, as well as both PLD and MS processes separately. The unsynchronized deposition was performed with identical conditions, except that the laser operated from its own internal trigger at a 30 Hz repetition rate, as opposed to using the external triggering mode that was required for synchronization. For the synchronized depositions, each deposition was performed with a specific delay time, between 0 and 10 µs, with the triggering of the oscilloscope at the transition of magnetron voltage from negative to positive (Fig. 2) defining the start of each event and the output of the laser pulse defining the end of each event. These triggering events were repeated at a 30 Hz repetition rate by defining a second channel of the delay generator to output a 33.3 ms event.

The current waveform of the MS process (Fig. 3) shows that from 5 to 8.3 µs the sputtering process is first initiated with a large current spike and sustained over the 3.3 µs interval by a negative voltage (Fig. 2). At the 8.3 µs point, the MS power

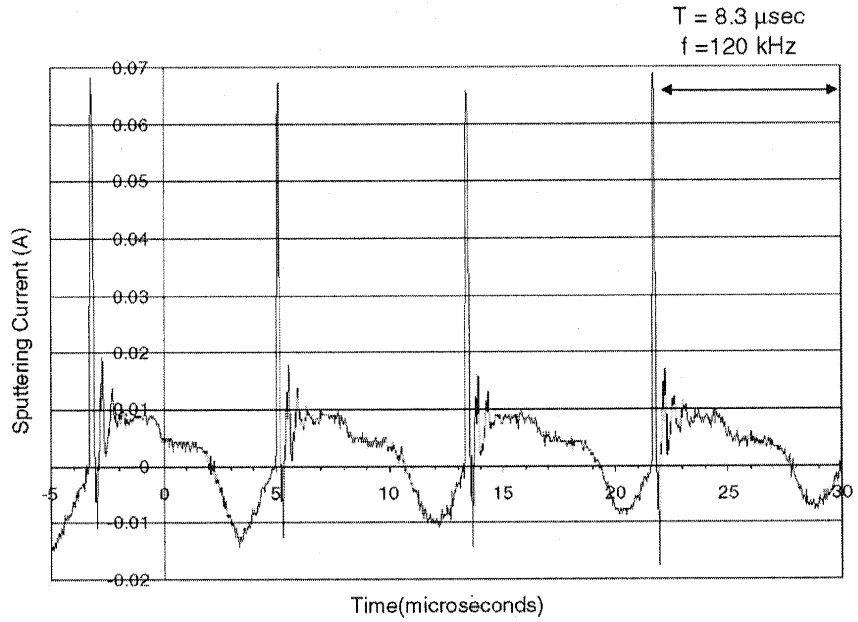


Fig. 3. Magnetron current waveform at 30 W and 1.3 Pa argon.

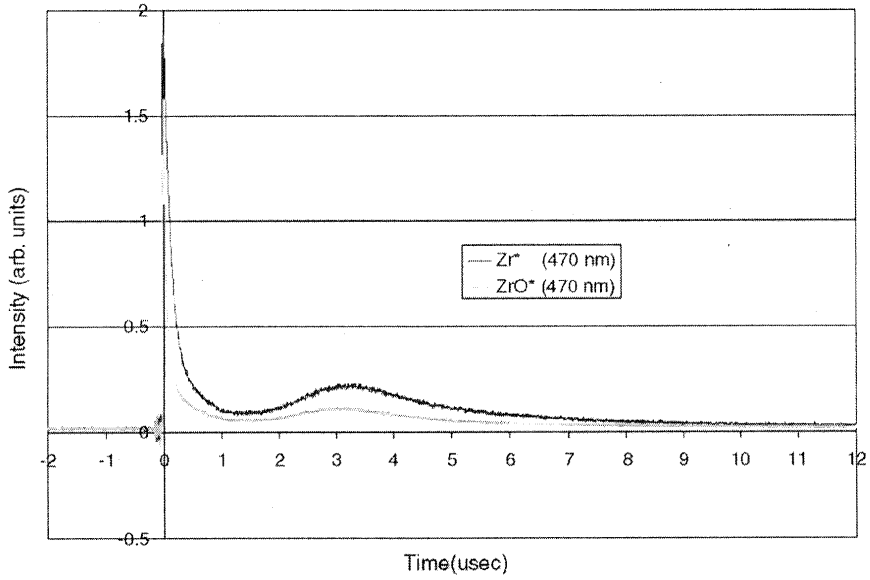
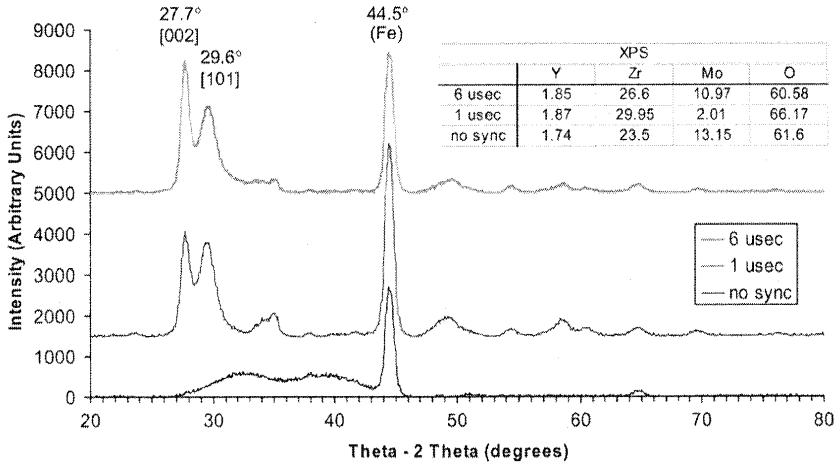


Fig. 4. Yttria stabilized zirconia time of flight waveforms with pulsed laser deposition energy of 800 mJ and 1.3 Pa argon.

supply transitions to a large positive voltage to stop the sputtering process, and maintains this positive potential for some 3 μs (as displayed between 0 and 3 μs interval Fig. 2). Between 3 and 5 μs the MS power supply transitions to a negative voltage in order to reinitiate the MS pulsed DC process. Consequently there are three modes of operation of the MS power supply: initiation and maintaining sputtering power level for 3.3 μs, shutoff and recovery from sputtering for 3 μs, and then transition of the voltage to reinitiate MS for 2 μs. This information was used to select synchronization points for the laser pulse insertion. The noise associated with the current and voltage waveforms (Figs. 2 and 3), as well as the spikes, are associated with the time varying nature of the electrical impedance of the plume and not indicative of plasma arcing.

Laser plasma timing was explored with Time of flight (TOF) by measuring the optical emission of two components of the PLD plume, Zr* and ZrO*, (Fig. 4) using a photomultiplier tube in conjunction with a 10 nm bandpass optical filter. Filters of 470 nm for Zr* and 480 nm for ZrO* were used with PLD conditions of 1.3 Pa Ar, and 800 mJ laser energy with the oscilloscope used to capture the data. A 1 cm diameter collimating tube was used to sample the optical emissions half way between the target and substrate, approximately 4 cm. As shown by the TOF waveforms (Fig. 4) the intensity of these two species is all but dissipated by 7 μs after the pulsing of the laser. Comparing this to the duration of the magnetron sputter pulse, only one full magnetron sputtering cycle (8.3 μs) and one PLD plume (~ 9 μs) can possibly interact in the hybrid process.

YSZ–Mo films were produced by generating a laser pulse 0–7 μs after detecting transition of a magnetron pulse. The magnetron pulses were continuously generated and detected at 130 kHz, and the individual laser pulses were only inserted at a rate of 30 Hz. XPS characterization of the films showed that all films had an approximate atomic composition consisting of some 61% O, 24% Zr, 13% Mo, and 2% Y, Fig. 5. Each film was then analyzed using X-ray diffraction, Fig. 5. Most films



XPS

	Y	Zr	Mo	O
6 usec	1.85	26.6	10.97	60.58
1 usec	1.87	29.95	2.01	66.17
no sync	1.74	23.5	13.15	61.6

Fig. 5. X-ray diffraction and X-ray photoelectron spectroscopy of magnetron sputtering with pulsed laser deposition thin-films.

were X-ray amorphous, just as is the case without any synchronization. However, the samples which were deposited using synchronization of 1 and 6 μs delay times resulted in diffraction patterns that were significantly different than what would otherwise result. In these two cases there are clear crystallization peaks at 27.7° and 29.6° degrees two-theta with additional higher order peaks occurring between 32.8° and 70° two-theta, Fig. 5. These peaks appear to be related to a ZrO_2 orthorhombic structure, which has peaks located at 27.5 and 30.3° two-theta according to PDF Card #41-0017. The 440 C steel substrate was clearly visible at 44.5° for all of the samples. With this composition information, and the X-ray diffraction data, it suggests that the synchronization helped in crystallizing the zirconium oxide, ZrO_2, which also happens to be the biggest contributor to the thin-film composition. Interaction of the laser plume with the first 3 μs (Fig. 2) in which the magnetron voltage is positive results in an increased plasma potential. This plasma potential increase combined with synchronization had an effect on the film crystallinity but not on the film chemical composition. This was correlated to the plasma spectroscopy studies where we could not detect any variations in the plasma excitation states and chemistry for the synchronized and non-synchronized plasmas. The challenge was then to evaluate kinetics of the hybrid plasma developments to detect any variation in the depositing plasma energy in synchronized and non-synchronized regimes. As demonstrated in Fig. 5, the Mo content does not appear to affect the resulting crystallinity. The 1 μs and 6 μs thin-films deposited have very similar XRD patterns of crystallinity, but the films contain 2% and 11% Mo, respectively.

Gated imaging of hybrid plasma with high speed ICCD camera was applied to obtain information about kinetics of the pulsed process due to the fact that an image provides spatial information about the evolution of the plumes. Fig. 6 shows sequences of image frames collected from synchronized MSPLD process at 9 μs delay, or equivalently 0.7 μs, in laser pulse insertion (Fig. 6a) and non-synchronized MSPLD process (Fig. 6b). Each sequence was taken with a 1 μs time step from when the laser is first fired. In both sequences of images the PLD plume can clearly be seen for the first 5 μs, and dissipating over the next 5 μs – which is normal for PLD process operating alone. However, for synchronized operation (Fig. 6a) in the 12th frame there was clearly visible emission both from the magnetron gun and remains of the laser plume. This time in the hybrid synchronized MSPLD process corresponds to the magnetron voltage swings to a large negative value which initiates sputtering. This large negative voltage and

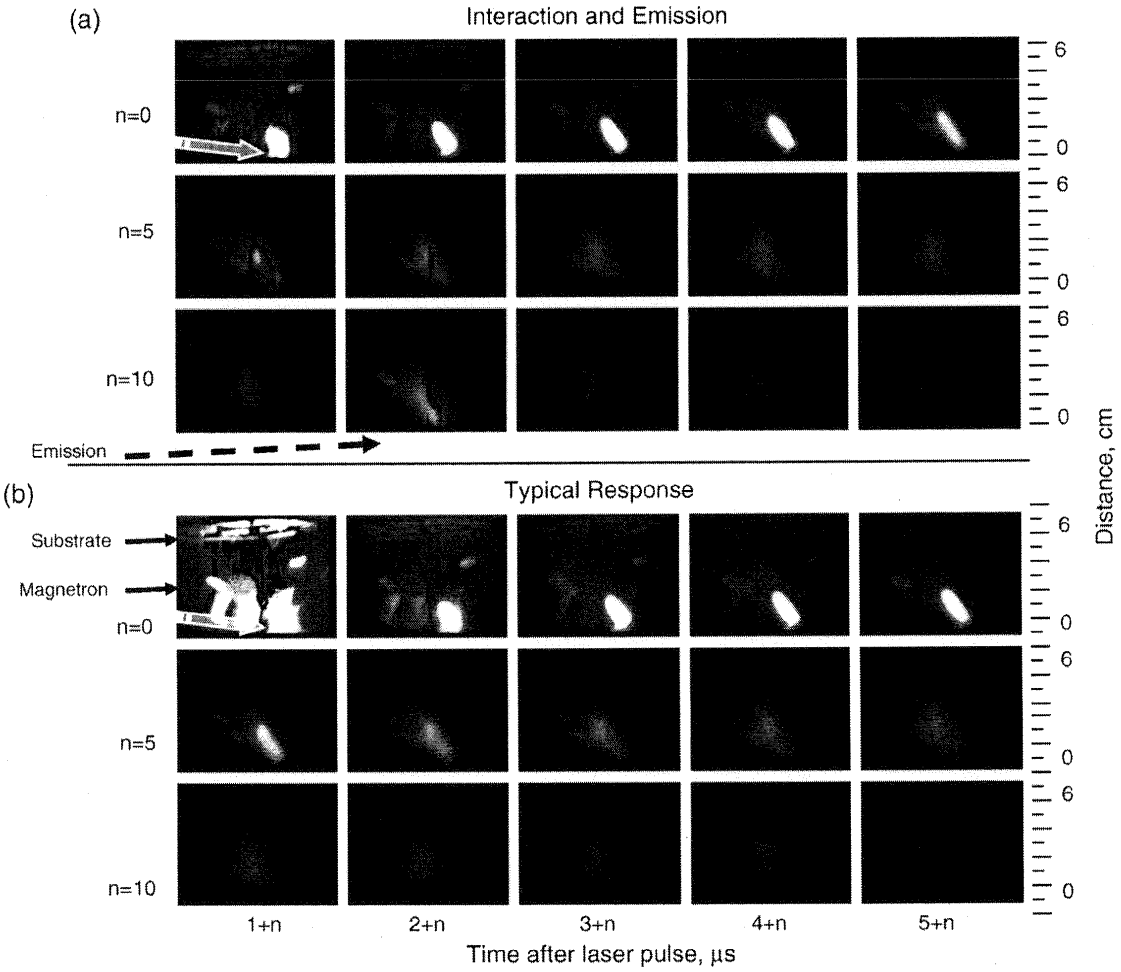


Fig. 6. Optical Multichannel analyzer image sequences showing plume evolution.

subsequent current spike must excite what remains of the laser plume, mostly zirconium and oxygen, causing the optical emission. This late excitation effect was absent in running the process without synchronization (Fig. 6b). In such we propose that the synchronized operation helps to increase energetic and excitation of neutral components of the laser plume traveling with relatively low speed in the tail of the laser ablated plasma. This additional excitation must be responsible for adding to the condensation surface energy of the arriving laser ablated Zr and O species, which should help to increase their mobility at low substrate temperatures. This observation is consistent with arguments presented that an increase in the effective electron temperature coincides with the onset of the negative pulse [6–9]. Although exact mechanisms are yet to be verified, it is likely that MSPLD synchronization helps to enhance the laser ablated plume energetics. Clearly that by the synchronization on a continuous basis, repeated interactions have the chance of changing the thin-film structure promoting YSZ crystallization even at the low substrate temperatures.

3. Conclusions

Synchronization of a hybrid process of MSPLD can deposit a nanocomposite structure having crystalline oxides from PLD with metal being deposited simultaneously by pulsed DC MS at substrate temperatures of 200 °C. Voltage and current measurements of the DC sputtering process show three modes of operation in which a laser pulse could be inserted using the synchronization timing set-up: 1) sputtering with large negative voltage and initial current spike to begin the MS and optical emission, 2) positive reverse voltage to stop the process of MS, and 3) transition of voltage from positive to negative to repeat the process. The synchronization of the laser plume developing from YSZ target with the third mode of the MS process on Mo target was found to yield a nanocrystalline film growth. All other synchronization times yielded X-ray amorphous films. Spectra of the process integrated over many seconds could not reveal significant plasma chemistry changes. However, hybrid plasma image sequences showed that there is plume interaction and emission, and that under the right timing conditions of MS voltage transition the PLD plume can be additionally excited producing emission. Crystallinity was verified by XRD and composition was measured with XPS. The crystalline structure deposited is indicative of a form of ZrO_2 in a $Zr(Y)O_2$/Mo film. Using the right timing throughout a deposition appears to lead to crystalline nanocomposite thin-films at low temperatures that would otherwise not form.

References

[1] A.A. Voevodin, M.A. Capano, A.J. Safriet, M.S. Donley, J.S. Zabinski, Appl. Phys. Lett. 69 (1996) 188.
[2] A.A. Voevodin, J.S. Zabinski, Hybrid Plasma Deposition Methods for Synthesis of Nanostructured Materials, in: A.A. Voevodin, D.V. Shtansky, E.A. Levashov, J.J. Moore (Eds.), Nanostructured thin films and nanodispersion strengthened coatings, Kluwer Academic Publishers, Dordrecht, The Netherlands, 2005, p. 103.
[3] A.A. Voevodin, J.S. Zabinski, Thin Solid Films 370 (2000) 223.
[4] A.A. Voevodin, J.J. Hu, T.A. Fitz, J.S. Zabinski, J. Vac. Sci.Technol., A 20 (2002) 1434.
[5] C. Muratore, A.A. Voevodin, J.J. Hu, J.G. Jones, J.S. Zabinski, Surf. Coat. Technol. 200 (2005) 1549.
[6] Bradley, et al., Surf. Coat. Technol. 200 (2005) 616.
[7] C. Muratore, J.J. Moore, J.A. Rees, Surf. Coat. Technol. 163–164 (2003) 12.
[8] P.J. Kelly, R.D. Arnell, J. Vac. Sci. Technol., A 17 (1999) 945.
[9] J.W. Bradley, H. Backer, Y. Aranda-Gonzalvo, P.J. Kelly, R.D. Arnell, Plasma Sources Sci. Technol. 11 (2002) 165.

Tribology Letters, Vol. 24, No. 1, October 2006 (© 2006)
DOI: 10.1007/s11249-006-9162-0

Page 12

Tunable friction behavior of oriented carbon nanotube films

P.L. Dickrell[a,*], S.K. Pal[b], G.R. Bourne[a], C. Muratore[c], A.A. Voevodin[c], P.M. Ajayan[b], L.S. Schadler[b] and W.G. Sawyer[a]

[a]*Department of Mechanical and Aerospace Engineering, University of Florida, Gainesville, FL 32611, USA*
[b]*Department of Materials Science and Engineering, Rensselaer Polytechnic Institute, Troy, NY 12180, USA*
[c]*Air Force Research Laboratory, Wright Patterson AFB, OH 45433, USA*

Received 16 June 2006; accepted 25 September 2006; published online 17 October 2006

Measured friction coefficients of carbon nanotubes vary widely from $\mu < 0.1$–$\mu > 1.0$ [1–6], while theoretical studies suggest intrinsically high friction coefficients, approaching unity [7]. Here we report that measured friction coefficients of MWNT films are strong functions of surface chemistry and temperature, but are not dependent on the presence of water vapor. We hypothesize that the origin of the temperature dependence arises from the interaction of the surface chemical groups on the nanotubes [8–12] and rubbing counterface. The friction coefficient of individual films can be easily tuned by changing the surface temperature and chemistry of either the countersurface or the nanotubes, we have demonstrated the ability to create and control high and low friction pairs through plasma treatments of the nanotube films with argon, hydrogen, nitrogen, and oxygen. This behavior is completely reversible, and when coupled with the superior strength, thermal, and electrical properties of nanotubes, provides a versatile tunable, multifunctional tribological system.

KEY WORDS: carbon nanotubes, coefficient of friction, micro-tribology, engineered surfaces

A schematic of the MWNT film grown with a vertical orientation is shown in figure 1 (a). Scanning electron microscopy images of a free edge of the vertical film are shown in figures 1(b)–1(d). The vertically aligned film was grown by a chemical vapor deposition (CVD) process using ferrocene and xylene precursors [13]. Following CVD growth, the MWNT films are cleaned using an oxygen plasma treatment. The vertically aligned MWNT films are approximately 65 μm thick and 5% dense. The MWNTs were vertically aligned, with the last few micrometers from the top surface the films entangled and intertwined as shown in figures 1(b)–1(d). A sample of transversely orientated nanotubes was also prepared by mechanically removing the vertical MWNTs, sonicating in acetone and dispersing onto an identical quartz substrate. After drying, this transversely oriented nanotube film was found to be approximately 5 μm thick and was comprised of a distributed ensemble of entangled nanotubes oriented in plane with the quartz substrate (figure 1(e) and 1(f)).

The mechanical, electrical, and thermal properties of individual nanotubes are highly anisotropic [14–18], and the frictional behavior was also recently found to be anisotropic [6]. These friction experiments used a countersurface made from a borosilicate glass pin (schematically shown in figure 2 (a)) and were run in a regime where wear was not observed. Under both inert gas and ambient conditions, the transversely distributed films were repeatedly found to have friction coefficients $\mu \sim 0.1$, while the vertically aligned sample had $\mu \sim 0.9$. Molecular dynamics studies report nanotube films can accommodate relative motions or slip by rolling, sliding, or a combination of rolling and sliding at the interface [19]. However, this mobility related hypothesis seems unlikely considering the degree of nanotube entanglement observed in these films.

The recently found super-compressibility of the vertically aligned nanotube films [20] predicts an order-of-magnitude difference in contact area between the transverse and vertical arrangement. The calculated interfacial shear stresses are nearly the same for both films (0.1–0.2 MPa) indicating that the contact area difference between orientations is a reasonable explanation of the frictional anisotropy. However, the exceptionally low value of predicted shear stress suggests that there are a number of very small intimate contact points supporting load. This is consistent with observed tangled and open morphology of the surface contacting regions (figure 1).

In this study, a series of tribological experiments were performed on vertically aligned and transversely distributed nanotube films using a borosilicate glass countersurface while varying the film temperature from 303–393 K. These experiments had a prescribed 2 mN normal load, 300 μm/sec sliding speed, and a track length of 600 μm. A total of 100 reciprocating cycles were run in open laboratory air (45% RH) at each temperature. As previously found, the friction coefficient

*To whom correspondence should be addressed.
E-mail: pld@ufl.edu

1023-8883/06/1000-0085/0 © 2006 Springer Science+Business Media, Inc.

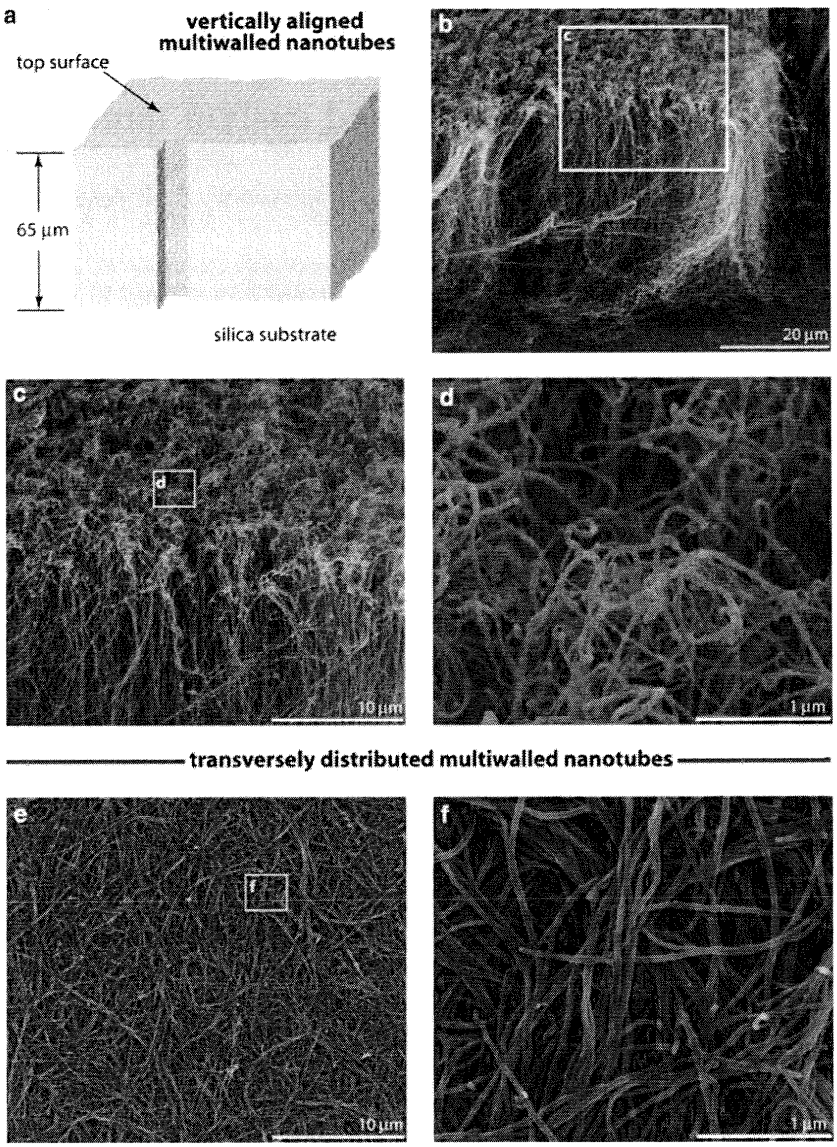


Figure 1. Oriented MWNT film structures. (a) A schematic of an SEM image (b) taken of an exposed edge of the vertically aligned MWNT films. The image is taken at a 52° tilt, and was found to have a characteristic height of 65 μm. Images (c) and (d) are indicated in (b) and (c) respectively. The top surface shown in (d) is typical of the tangled morphology that does not have a preferential vertical orientation, which is clearly visible in (b) and (c). Image (e) is a top view of a transversely distributed sample prepared from the same tubes shown in (b)–(d). This sample was prepared by sonicating mechanically removed tubes in acetone and then drying them onto a quartz sample. Image (f) is a higher magnification of the region indicated in (e).

of the vertically aligned film was approximately ten times higher than the transversely distributed film at 303 K (figure 2(b)). The value at 303 K (the lowest temperature tested) is indicated as μ_o for each of the films and was used as a reference friction coefficient in the analysis. As the film temperature was increased there was a monotonic decrease in the friction coefficient. This behavior was completely recoverable and reversible. The friction coefficient of both oriented MWNT films could be tuned by an order of magnitude by simply varying the temperature of the nanotube films. This result demonstrates the potential opportunity to use nanotube films as active surfaces that can provide high friction coefficient or lubricity on demand.

In figure 2(b) it appears that this temperature effect is more pronounced in the vertically aligned films, however, when the friction coefficients are normalized to the 303 K values (μ_o) the relative changes in friction coefficient are nearly the same for the two films. This is shown in figure 2(c) over the range of temperatures examined. For this data set two points were collected at each temperature: one during heating and the other during cooling. An Arrhenius plot of this normalized friction coefficient behavior, shown in figure 2(d), gives an activation energy of Ea = 16 kJ/mol. This value of activation energy is consistent with hydrogen bonding; silica glasses are known to have hydoxy-groups on their surfaces [21], and post-production plasma treatment

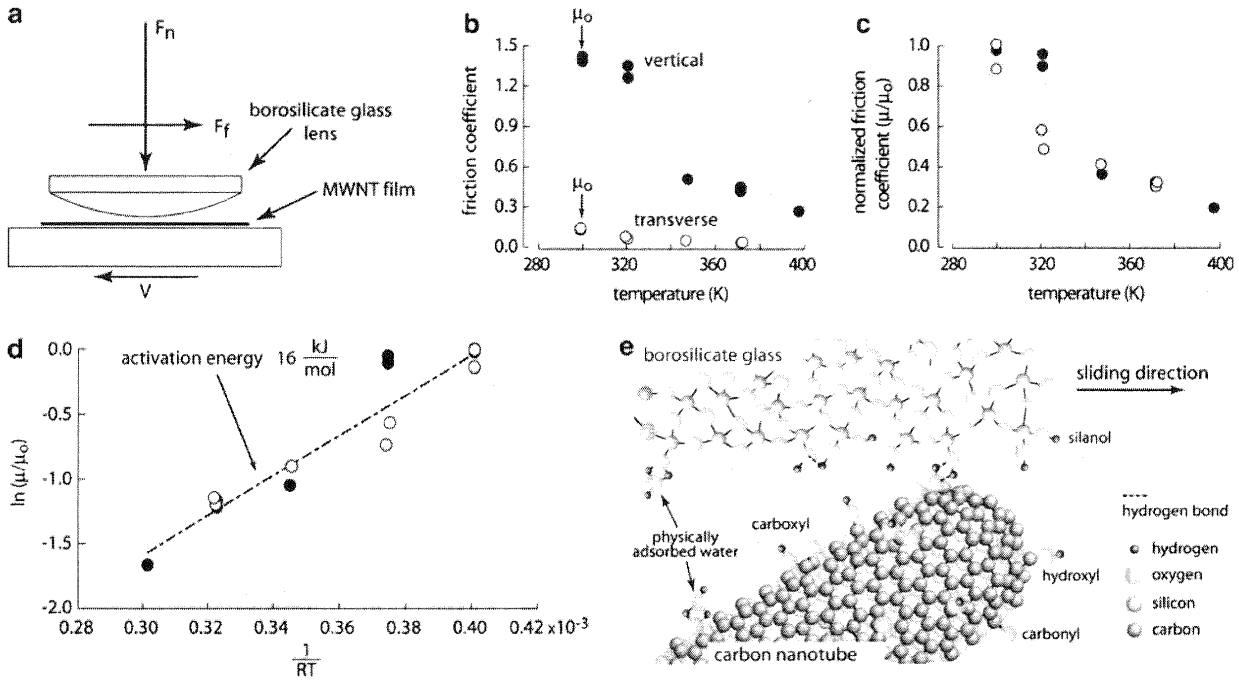


Figure 2. Temperature, orientation, and interface bond dependent friction. (a) The experimental schematic the MWNT films are located on a reciprocating stage the slide under replaceable countersurfaces, the experiments described here were run on a borosilicate glass lens that had an ~8 mm radius of curvature, (b) The friction coefficient of the two films versus surface temperature in an open-air environment, (c) The friction coefficient is normalized by the 303 K value revealing that the relative changes for the two films were the same, (d) An Arrhenius plot of the normalized friction coefficient suggesting that hydrogen bond breaking is the dominant contribution to friction coefficient during the interfacial sliding between the MWNT films and the glass counter surface, (e) A schematic of the molecular view inferred from these experiments.

with oxygen moieties shows unambiguous evidence that the functionalization of the nanotube framework includes carboxyls (–COOH), hydroxyls (–OH) and carbonyls (–C = O) [8–12, 22, 23]. This leads to the molecular view of the contact illustrated in figure 2e, where the frictional response is controlled by the unintentionally attached functional groups on the surface of the glass and the nanotubes suggesting the tribology of these surfaces can be intentionally modified through different chemistries and functionalization.

A relatively simple test of this hypothesis was to repeat tribological experiments using countersurfaces of gold instead of borosilicate glass. Gold surfaces have been well characterized and electron beam evaporation of gold onto the borosilicate glass lens surface gives nearly the same polished finish. The gold coated surfaces are devoid of the –OH groups that we hypothesize are responsible for the hydrogen bond dominated friction response. The same experimental protocol was repeated using the gold coated lenses, and was expanded to include lenses of three curvature radii: 7.78, 4.65 and 1.00 mm. The results of these experiments are shown in figure 3 (a). The data show that the friction coefficients are reduced by nearly a factor of two, and the friction coefficients can be further lowered by reducing the radii of curvature, which reduces the nominal contact area. Previous publications [6, 24] demonstrated friction coefficients of the nanotube films are not altered by changes from open air conditions to inert environments. In this study, the set of experiments with the 1.00 mm gold coated lenses (plotted in figure 3) demonstrate that this temperature effect on friction coefficient is also insensitive to the gaseous environment. The experiments run in open laboratory air had a relative humidity of 45% and the experiments in the argon environment used gases that had a reported purity of less than 5 ppm H_2O and O_2.

Normalizing the friction coefficients to the 303 K values (μ_o) shows that the relative changes in friction coefficient with increasing temperature are similar for all gold coated samples and conditions (figure 3(b)). The relative change in friction coefficient with temperature is much less than for the borosilicate glass counterfaces. The activation energy fit to the gold data set (figure 3(c)) is 3 kJ/mol, which is indicative of van der Waals bond breaking during sliding between the MWNT and the gold [25].

The purification of nanotubes by removing amorphous carbon films through plasma etching is widely used. In order to demonstrate tunable friction coefficient, the vertically aligned MWNT films were treated in a 100 W glow discharge plasma with combinations of argon & nitrogen, and argon & hydrogen. After etching for 45 s, the surfaces were examined with x-ray photoelectron spectroscopy (XPS) (figure 4 (a)–(d)). The C1s peak of the argon & hydrogen treatment (figure 4(b))

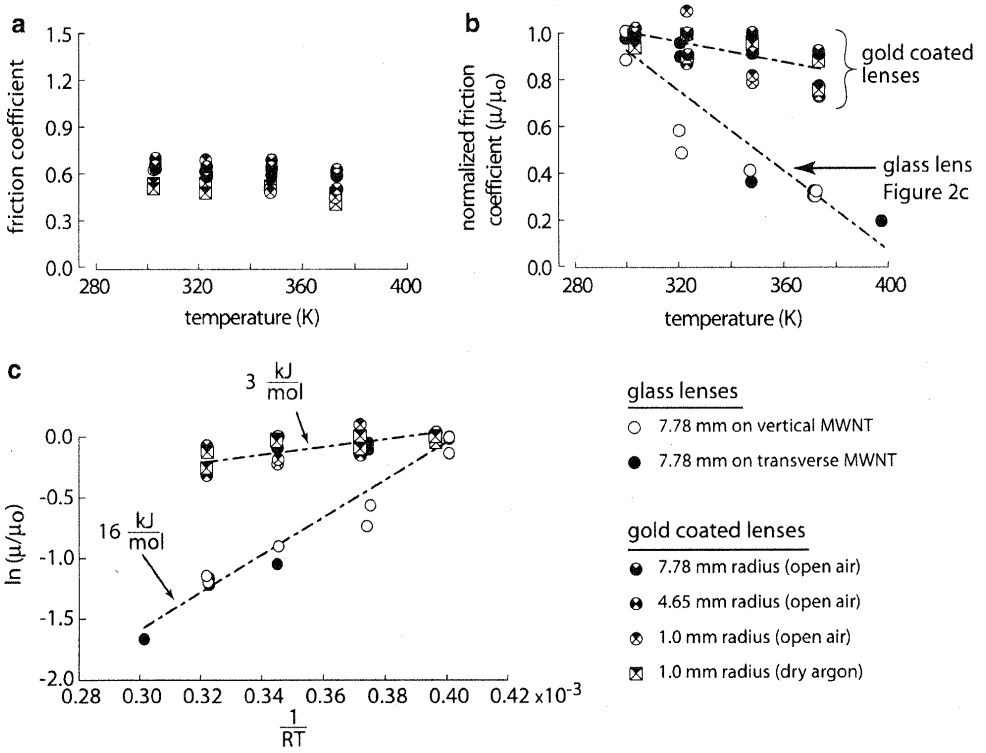


Figure 3. Gold-MWNT sliding interface friction and activation energy. (a) A plot of the friction coefficient for gold coated countersurface conditions against the vertically aligned MWNT film versus surface temperature run on a vertically aligned MWNT film using multiple radii and both laboratory air and dry argon, (b) The friction coefficient is normalized by each 303 K value revealing that the relative changes for all gold countersurface conditions were the same, but was distinctly different than the normalized trend for the borosilicate glass countersurface, (c) An Arrhenius plot of the normalized friction coefficient suggests that hydrogen bond breaking is the dominant contribution to friction coefficient during the interfacial sliding between the MWNT films and the glass counter surface and van der Waals bond breaking is the dominant contribution to friction coefficient when sliding against a gold countersurface.

was slightly broadened in comparison to the untreated sample (figure 4(a)), which is expected with the addition of C-H bonds. From previous XPS studies of hydrocarbons, the C1s peak of C–H bonding is at higher energies as compared to 284.6 eV for C–C bonds in graphite [26] contributing to the C1s peak broadening. The C1s peak broadening was more pronounced for the argon & nitrogen treatment (figure 4(c)), evolving in the direction of higher bonding energies. This is in correspondence to formation of C–N bonds, where C1s bonding energy was reported to vary from 285.9–287.8 eV as a function of carbon atom electron hybridization [27]. For all plasma treated carbon nanotubes, there was no oxygen contamination or C–O bond formation. This is evidenced in figure 4 from the absence of C1s peak features at 290–292 eV which would be typical for thermally oxidized carbon or oxygen plasma treated polymers [28].

Interestingly, the XPS analyses of N1s region for the argon & nitrogen treatment in figure 4(d) presents clear evidence of a doublet structure of the nitrogen atom bonding. This duplet structure of N1s region is exactly the same as the one observed in studies of fullerene-like CN_x [29, 30]. The possibility of generating fullerene CN_x structures on the ends of carbon nanotubes in argon & nitrogen treatment, as hinted by the XPS analyses, is an interesting avenue of further investigations.

When plasma treated nanotubes were tested in sliding against the borosilicate glass surface in open laboratory air, the friction coefficients of both plasma treated films showed a weak dependence on temperature (figure 4(e)). The activation energy fit from both plasma treated MWNT films (figure 4(f)) is 3 kJ/mol. Examination of both the borosilicate glass lens and gold coated pin surfaces after test completion revealed no evidence of transfer film formation. This in combination with the lack of wear on the MWNT film surfaces supports the mechanism of pin-counterface chemical bond activation energy as the dominating frictional mechanism.

This work demonstrates that the friction coefficients can be tuned by tailoring the chemical interfaces between nanotubes and countersurfaces, and the contact temperature. Smart surfaces and multifunctional structures with tunable friction behavior can be designed using multiwalled nanotube films as foundation and tailoring the surface treatments and counterface chemistries for the target application. The ability to reduce the friction coefficient with surface heating (potentially using the nanotubes themselves as the resistive elements) provides a path for dynamic control of the friction

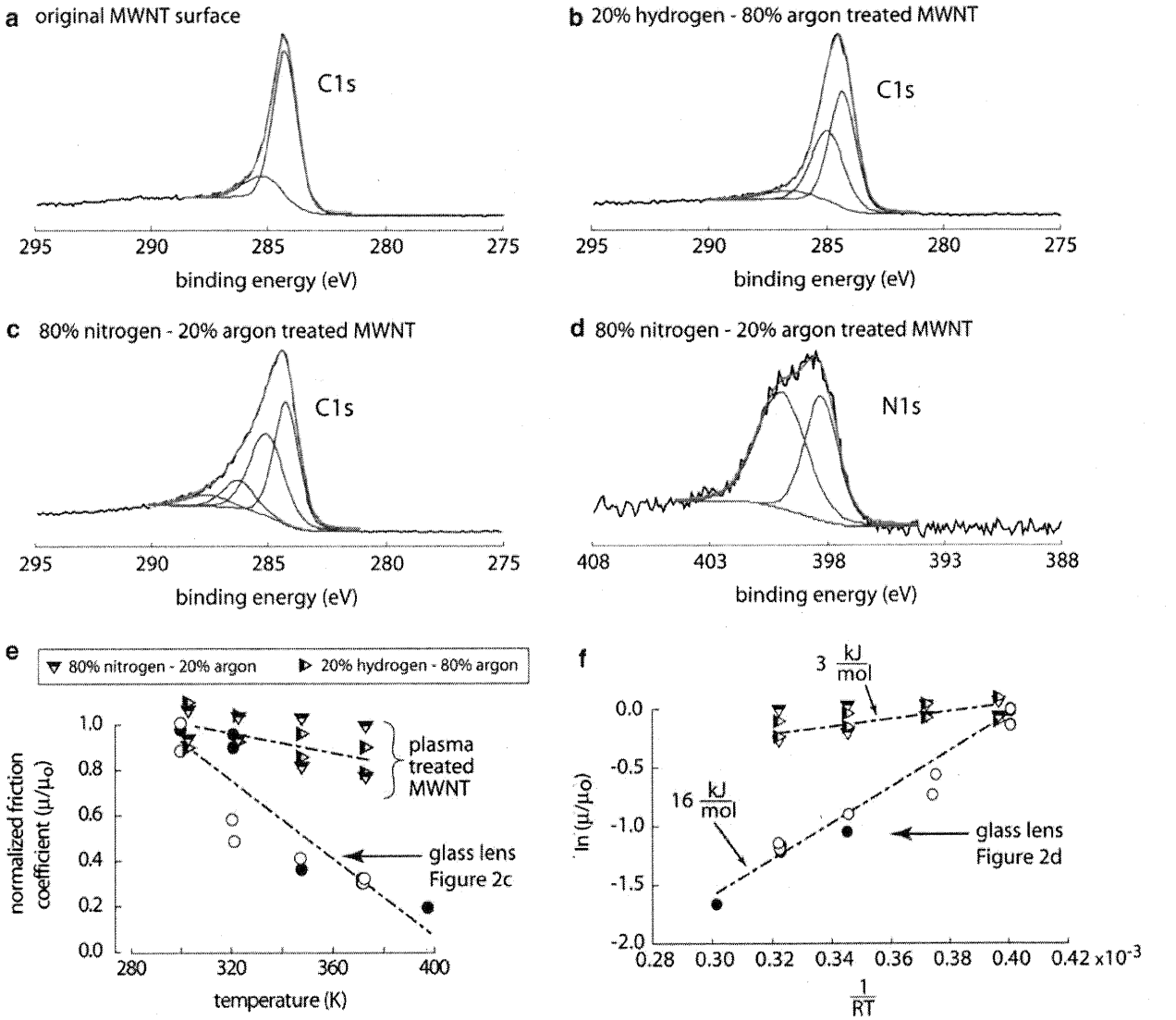


Figure 4. Effects of MWNT plasma treatment on sliding interface temperature dependence. XPS spectra of the carbon 1s peak of MWNT vertically aligned films (a) non-plasma treated, (b) argon & hydrogen plasma treatment, and (c) argon & nitrogen plasma treatment, (d) XPS spectra of the nitrogen 1s region of the of the argon & nitrogen plasma treatment, (e) The friction coefficient normalized by each 303 K value reveals that the nitrogen and hydrogen treatments were successful at removing the temperature sensitivity on friction coefficient, and (f) suggests a shift from hydrogen bonding dominated friction (figure 2d) to van der Waals dominated friction.

coefficient over a wide range of operational environments.

Acknowledgments

This material is based upon an AFOSR-MURI grant FA9550–04–1-0367. Any opinions, findings, conclusions or recommendations expressed in this material are those of the authors and do not necessarily reflect the views of the Air Force Office of Scientific Research.

References

[1] A. Hirata and N Yoshioka, Tribol. Int. 37 (2004) 11–12.
[2] J. Tu et al., Mater Lett. 58 (2004) 10.
[3] X. Ma, H Wang and W Yang, J. Eng. Mater. Technol.-ASME 126 (2004) 3.
[4] J. Hu et al., Tribol. Lett. 19 (2005) 2.
[5] K. Miyoshi et al., Tribol. Lett. 19 (2005) 3.
[6] P. Dickrell et al., Tribol. Lett. 18 (2005) 1.
[7] S. Sinnott et al., Carbon 36 (1998) 1–2.
[8] A. Felten et al., J. Appl. Phys. 98 (2005) 7.
[9] V. Chirila, G. Marginean and W Brandl, Surf. Coat. Technol. 200 (2005) 1–4.
[10] N. Chopra, M. Majumder and B Hinds, Adv. Funct. Mater. 15 (2005) 5.
[11] Z. Utegulov et al., J. Appl. Phys. 97 (2005) 10.
[12] H. Bubert et al., Diam. Relat. Mater. 12 (2003) 3–7.
[13] B. Wei et al., Nature 416 (2002) 6880.
[14] L. Langer et al., J. Mater. Res. 9 (1994) 4.
[15] J. Heremans, C. Olk and D Morelli, Phys. Rev. B 49 (1994) 21.
[16] L. Langer et al., Phys. Rev. Lett. 76 (1996) 3.
[17] J. ISSI et al., Carbon 33 (1995) 7.
[18] M. Treacy, T. Ebbesen and J Gibson, Nature 381 (1996) 6584.

[19] B. Ni and S Sinnott, Surf. Sci. 487 (2001) 1–3.
[20] A. Cao et al., Science 310 (2005) 5752.
[21] A.P. Legrand, *The surface properties of silicas* (Wiley, New York, 1998).
[22] W. Feng et al., JPN J. Appl. Phys. 2 43 (2004) 1A–B.
[23] B. Khare et al., Nano Lett. 2 (2002) 1.
[24] V. Turq et al., Tribol. Lett. 19 (2005) 1.
[25] N.L. McCook et al., Tribol. Lett. 20 (2005) 2.
[26] Kikuma J. *et al.*, J. Electron Spectrosc. 88(1998).
[27] D. Marton et al., Phys. Rev. Lett. 73 (1994) 1.
[28] K. Kim et al., Polymer 44 (2003) 20.
[29] A. Voevodin et al., J. Appl. Phys. 92 (2002) 9.
[30] J. Neidhardt, L. Hultman and Z Czigany, Carbon 42 (2004) 12–13.

Paper 13

Volume 1 • Number 3 • June 2007

Engineering Solutions for Military and Aerospace

DEFENSE TECH BRIEFS

Training and Simulation Technology Helps Produce Mission-Ready Warfighters

Rebuilding New Orleans: A Perspective from Colonel Lewis F. Setliff III

Semiconductor & IC Spinoffs From Military R&D



www.defensetechbriefs.com

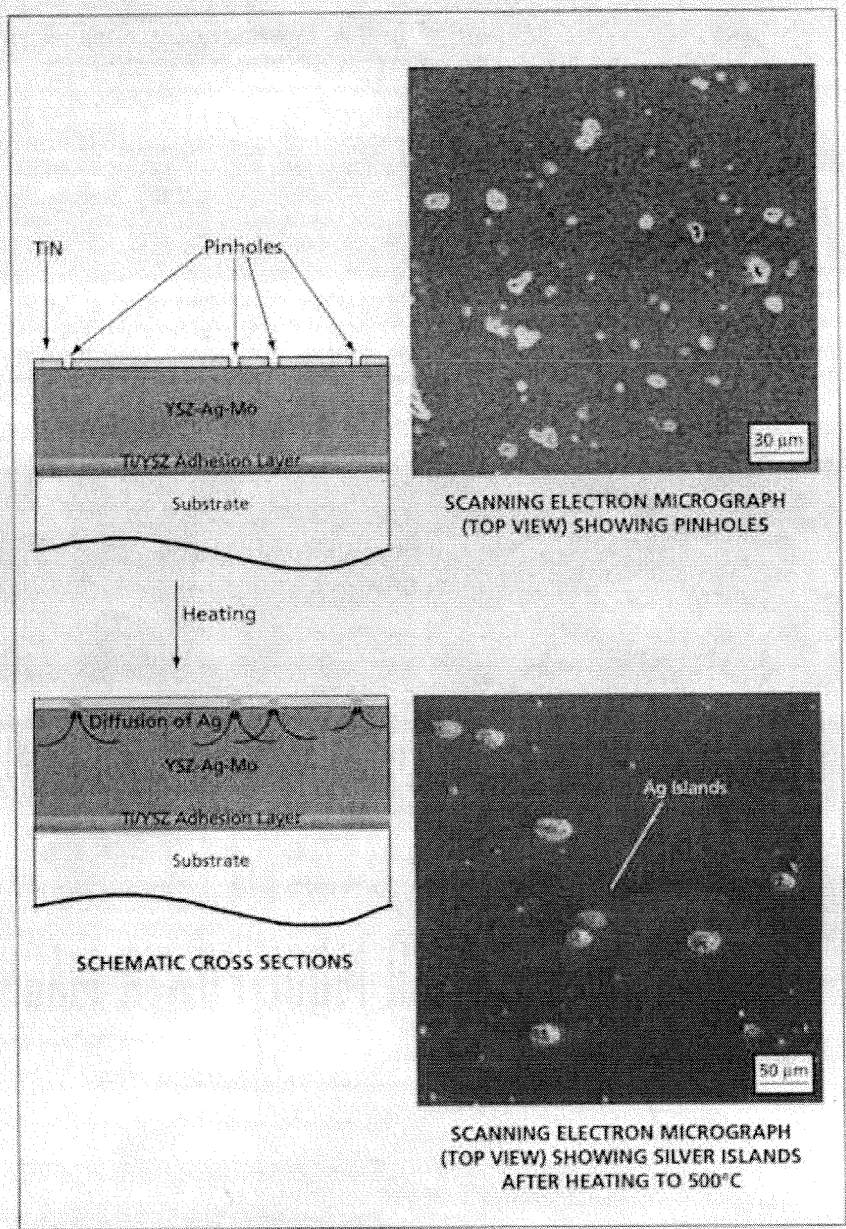
Self-Lubrication of Hot YSZ-Ag-Mo Nanocomposite Coatings

Diffusion of silver to surfaces plays a major part in high-temperature lubrication.

Air Force Research Laboratory, Wright-Patterson Air Force Base, Ohio

An experimental study has been performed to learn about the physical and chemical mechanisms of self-lubrication of coatings that comprise nanostructured composites of yttria-stabilized zirconia (YSZ), silver, and molybdenum. These and other YSZ-based nanocomposite coatings have received increasing attention in recent years because they offer a combination of hardness, toughness, resistance to wear, and low-friction C properties that make them attractive for reducing wear and friction and increasing the lifetimes of hot, sliding components of mechanical systems. In addition to the excellent mechanical and thermal stability of the basic YSZ ceramic material, the nanocomposite structures of these coatings, consisting of combinations of amorphous and crystalline phases, provide a "chameleon" surface adaptation, in which different phases turn into lubricants in response to different test environments, contact loads, sliding speeds, and temperatures. Moreover, proper sizing of nanocrystalline grains can restrict crack sizes and create large volumes of grain boundaries, thereby increasing the toughness and contact-load-bearing capabilities of these coatings.

The YSZ-Ag-Mo composite coatings for the present experimental study were deposited on steel and nickel-alloy substrates in a hybrid process that included deposition of 100-nm-thick titanium adhesion layers by use of a filtered titanium arc plasma, followed by pulsed-layer deposition of YSZ from a YSZ target. Ag and Mo were added to the coatings by magnetron sputtering from Ag and Mo targets. All of the coatings were grown to a thickness of about 2 μm. In some cases, the coating was formed as two 1-μm-thick YSZ-Ag-Mo layers, and a 100-nm-thick TiN diffusion-barrier layer was deposited between the YSZ-Ag-Mo layers by introducing a flow of nitrogen into the deposition chamber during



The **YSZ-Ag-Mo Coating Is Covered** with a TiN surface layer containing a random array of pinholes. This layer retards the diffusion of Ag to the surface, thereby reducing the rate of depletion of lubricant in order to prolong the high-temperature wear lifetime.

operation of the filtered titanium arc plasma source. In other cases, TiN barrier layers containing pinholes were deposited on the surfaces of YSZ-Ag-Mo coatings to limit through-the-thickness diffusion of silver (see figure).

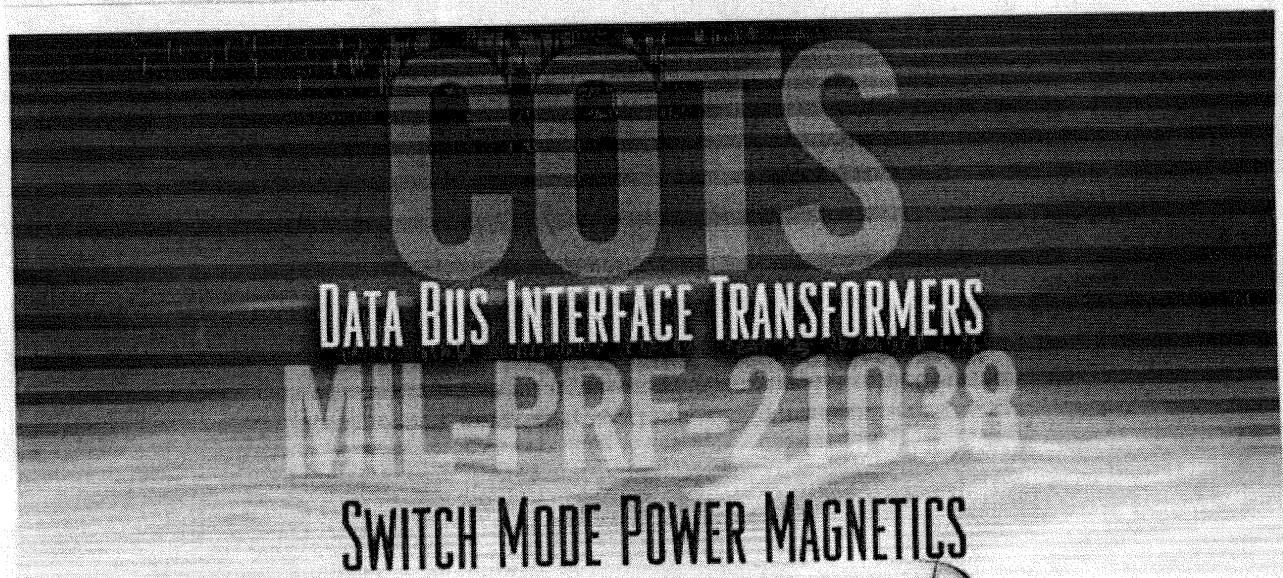
In the study, the focus was on the evolution of microstructure, diffusion of silver, and contact surface oxidation processes in sliding contact at high temperature in air. The microstructures of the coatings were determined by x-ray diffraction and transmission electron microscopy. Coefficients of friction were measured by use of a high-temperature ball-on-disk tribometer. The wear scar surfaces and coating cross-sections were studied by use of scanning electron, transmission electron, scanning transmission electron, and focused ion beam microscopes, which provided the information on spatial distributions of chemical compositions, including distributions of silver and molybdenum along with microstructural features.

The study revealed different "chameleon"-like high-temperature-adaptive lubrication mechanisms in the nanocomposite coatings. Coefficients of friction of about 0.4 or less were found to be maintained at all temperatures from 25 to 700 °C. The as-deposited coatings were found to include silver nanograins embedded in amorphous/nanocrystalline YSZ-Mo matrices. At high temperatures, heating-induced diffusion and coalescence of silver were found to result in microstructural and chemical changes that included formation of silver films on surfaces with silver-depleted YSZ-Mo layers left underneath. Crystallization of zirconia matrices was found to occur simultaneously with diffusion of silver to surfaces when the coatings were heated. It was confirmed that the diffusion of silver to, and coalescence of silver on, the surfaces of YSZ-Ag-Mo nanocomposite coatings plays an important part in high-temperature lubrication.

Silver was determined to be an effective lubricant at temperatures below 500 °C, and coalescence of silver on surfaces was found to isolate molybdenum inside the composites from ambient oxygen. At temperatures above 500 °C, the silver surface layers were found to be rapidly removed from wear tracks and, hence, the reactive molybdenum inside the silver-depleted YSZ-Mo layers was exposed to ambient air. Contact tribochemistry was found to result in the formation, in wear tracks, of molybdenum oxides, which provided lubrication at 700 °C.

In the cases of specimens containing the internal TiN barrier layers, these layers were found to preserve lubricants underneath, thereby providing for continuous replenishment of lubricants. The TiN layers were also found to force subsurface silver to diffuse laterally toward wear scars, once the TiN layers were breached by wear. This behavior affords an adaptive response, which includes on-demand supply of lubricant from storage volumes inside YSZ-Ag-Mo composites to surface contact areas. The YSZ-Ag-Mo coatings that contained the internal TiN barrier layers were found to maintain coefficients of friction of approximately 0.4 during more than 25,000 cycles, while the monolithic YSZ-Ag-Mo coatings lasted fewer than 5,000 cycles. The specimens having TiN surface layers with pinholes were found to have wear lifetimes greater than 50,000 cycles.

This work was done by J. J. Hu of the Air Force Research Laboratory, and C. Muratore, and A.A. Voevodin of UES, Inc. ***For more information, download the Technical Support Package (free white paper) at www.defensetechbriefs.com/tsp under the Materials category.*** *AFRL-0023*



Free Info at http://info.hotims.com/10970-835

Available online at www.sciencedirect.com
ScienceDirect
Composites Science and Technology 67 (2007) 336–347
COMPOSITES SCIENCE AND TECHNOLOGY
www.elsevier.com/locate/compscitech

Silver diffusion and high-temperature lubrication mechanisms of YSZ–Ag–Mo based nanocomposite coatings

J.J. Hu *, C. Muratore, A.A. Voevodin

Materials and Manufacturing Directorate, Air Force Research Laboratory (AFRL/MLBT), Building 654, 2941 Hobson Way, Wright-Patterson Air Force Base, Dayton, OH 45433-7750, United States of America

Received 5 June 2006; received in revised form 24 August 2006; accepted 7 September 2006
Available online 27 October 2006

Abstract

Yttria-stabilized zirconia (YSZ) nanocomposite coatings consisting of silver and molybdenum were produced by a hybrid process of filtered vacuum arc, magnetron sputtering and pulsed laser depositions for tribological investigations at different temperatures. The coatings with 24 at.% Ag and 10 at.% Mo contents showed a friction coefficient of 0.4 or less for all temperatures from 25 to 700 °C. The wear scar surfaces and coating cross-sections were studied using scanning electron, transmission electron, scanning transmission electron and focused ion beam microscopes, which also provided the information on chemical composition distributions of silver and molybdenum along with microstructure features. It was demonstrated that silver diffusion and coalescence on surfaces played an important part in the high-temperature lubrication mechanism of the YSZ–Ag–Mo coatings. Silver was found to be an effective lubricant at temperatures below 500 °C and its coalescence on the surface isolated molybdenum inside coatings from ambient oxygen. Lubricious oxides of molybdenum were formed and lubricated at temperatures above 500 °C when the silver was worn off the contact surface. For silver containment inside the coating at high temperatures, a multilayer architecture was built by inserting a TiN diffusion barrier layer in the composite coatings. Microscopic observations showed that this barrier layer prevented silver exit to the coating surface. At the same time, this enabled a subsequent lateral lubricant supply toward a wear scar location where the diffusion barrier layer was worn through and/or for a next thermal cycle. The multilayer coating maintained a friction coefficient of 0.4 or less for more than 25,000 cycles, while the monolithic coating lasted less than 5000 cycles. In addition, a TiN surface barrier layer with pinholes was deposited on the YSZ–Ag–Mo composite surface to control vertical silver diffusion. With this coating design, the coating wear lifetime was significantly increased beyond 50,000 cycles.
© 2006 Elsevier Ltd. All rights reserved.

Keywords: Yttria-stabilized zirconia; Nanocomposite; Multilayer; Silver; High-temperature lubrication

1. Introduction

Yttria-stabilized zirconia (YSZ) based nanocomposite coatings have received growing attention for their remarkable properties such as high hardness, toughness, wear resistance and low friction [1–13]. These properties are highly desirable for aerospace applications in order to increase the lifetime and performance of mechanical systems. The nanocomposite structure of the coatings provided a "chameleon" surface adaptation in addition to excellent mechanical and thermal stability of YSZ ceramic itself, which was previously studied for surface wear protection at different test environments, contact loads, sliding speeds, and temperatures [14–20]. The aerospace materials require a very demanding self-adapting performance to a wide range of environments and temperatures. The "chameleon" coating concept was developed with a series of tribological adaptive nanocomposite coatings consisting of amorphous and nanocrystalline phases, which can transform into lubricants when exposed to changes in environments and temperatures [8,21–23]. Proper sized nanocrystalline grains can restrict crack size, create a large

* Corresponding author. Tel.: +1 937 255 3312; fax: +1 937 255 2176.
E-mail address: Jianjun.Hu@WPAFB.AF.MIL (J.J. Hu).

0266-3538/$ - see front matter © 2006 Elsevier Ltd. All rights reserved.
doi:10.1016/j.compscitech.2006.09.008

volume of grain boundaries, and hence improve the coating toughness and contact load support [24,25]. The nanocomposite coatings consisting of YSZ ceramics and noble metals were initially studied for tribological uses at high temperatures [6–9].

The early investigations of YSZ–Au nanocomposite coatings showed that soft ductile gold was able to provide a low friction for up to 500 °C [6]. The weak bonding between ceramic and metallic components can facilitate the grain boundary sliding and improve the composite toughness. The in-situ transmission electron microscopy studies of YSZ–Au nanocomposites during heating showed that the diffusion process was accompanied by the coating microstructural and chemical changes [9]. Increased temperatures initiated the crystallization and growth of zirconia and gold nanograins inside the coatings and formation of 100–500 nm gold islands on the coating surfaces. A primary mechanism for the friction reduction of YSZ–Au coatings was based on the low shear deformation of the surface gold islands under friction-induced stress. Recently, YSZ–Ag–Mo nanocomposite coatings were produced by a hybrid process of magnetron sputtering and pulsed laser depositions [10,11]. Silver is an effective lubricant at moderately high temperatures [26–31], and molybdenum-based compounds are lubricious at higher temperatures in air, as shown by other researchers [32–36]. The YSZ–Ag–Mo coatings provided lubrication by forming a silver rich surface at 300–500 °C and by oxide formation in friction contact at above 500 °C. Studies on the YSZ–Ag–Mo coatings have been conducted on growth, characterization, mechanical and tribological properties.

The noble metals such as gold and silver have a large diffusion coefficient and high mobility at elevated temperatures. Heating activates diffusion out of highly strained sites in the YSZ matrix to open surfaces, where the reduction of system potential and surface energies thermodynamically drives metal grain nucleation and growth. After the noble metal transport to the surface, the coating becomes depleted in the lubricious metal and cannot act as a self-lubricated composite for long. Control of such diffusion processes is, hence, needed for an extended lubrication. Transition metal nitrides were reported as effective diffusion barrier materials for noble metals [37]. The wear lifetime of YSZ–Ag–Mo nanocomposite coatings was shown to be significantly increased when using a TiN diffusion barrier to restrict the silver diffusion [12,13]. For such composite coatings, the high temperature tribological performance strongly depends on the thermodynamic activation of silver diffusion in the coating matrix, diffusion process control with barrier layers, tribochemical reactions in the contact surface, and structural stability of the ceramic matrix.

In this paper, we focused on the microstructure evolution, silver diffusion development, and contact surface oxidation processes for a series of YSZ–Ag–Mo based nanocomposite coatings in sliding contacts at high temperatures in air. The silver diffusion behavior in the coatings after heating was directly observed by using electron microscopes. Focused ion beam (FIB) microscope was used to set-up observations of microstructural and chemical studies in coating cross-sections. Such experiments have not been reported in detail or used in tribological investigations before. The friction coefficients were measured at different high temperatures, and were examined in a close relationship with the coating surface changes in microstructure and chemistry. The results of our investigations reveal different high-temperature-adaptive lubrication mechanisms in the nanocomposite "chameleon" coatings.

2. Experimental

The YSZ–Ag–Mo nanocomposite coatings were produced with a hybrid process of filtered vacuum arc, magnetron sputtering and pulsed laser deposition in a stainless steel chamber, as shown in Fig. 1. The chamber was evacuated using a 520 l s^{-1} turbo pump to a base pressure of 7×10^{-6} Pa or less. Mirror polished M50 steel and Inconel 718 super-alloy substrates of 25 mm diameter were ultrasonically degreased and loaded into the chamber. The substrates were heated to 150 °C, and then bombarded with energetic argon ions (~800 eV) and metal ions (~650 eV) to clean the surface before deposition. A thin titanium adhesion layer (<100 nm) was deposited on substrates by using the filtered titanium vacuum arc plasma. Pulsed laser deposition of YSZ was then initiated with a laser pulse repetition rate gradually ramped from 1 to 30 Hz to produce a graded Ti/YSZ transition layer and further promote the coating adhesion to the substrates. A KrF excimer laser (LPX300 Lambda Physik) produced 800 mJ, 25 ns width UV pulses (248 nm). The laser beam was directed by a set of programmable mirrors to random positions on a rotating YSZ target. The chamber was then filled with

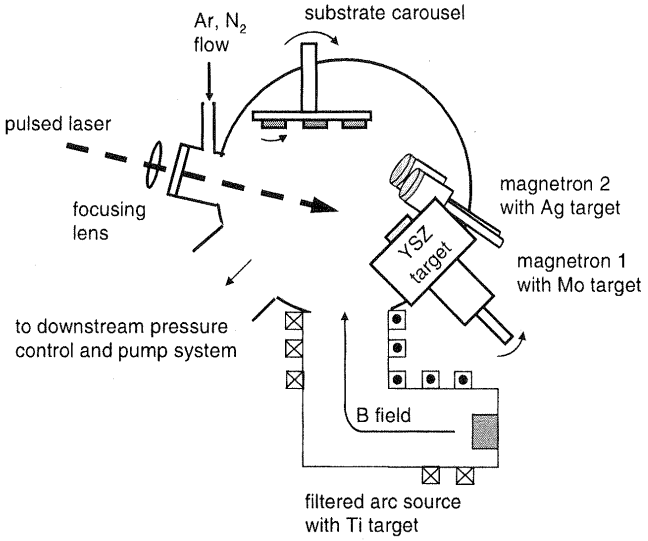


Fig. 1. Schematic diagram of the deposition chamber, combining filtered vacuum arc, magnetron sputtering, and pulsed laser deposition.

1.6 Pa Ar (99.99% pure) at a flow rate of 100 sccm to facilitate sputtering. Silver and molybdenum were added to the coatings by magnetron sputtering from metal targets made of pure silver and pure molybdenum. The dc power density on the both magnetron targets was adjusted from 1 to 5 W cm^{-2} in order to control metal contents in the produced composite YSZ–Ag–Mo coatings. During deposition, the substrates were biased to −150 V dc, and maintained at 150 °C. For multilayer architectures, a 100 nm thick TiN diffusion barrier layer was reactively deposited between two 1 μm thick YSZ–Ag–Mo layers by flowing 30 sccm nitrogen into the chamber while operating the filtered titanium arc plasma source. All coatings were grown to a thickness of approximate 2 μm in one to two hours depending on the magnetron power density. X-ray photoelectron spectroscopy (XPS) was used to determine that the YSZ–Ag–Mo coatings contained 5–24 at.% of Ag and 9–24 at.% of Mo. The TiN coatings were determined to be stoichiometric.

X-ray diffraction (XRD) data of the coatings were collected using a Rigaku diffractometer equipped with a monochromator in front of the CuKα X-ray source. Glancing incidence XRD was done with θ fixed at 8° for all scans in order to reduce the signal from substrates. Standard powder XRD patterns of tetragonal (t) ZrO_2 and face-centered cubic (fcc) Ag were used for data interpretation [38,39]. Transmission electron microscope (TEM) observations were performed using a Philips CM200 FEG (Field Emission Gun) microscope operated at 200 kV accelerating

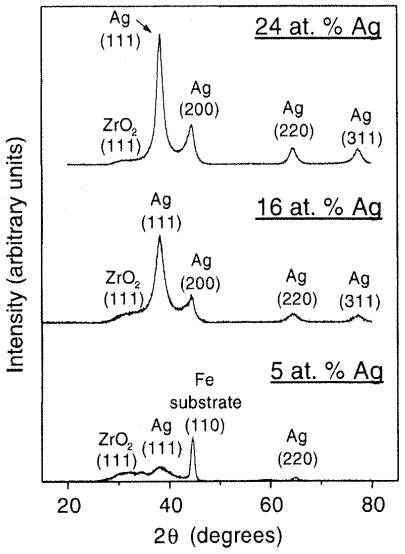


Fig. 2. XRD spectra of YSZ–Ag–Mo composite coatings with different Ag contents and 10 at.% Mo. Spectra are shifted on the vertical scale for clarity.

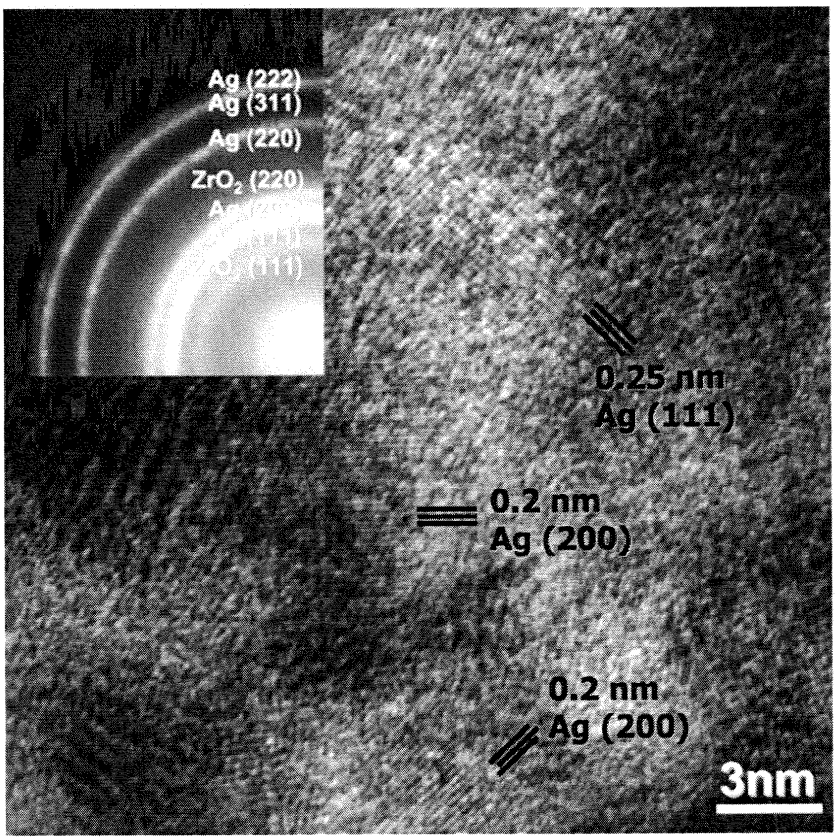


Fig. 3. High-resolution TEM image and the corresponding SAED pattern taken from the YSZ–24 at.% Ag–10 at.% Mo composite coating.

voltage. The FEG provided a complete coherent electron source and nm-sized probe, which were especially important for the high-spatial-resolution microstructure characterization. A NORAN X-ray energy dispersive spectrometer (EDS) was installed on the TEM and was used for chemical microanalyses of the coatings.

Friction coefficients in air with 40% (±1%) relative humidity (RH) were measured with a high-temperature (HT) ball-on-disk tribometer at 25, 300, 500 and 700 °C. Silicon nitride balls of 6.35-mm-diameter and 1 N normal load were used for all tests (approximate 0.7 GPa initial Hertzian contact stress). The tribotests were started after the coating samples were heated to the desired temperatures in about 20–35 min, and allowed to equilibrate for 5–10 min. Upon completion of the ball-on-disk measurements, samples were immediately removed from the furnace and allowed to cool in air. A series of annealing experiments were also performed using the same HT tribometer oven.

After tribotests, wear scars and sample surfaces were examined using a Leica 360 FEG scanning electron microscope (SEM) operating at 25 kV, which was equipped with a Link ISIS system of EDS for chemical analyses. A focused ion beam (FIB) microscope, FEI-DB235, was used to prepare lift-out specimens for showing the cross-sectional microstructure of the coatings. It was operated using 5 keV electron beams and 30 keV Ga^+ ion beams. To protect the coating surface, an approximately 2 μm thick Pt cap was deposited on the top of the samples using a gas injection system at a moderate ion beam current. Scanning transmission electron microscopy (STEM) and TEM/EDS were employed to study the cross-sectional microstructure and chemistry of the coatings after annealing. All these measurements were performed in order to understand the lubrication mechanism of YSZ–Ag–Mo nanocomposite coatings at high temperatures.

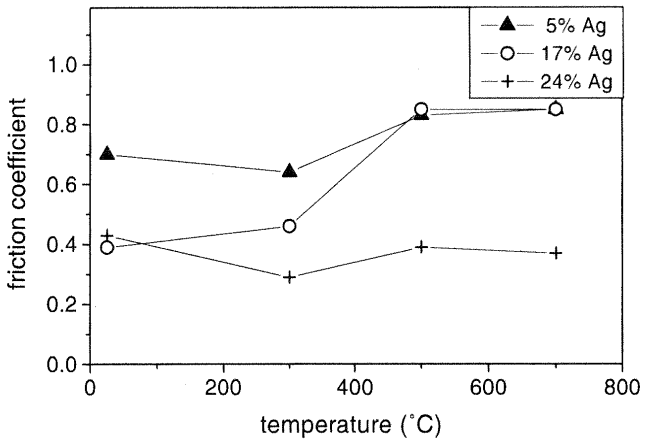


Fig. 4. Friction coefficients of YSZ–Ag–Mo composite coatings with different Ag contents and 10 at.% Mo from room to high temperatures.

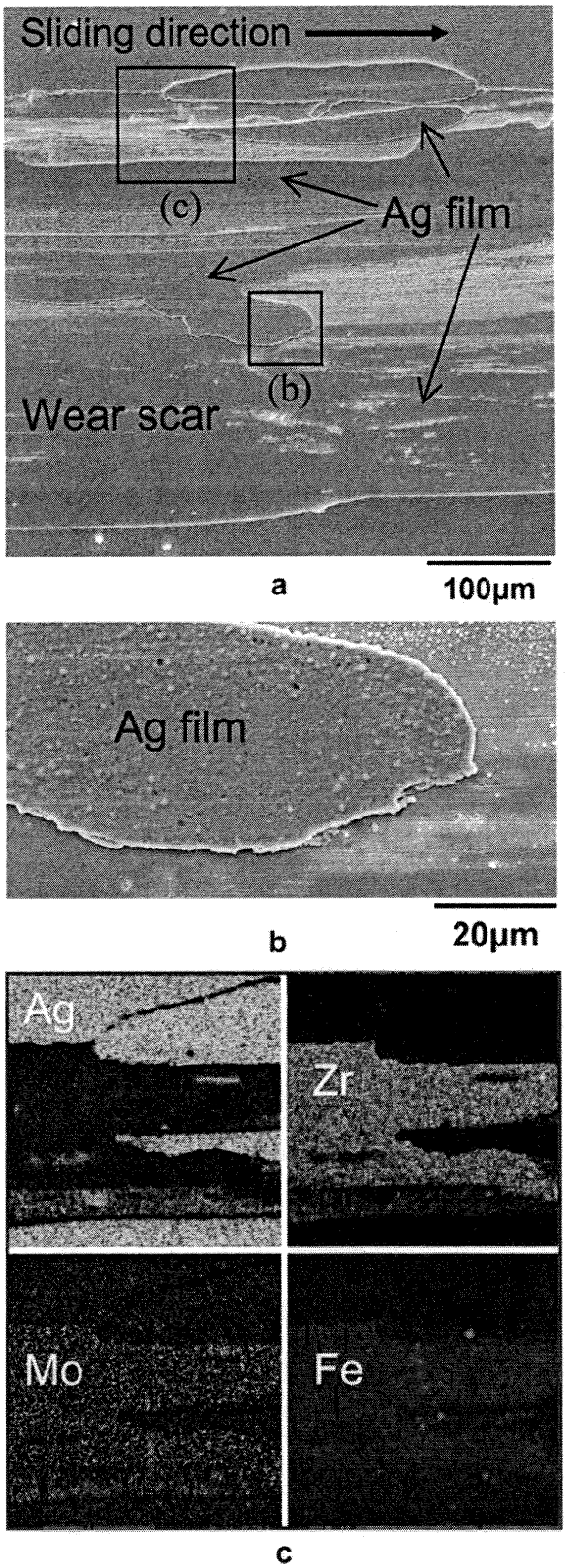


Fig. 5. (a) SEM image taken from the wear scar surface after friction coefficient measurements at 500 °C prior to coating failure. (b) High magnification image of a smeared Ag film inside the wear track. (c) EDS elemental mappings of Ag, Zr, Mo and Fe. The silver-covered regions on the wear scar surface show bright contrast in the Ag mapping.

3. Results and discussion

3.1. Studies of structure evolution and lubrication mechanisms in YSZ–Ag–Mo composite coatings

Pure metallic Ag and Mo were added into the YSZ coatings at a different atomic percentage to reach desirable mechanical and tribological properties of the coatings [10,11]. Fig. 2 shows the XRD spectra of the YSZ–Ag–10 at.% Mo composite coatings containing 5, 16 and 24 at.% Ag, which exhibit weak tetragonal zirconia peaks and stronger cubic silver peaks. The intensity of t-ZrO_2(1 1 1) peaks decreased with increasing silver contents, while the molybdenum diffraction was not detected. The strong silver peaks dominated the XRD spectra from the coatings with higher silver contents, and the Fe(1 1 0) peaks from M50 steel substrates were obscured by the Ag(2 0 0) peaks. Silver nanograins are visible in the high-resolution TEM image, as shown in Fig. 3. The corresponding selected-area electron diffraction (SAED) pattern exhibits diffraction rings indexing randomly oriented t-ZrO_2 and fcc-Ag phases, as shown in Fig. 3 – insert.

Fig. 4 shows the friction coefficients of the YSZ–Ag–Mo composite coatings grown with 5–24 at.% silver contents and 10 at.% molybdenum content at room to high temperatures. The 5 at.% Ag coating exhibited high friction at all temperatures, and the 17 at.% Ag coating exhibited a high friction at 500 °C and over. The 24 at.% Ag coating had a friction coefficient of 0.4 or less for all temperatures from 25 to 700 °C. Therefore, a sufficient amount of silver in the coating is required to facilitate lubrication at high temperatures. Unless otherwise noted, the YSZ–Ag–Mo composites in the following analyses and discussions contained 24 at.% Ag and 10 at.% Mo.

Coating wear tracks after sliding tests at 500 °C and prior to coating failure were analyzed using SEM/EDS (Fig. 5). Smeared regions were found inside wear tracks, which were predominantly composed of silver, as shown in Fig. 5a. A high magnification image of the smeared silver film is shown in Fig. 5b. EDS elemental mappings of Ag, Zr, Mo and Fe (Fig. 5c) reveal the silver-covered regions on the surface as Ag is in bright contrast, while Zr and Mo are visible on the silver-worn-off surfaces as Zr and Mo are in bright contrast. The weak Fe signal contrast resulted from steel substrates being under a less thick YSZ–Ag–Mo layer in worn wear track areas.

After 1000 cycles of sliding tests at 700 °C, some oxidization products like MoO_3 were found inside the wear

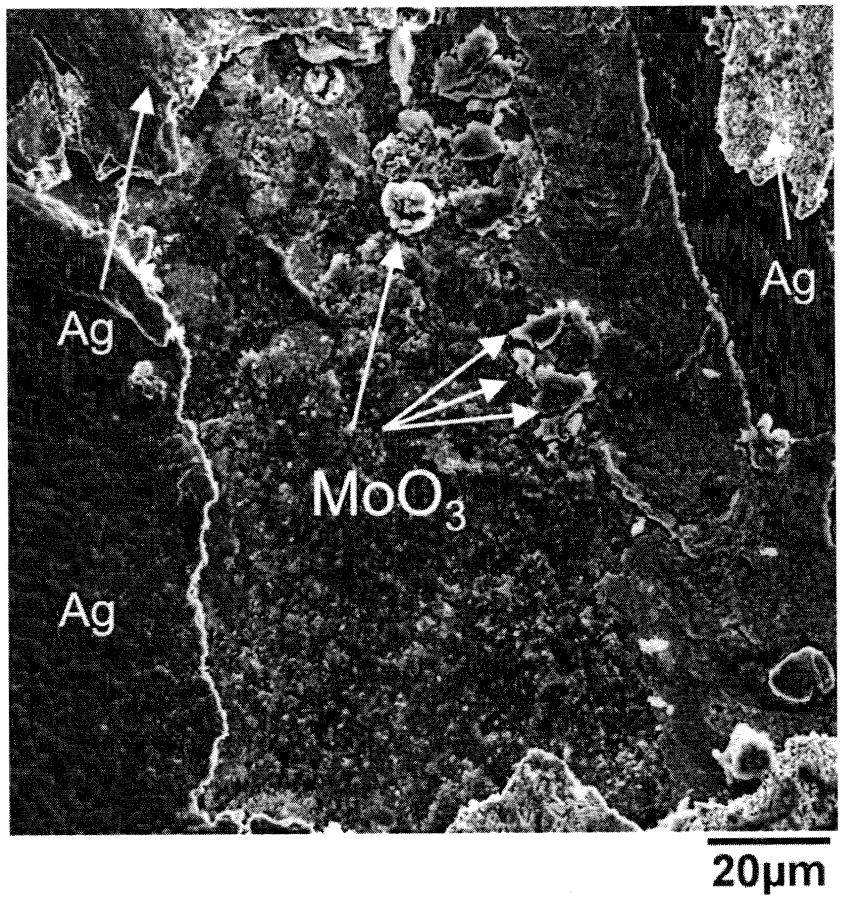


Fig. 6. SEM image taken from the wear scar surface after 1000 cycles of tribometer tests at 700 °C. MoO_3 grains exist inside the wear track along with smeared silver films.

track between smeared silver regions, as shown in Fig. 6. MoO_3 demonstrates a low shear stress at 700 °C and has been recommended to use as a lubricant at high temperatures. Fig. 6 also shows the coverage of the coating surface outside wear track with heating-induced silver surface layer, which was disrupted inside wear tracks since silver, as a lubricant, does not work well above 500 °C. The thermodynamic activation of silver diffusion is inevitable during HT sliding. Results of the silver diffusion studies in the YSZ–Mo–Ag composite coatings after heating are discussed next.

Figs. 7a and b show the SEM images taken from (a) the cross-sectional specimen of the coating as cut in a FIB microscope, and (b) the coating surface outside the wear track after heating to 500 °C during tribometer tests. The initial monolithic YSZ–Ag–Mo composite coating developed into two distinct layers after heating, as shown in Fig. 7a, where a platinum cap was deposited on the coating surface for protection during FIB sample preparation. EDS measurements determined that the chemical composition of the bright top layer was silver. The lower layer was a sliver-depleted coating, which mainly consisted of YSZ and molybdenum. Dense silver grains of 1–2 μm in size grew, coalesced, and completely covered the coating sur-

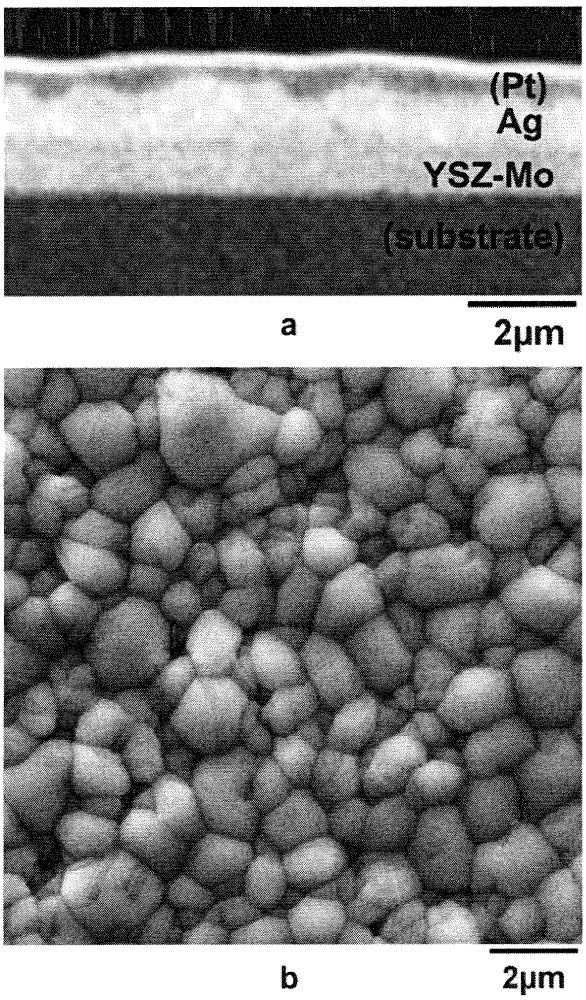


Fig. 7. (a) Cross-sectional micrograph and (b) surface micrograph of the YSZ–24 at.% Ag–10 at.% Mo composite coating after heating to 500 °C as observed using a FIB microscope.

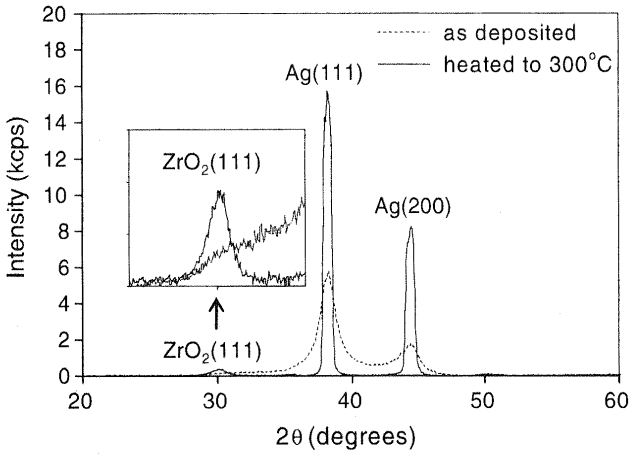


Fig. 8. XRD spectra of the YSZ–24 at.% Ag–10 at.% Mo composite coating before (dotted line) and after (solid line) heating. The inset is a zoom-in pattern of the (1 1 1) Zr_2O diffraction region.

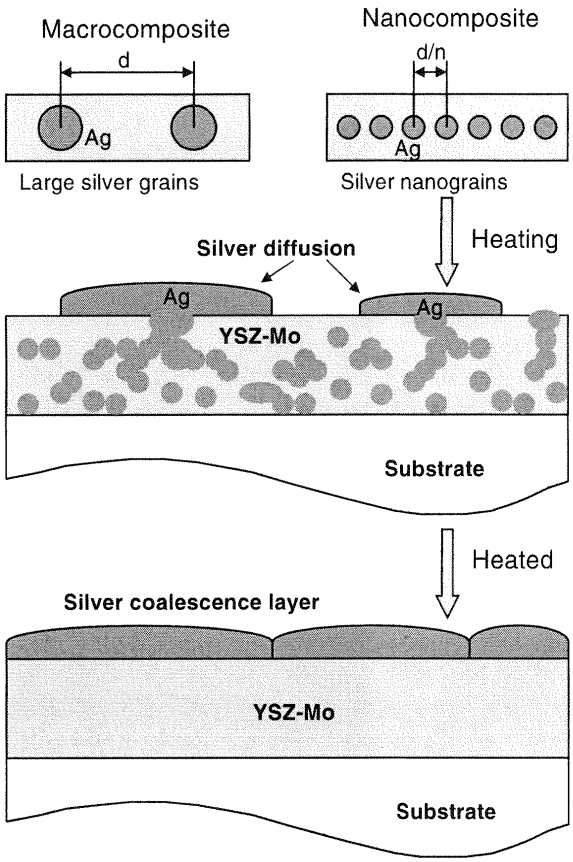


Fig. 9. Schematic diagram of the thermodynamic migration of silver inside the YSZ–Ag–Mo nanocomposite coating after heating.

face after heating, as shown in Fig. 7b. The grains are significantly larger than the initial silver nanograins in the as-deposited coatings (compare to Fig. 3).

XRD patterns were measured from the annealed coatings in order to further investigate the coating microstructure evolution during heating. Narrower fcc-Ag(1 1 1) and (2 0 0) peaks developed after annealing in comparison to the as-deposited coating, as shown in Fig. 8, which indicated a largely increased grain size of silver. In addition, a well-defined t-ZrO_2(1 1 1) peak was found for the annealed coating pattern, which was nearly invisible in the as-deposited coating. Low temperature growth of YSZ–Ag–Mo composites in this study possibly resulted in a formation of solid solutions of silver and molybdenum in highly defective and distorted zirconia nanocrystalline grains in addition to silver grains. At equilibrium conditions, silver is immiscible with zirconia and, hence, it would diffuse out of zirconia lattice defects under temperature activation. This process was accompanied by zirconia lattice relaxation, ordering and crystallization, and was evidenced by the XRD pattern in Fig. 8.

Fig. 9 provides a schematic diagram of silver diffusion stages in heating sequences to facilitate a discussion on the thermodynamic behavior of silver inside the nanocomposite matrix. As produced, silver exists as nanocrystalline grains inside YSZ–Ag–Mo nanocomposites and as metastable solid solution inside defected zirconia lattice (first stage – right in Fig. 9). This is a distinct difference in comparison to the distribution of large silver grains (first stage – left in Fig. 9) in macrocomposites, for example, produced by plasma spay techniques, such as the NASA PS200 and PS300 series high-temperature lubricating coatings [28,29]. At the same volume of silver contents, there are two major factors that thermodynamically accelerate silver diffusion in nanocomposites as compared to macrocomposites: (1) a much larger surface area of the embedded silver nanograins provides a significantly larger decrease in grain boundary surface energy by the grain coalescence; and (2) a much shorter distance between the embedded silver nanograins makes the grain growth kinetic much faster.

From the above considerations, YSZ–Ag–Mo nanocomposite coatings require less heating energy for the silver atoms to overcome the potential barrier and cover the distance between neighboring silver grains for their growth. In addition to the silver diffusion, the heating activates zirconia structure ordering and crystallization (Fig. 8). This ordering process pushes inserted silver atoms out of the defects inside zirconia grains. However, the YSZ–Ag–Mo coatings produced in this study are dense and free of voids to accommodate space requirements for the silver grain growth, in contrast to typical porosity and voids in plasma sprayed macrocomposite coatings. This creates a space

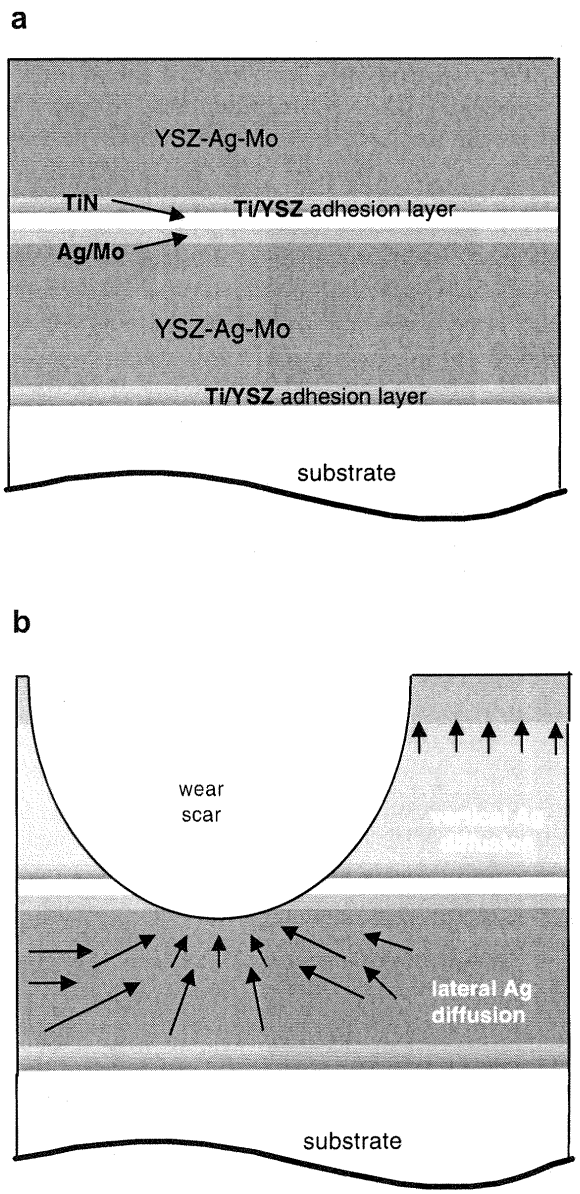


Fig. 10. (a) Schematic of the multilayer structure divided by a TiN diffusion barrier layer. (b) Schematic of the expected response of the multilayer coating during high-temperature tribotests.

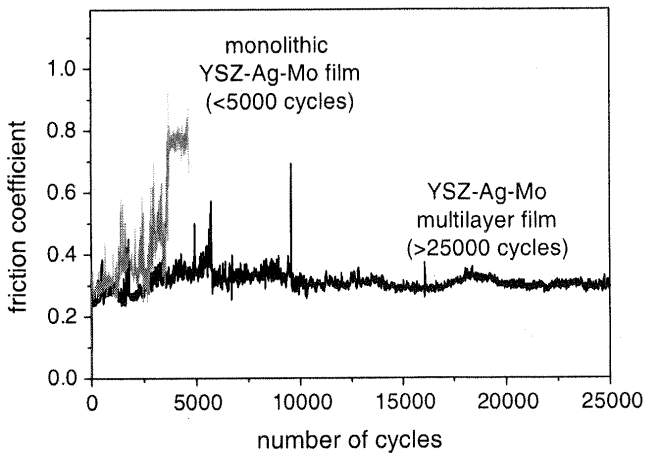


Fig. 11. Friction trace of the multilayer YSZ–Ag–Mo/TiN coating in the ball-on-disk test at 500 °C. The friction trace of monolithic YSZ–Ag–Mo coating measured under the same conditions is shown for comparison.

restriction for the silver grain growth inside the nanocomposite coating matrix. Such space for the silver grain growth is available at the coating surface and vertical silver diffusion transports the silver from the coating bulk to the surface for the silver grain formation and growth (Fig. 7b). This heating-induced silver diffusion and coalescence in YZS-Ag–Mo nanocomposite coatings provide a thermodynamically driven mechanism for the formation of a dense silver layer on the coating surface, which seals a silver-depleted YSZ–Mo composite layer inside the coating (final stage in Fig. 9).

3.2. Silver diffusion control and lubrication mechanisms in multilayered YSZ–Ag–Mo/TiN coatings

In an effort to increase the coating endurance and move toward thermal cycling capability, a multilayer architecture was produced by interleaving a 100 nm thick TiN diffusion barrier in YSZ–Ag–Mo composites, as schematically shown in Fig. 10a [12]. A thin (<50 nm) titanium adhesion layer with Ti–YSZ graded compositions was deposited between the TiN barrier layer and top YSZ–Ag–Mo composite layer. Also, a thin (<50 nm) Ag–Mo layer was deposited under the TiN layer to direct the silver composition gradient downward. This Ag–Mo underlayer also provided lubrication upon initial contact of the ball with the coating under the TiN layer at the moment when it was breached in the wear process. This multilayer architecture provided a fresh layer of composite lubricants after the TiN barrier layer was worn through, as shown in Fig. 10b. The lateral diffusion of silver from within the lower composite layer toward the relatively small wear scar provides a continuous supply of the lubricant (compare 10–100 μm typical wear track width with 10–100 mm typical substrate surface dimensions). This can considerably increase the coating wear lifetime [12]. Fig. 11 shows the friction traces of both monolithic and multilayer YSZ–Ag–Mo coatings in sliding tests at 500 °C in air. The YSZ–Ag–Mo/TiN multilayer coating maintained a friction coefficient of approximately less than 0.4 for over 25,000 cycles, while the YSZ–Ag–Mo monolithic coating could only provide lubrication for about 4500 cycles. The present

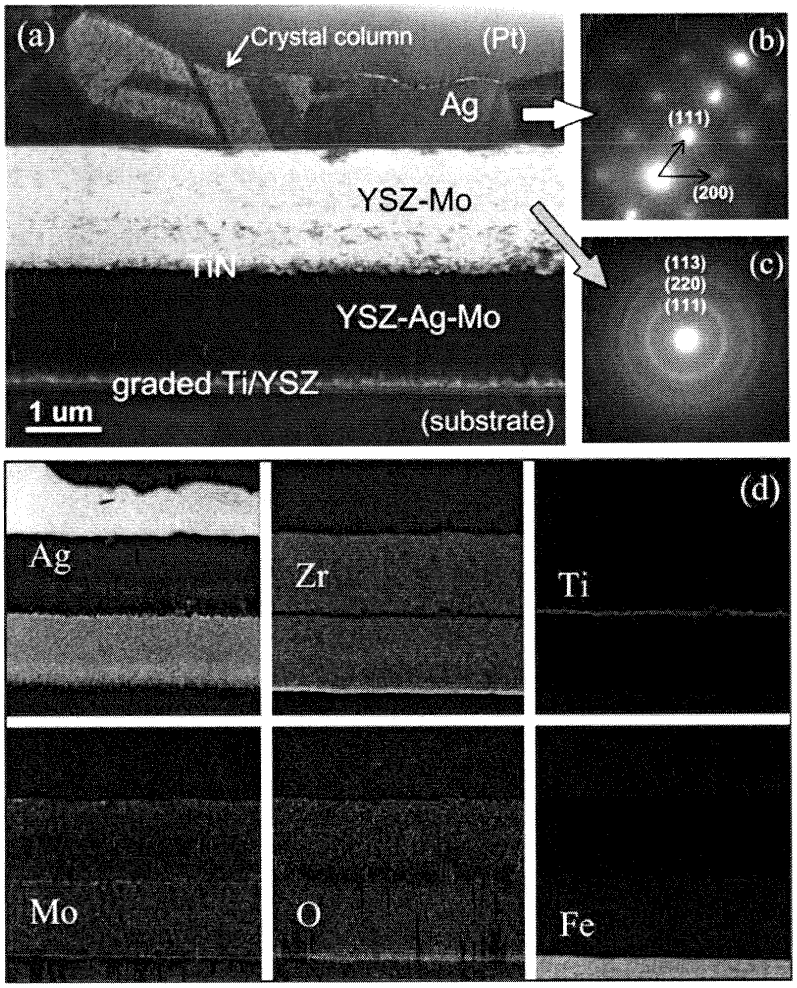


Fig. 12. (a) TEM image of the multilayer YSZ–Ag–Mo/TiN coating cross-section after heating to 500 °C. (b) SAED pattern taken from the top silver layer. (c) SAED pattern taken from the silver-depleted YSZ–Mo composite layer. (d) EDS elemental mappings of Ag, Zr, Ti, Mo, O, and Fe recorded for the same coating cross-section as shown in (a).

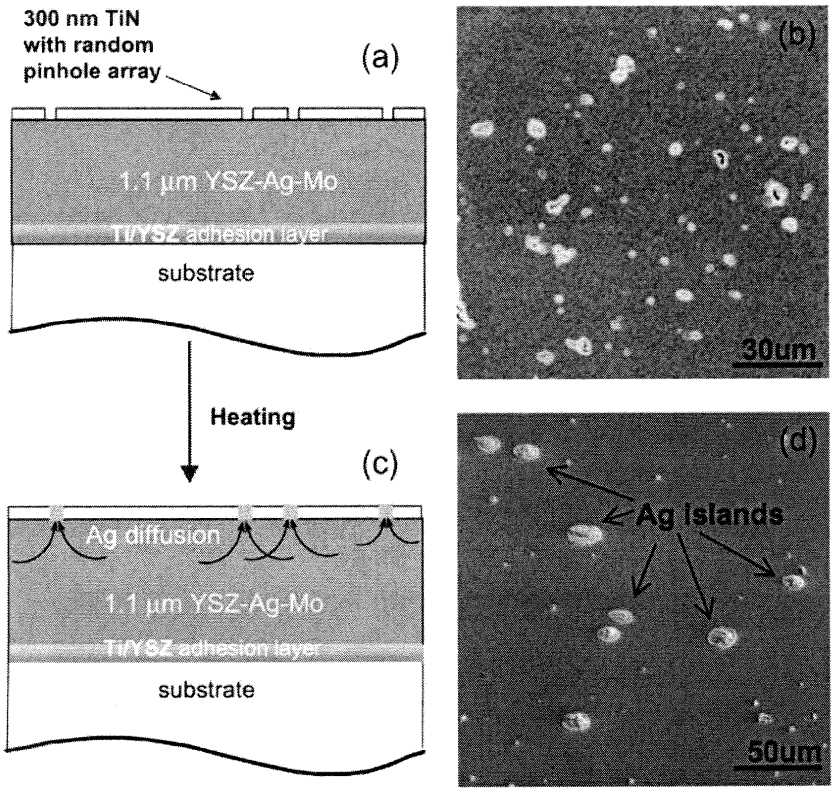


Fig. 13. (a) Schematic of the coating structure design with a TiN diffusion barrier mask on the surface. (b) SEM image showing the TiN/YSZ–Ag–Mo coating prepared with micron pinholes on the surface. (c) Schematic illustration of the heating-induced silver diffusion path in the coating. (d) SEM image showing dome-like silver islands formed on the surface after heating at 500 °C for 45 min.

results demonstrate the benefit of the multilayer composite design to increase the coating endurance for HT lubrications.

The multilayer coating microstructure after heating to 500 °C was further studied using a TEM. Fig. 12a shows a TEM image of the coating cross-section as prepared by lift-out in a FIB microscope. The top silver layer was formed by the heating-induced silver diffusion and coalescence on surfaces from the upper YSZ–Ag–Mo layer of the multilayer composite coating – similar as discussed in the Section 3.1. Micron-sized columnar silver crystals grew on the surface, as indicated in Fig. 12a. Fig. 12b shows a SAED pattern taken from one of the silver grains. The pattern consists of individual diffraction spots of a single crystal indexing fcc-Ag(1 1 1) and (2 0 0) planes.

A silver-depleted YSZ–Mo composite layer remained beneath the silver surface after the silver diffusion to the coating surface. A SAED pattern from this silver-depleted YSZ–Mo layer is shown in Fig. 12c. The diffraction rings were indexed to t-ZrO_2(1 1 1), (2 2 0), and (1 1 3) planes with random orientations in the layer. The heating effects caused the crystallization of zirconia, which was more like an amorphous phase in the as-deposited composite coatings. These TEM results of the top YSZ–Ag–Mo composite layer are in a good agreement with the above SEM and XRD studies as discussed in the Section 3.1 and shown in Figs. 7 and 8.

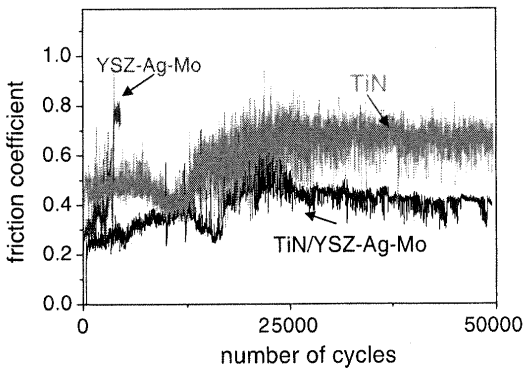


Fig. 14. Friction trace of the TiN-barrier-masked TiN/YSZ–Ag–Mo coating in the ball-on-disk test at 500 °C. The friction traces of monolithic YSZ–Ag–Mo and TiN coatings measured under the same conditions are shown for comparisons.

In contrast to the changes of the upper YSZ–Ag–Mo layer, there was no detectable chemical composition change in the YSZ–Ag–Mo layer under the TiN barrier layer. The chemical compositions of the different layers were measured by the EDS elemental mappings of Ag, Zr, Ti, Mo, O and Fe, as shown in Fig. 12d. From these analyses, it was confirmed that the chemical compositions were well maintained in the lower YSZ–Ag–Mo layer deposited under the TiN barrier layer. Cross-sectional TEM of the annealed multilayer coating did not show visible morphol-

ogy and structural changes inside this lower composite layer in comparison to the as-deposited coating.

Therefore, YSZ–Ag–Mo/TiN multilayer design helped to increase wear life by the restriction of silver diffusions in a vertical direction and created conditions for guiding subsurface silver diffusion laterally toward the wear scar area. This novel lateral diffusion mechanism is very beneficial for HT lubrication and extends lubricant supply to the wear track over longer time periods. It can be easily controlled through an optimization of the individual composite layer thickness (defines diffusion cross-section area) and the number of layers in the coating stack (defines total availability of the preserved lubricant reservoirs). Also, the insertion of dense and thin TiN barrier layers is an efficient way to prevent undesirable permanent changes in microstructures and chemistries in the depth of underlying YSZ–Ag–Mo composite layers. This enhances the overall coating stability and endurance in HT applications.

3.3. Retardation of silver surface release via a porous TiN barrier "mask"

Instead of a dense TiN barrier interlayer for completely sealing the underneath YSZ–Ag–Mo composite, a TiN barrier surface layer with a random array of pinholes – a porous TiN (p-TiN) "mask" – was produced to prolong the wear lifetime of the YSZ–Ag–Mo composite coatings [13]. This approach restricted the lubricant transport to the coating surface through those holes and reduced the silver depletion rate at high temperatures. Fig. 13a shows a schematic structural design of the coating with a p-TiN diffusion barrier mask, and (b) shows a SEM image taken

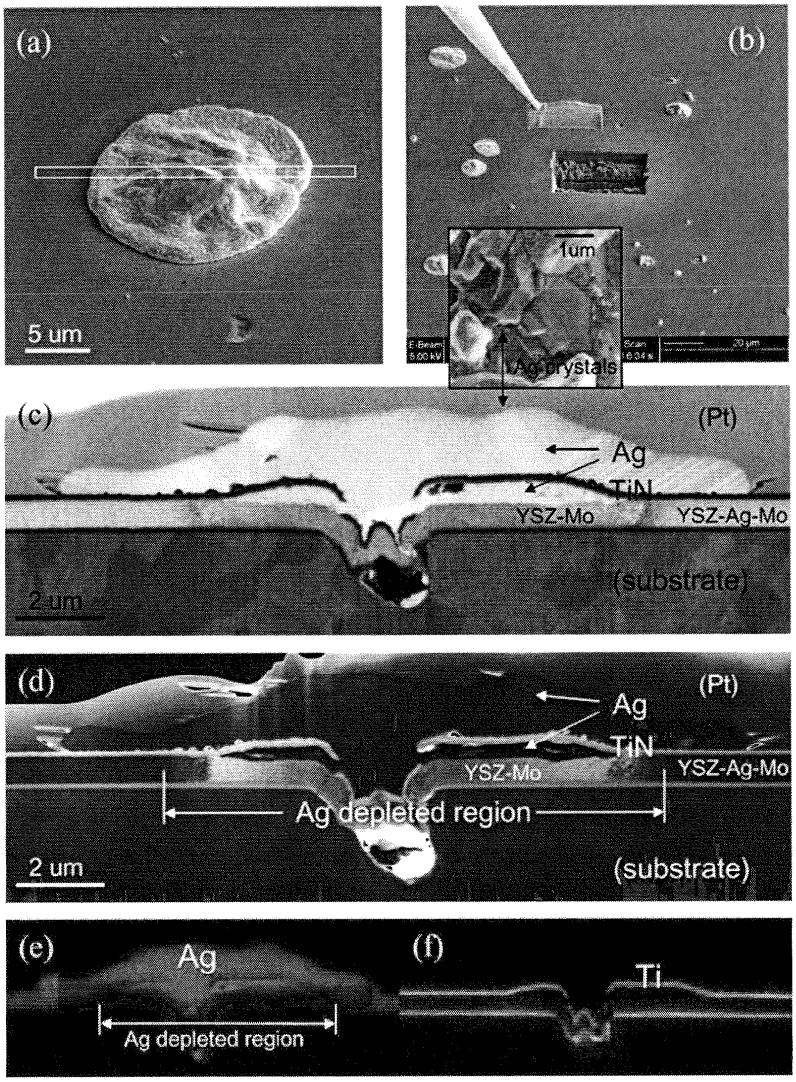


Fig. 15. (a) SEM image of a dome-like silver island on the TiN-barrier-masked TiN/YSZ–Ag–Mo coating surface after heating to 500 °C, in which a white box indicates the cross-section position for FIB cutting. (b) In-situ lift-out of the thin foil of the coating cross-section. (c) SEM image taken from the coating cross-section showing silver regions in bright contrast. Inset is a SEM image taken from the top of the sample. (d) DF-STEM image of the coating cross-section showing silver regions in dark contrast with a high sensitivity to silver concentrations. (e,f) EDS elemental mappings of Ag and Ti recorded for the same coating cross-section as shown in (c).

from the TiN/YSZ–Ag–Mo coating with pinholes on the p-TiN surface. The silver diffusion paths by heating are schematically shown in Fig. 13c. Dome-like silver islands formed on the surface (Fig. 13d), after the coating was heated to 500 °C in the tribometer furnace and maintained at that temperature for 45 min. The size of the islands was varied within approximate 10–50 μm. The SEM results demonstrated that the p-TiN barrier mask restricted the silver transport to the surface, as compared to the unrestricted silver diffusion out of YSZ–Ag–Mo coatings discussed in Section 3.1 and shown in Fig. 7.

Fig. 14 shows the friction trace of the above TiN/YSZ–Ag–Mo coating in the ball-on-disk tests at 500 °C. For comparison purposes, monolithic YSZ–Ag–Mo and dense monolithic TiN coatings of the same total thickness as the TiN/YSZ–Ag–Mo coating were also measured under the same tribotest conditions. The monolithic YSZ–Ag–Mo coating showed a steady-state friction coefficient of 0.4 before failure at 4500 cycles, as indicated by a sudden increase in friction coefficients. The friction coefficient of the TiN coating was maintained at 0.5 for 12,000 cycles before increasing to 0.65, which was consistent with the friction coefficient of uncoated M50 steel substrates at 500 °C. The TiN/YSZ–Ag–Mo coating did not fail in our tests over 50,000 cycles, and it maintained a friction coefficient of approximate 0.4. Therefore, a significant extension of the wear lifetime was demonstrated for the coating covered with a p-TiN barrier mask, which helped to restrict the silver diffusion to the surface and to reduce the depletion rate of silver in under-surface coating volumes.

For further studying the silver diffusion mechanisms in YSZ–Ag–Mo composites under a p-TiN barrier mask, cross-sectional specimens were prepared using a FIB to cut sections in the middle of dome-like silver islands, as shown in Fig. 15a. In-situ lift-out of the thin foils of coating cross-sections was performed by using an Omniprobe manipulator attached to FIB, as shown in Fig. 15b. Electron transparent specimens were finally produced by ion beam polishing the section foils welded on Omniprobe grids. Fig. 15c shows a SEM image of the above FIB-cut coating cross-section, and Fig. 15d shows the corresponding dark field (DF) STEM image, which was taken by using an annular STEM detector installed under the specimen. EDS analyses determined that the dome-like islands formed on the surface consisted of pure silver while zirconia and molybdenum were maintained inside the coating body. Figs. 15e and f show the EDS elemental mapping results for Ag and Ti, respectively. Diffusion affected regions inside YSZ–Ag–Mo composite layer, which were sandwiched between adhesive Ti and barrier p-TiN layers, are clearly visible in those images.

The SEM image shows the silver regions in bright contrast and some columnar silver crystals are indicated by arrows in Fig. 15c. The columnar crystal growth of silver can also be visible in the insert SEM image taken from the top of the sample. The DF-STEM image showed the silver regions in dark contrast and was more sensitive to the variation of silver contents. From these analyses, the silver-depleted region in the coating was reasonably defined, as indicated in Figs. 15d and e. The region width was measured as approximate 12 μm. Beyond this region, the silver composition was maintained unchanged and could act as a subsequent lubricant reservoir. These silver atoms will take longer time (more than 45 min of this annealing experiment) to diffuse out of the coating to the surface.

These microstructure characterizations provided the evidence of the lateral silver diffusion mechanism from inside the coating toward the holes of the p-TiN barrier mask and then vertically to the surface with a grain growth on the exit of the p-TiN layer holes. The silver surface release was restricted by the size and surface area density of holes in the p-TiN layer. This mechanism explains why the thin p-TiN barrier mask can provide a multifold increase of the YSZ–Ag–Mo coating endurance during HT sliding in air.

4. Conclusions

YSZ–Ag–Mo nanocomposite coatings were produced by combining filtered vacuum arc, magnetron sputtering and pulsed laser depositions. They maintained a friction coefficient of approximate 0.4 or less for all the temperatures from 25 to 700 °C during HT ball-on-disk tribometer tests. The XRD and TEM analyses of as-deposited coatings determined their nanocomposite structure consisted of silver nanograins embedded in an amorphous/nanocrystalline YSZ–Mo matrix. At high temperatures, the heating-induced silver diffusion and coalescence resulted in coating microstructure and chemistry changes with a granular silver film formed on the coating surface and a silver-depleted YSZ–Mo layer left underneath. Zirconia matrix crystallization occurred in parallel with silver surface diffusion when the coating was heated. It was confirmed that the silver diffusion and coalescence on the surface played an important part for HT lubrication mechanisms of YSZ–Ag–Mo nanocomposite coatings. Silver was an effective lubricant at temperatures below 500 °C, and the silver coalescence on surfaces isolated molybdenum inside the composites from ambient oxygen. At temperatures above 500 °C, the silver cap layer was rapidly removed from wear tracks and hence the reactive molybdenum inside the silver-depleted YSZ–Mo layer was exposed to ambient air. Contact tribochemistry resulted in the formation of molybdenum oxides in wear tracks, which provided lubrication at 700 °C.

For controlling silver diffusion, multilayer-structured coatings were prepared by inserting a dense TiN diffusion barrier layer between two YSZ–Ag–Mo nanocomposite layers. This TiN barrier preserved lubricants underneath for a continuous lubricant replenishment and forced a subsurface silver to diffuse laterally toward the wear scars, once the TiN layer was breached by wear. Such a mechanism provided an adaptive system response with "on

demand" lubricant supply from storage volumes inside YSZ–Ag–Mo composites to the surface contact areas. These multilayer YSZ–Ag–Mo/TiN coatings maintained a friction coefficient of approximately 0.4 for more than 25,000 cycles, while the monolithic YSZ–Ag–Mo coatings lasted less than 5000 cycles. Finally, a p-TiN barrier mask was coated on the YSZ–Ag–Mo composite surface to reduce the silver diffusion rate to the surface as demonstrated by FIB microscopic studies. The wear lifetime of p-TiN-barrier-masked coatings was increased beyond 50,000 cycles, and was significantly longer than that of monolithic YSZ–Ag–Mo or dense TiN coatings. The present studies establish basic mechanisms and concept foundation for developing YSZ–Ag–Mo nanocomposite coatings with dense TiN barrier interlayers and porous TiN surface masks for HT sliding in air with moderately low friction and long lifetime.

Acknowledgement

The Air Force Office of Scientific Research (AFOSR) is gratefully acknowledged for financial support.

References

[1] Voevodin AA, Jones JG, Zabinski JS. J Appl Phys 2000;88:1088.
[2] Voevodin AA, Jones JG, Zabinski JS. Appl Phys Lett 2001;78:730.
[3] Voevodin AA, Jones JG, Zabinski JS. J Vac Sci Technol A 2001;19(4):1320.
[4] Jones JG, Voevodin AA, Zabinski JS. Surf Coat Technol 2001;146:258.
[5] Voevodin AA, Jones JG, Zabinski JS. Laser ablation, low temperature fabricated yttria-stabilized zirconia oriented films. US Patent # 6,509,070, January 21, 2003.
[6] Voevodin AA, Hu JJ, Fitz TA, Zabinski JS. Surf Coat Technol 2001;146:351.
[7] Voevodin AA, Hu JJ, Jones JG, Fitz TA, Zabinski JS. Thin Solid Films 2001;401:187.
[8] Voevodin AA, Fitz TA, Hu JJ, Zabinski JS. J Vac Sci Technol A 2002;20(4):1434.
[9] Hu JJ, Voevodin AA, Zabinski JS. J Mater Res 2005;20:1860.
[10] Muratore C, Voevodin AA, Hu JJ, Jones JG, Zabinski JS. Surf Coat Technol 2005;200:1549.
[11] Muratore C, Voevodin AA, Hu JJ, Zabinski JS. Wear, in press.
[12] Muratore C, Voevodin AA, Hu JJ, Zabinski JS. Tribol Lett, in press.
[13] Muratore C, Hu JJ, Voevodin AA. Thin Solid Films, in press.
[14] Fischer TE, Anderson MP, Jahanmir S, Salher R. Wear 1988;124:133.
[15] Fischer TE, Anderson MP, Jahanmir S. J Am Ceram Soc 1989;72:252.
[16] Stachowiak GW, Stachowiak GB. Wear 1989;132:151.
[17] Stachowiak GW, Stachowiak GB. Wear 1991;143:277.
[18] Carter GM, Hooper RM, Henshall JL, Guillou MO. Wear 1991;148:147.
[19] Lee SW, Hsu SM, Shen MC. J Am Ceram Soc 1993;76:1937.
[20] Tucci A, Esposito L. Wear 1994;172:111.
[21] Voevodin AA, O'Neill JP, Zabinski JS. Surf Coat Technol 1999;119:36.
[22] Voevodin AA, Zabinski JS. Thin Solid Films 2000;370:223.
[23] Voevodin AA, Zabinski JS. Compos Sci Technol 2005;65:741.
[24] Veprek S, Reiprich S, Li SZ. Appl Phys Lett 1995;66:2640.
[25] Musil J, Zeman P, Hruby H, Mayrhofer PH. Surf Coat Technol 1999;120–121:179.
[26] Sliney HE. Tribol Int 1982;15:303.
[27] Sliney HE. ASLE Trans 1985;29:370.
[28] DellaCorte C, Sliney HE. Lubr Eng 1991;47:298.
[29] DellaCorte C. Surf Coat Technol 1996;86–87:486.
[30] Erdemir A, Erck RA, Fenske GR, Hong H. Wear 1997;203–204: 588.
[31] Endrino JL, Nainaparampil JJ, Krzanowski JE. Surf Coat Technol 2002;157:95.
[32] Peterson MB, Murray SF, Florek JJ. ASLE Trans 1959;2:225.
[33] Murray SF, Calabrese SJ. Lubr Eng 1992;49:955.
[34] Wahl KJ, Seitzman LE, Bolster RN, Singer IL. Surf Coat Technol 1997;89:245.
[35] Woydt M, Skopp A, Dorfel I, Witke K. Wear 1998;218:84.
[36] Strong KL, Zabinski JS. Thin Solid Films 2002;406:174.
[37] Nicolet MA. Thin Solid Films 1978;52:415.
[38] PDF Card#27-0997. JCPDS powder diffraction file. International Center for Powder Diffraction Data, Swarthmore (PA), 1998.
[39] PDF Card#04-0783. JCPDS powder diffraction file. International Center for Powder Diffraction Data, Swarthmore (PA), 1998.

Paper 15

Tribol Lett (2008) 29:95–103
DOI 10.1007/s11249-007-9286-x

ORIGINAL PAPER

Adaptive $Mo_2N/MoS_2/Ag$ Tribological Nanocomposite Coatings for Aerospace Applications

Samir M. Aouadi · Yadab Paudel · Brandon Luster · Shane Stadler · Punit Kohli · Christopher Muratore · Carl Hager · Andrey A. Voevodin

Received: 24 September 2007 / Accepted: 29 November 2007 / Published online: 20 December 2007
© Springer Science+Business Media, LLC 2007

Abstract Reactively sputtered $Mo_2N/MoS_2/Ag$ nanocomposite coatings were deposited from three individual Mo, MoS_2, and Ag targets in a nitrogen environment onto Si (111), 440C grade stainless steel, and inconel 600 substrates. The power to the Mo target was kept constant, while power to the MoS_2 and Ag targets was varied to obtain different coating compositions. The coatings consisted of Mo_2N, with silver and/or sulfur additions of up to approximately 24 at%. Coating chemistry and crystal structure were evaluated using X-ray photoelectron spectroscopy (XPS) and X-ray diffraction (XRD), which showed the presence of tetragonal Mo_2N and cubic Ag phases. The MoS_2 phase was detected from XPS analysis and was likely present as an amorphous inclusion based on the absence of characteristic XRD peaks. The tribological properties of the coatings were investigated in dry sliding at room temperature against Si_3N_4, 440C stainless steel, and Al_2O_3. Tribological testing was also conducted at 350 and 600 °C against Si_3N_4. The coatings and respective wear tracks were examined using scanning electron microscopy (SEM), optical microscopy, profilometry, energy dispersive X-ray spectroscopy (EDX), and micro-Raman spectroscopy. During room temperature tests, the coefficients of friction (CoF) were relatively high (0.5–1.0) for all coating compositions, and particularly high against Si_3N_4 counterfaces. During high-temperature tests, the CoF of single-phase Mo_2N coatings remained high, but much lower CoFs were observed for composite coatings with both Ag and S additions. CoF values were maintained as low as 0.1 over 10,000 cycles for samples with Ag content in excess of 16 at% and with sulfur content in the 5–14 at% range. The chemistry and phase analysis of coating contact surfaces showed temperature-adaptive behavior with the formation of metallic silver at 350 °C and silver molybdate compounds at 600 °C tests. These adaptive $Mo_2N/MoS_2/Ag$ coatings exhibited wear rates that were two orders of magnitude lower compared to Mo_2N and Mo_2N/Ag coatings, hence providing a high potential for lubrication and wear prevention of high-temperature sliding contacts.

Keywords Self-lubricating friction · Solid lubricants · Raman · Solid lubricated wear · Coatings · Friction-reducing

S. M. Aouadi (✉) · Y. Paudel · B. Luster · S. Stadler
Department of Physics, Southern Illinois University, Carbondale, IL 62901, USA
e-mail: saouadi@physics.siu.edu

P. Kohli
Department of Chemistry, Southern Illinois University, Carbondale, IL 62901, USA

C. Muratore · C. Hager · A. A. Voevodin
Air Force Research Laboratory, Materials and Manufacturing Directorate, Wright-Patterson Air Force Base, Dayton, OH 45433, USA

1 Introduction

In the last decade, thin layers of molybdenum nitride (Mo–N) have been investigated as materials with a wide variety of potential applications that include catalysis [1, 2], superconductivity [3, 4], diffusion barriers for copper interconnects [5], gate electrode materials for high-k gate dielectrics [6, 7], and as corrosion- and wear-resistant coatings [8, 9]. The Mo–N system was reported to crystallize in three possible phases, namely, face-centered cubic Mo_2N, tetragonal Mo_2N, and hexagonal MoN [8].

Unlike other transition metal nitrides, such as TiN and CrN, which have been investigated for a few decades now, interest in Mo–N as a potential material for tribological

applications is very recent. The impetus for investigating this material stems from its superior mechanical properties (hardness reported to be in the 28–34 GPa range compared to 18–24 GPa for TiN and CrN) and the lubricating properties of its surface oxides (MO_x) at elevated temperatures (>300 °C) which is due to the presence of lamellar structures (Magnéli phases) that shear easily during contact loading [10–13].

Recently, additional alloying elements were incorporated into the design of Mo–N based materials to produce nanocomposite coatings [14]. These materials usually exhibit superior mechanical and tribological properties compared to their constituent phases [14, 15]. Two groups of hard nanocomposite structures are known to provide such enhanced mechanical and tribological properties [16]: (1) coatings containing two hard phases such as nc-TMN/a-Si_3N_4 (TM = transition metals such as Ti, Cr, Nb, etc.; nc- and a- denote the nanocrystalline and amorphous phases, respectively) or nc-TiN/a-BN, and (2) materials containing a hard phase and a soft phase such as nc-TMN/Me (Me = soft metals such as Cu, Ag, Co, etc.). Some of the advantages of the former group include the possibility to reach hardness values in excess of 40 GPa (ultra-hard coatings) and thermal stability at temperatures up to 1,100 °C (properties that would be valuable for cutting tools, for example). The benefit of using the latter group of materials is the improved fracture toughness and the self-lubricating potential, provided by the soft metal, at high temperature (properties that are important for rolling element bearings, air foil bearings, gears, etc.) In the literature, alloying elements that were incorporated in the MO–N coatings include Cu [17, 18], Ag [19, 20], Si [21, 22], and C [23]. The addition of the optimum amount of these alloying elements was found to provide enhanced mechanical (toughness) and tribological (reduced friction coefficient and wear rate) properties. This is explained further in this article for a complex 3-phase material system made of Mo_2N, MoS_2, and Ag.

The aim of the current article is to provide a comprehensive study of the mechanical and frictional properties of $Mo_2N/MoS_2/Ag$ self-lubricating coatings for high-temperature tribological applications. It is intended that these coatings will provide a "chameleon" surface adaptation that adjusts its surface composition and structure to minimize friction as the working environment changes [13, 24–26]. The Mo_2N phase offers good mechanical and lubricating properties at high temperature, as indicated earlier in this section. The addition of both MoS_2 and Ag can reduce friction at moderately high temperatures (300–400 °C) since both ingredients are lubricious under these conditions. At higher temperatures, however, the formation of silver molybdate compounds [19, 24], such as Ag_2MoO_4, $Ag_2Mo_2O_7$, and $Ag_2Mo_4O_{13}$, facilitated by the presence of MoS_2 [24], is expected to be an effective mechanism for friction reduction. These molybdate compounds were predicted to be lubricious by the crystal chemical model [27], which was used to account for the formation of low shear/friction tribofilms in sliding contacts.

The tribological properties of $Mo_2N/MoS_2/Ag$ self-lubricating coatings deposited by unbalanced magnetron sputtering were evaluated at room temperature (RT), at 350, and at 600 °C. Emphasis is placed on the high-temperature tribological properties, since these materials were designed to be self-lubricating under these conditions. Also, most of the tribotesting was carried out using Si_3N_4 as a counterpart material in dry sliding conditions since it is stable throughout the desired test temperature range practically used in hybrid bearings of jet engines and other high temperature and space applications. It is important to note that the friction coefficient values of nitride on nitride surfaces reported in the literature were very high (friction coefficients in excess of 0.8 at RT) [28, 29]. The CoF of nitride-based coatings at high temperature are also high (usually >0.5) [30] even against other counterfaces such as stainless steel or alumina [31]. It was expected that the addition of the selected lubricious phases would significantly improve the tribological properties of these coatings.

2 Experimental Procedure

$Mo_2N/MoS_2/Ag$ thin coatings were deposited on hardened 440C grade stainless steel and on inconel 600 substrates using an unbalanced magnetron sputtering apparatus that was described in detail elsewhere [32]. The substrates were cleaned ultrasonically in acetone and methanol for 15 min and successively rinsed with deionized water and blown with dry N_2. The coatings were grown using individual targets of Mo, MoS_2, and Ag that were 5 cm in diameter. The base pressure of the system was lower than 1×10^{-5} Pa prior to each coating deposition. The coatings were grown in a mixed atmosphere of Ar (99.999% purity) and N_2 (99.99% purity) with partial pressures that were set to 0.3 and 0.04 Pa, respectively. During deposition, the power to the Mo target was fixed at 200 W and the power to the MoS_2 and Ag sources were varied, as shown in Table 1. Table 1 provides the coating nomenclature designation, which is used throughout the text and figures. The substrates were held at a bias voltage of −60 V and were continuously rotated about their polar axis with a rotational speed of 50 rpm. The coatings were grown for 1.5 h at a substrate temperature of 350 °C leading to coating thicknesses in the 2.8 ± 0.3 μm range.

Structural characterization of the deposited coatings was carried out using a GBS MMA (Mini materials analyzer) X-ray diffractometer. All spectra were taken using Cu-Kα

Table 1 Nomenclature, deposition conditions, and composition of $Mo_2N/MoS_2/Ag$ coatings obtained by magnetron sputtering of Mo, Ag, and MoS_2 targets. The first number in the coating nomenclature corresponds to the power to the Ag target whereas the second number corresponds to the power to the MoS_2 target. Both powers were the variable deposition parameters in this study

Coating	S-0-0	S-50-40	S-30-20	S-27-0	S-14-40	S-20-20
P_{Ag} (W)	0	50	30	27	14	20
P_{MoS2} (W)	0	40	20	0	40	20
Mo (at%)	63	40	45	48	47	47
N (at%)	37	27	34	36	32	35
S (at%)	0	9	5	0	13	6
Ag (at%)	0	24	16	16	8	12

radiation with an accelerating voltage of 35 kV and a current of 30 mA. The elemental and phase compositions were determined using a Leybold Max 200 X-ray photoelectron spectroscopy (XPS) analyzer and a Renishaw SPM micro-Raman system. Scanning electron microscopy (SEM) was performed using a Hitachi S570, operating at 20 kV, to analyze the morphology of the coatings before and after wear testing. The SEM system was equipped with an energy dispersive X-ray (EDX) apparatus for elemental analysis.

A Nanovea ball on disk tribotester (Microphotonics, Irvine, CA) was employed for the evaluation of wear and friction behavior at room temperature under two conditions: (1) in air (50 ± 5% relative humidity) and (2) in dry nitrogen. Three different counterpart materials were used during tribotesting: (1) alumina, (2) 440C stainless steel (SS), and (3) Si_3N_4 balls with a diameter of 6 mm. The measurements were carried out using a normal load of 1 N and a sliding rate of 0.2 m/s for 10,000 cycles. A high-temperature tribotester was subsequently used to test the performance of the deposited coupons at 350 and 600 °C using Si_3N_4 balls as counterparts with the same conditions as those used for room temperature testing. Wear rates were then determined from the cross section of the wear track, measured using multiple profilometry line scans of the surface. Counterpart wear was investigated qualitatively with microscopy and also by identification of counterpart species via surface analysis in coating wear tracks.

3 Results and Discussion

3.1 As Deposited Coatings

The X-ray diffraction pattern of MO–N coatings, shown in Fig. 1, is characteristic of tetragonal β-Mo_2N (JCPDS card no.: 75-1,150) [33]. Grain size was estimated from the

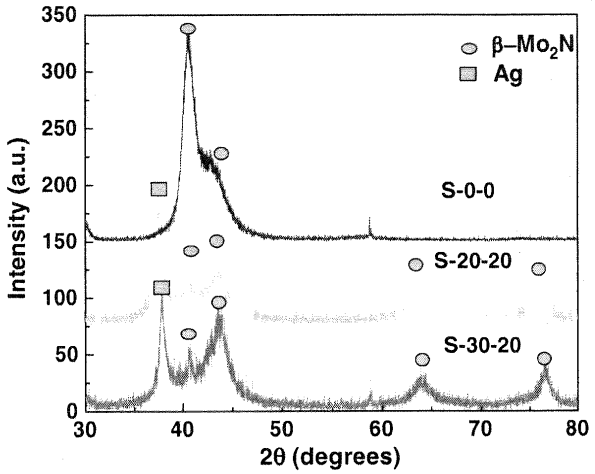


Fig. 1 XRD data for selected as deposited coatings

Scherrer formula to be about 15 nm [32]. The addition of Ag and MoS_2 resulted in a broadening in the β-Mo_2N diffraction peaks (due to the grain refinement that originated from the creation of a nanocomposite structure [32, 34] and the appearance of new ones that correspond to face centered cubic silver, as shown in Fig. 1.

The atomic concentrations of Mo, Ag, S, and N were quantified with the XPS technique and are summarized in Table 1. The Mo_{3d}, Ag_{3d}, S_{2p}, and N_{1s} peaks were located at 228.2, 368.5, 162.4, and 397.2 eV, respectively. A conventional curve-fitting method was utilized to determine the contribution from the N_{1s} peak since it overlapped with the tail of the Mo_{3p} peak [35]. The binding energy of the $Mo_{3d5/2}$ peak was similar to the one reported for the lower valence state Mo^{2+} that corresponds to molybdenum nitride (228.4 ± 0.2 eV) [35]. The position of the N_{1s} peak was in agreement with the values reported for Mo_2N (397.4 ± 0.2 eV) [35]. The S_{2p} line consists of a singlet peak with a binding energy value that corresponds to S^{2-} [36]. This indicates that the sulfur species were bonded to Mo atoms in an MoS_2 phase which was, however, amorphous as suggested by the absence of characteristic hexagonal MoS_2 peaks in XRD spectra. Finally, the binding energy of the Ag_{3d} peak is typical of a metallic Ag–Ag bond (368.7 ± 0.2 eV) [32].

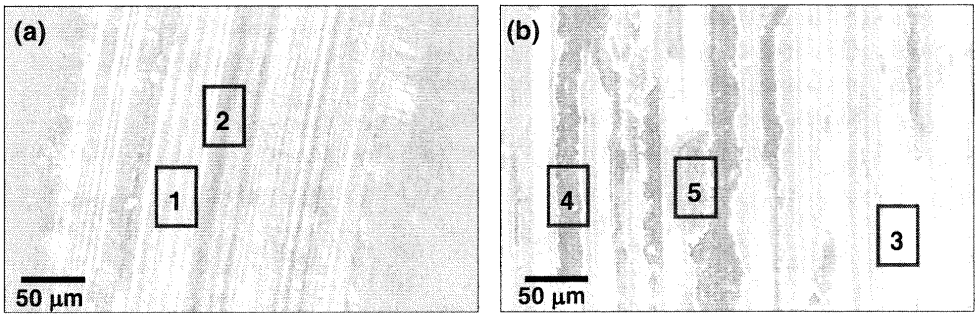
3.2 Room Temperature Tests

The average coefficients of friction (CoF) measured during tribological tests with the different counterpart materials in both air and dry nitrogen environments are presented in Table 2. In air, the CoF for Mo_2N was found to be the highest when tested against Si_3N_4 ($\mu = 1.06$) and the lowest when tested against Al_2O_3 ($\mu = 0.28$). In dry nitrogen, however, the CoF was found to be the highest

Table 2 Coefficients of friction and wear rates for $Mo_2N/MoS_2/Ag$ coatings obtained in sliding tests against Al_2O_3, Si_3N_4, and stainless steel (SS) balls tested at room temperature in air and in dry nitrogen, at 350 °C in air, and at 600 °C in air

Coating	S-0-0	S-50-40	S-30-20	S-27-0	S-14-40	S-20-20
Coefficients of friction at room temperature						
Al_2O_3/Air	0.28	0.52	0.54	0.69	0.56	0.67
Al_2O_3/N_2	0.85	0.49	0.60	0.68	0.59	0.72
Si_3N_3/Air	1.06	0.62	0.42	0.55	0.80	0.70
Si_2N_3/N_2	0.67	0.80	0.52	0.60	0.76	0.73
SS/Air	0.42	0.68	0.54	0.62	0.74	0.72
SS/N_2	0.27	0.70	0.45	0.57	0.69	0.66
Wear rates in $mm^3/(nm)$ at room temperature						
Al_2O_3/Air	Little wear	3×10^{4}	2×10^{-4}	4×10^{-4}	9×10^{-5}	9×10^{-5}
Al_2O_3/N_2	9×10^{-5}	5×10^{-4}	3×10^{-4}	6×10^{-4}	1×10^{-4}	2×10^{-4}
Si_3N_3/Air	Little wear	6×10^{-4}	3×10^{-4}	7×10^{-4}	1×10^{-4}	6×10^{-5}
Si_2N_3/N_2	5×10^{-5}	4×10^{-4}	4×10^{-4}	8×10^{-4}	2×10^{-4}	1×10^{-4}
SS/Air	3×10^{-6}	5×10^{-4}	4×10^{-4}	7×10^{-4}	9×10^{-5}	3×10^{-4}
SS/N_2	Little wear	3×10^{-4}	3×10^{-4}	5×10^{-4}	8×10^{-5}	2×10^{-4}
Coefficients of friction and wear rates in $mm^3/(nm)$ against Si_3N_4 at 350 °C air						
CoF	0.80	0.37	0.37	0.40	0.45	0.40
Wear rate	7×10^{-5}	9×10^{-5}	7×10^{-5}	6×10^{-5}	5×10^{-5}	4×10^{-5}
Coefficients of friction and wear rates in $mm^3/(nm)$ against Si_3N_4 at 600 °C air						
CoF	0.72	0.10	0.10	0.45	0.18	0.23
Wear rate	5×10^{-4}	8×10^{-6}	1×10^{-5}	1×10^{-4}	6×10^{-5}	4×10^{-5}

against Al_2O_3 ($\mu = 0.85$), and the lowest against SS ($\mu = 0.27$). The addition of MoS_2 and Ag was found to improve the frictional properties against Si_3N_4. For example, the measured CoF for coating S-30-20 was 0.42 and 0.52 in air and dry nitrogen, respectively. SEM images of the wear tracks for this particular coating sample are shown in Fig. 2. The wear in contact with Al_2O_3 was less than with SS or Si_3N_4. However, the counterpart wear of Al_2O_3 was greater than that of SS or Si_3N_4. The wear tracks were analyzed using Raman spectroscopy. All spectra displayed a broad peak centered at 903 cm^{-1} which belongs to the monoclinic β-MoO_3 phase [37]. EDX data displayed in Fig. 2 revealed that some of the coating was worn through (dark regions) when tested in air against Al_2O_3 and Si_3N_4. This was probably due to the relatively high silver content which would result in a much softer coating. Very little coating wear was measured for coating compositions that had little or no Ag (e.g. see data in Table 2 for coating S-0-0 at room temperature). However, the wear of the counterfaces was more pronounced because the hardness of such coatings was much higher than that of the counterface material. For example, the hardness of the



Area 1: Mo(30), N(14), S(11), Ag(14), O(31), Si(0)
Area 2: Mo(22), N(7), S(7), Ag(7), O(56), Si(1)
Area 3: Mo(42), N(13), S(10), Ag(19), O(14), Si(2)
Area 4: Mo(3), N(4), S(0), Ag(1), O(11), Si(3), Fe (78)
Area 5: Mo(19), N(11), S(9), Ag(9), O(35), Si(6), Fe(11)

Fig. 2 SEM micrographs for a S-30-20 coating tested at room temperature (**a**) in dry nitrogen and (**b**) in air against Si_3N_4 balls as counterface materials. Also shown are the elemental compositions (at%) of the different regions identified on the micrographs

Mo_2N coating (S-0-0) was measured to be 30 ± 2 GPa compared to 15, 12, and 5 GPa for Al_2O_3, Si_3N_4, and SS, respectively. Silicon (2–14 at%) was detected by EDX on coating samples tested against Si_3N_4 balls suggesting that ball material transfer to coating wear tracks occurred during testing. The amount of transferred Si increased with decreasing atomic fractions of lubricating phases added to the hard Mo_2N matrix, with the maximum Si detected inside wear tracks for single-phase Mo_2N coating (S-0-0). The addition of MoS_2 and Ag substantially decreased the wear of Si_3N_4 balls, which explains the improved CoF (see Table 2, Si_3N_4/Air). Neither of the Mo_2N/MoS_2/Ag coatings investigated here demonstrated the frictional response of MoS_2, at room temperature. This suggests that the amorphous MoS_2 component in the coating was incapable of developing a surface lubricating film at the contact surface, as observed in previously investigated chameleon coatings [38, 39]. This discrepancy could be the result of the relatively small amount of MoS_2 in the current study.

3.3 350 °C Tests

Table 2 shows the CoF measured at 350 °C for the different Mo_2N/MoS_2/Ag coatings. The results shown in this table indicated that the addition of the lubricious phases provided significant improvements toward reducing friction. For instance, the CoF decreased from $\mu = 0.72$ for pure Mo_2N to 0.37–0.4 for coatings with silver contents in excess of 12 at%, which is typical for hard surfaces lubricated with noble metals in this temperature range [13, 40]. The addition of MoS_2 did not, however, seem to significantly affect the CoF. Shown in Fig. 3 are Raman spectroscopy data for S-27-0 coating outside the wear track (a) and for S-30-20 coating outside (b) and inside (c) the wear track. The Raman data measured for all Mo_2N/MoS_2/Ag coatings revealed that only the α-MoO_3 readily formed on the surface. However, a broad peak in the 850–950 cm^{-1} region was also observed in the wear track, especially for the sulfur-containing coatings, as shown in Fig. 3 for S-30-20. This broad peak could correspond to contributions from the $Ag_2Mo_4O_{13}$ Raman modes with peaks located at 865, 903, and 953 cm^{-1} [19]. Another important phase that formed on the surface of the coatings is pure silver, similar to reports on silver surface diffusion and coalescence at elevated temperatures for other nanocomposite coatings [13, 25, 30]. Silver provides no Raman response and, hence, complementary techniques were used to confirm its presence. XRD and SEM measurements (not shown) indicated that metallic silver formed on the surface of the coatings after heating at 350 °C. Its content in the wear track was found to be higher than in other areas of the coating using both EDX and XPS. Hence, silver and α-MoO_3 are the predominant phases in the wear track. In this temperature range, silver diffusion to the surface is rapid, and controls the sliding mechanism as evidenced by corresponding COF values in Table 2. The formation of α-MoO_3 and very small amounts of $Ag_2Mo_4O_{13}$ in the wear tracks detected with Raman analyses suggest that 350 °C may be close to the onset temperature of chemical reactions in the contact, which reduce friction at higher temperatures and allow for coating self-adaptation to temperature.

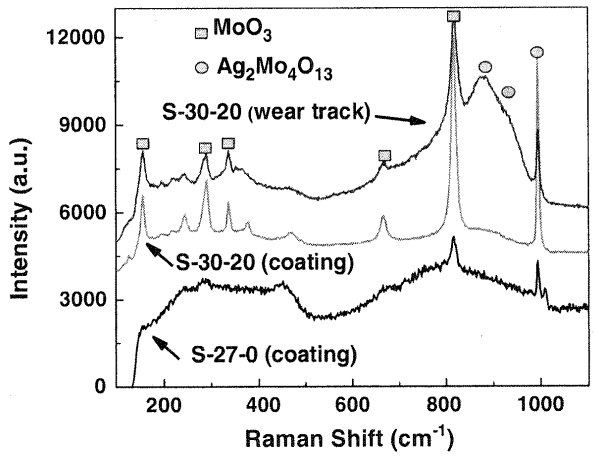


Fig. 3 Raman spectroscopy data for (**a**) S-27-0 coating outside wear track, (**b**) S-30-20 coating outside wear track, and (**c**) S-30-20 coating in wear track, after 350 °C sliding tests against Si_3N_4

3.4 600 °C Tests

Figure 4 shows the friction coefficients for the Mo_2N/MoS_2/Ag nanocomposite coatings at 600 °C. The Mo_2N reference coating (S-0-0) exhibited a high friction coefficient ($\mu = 0.8$) against Si_3N_4 counterfaces. The addition of Ag and/or MoS_2 was found to reduce the friction coefficient substantially. For example, a very low value of $\mu = 0.1$ was obtained for S-30-20 and S-50-40 coatings. This is most significant, since all reported CoF of nitride-based materials against Si_3N_4 had much higher values (in excess of 0.8). Even against alumina counterparts, which typically yield lower friction coefficients, the reported CoF for self-lubricating nitride coatings was significantly higher. For example, Gulbinski and Susko [19] recently reported that the value for Mo_2N/Ag against Al_2O_3 was $\mu = 0.5$ when tested at 400 °C. This was close to that measured in the current work for the Mo_2N/Ag coating (Table 2, coating S-27-0). Also, Kutchej et al. [41] reported CoF values greater than 0.4 for the CrN/Ag system with different Ag contents when tested at 600 °C against Al_2O_3. Unfortunately, neither of these literature reports provide data for tests against Si_3N_4 balls.

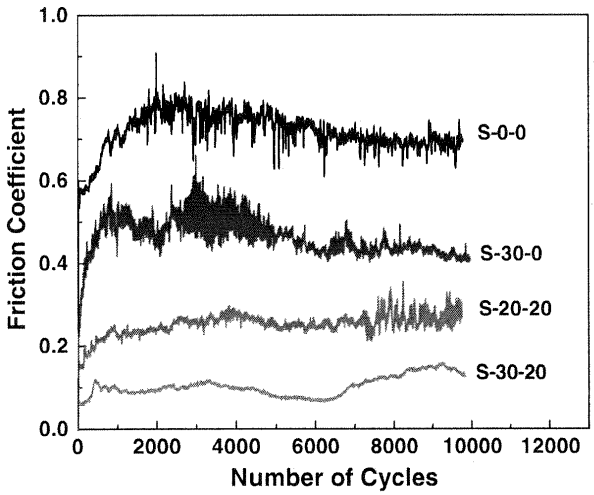


Fig. 4 CoF for selected coatings recorded at 600 °C sliding tests against Si_3N_4

Wear rates were determined by evaluating the topography of the wear tracks using a stylus profilometer. The calculated wear rates, listed in Table 2, clearly demonstrate that the tribological properties of Mo_2N are improved with the addition of lubricious phases. The wear rate for S-50-40 was found to be 8×10^{-6} mm^3/nm, which is approximately two orders of magnitude better than that of Mo_2N (5×10^{-4} mm^3/nm for S-0-0). The wear rate of the balls was also reduced because of the lubricious nature of the coatings.

Figure 5 shows the surface topography of the wear tracks for selected $Mo_2N/MoS_2/Ag$ nanocomposite coatings after 10,000 sliding cycles. The corresponding elemental compositions of different regions in these micrographs were estimated by EDX and were also reported in this figure. Silver was distributed throughout the wear tracks for coatings with silver content greater than 12% (S-20-20, S-30-20, and S-50-40). The bright particles shown outside of the wear track in $Mo_2N/MoS_2/Ag$ coatings correspond to Ag-based agglomerates of various sizes that were uniformly distributed on the coating surface (Fig. 5a). Both the size and density of these particles increased with Ag content in the coatings. The surface topography of coatings with relatively high MoS_2 content is shown in Fig. 5b. Equiaxed grains and one-axis elongated phases appear on the surface of the coatings outside of the wear tracks and some are spread homogeneously in the wear tracks. Similar surface morphology was observed in earlier studies with YSZ-MoS_2–Ag adaptive coatings and was explained by the formation of significant amounts of silver molybdate phases on the surface [25].

To investigate the wear track chemistry and structural changes, phase composition of the surface oxides were evaluated using micro-Raman spectroscopy (Fig. 6). Raman spectroscopy measurements indicated that the surface of the S-0-0 coating consisted primarily of the MoO_2 phase whereas data taken in its wear track revealed the presence of the α-MoO_3 phase in addition to MoO_2. Both phases are the most stable oxides of molybdenum where the oxidation states of Mo are tetravalent and hexavalent for MoO_2 and α-MoO_3, respectively [42]. However, the Raman spectra for $Mo_2N/MoS_2/Ag$ nanocomposite coatings indicated the presence of $Ag_2Mo_4O_{13}$ silver molybdate phase [19] in addition to α-MoO_3 and MoO_2. The formation of the $Ag_2Mo_4O_{13}$ phase rather than the Ag_2MoO_4 or $Ag_2Mo_2O_7$ phases was expected given the relatively large Mo content in the coatings, according to the phase diagram of the MoO_3–Ag_2O system [43]. The Raman spectroscopy data also revealed that coatings with relatively high sulfur content favor the formation of silver molybdate over the formation of molybdenum oxide phases. The formation of silver molybdate compounds was reported to be the result of the reaction $MoS_x \pm Ag \rightarrow AgMoS_x$ with the sulfur atoms being replaced by oxygen atoms at temperatures above 500 °C [25]. This agrees well with reports that sulfur

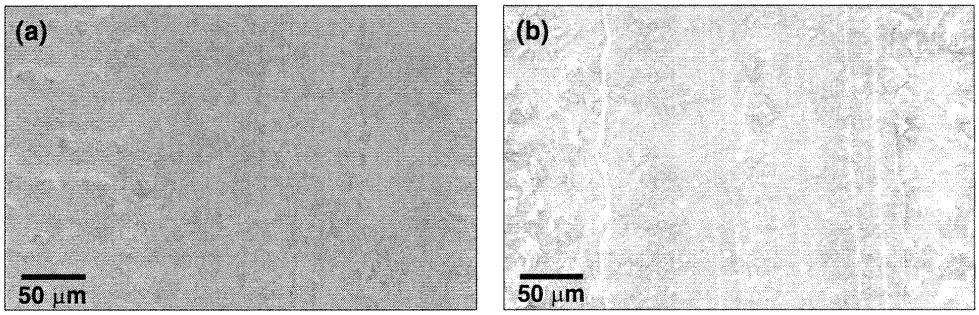


Fig. 5 SEM micrographs after tribotesting at 600 °C for (**a**) S-30-20 coating and (**b**) S-14-40 coating. Also shown are the elemental compositions (at%) of the different regions identified on the micrographs

Area 1: Mo(10), N(12), S(1), Ag(36), O(40), Si(1)
Area 2: Mo(9), N(5), S(1), Ag(69), O(9), Si(7)
Area 3: Mo(14), N(15), S(2), Ag(26), O(41), Si(3)
Area 4: Mo(21), N(5), S(3), Ag(7), O(63), Si(1)
Area 5: Mo(13), N(3), S(4), Ag(19), O(60), Si(1)

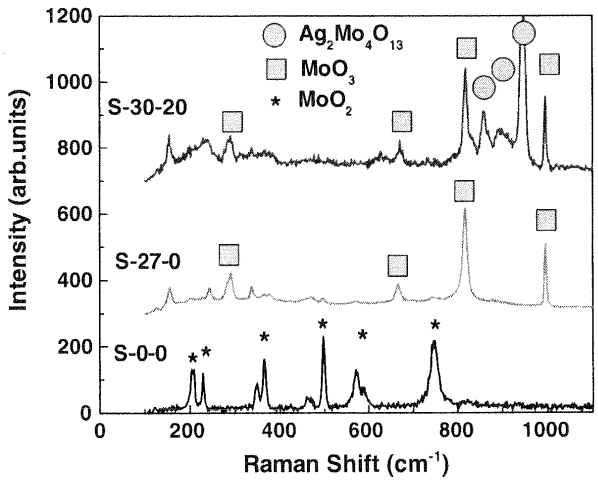


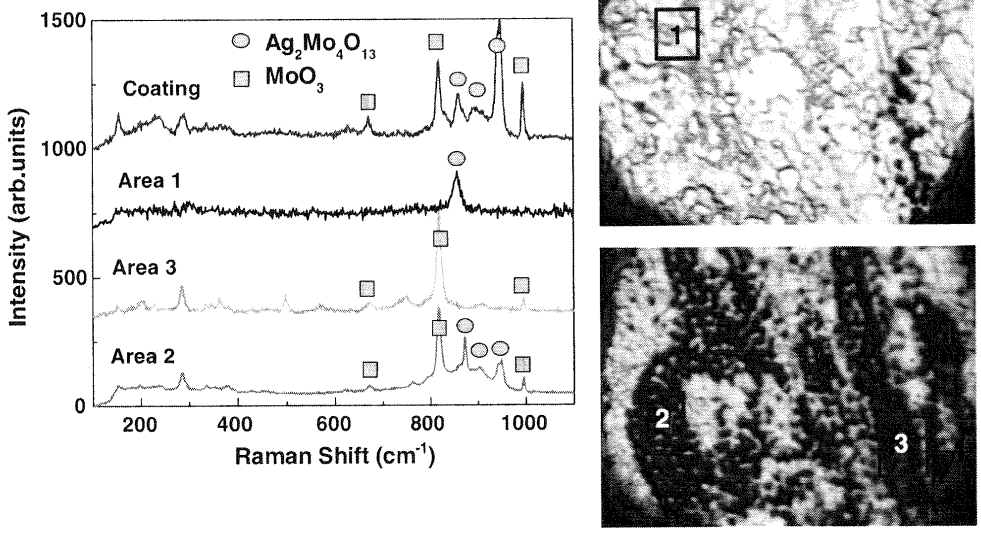
Fig. 6 Raman data from the surface of selected coatings after tribotesting at 600 °C

acts as a catalyst in the formation of lubricious molybdate phases at high temperatures [25]. Thus, $Mo_2N/MoS_2/Ag$ coatings in the current work had maintained a low friction coefficient at high temperatures due to the formation of $Ag_2Mo_4O_{13}$.

Raman spectra were also recorded in different regions of the wear track, as shown in Fig. 7 for S-30-20. Optical micrographs of the regions analyzed with the Raman microprobe are also shown. Under an optical microscope, the majority of the wear track surface is covered by white patches. A much smaller area is covered by black regions where occasional orange spots were seen. Micro-Raman analysis of these regions indicated that: (1) the coating consisted primarily of $Ag_2Mo_4O_{13}$ and α-MoO_3; (2) the white areas in the wear tracks (region 1 in Fig. 7) were exclusively $Ag_2Mo_4O_{13}$, which explains the low measured friction coefficient; (3) the black patches in the wear tracks (region 2 in Fig. 7) were a mixture of $Ag_2Mo_4O_{13}$ and α-MoO_3; and (4) the orange spots in the black areas (region 3 in Fig. 7) corresponded to α-MoO_3. A comparison between Raman data outside and inside the wear track indicates that the contact process between rubbing surfaces promotes the formation of the molybdate phase over the molybdenum oxide phase. This adaptive behavior in friction contact areas was also in agreement with observations made when the coatings were tribotested at 350 °C.

The results of the Raman investigation were confirmed by the XRD data shown in Fig. 8 for S-0-0 and S-30-20 coatings after 600 °C tests. The diffraction peaks for Mo_2N correspond to the tetragonal β-Mo_2N already observed prior to going through the high-temperature wear testing in addition to the monoclinic MoO_2 phase (JCPDS card no.: 78-1,070). In addition to these peaks, the spectra of the $Mo_2N/MoS_2/Ag$ coatings included peaks that matched those of $Ag_2Mo_4O_{13}$, α-MoO_3, and metallic Ag. XPS data were also collected on the coating and in the wear track regions. The main difference between the peak positions measured before and after wear testing was the broadening of the Mo_{3d} peak due to the emergence of peaks reported for the higher valence states Mo^{4+} and Mo^{6+} that correspond to molybdenum oxides MoO_2 (230.0 ± 0.2 eV) and MoO_3 (232.5 ± 0.2 eV), respectively [31]. The other peaks remained at about the same positions (within the accuracy of the measurement) and there was no noticeable difference between the data collected outside and inside wear tracks. Peak intensities, however, changed significantly due to the migration of silver to the surface.

Fig. 7 Raman spectroscopy data for different regions of a S-30-20 coating after tribotesting at 600 °C



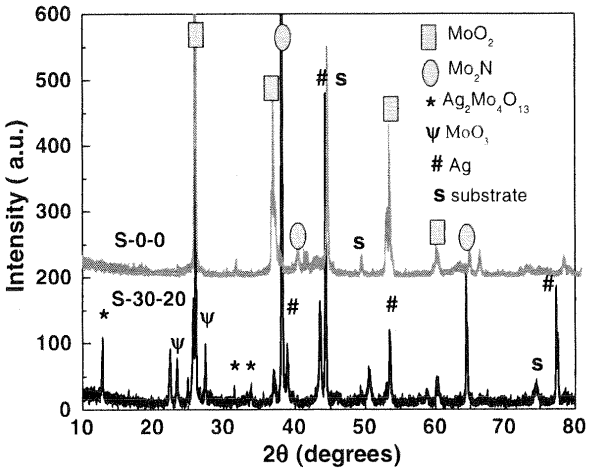


Fig. 8 XRD data for selected coatings after wear testing at 600 °C

4 Conclusions

Composite coatings of $Mo_2N/MoS_2/Ag$ were deposited using unbalanced magnetron sputtering, which included crystalline phases of Mo_2N and silver, and an amorphous MoS_2. The coating composition was systematically varied to provide coatings with β-Mo_2N main phase and additions of MoS_2 and Ag phases, with total variations of 0–13 at% S and 0–24 at% Ag contents. The friction coefficients of these materials were measured at 25, 350, and 600 °C. Relatively high friction coefficients in the range of 0.5–1.0 were recorded when the coatings were tested at room temperature against Al_2O_3, Si_3N_4, and 440C steel counterparts, where tests against Al_2O_3 provided the lowest friction and tests against Si_3N_4 the highest friction coefficients The friction coefficient at room temperature was at the lower range of 0.5 for coatings with a high amount of sulfur; however, the total fraction of amorphous MoS_2 in the coating composition was not significant for providing hexagonal MoS_2 behavior. At higher temperatures, the addition of both Ag and MoS_2 was found to significantly decrease the friction coefficients as a result of the migration of Ag to the surface at 350 °C and the formation of lubricious silver molybdate phases at 600 °C inside wear tracks, which dominated over the formation of molybdenum oxides. The presence of sulfur in the coatings was instrumental in promoting these lubricious phases and achieving temperature-adaptive behavior. The lowest friction coefficient ($\mu = 0.1$) was recorded for samples with Ag content >16 at% and with S content in the 5–14 at% range. This is a significant result given that CoF of self-lubricating nitride-based coatings reported in the literature were significantly higher. The composite $Mo_2N/MoS_2/Ag$ coatings also showed up to a two-order magnitude wear rate reduction in comparison to Mo_2N single-phase coatings. The observed reduced friction coefficients and wear endurance of these composite coatings with a self-lubricating adaptive behavior may be beneficial for friction and wear reduction in hybrid bearings and other mechanical components operating at elevated temperatures.

Acknowledgments This research was supported by the National Science Foundation (award # CMMI-0653986) and by an award from the Air Force Summer Faculty Fellowship Program. The authors also wish to thank Clay Watts of Southern Illinois University and Art Safriet of the Air Force Research Laboratory for their technical assistance.

References

1. Zhong, H.X., Zhang, H.M., Liu, G., Liang, Y.M., Hu, J.W., Yi, B.L.: A novel non-noble electrocatalyst for PEM fuel cell based on molybdenum nitride. Electrochem. Commun. **8**, 707–712 (2006)
2. Shi, C., Zhu, A.M., Yang, X.F., Au, C.T.: On the catalytic nature of VN, Mo_2N, and W_2N nitrides for NO reduction with hydrogen. Appl. Catal. A **276**, 223–230 (2004)
3. Inumaru, K., Baba, K., Yamanaka, S.: Preparation of superconducting molybdenum nitride MoN, ($0.5 \leq x \leq 1$) films with controlled composition. Physica B **383**, 84–85 (2006)
4. Inumaru, K., Baba, K., Yamanaka, S.: Superconducting molybdenum nitride epitaxial thin films deposited on MgO and α-Al_2O_3 substrates by molecular beam epitaxy. Appl. Surf. Sci. **253**, 2863–2869 (2006)
5. Alen, P., Ritala, M., Arstila, K., Keinonen, J., Leskela, M.: Atomic layer deposition of molybdenum nitride thin films for Cu metallizations. J. Electrochem. Soc. **152**, G361–G366 (2005)
6. Lu, J., Kuo, Y., Chatterjee, S., Tewg, J.Y.: Physical and electrical properties of Ta-N, Mo–N, and W-N electrodes on HfO_2 high-k gate dielectric. J. Vac. Sci. Technol. B **24**, 349–357 (2006)
7. Tsui, B.Y., Huang, C.F., Lu, C.H.: Investigation of molybdenum nitride gate on SiO[2] and HfO[2] fro MOSFET application. J. Electrochem. Soc. **153**, G197–G202 (2006)
8. Sarioglu, C., Demirler, U., Kazmanli, M.K., Urgen, M.: Measurement of residual stresses by X-ray diffraction techniques in MoN and Mo_2N coatings deposited by arc PVD on high-speed steel substrate. Surf. Coat. Technol. **190**, 238–243 (2005)
9. Li, X.Y., Tang, B., Pan, J.D., Liu, D.X., Xu, Z.: Tribological properties of Mo–N hard coatings on Ti6Al4V by double glow discharge technique. J. Mat. Sci. Technol. **19**, 291–293 (2003)
10. Woydt, M., Skopp, A., Dorfel, I., Witke, K.: Wear engineering oxides/anti-wear oxides. Wear **218**, 84–95 (1998)
11. Gassner, G., Mayrhofer, P.H., Kutschej, K., Mitterer, C., Kathrein, M.: Magnéli phase formation of PVD Mo–N and W–N coatings. Surf. Coat. Technol. **201**, 3335–3341 (2006)
12. Peterson, M.B., Murray, S.F., Florek, J.J.: Consideration of lubricants for temperatures to 1000°F. ASLE Trans. **2**, 225–234 (1960)
13. Muratore, C., Voevodin, A.A., Hu, J.J., Zabinski, J.S.: Tribology of adaptive nanocomposite yttria-stabilized zirconia coatings containing silver and molybdenum from 25 to 700 °C. Wear **261**, 797–805 (2006)
14. Hauert, R., Patscheider, J.: From alloying to nanocomposites—Improved performance of hard coatings. Adv. Eng. Mat. **2**, 247–259 (2000)
15. Petrov, I., Barna, P.B., Hultman, L., Greene, J.E.: Microstructural evolution during film growth. J. Vac. Sci. Technol. A **21**, S117–S128 (2003)

16. Raveh, A., Zukerman, I., Shneck, R., Avni, R., Fried, I.: Thermal stability of nanostructured superhard coatings: a review. Surf. Coat. Technol. **201**, 6136–6142 (2006)
17. Suszko, T., Gulbinski, W., Jagielski, J.: Mo_2N/Cu thin films—the structure, mechanical and tribological properties. Surf. Coat. Technol. **200**, 6288–6292 (2006)
18. Joseph, M.C., Tsotsos, C., Baker, M.A., Kench, P.J., Rebholz, C., Matthews, A., Leyland, A.: Characterisation and tribological evaluation of nitrogen-containing molybdenum–copper PVD metallic nanocomposite films. Surf. Coat. Technol. **190**, 345–356 (2005)
19. Gulbinski, W., Suszko, T.: Thin films of Mo2N/Ag nanocomposite—the structure, mechanical and tribological properties. Surf. Coat. Technol. **201**, 1469–1474 (2006)
20. Turutoglu, T., Urgen, M., Cakir, A.F., Ozturk, A.: Characterization of Mo2N/Ag nanocomposite coatings produced by magnetron sputtering. Key Eng. Mat. **264–268**, 489–492 (2004)
21. Heo, S.J., Kim, K.H., Kang, M.C., Suh, J.H., Park C.G.: Syntheses and mechanical properties of Mo–Si–N coatings by a hybrid coating system. Surf. Coat. Technol. **201**, 4180–4184 (2006)
22. Liu, Q., Fang, Q.F., Liang, F.J., Wang, J.X., Yang, J.F., Li, C.: Synthesis and properties of nanocomposite MoSiN hard films. Surf. Coat. Technol. **201**, 1894–1898 (2006)
23. Liu, Q., Liu, T., Fang, Q.F., Liang, F.J., Wang, J.X.: Preparation and characterization of nanocrystalline composites Mo–C–N hard films. Thin Solid Films **503**, 79–84 (2006)
24. Voevodin, A.A., Zabinski, J.S.: Nanocomposite and nanostructured tribological materials for space applications. Composites Sci. Technol. **65**, 741–748 (2005)
25. Muratore, C., Voevodin, A.A.: Molybdenum disulfide as a lubricant and catalyst in adaptive nanocomposite coatings. Surf. Coat. Technol. **201**, 4125–4130 (2006)
26. Voevodin, A.A., Zabinski, J.S.: Supertough wear-resistant coatings with 'chameleon' surface adaptation. Thin Solid Films **370**, 223–231 (2000)
27. Erdemir, A.: A crystal chemical approach to the formulation of self-lubricating nanocomposite coatings. Surf. Coat. Technol. **200**, 1792–1796 (2005)
28. Bobzin, K., Lugscheider, E., Nickel, R., Bagcivan, N., Kramer, A.: Wear behavior of $Cr_{1-x}Al_xN$ PVD-coatings in dry running conditions. Wear **263**, 1274–1280 (2007)
29. Mo, J.L., Zhu, M.H., Lei, B., Leng, Y.X., Huang, N.: Comparison of tribological behaviours of AlCrN and TiAlN coatings deposited by physical vapor deposition. Wear **263**, 1423–1429 (2007)
30. Muratore, C., Hu, J.J., Voevodin, A.A.: Adaptive nanocomposite coatings with a titanium nitride diffusion barrier mask for high-temperature tribological applications. Thin Solid Films **515**, 3638–3643 (2007)
31. Badischa, E., Fontalvo, G.A., Stoiber, M., Mitterer, C.: Tribological behavior of PACVD TiN coatings in the temperature range up to 500 °C. Surf. Coat. Technol. **163–164**, 585–590 (2003)
32. Aouadi, S.M., Debessai, M., Filip, P.: Zirconium nitride/silver nanocomposite structures for biomedical applications. J. Vac. Sci. Technol. B **22**, 1134–1140 (2004)
33. Mändl, S., Gerlach, J.W., Rauschenbach, B.: Nitride formation in transition metals during high-fluence high-temperature implantation. Surf. Coat. Technol. **200**, 584–588 (2005)
34. Muratore, C., Voevodin, A.A., Hu, J.J., Jones, J.g., Zabinski, J.S.: Growth and characterization of nanocomposite yttria-stabilized zirconia with Ag and Mo. Surf. Coat. Technol. **200**, 1549–1554 (2005)
35. Kim, G.-T., Park, T.-K., Chung, H., Kim, Y.-T., Kwon, M.-H., Choi, J.-G.: Growth and characterization of chloronitroaniline crystals for optical parametric oscillators I. XPS study of Mo-based compounds. Appl. Surf. Sci. **152**, 35–43 (1999)
36. Wei, Z.B.Z., Grange, P., Delmon, B.: XPS and XRD studies of fresh and sulfided Mo_2N. Appl. Surf. Sci. **135**, 107–114 (1998)
37. Camacho-López, M.A., Escobar-Alarcón, L., Haro-Poniatowski, E.: Haro-Poniatowski, E.: Structural transformations in MoOx thin films grown by pulsed laser deposition. Appl. Phys. A **78**, 59–65 (2004)
38. Wu, J.-H., Rigney, D.A., Falk, M.L., Sanders, J.H., Voevodin, A.A., Zabinski, J.S.: Tribological behavior of WC/DLC/WS2 nanocomposite coatings. Surf Coat Technol **188–189**, 605–611 (2004)
39. Voevodin, A.A., Fitz, T.A., Hu, J.J., Zabinski, J.S.: Nanocomposite tribological coatings with chameleon friction surface adaptation. J. Vac. Sci. Technol. A **20**, 1434–1444 (2002)
40. Erdemir, A., Erck, R.A., Fenske, G.R., Hong, H.: Solid/liquid lubrication of ceramics at elevated temperatures. Wear **203–204**, 588–595 (1997)
41. Kutschej, K., Mitterer, C., Mulligan, C.P., Gall, D.: High-temperature tribological behavior of CrN-Ag self-lubricating coatings. Adv. Eng. Mat. **8**, 1125–1129 (2006)
42. Kumari, L., Ma, Y.-R., Tsai, C.-C., Lin, Y.-W., Wu, S.Y., Cheng, K.-W., Liou, Y.: X-ray diffractiom and Raman scatteringstudies on large-area array and nanobranched structure of 1D MoO_2 nanorods. Nanotechnology **18**, 115717 (2007)
43. Wenda, E.: High temperature reactions in the MoO_3-Ag_2O system. J. Therm. Anal. **53**, 861–870 (1998)

Plasma Treatment of Carbon Nanotubes

J.G. Jones[a], C. Muratore[a], A.R. Waite[a], and A.A. Voevodin[a]

[a]*Air Force Research Laboratory, Materials and Manufacturing Directorate*
Wright-Patterson AFB, OH, 45433-7746

This paper investigates plasma treatment of vertically aligned multi-wall carbon nanotubes (CNTs) treated in different plasma environments including for modification of surface chemistry and morphology. A pulsed plasma treatment was used to modify CNT surfaces by attaching N and H atoms. Optical emission spectroscopy was used to detect atomic and molecular excitation for the gas mixtures of pure hydrogen, pure nitrogen, pure argon, argon/hydrogen, and argon/nitrogen. Results demonstrated the presence of atomic, excited, and ionized species in the vicinity of the CNT sample surfaces. In situ X-ray photoelectron spectroscopy (XPS) was performed on the treated samples to examine CNT surface chemistry after treatment. The analyses show formation of both C-N and C-H bonds indicating CNT surface functionalization. Correlations of the plasma characteristics, chemistry, and bonding of the modified CNT surfaces are discussed for different environments.

Keywords: Multi-Wall Carbon Nanotubes, Plasma Treatment, Nitrogen, Hydrogen
Contact: john.jones@wpafb.af.mil

1. INTRODUCTION

Carbon Nanotubes (CNTs) are currently of tremendous interest in many research areas due to their unique properties of strength, thermal conductivity, electrical impedance, and chemical resistance. CNTs can be envisioned as a 2-D hexagonal array of carbon atoms rolled into tubes. Tube diameters can range from a few angstroms to tens of nanometers. Because of the possibility of different CNT diameters, single wall and multi-wall structures are possible. Ever since the discovery of CNTs, material scientists around the world have been studying them due to their properties[1] electrical conductivity and strength. One of the challenges in actual applications of CNTs is to functionalize the outer surface using hydrogen or nitrogen in order to both remove unbonded carbon sites as well as to change the surface interface in order to enable better mechanical adhesion. This work seeks to determine the ability to functionalize the CNT surfaces through the use of various plasma treatments.

By using a pulsed glow discharge plasma at low temperature and low pressure, functional groups can be attached to the CNT surface without causing significant structural damage[2]. The use of a pulsed power supply was chosen so that both conducting and insulating samples could be used as the cathode. This pulsed DC power supply was chosen over a RF power supply because it offers more flexibility in the process parameters and is therefore more powerful. With the pulsed power supply, the user specified parameters are the pulse frequency, the amplitude, the duty cycle, and reverse time. The reverse time is the duration that the polarity of the voltage is reversed in order to clear the buildup of charge by attracting particles of the opposite charge. This minimization of charging also tends to eliminate arcs. If arcs do occur, the arc

suppression circuitry extinguishes them in 5 to 200 μs, thereby eliminating any significant substrate damage.

With optical emission spectroscopy, specific wavelength optical emissions can be detected and continuously monitored during plasma treatment. These detected optical emissions are indicative of specific electronic transitions that occur due to both the plasma and plasma-surface interaction. Knowing the major species in the plasma assists in determining effective gas mixtures for obtaining the desired surface properties on the CNT arrays. XPS was chosen to analyze surface chemistry of the CNTs. XPS allows compositional analysis of the surface without penetrating into the sample allowing for direct analysis of the sample surface and degree of functionalization.

II. EXPERIMENT

Vertically aligned multi-wall CNTs were obtained from Rensselaer Polytechnic Institute for modification with a high power pulsed plasma treatment in order to attach nitrogen or hydrogen atoms to the unbonded C sites of the CNT surfaces. Samples were each sequentially placed in a UHV chamber and evacuated to 1.3×10^{-5} Pa before processing, first with an ion beam. Before the plasma treatment, the CNTs were sputter cleaned with an ion beam source for 5 seconds at 3.5 amps and 300 volts in an argon gas environment being leaked into the chamber through the ion beam at 4 sccm. The reactive plasma treatment was accomplished using an Advanced Energy DC Pinnacle Plus pulsed plasma source running at a nominal 600 volts, with a pulse frequency of 150 kHz, and a reverse time of 1 μs. Power was directly applied to the sample making it the cathode for the plasma source, while the ground for the power supply was connected to the chamber. Samples were exposed to the plasma for 50 seconds, Fig. 1. This configuration created a

plasma discharge around the CNT's. After processing each sample, the chamber was evacuated, a different gas ratio established, and the chamber pressurized to 4 Pa. The gases utilized in the plasma treatments were argon (Ar), hydrogen (H_2), and nitrogen (N_2). For each gas mixture, the chamber pressure was maintained at 4 Pa with a total gas flow rate of 50 sccm. This process was repeated for both hydrogen with argon and nitrogen with argon with ratios of 0, 20, 40, 60, 80, and 100% respectively. Spectra of each plasma gas mixture was collected with an Ocean Optics HR4000CG-UV-NIR high resolution spectrometer with a 200-1100 nm range, a fiber collection bundle coupling with fixed position focusing optics with spectrometer settings of an integration time of 1000 ms and a 4 scan average. The five gas mixtures utilized for plasma treatment of actual CNT carpet samples was as follows: 10 sccm Ar/40 sccm H_2, 40 sccm Ar/10 sccm H_2, 10 sccm Ar/40 sccm N_2, 40 sccm Ar/10 sccm N_2, and 50 sccm Ar.

X-ray photoelectron spectrometer (XPS) scans of the 5 treated samples were performed in situ under ultra high vacuum conditions in order to analyze the surface chemistry of the CNT's as shown in Fig. 1. The in situ XPS scans were performed using a Staib XPS system with a magnesium x-ray source operating at 100 watts. XPS scans of each sample were taken "as received", then again after a 5 second ion beam cleaning, and finally after the 45 second plasma surface treatment. From the XPS analyses, the relative peak heights were measured to obtain the CNT surface compositions. Ex-situ high resolution scans were also taken on selected samples, after they were exposed to the atmosphere.

III. RESULTS AND DISCUSSION

Spectra collected for mixtures of hydrogen and nitrogen with argon, Fig. 2, show predominantly excited transitions, such as H^* at 656.3 and 486.1 nm for the pure hydrogen case; and these two peaks having their maximum intensity in a mixture of 80% hydrogen and 20% argon. The excited hydrogen emission intensity for the case of having 100% hydrogen was actually comparable to having 20% hydrogen with 80% argon. For the cases of 20, 40, 60, and 80% hydrogen with the remaining percentage being argon, there seemed to be a monotonic increase in excited hydrogen emission, and a linear decrease in excited argon emissions, Fig. 2. The images of plasma emission from hydrogen and argon show a narrowing of the diameter of the plasma at the substrate surface with increasing hydrogen concentration. The images of plasma emission from nitrogen and argon show very little change with regard to nitrogen concentration, excluding the pure argon case. Optical emission spectra collected for nitrogen and argon do show subtle changes with increasing nitrogen concentrations, such as the increase in ionized nitrogen, N^{+1}, indicated by the peak located at 391 nm. All of the other nitrogen peaks increase in a more subtle fashion, but nonetheless increased with increasing nitrogen concentration. Table 1[3-9] details the detected species and corresponding transitions sorted by wavelength detected. The list corresponds with detected atomic and molecular, excited and ionized, nitrogen, excited hydrogen, and excited argon.

SEM images show the morphological changes that occur from the different plasma treatments, Fig. 3. The 80% nitrogen and to a lesser degree the 20% nitrogen plasma treatments show an increased surface roughness as well as clusters at the surface. The 80% hydrogen and less so the 20% hydrogen plasma treatments show a much

smoother surface that what was originally shown with the "as received" surface. No effect of exposure to air on surface morphology on this scale is observed.

In situ XPS characterization was performed without contaminating the samples through exposure to air, Fig. 4. Samples were processed first with a 5 second ion beam, and subsequently with a plasma for 45 seconds. For the case of the 80% and 20% nitrogen treated samples, there is clearly a N 1s peak present that was not present before. Clearly, the nitrogen plasma is causing bonding of nitrogen with the CNT's, and a small amount of O 1s indicative of oxygen contamination. For the 80% nitrogen treated sample, the XPS N 1s peak measurement represents 13% atomic nitrogen in the CNT sample. For the other two samples having been treated with 80% and 20% hydrogen, the XPS scans show minimal oxygen and nitrogen content through the small O 1s and N 1s peaks. XPS does not detect hydrogen bonding, but the carbon peak will be shifted subtly with hydrogen bonds.

Using a ex situ high resolution XPS, measurements were taken of selected samples to show the shift of the carbon peak, C 1s, with exposure to 80% hydrogen and nitrogen plasmas, Fig. 5. The first XPS C 1s peak was measured from an as received CNT carpet sample, showing a peak at 284.5 eV which corresponds to literature of C-C bonds being at 284.5-284.7 eV. The second sample analyzed ex situ was treated with 80% hydrogen, showing a shift in the C 1s peak to 285 eV, again in good agreement with literature of a C-H bond energy of 285 eV. Lastly, a sample treated with 80% nitrogen demonstrated an even larger peak shift, and again in good agreement with literature of C=N bonding being at 286.2 eV, and C-N bonding being at 287.23 eV. For reference, a C-O bond would show a peak location of 289-290 eV. This last sample treated in 80%

nitrogen showed an asymmetric peak, so clearly not all of the bonds are between carbon and nitrogen as there are many C-C bonds as well.

IV. CONCLUSIONS

Vertically aligned multi-wall carbon nanotubes on a silicon wafer were treated with both hydrogen and nitrogen based plasmas. Optical emission spectroscopy showed that maximizing the hydrogen concentration in a plasma requires some argon to significantly increase the excitation of hydrogen at room temperature and 4 Pa. Optical emission spectroscopy also showed that maximum nitrogen concentrations can be achieved with pure nitrogen, but 80% nitrogen was used for sample treatment for comparison with hydrogen treated samples. Using a pulsed plasma power supply with the sample acting as the cathode provides the ability for surface modification at room temperatures for the purposes of CNT functionalization.

4. References

References

1 S. Iijima, Nature **354**, 56 (1991).

2 H. Bubert, S. Haiber, W. Brandl, G. Marginean, M. Heintze, and V. Bruser, Diamond and Related Materials **12**, 811 (2003).

3 L. Y. Chen, C. Y. Cheng, and F. Chau-Nan Hong, Diamond and Related Materials **11**, 1172 (2002).

4 A. A. Voevodin, J. G. Jones, J. S. Zabinski, and L. Hultman, Journal of Applied Physics **92**, 724 (2002).

5 X. W. Liu, J. H. Lin, C. H. Tseng, and H. C. Shih, Materials Chemistry and Physics **72**, 258 (2001).

6 A. Khandelwal, H. Niimi, G. Lucovsky, and H. H. Lamb, Journal of Vacuum Science & Technology A: Vacuum, Surfaces, and Films **20**, 1989 (2002).

7 H. Seo, J. H. Kim, K. H. Chung, J. Y. Kim, S. H. Kim, and H. Jeon, Journal of Applied Physics **98**, 043308 (2005).

8 NIST Atomic Spectra Database. http://physics.nist.gov/PhysRefData/ASD/index.html Version 3.1.0. 2006.
Ref Type: Electronic Citation

9 D. R. Lide, in *CRC Handbook of Chemistry and Physics*, edited by D. R. Lide, Ed. 1995) ,chap. 10 p. 1.

Figure Captions

Figure 1: UHV Vacuum chamber used for Plasma Processing Multi-wall carbon nanotube carpets; with XPS surface analysis chamber available via sample transfer arms.

Figure 2: Plasma emission spectra recorded at 4 Pa background pressures for a) mixtures of argon and hydrogen and b) mixtures of argon and nitrogen.

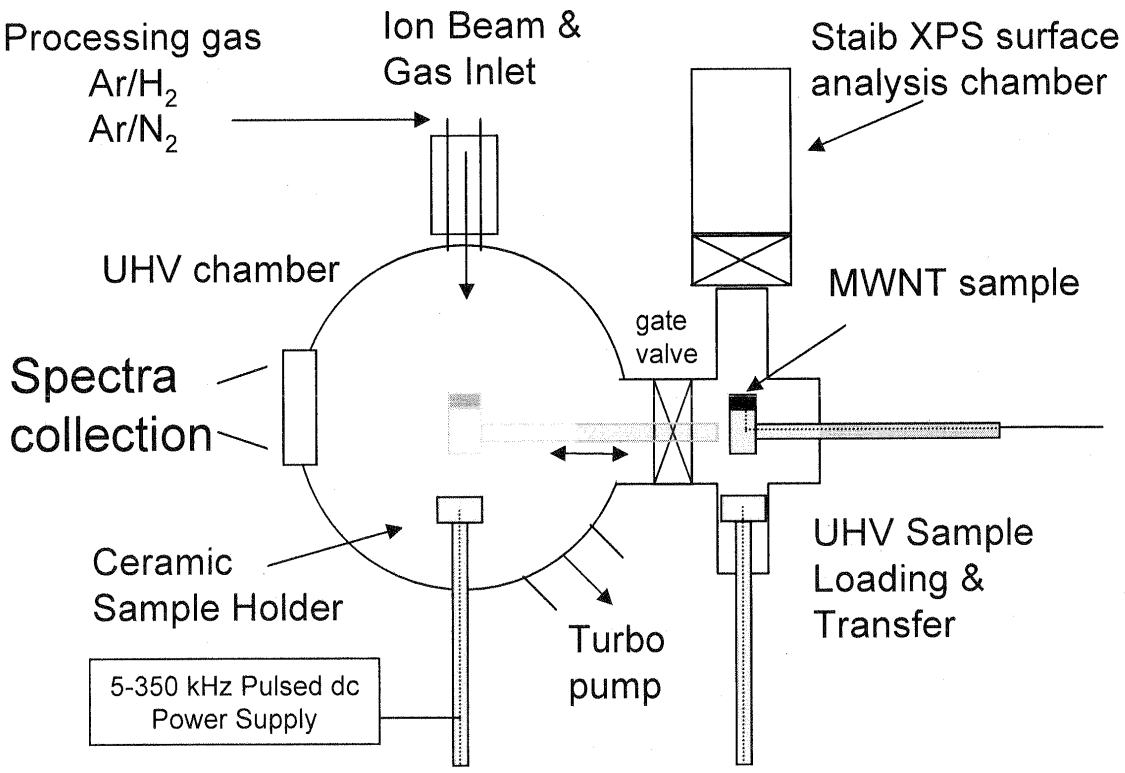
Table 1: Detected species, identified transitions, and corresponding wavelengths in nm.

Figure 3: SEM images for a) as received multi-wall nanotube carpet sample, b) sample after treatment with 80% N_2 / 20% Ar, c) after treatment with 20% N_2 / 80% Ar, d) after treatment with 80% H_2 / 20 % Ar, and e) after treatment with 20% H_2 / 80% Ar.

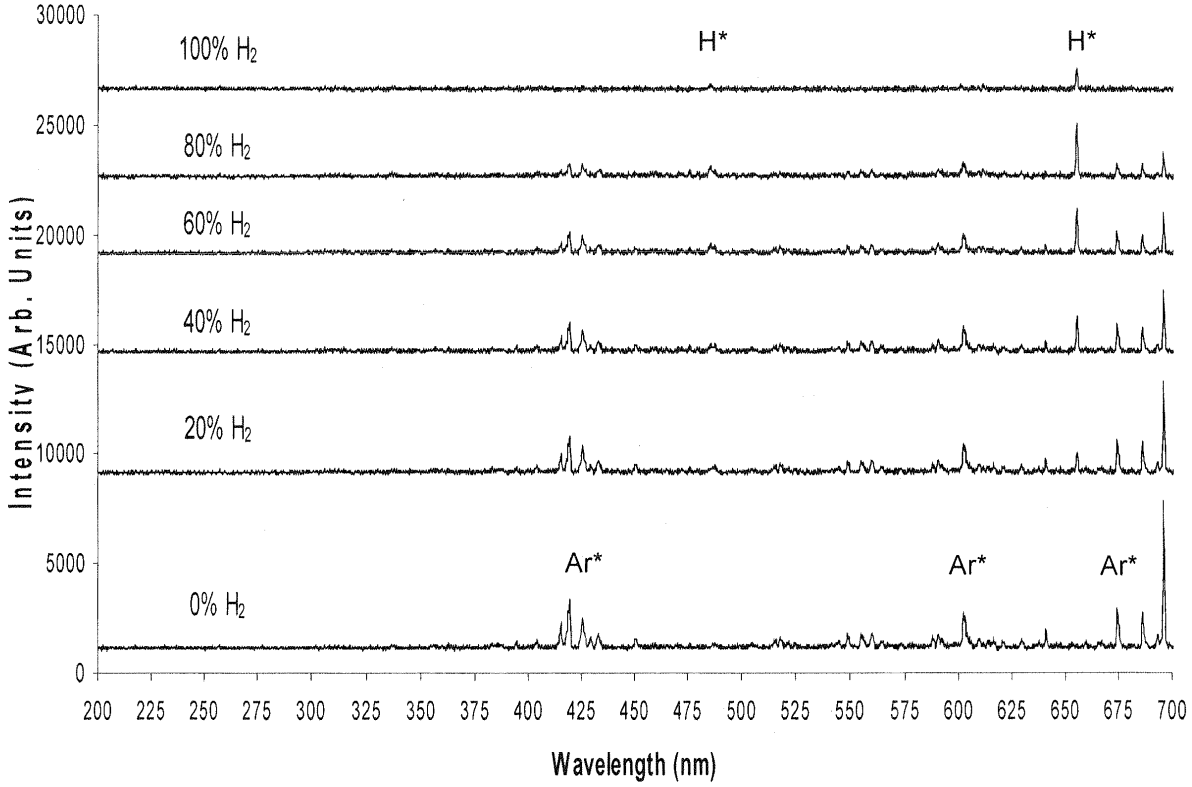
Figure 4: XPS scan after plasma treatment with four different environments of argon gas in combination with 80% & 20% N_2 and H_2, all at the same 4 Pa pressure.

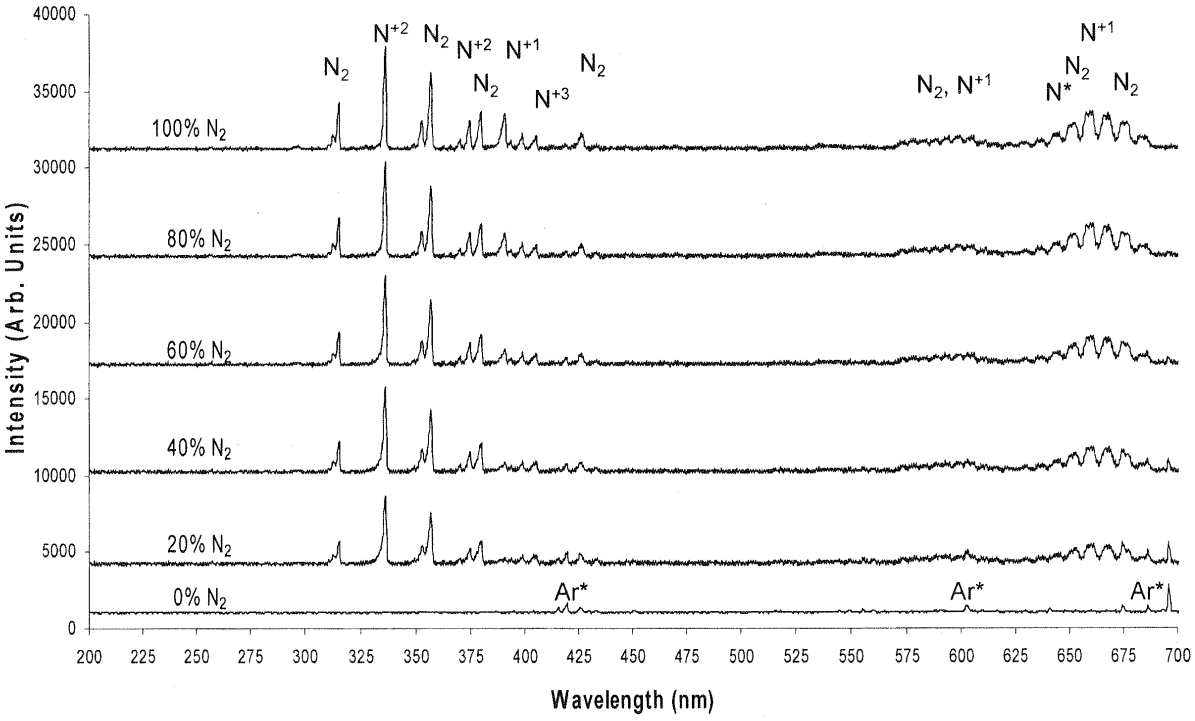
Figure 5: Comparison of XPS C1s bonding energies for a) as received multi-wall nanotube carpet, b) after treatment with 80% H_2 / 20% Ar, and c) after treatment with 80% N_2 / 20% Ar.

Jones, et. al.
Figure 1



Jones, et. al.
Figure 2 (a,b)



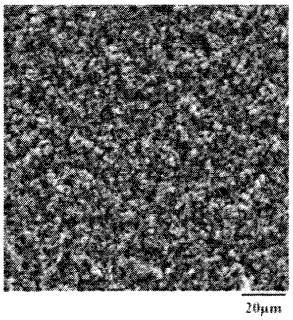


Jones, et. al.
Table 1

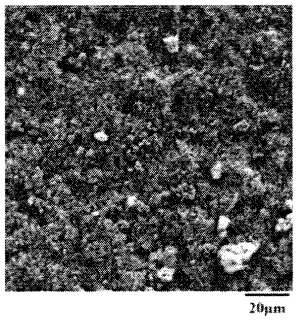
Specie	Transition	nm
N2 (2nd pos)	$C^3\Pi_u - B^3\Pi_g$	307-316
N2 (2nd pos)	$C^3\Pi_u - B^3\Pi_g$	315.4
N III	4P° - 4P	336.734
N2 II	$B^2\Sigma_h^+ - X^2\Sigma_g^+$	353.9
N2 II	$B^2\Sigma_h^+ - X^2\Sigma_g^+$	358
N2 (2nd pos)	$C^3\Pi_u - B^3\Pi_g$	370-380
N IV	1P° - 1 D	374.754
N2 (2nd pos)	$C^3\Pi_u - B^3\Pi_g$	380
N II	1P - 1P°	391.9
N II	1P° - 1D	399.5
N IV	1P° - 1D	405.776
Ar I	2[3/2]° - 2[3/2]	415.859
Ar I	2[3/2]° - 2[1/2]	419.8317
Ar I	2[1/2]° - 2[1/2]	425.9362
N2 (2nd pos)	$C^3\Pi_u - B^3\Pi_g$	427
Ar I	2[1/2]° - 2[3/2]	433.3561
H I	2p° - 2D	434.047
Ar II	2p - 2p°	476.4865
H I	2p° - 2D	486.133
N II	1P° - 3D	574.73
N2 (1st pos)	$B^3\Pi_g - A^3\Sigma_u^+$	536-612
N II	3P - 3D°	592.781
N II	3P - 3D°	595.239
N I	2S° - 2P	599.943
Ar I	2[3/2] - 2[1/2]°	602.515
Ar I	2[5/2] - 2[7/2]°	603.2127
N2 (1st pos)	$B^3\Pi_g - A^3\Sigma_u^+$	630-690
Ar I	2[1/2] - 2[3/2]°	641.6307
N III	4P - 4D°	646.702
H I	2p° - 2D	656.2852
N II	1D - 1F°	661.056
Ar I	2[1/2] - 2[3/2]°	675.2834
Ar I	2[1/2] - 2[1/2]°	687.1289
Ar I	2[3/2]° - 2[1/2]	696.5431

Jones, et. al.
Figure 3 (a,b,c,d,e)

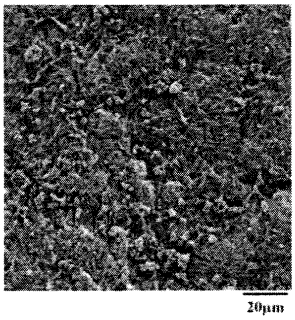
a) as-received



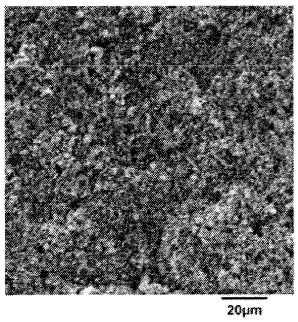
b) 80% nitrogen plasma



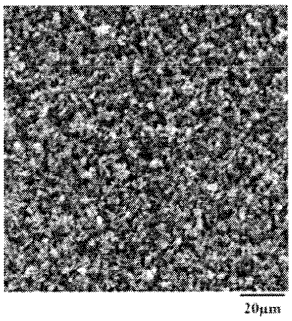
c) 20% nitrogen plasma



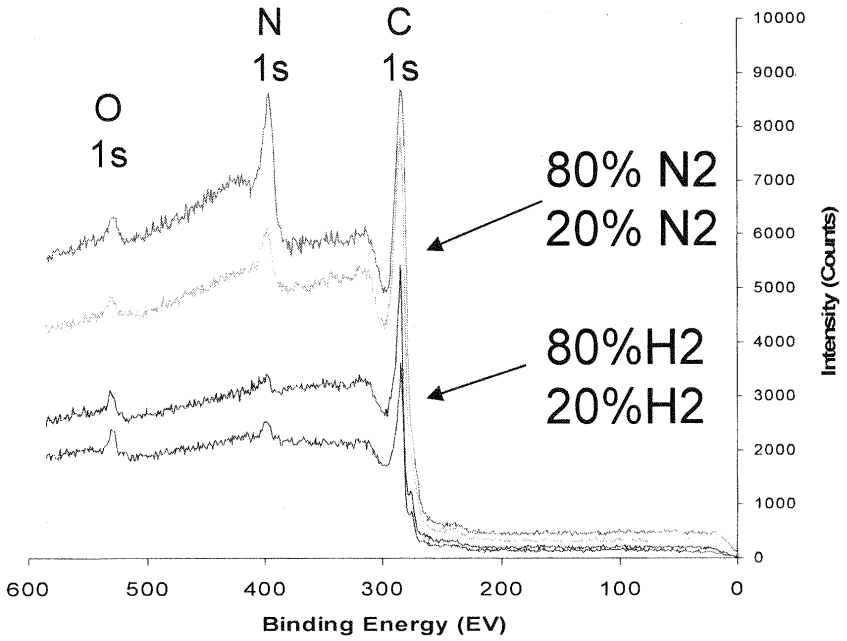
d) 80% hydrogen plasma



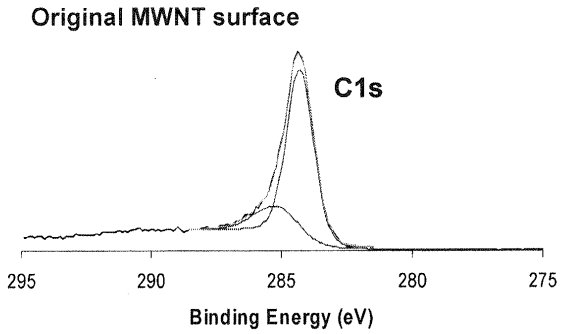
e) 20% hydrogen plasma

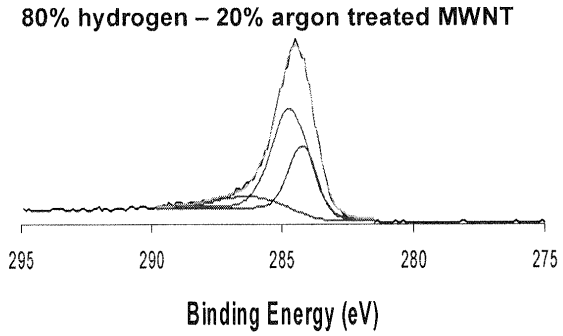


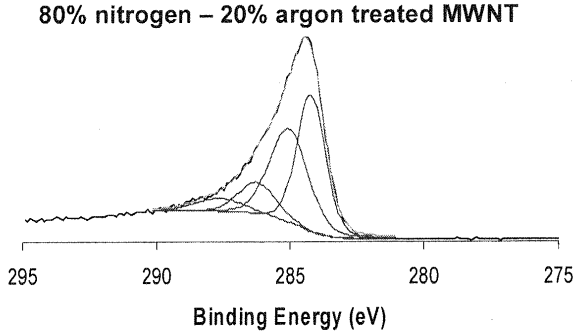
Jones, et. al.
Figure 4



Jones, et. al.
Figure 5 (a,b,c)







Paper 17

Electrical Switching Using Compliant Metal Infiltrated Multi-Wall Nanotube Arrays

Justin Bult[1], W. Gregory Sawyer[2], Andrey Voevodin[3], Chris Muratore[3], Pam Dickrell[2], Sunil Pal[1], Pulickel Ajayan[1], and Linda Schadler[1]

[1]Materials Science and Engineering, Rensselaer Polytechnic Institute, Troy, NY, 12180

[2]Mechanical and Aerospace Engineering, University of Florida, Gainesville, FL, 32611

[3]Air Force Research Laboratory, Wright-Patterson AFB, OH, 45433

ABSTRACT

The topology of conventional noble-metal-coated switch counterfaces creates modes of switch failure via fouling, arcing, and local melting when impacted. To avoid these failure phenomena, compliant conductive contact surfaces of vertically aligned multi-wall nanotube arrays grown on conductive substrates have been fabricated. Infiltration of the array by noble metal results in a robust compliant switch contact surface. Cyclic hot-switch testing of the nanotube based switch, via modified nano-indentation, results in performance surpassing conventional designs with stable resistance of 0.4Ω over 3000 cycles for 20mN contacting force. Investigating the physical performance of the array shows the array is compacted less than 3% over the first 500 cycles with no observable compaction through the remaining cycles. The improvement in performance of the nanotube based switch is attributed to the ability for the compliant contact surface to conform to the probe tip geometry, increasing the effective contact surface area.

INTRODUCTION

In metal-metal low-force electrical switch contacts there are a limited number of design variables to be considered. One can look at modifying the contacting configuration, the contacting force, or the contacting materials of the switch counterfaces. The fundamental criteria used to optimize these variables within the design envelope are the contact resistance and functional lifetime of the switch over a given operational range. To improve and prolong the switch operation, the detrimental effects of contamination, oxidation, and local welding must be avoided in the context of the design modifications being undertaken.

For the case of switch contact counterface material; the most conventional material is the gold-gold contact. Gold exhibits superior performance due to its inert nature, low potential to be oxidized, and low electrical resistance [1]. Yet the nature of the gold-gold contact causes asperity driven failure [2,3]. The true contact area of the counterfaces is considerably lower than would be calculated for theoretically ideal smooth surfaces [4]. This leads to excessive current being passed through asperity created constrictions and to reduced performance both in terms of resistance and switch lifetime [3].

An as yet unexplored avenue for a switch contacting material is a contacting surface with a tailored compliant counterface with conductivity and thermal stability similar to that of the noble metals already in use. To produce such a material, a composite approach is undertaken herein; combining the elastic capability of vertically aligned carbon nanotubes [5] with the conductive properties of gold and silver. Aligned arrays of conductive carbon nanotubes, grown on a conductive metal substrate, are infiltrated with gold and silver to produce a switch surface with a significantly lower elastic modulus than a solid metal contact.
As previously reported, vertically aligned arrays of carbon nanotubes are exceptionally compliant when subjected to a compressive stress with an elastic modulus of approximately 50 MPa [5] (as compared to 77GPa for pure gold). Furthermore, it has been shown that even with deformations in excess of 85%, the nanotube array will maintain its mechanical integrity and return to its unloaded length with only modest permanent deformation occurring in the initial cycles [5]. By combining the elasticity of the carbon nanotube with a metallic coating, a metallic "sponge" is created. The switch performance characteristics of these composite materials are explored here using a nano-indenter configured for electrical contact resistance measurement.

EXPERIMENT

Materials

Vertically aligned multi-wall carbon nanotubes were grown on Inconel 600™ substrates using a Chemical Vapor Deposition growth furnace using ferrocene/xylene for the catalyst and carbon source respectively as described in [6]. Growth on this substrate has previously been shown to give excellent electrical contact to the nanotubes [6]. The nanotubes were grown to approximately 100μm over a 2cm by 2cm Inconel 600™ substrate. Figure 1 shows the basic carbon nanotube array grown on the Inconel™ substrate.

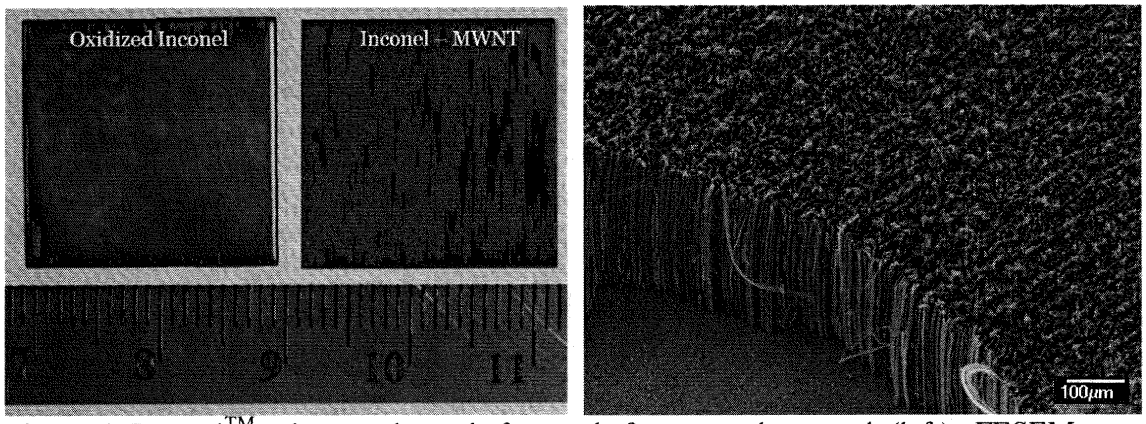


Figure 1. Inconel™ substrate shown before and after nanotube growth (left). FESEM micrograph of the MWNT growth cross-section (right).

The carbon nanotube array was infiltrated with gold and silver using a physical vapor deposition (magnetron sputtering) system as described in [7]. The deposition was carried out until a thin layer of metal roughly 5μm thick is formed on the outer surface as shown in Figure 2.

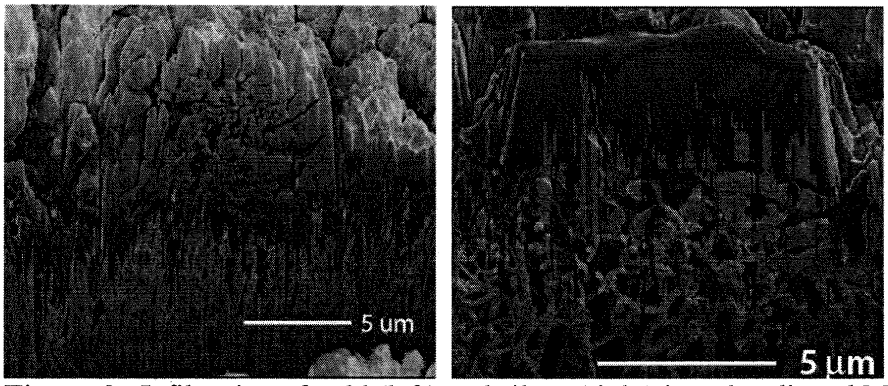


Figure 2. Infiltration of gold (left) and silver (right) into the aligned MWNT array. Both metals are deposited along the entire nanotube length and are topped by an approximate 5µm thick metal canopy.

Methods

To test the composite material's hot-switching performance, a modified MTS nano-indenter was employed for electrical contact resistance measurements. For each cycle, contact and compression is followed by a dwell period of 0.75 seconds while in contact, with subsequent tip withdrawal; each cycle takes a total of 2.5 seconds. The contact cycle is repeated for 3000 cycles to generate the electrical performance analysis, with 5V supplied voltage (hot-switched) and 5mA supplied current. The indenting surface for the switch experiments is a 2mm diameter gold coated sphere. The contacting force measured for each cycle was approximately 25mN, with voltage drop at less than 1mN. Figure 3 shows the force and voltage data for cycles 10, 100, 1000, and 3000 during the gold infiltrated test.

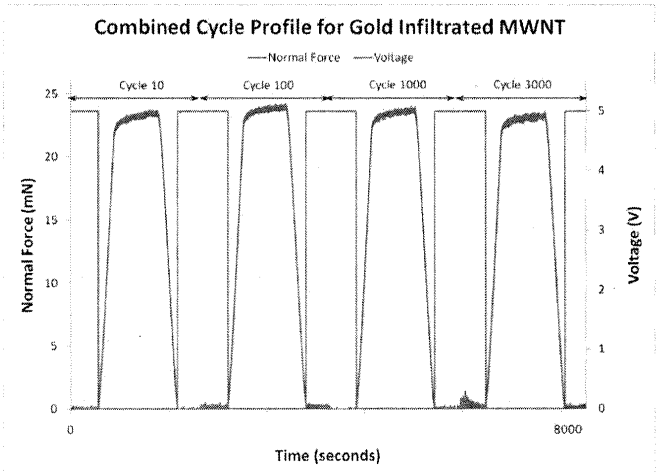


Figure 3. Representative cycle data for gold infiltrated switch experiment.

RESULTS AND DISCUSSION

A key concern in switch performance is its mechanical integrity over time. For a compliant substrate the concern is the durability of the spring-like supportive nanotube base material. Permanent substrate depression would cause a deterioration of performance over time and indicate a shorter life span for the switch. Such deformation, while not plastic by the continuous material definition, is caused by nanotubes moving past each other and losing their group supporting characteristic. Figure 4 gives the displaced compression of the bare nanotube (no metal infiltration), gold infiltrated, and silver infiltrated nanotubes as a function of the cycle/time.

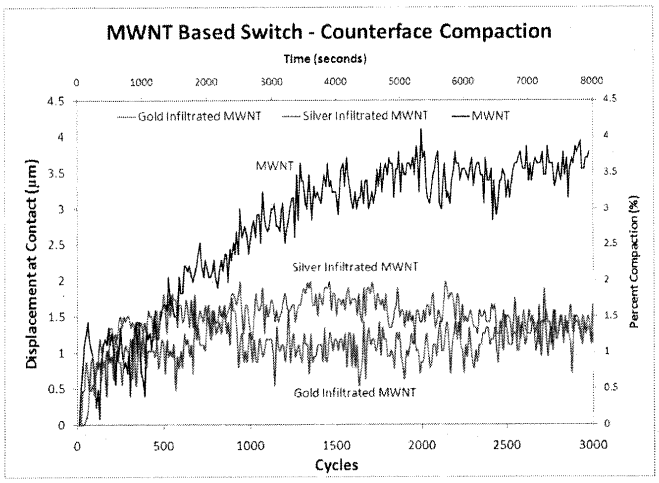


Figure 4. Displacement to contact profile for gold infiltrated, silver infiltrated, and bare nanotubes as a function of cycle/time.

From Figure 4 it can be seen that infiltration of metal reinforces the nanotube array. This is demonstrated via the reduced percent compaction and greater stability over time as compared to the bare nanotube array. The reinforcement is caused by the thin metal film tying the nanotube tips together, inhibiting the movement of the underlying nanotube structure. In the base nanotube material (without metal infiltration) there is no inhibition of this movement, permitting the nanotubes to move past each other causing a prolonged deformation region relative to the metal infiltrated samples. Figure 4 also shows that permanent deformation of the metal infiltrated samples is complete after 500 cycles with negligible compaction thereafter.
The resistance of a switch is the primary determinant of performance over time. Greater resistance generally indicates an increase in surface contamination and a reduction in the usable contact area for current passage. The causes of this performance degradation are most often attributed to asperity/constriction derived heating of the conducting pathways. Over time, the asperities develop oxides and contaminants due to the extreme heat generated when large currents are passed through the constricted pathway.
Figure 5 shows the results of the resistance measurements as a function of cycles/time for the base nanotube array, gold infiltrated array, and the silver infiltrated array. In the Y-axis there is a break indicating the large disparity between the resistance of the bare nanotubes and the metal infiltrated nanotube arrays.

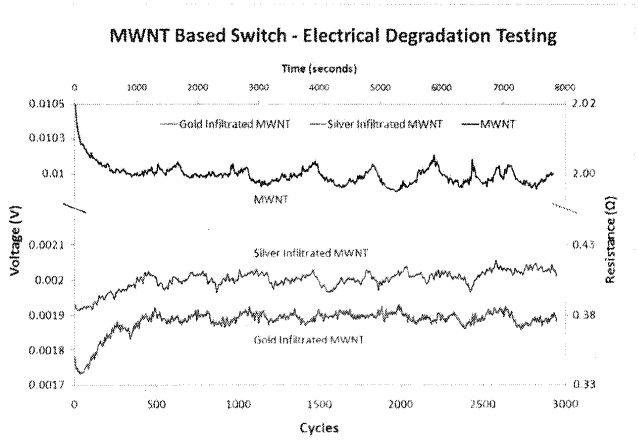


Figure 5. Voltage profile for gold infiltrated, silver infiltrated, and bare nanotubes. The dependent axis is broke to allow the larger resistance of the bare nanotubes to be plotted.

It is noteworthy that stability is achieved within the 500 cycle window observed in the compaction analysis. The resistance values of ≈0.4Ω achieved for the gold infiltrated nanotube array is similar to previously reported gold-gold based elastic switch contacts [8] utilizing similar contact force. Considering the significant increase in resistance between the gold infiltrated nanotube array and the base multiwall nanotube array (no infiltration), it is likely that the gold is the conductive medium and not the nanotubes. This assertion relegates the nanotubes to a predominantly mechanical support role in the switch.

The argument in the analysis above is that the surface compliance of the nanotube support affords much greater surface area to be in contact during compression. This greater surface area alleviates the constriction based failure modes by lowering the current density in any given electrical pathway. Knowing the surface roughness and mechanical properties of the contacting surfaces, a plot of the contacting area can be generated for a compliant substrate and a standard gold-gold contact. Figure 6 shows the result of this calculation for the metal-nanotube based contact and a standard metal-metal contact. Note that the load in the nanotube-metal switch scenario is 1 μN whereas the metal-metal contact is 100 μN. Based on these calculations it is clear that the contact surface area is significantly greater for the compliant surface contact.

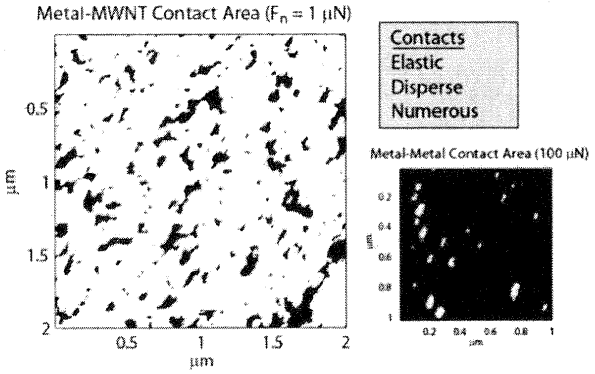


Figure 6. Analysis of contacting surface area for a nanotube surface (left) and a metal contacting surface (right). White indicates areas in contact between switch surfaces.

CONCLUSIONS

It has been shown that a robust and low resistance switch can be fabricated using a conductive, compliant counterface made of metal infiltrated aligned carbon nanotube arrays. Analyzing the compaction data as well as the resistance data shows that there is little to no degradation of the switch performance, either mechanical or electrically, across all 3000 cycles at moderate contact force. Stabilization of the switch surface occurs within 500 cycles of initial compression for both the silver and gold infiltrated switches. The enhanced longevity and performance (3000 cycles and 0.4Ω respectively) of the compliant switch surface has been attributed to the significant increase in contact surface area allowing for a reduction in current density. Furthermore, the fabrication process shows promise for dimensionally scaling down the process for low load micro-switch applications.

ACKNOWLEDGMENTS

This material is based upon an AFOSR-MURI grant FA9550-04-1-0367. Any opinions, findings, conclusions or recommendations expressed in this material are those of the authors and do not necessarily reflect the views of the Air Force Office of Scientific Research.

This work was also supported by the Nanoscale Science and Engineering Initiative of the National Science Foundation under NSF Award Number DMR-0117792.

Additional funding came from NASA GSRP grant number NNJ05JG72H under the auspices of Johnson Space Center.

REFERENCES

1. D. Hyman and M. Mehregany, *IEEE Transactions on Components and Packaging Technology* **22**, 357 (1999)
2. J.W. Tringe, T.A. Uhlman, A.C. Oliver and J.E. Houston, *J. App. Phys.* **93**, 4661 (2003)
3. J.W. Tringe, W. Wilson and J. Houston, "Reliability, Testing, and Characterization of MEMS/MOEMS," ed. R. Ramesham (*Proc. SPIE, 2001*) **4558** pp. 151-158.
4. J.A. Greenwood and J.P. Williamson, *Proc. Royal Soc. (London)* **A295**, 300 (1966).
5. A. Cao, P. Dickrell, W.G. Sawyer, M. Ghasemi-Nehjad and P.M. Ajayan, *Science* **310**, 1307 (2005).
6. S. Talapatra, S. Kar, S. Pal, R. Vajtai, L. Ci, P. Victor, M. Shaijumon, S. Kaur, O. Nalamasu, P. Ajayan, *Nature Nanotechnology* **1**, 112 (2006).
7. W. Li, S. Xie, L. Qian, B. Chang, B. Zou, W. Zhou, R. Zhao, G. Wang, *Science* **274**, 1701 (1996).
8. S. Hannoe and H. Hosaka, *Microsystem Technologies* **3**, 31 (1996).